

**Comparing Gaussian and Bessel-Gauss Beams for
translating Ultrafast Laser Ablation towards Soft Tissue
Surgery**

Donald Roddy Risbridger

Submitted for the degree of Doctor of Philosophy

Heriot-Watt University
School of Engineering and Physical Sciences

September 2022

The copyright in this thesis is owned by the author. Any quotation from the thesis or use of any of the information contained in it must acknowledge this thesis as the source of the quotation or information.

Abstract

The goal of this research was to further improve existing ultrafast laser surgery techniques. To do so, different beam shapes (Bessel-Gauss and Gaussian) were compared for performing ultrashort picosecond pulsed surgery on various soft biological tissues, with the goal of minimising collateral thermal damage.

Initially, theoretical modelling was performed using OpticStudio to test axicons of various conical angles. A 20° axicon was selected, but unfortunately early tests on murine intestinal tissue indicated a lack of sufficient intensity to achieve plasma-mediated ablation of the tissue with the 6ps input pulses of 85 μ J energy. Subsequently, a reimaged setup was designed in OpticStudio to demagnify the beam by a factor of 1.4x. The ability of this demagnified Bessel-Gauss beam to perform plasma-mediated ablation of murine intestinal tissue was confirmed through histological analysis. Another setup was also designed to produce a Gaussian beam of equivalent spot size.

These beams were then tested on porcine intestinal tissue using lower pulse repetition rates of 1, 2 and 3 kHz, with optimal ablation and thermal damage margins of less than 20 μ m (confirmed through histological analysis) being achieved with the Bessel-Gauss beam for spatial pulse overlaps of 70%, while for the Gaussian beam the prominence of cavitation bubble formation at both 2 and 3 kHz inhibited the respective ablation processes at this same spatial pulse overlap. As the numbers of passes were increased, the Bessel-Gauss beam also showed a trend of increased ablation depths. This was attributed to its large depth of focus of over 1 mm, compared to the theoretical 48 μ m depth of focus for the Gaussian beam.

After characterisation of fixated, non-ablated porcine intestine sample surfaces to quantify the inhomogeneity, another set of ablation trials was performed at higher pulse repetition rates (5, 10 and 20 kHz) to test more clinically viable processes. For the Bessel-Gauss beam, spatial pulse overlaps of up to around 50% at 5, 10 and 20 kHz offered excellent thermal confinement (with damage margins of < 30 μ m, < 50 μ m and < 25 μ m respectively) and shape control, but at 70% and greater pulse overlaps the ablated feature became hard to control despite good thermal confinement (< 40 μ m).

The Gaussian beam, while having the advantage of achieving plasma formation at lower input pulse energies, was again found to be more prone to undesirable cavitation effects. Cavitation bubbles were observed in the histology images for spatial pulse overlaps as low as 15% for 5 kHz and 30% for both 10 and 20 kHz. From the histology images it is clear to see that these effects became more pronounced as the pulse repetition rate was increased. Conversely, the more consistent spot size of the Bessel-Gauss beam across its longer focal depth resulted in a higher tolerance to cavitation bubble formation. This was also demonstrated by high-speed videos of the beams being scanned across porcine skin samples. This could be significant as it may allow for higher ablation rates. In addition, it could ease the design constraint of the maximum speed at which the beam can be scanned at the distal end of an endoscopic device.

Despite this, both beams were able to achieve distinct ablation with high thermal confinement for certain parameters. This work further highlights fibre-delivered ultrashort laser pulses as a promising alternative to existing endoscopic tumour resection techniques, which carry a higher risk of bowel perforation.

Acknowledgements

To begin, I would like to express my gratitude to Prof. Jonathan Shephard for his guidance, insight and enthusiasm throughout my research, as without his experience, patience and consideration this thesis would not have been possible. Similarly, I am thankful to Dr. Rainer Beck, who was always willing to take the time to discuss ideas with me, help with any experimental issues that arose and train me on various procedures and pieces of equipment. I would also like to thank my former colleague Dr. Mohanan, who was continually happy to answer any questions I had and provide helpful feedback during our group meetings.

In addition, I appreciate the support provided by various other members of staff within Heriot-Watt University. These include my second supervisor Prof. Robert Thomson for his support, as well as Dr. Richard Carter and Dr. Aongus McCarthy, who provided invaluable guidance regarding the theory and modelling of various axicons. I am also grateful to all the AOP group members for the assistance and friendly work environment they provided, as well as the School of Engineering and Physical Sciences for providing me with a James Watt Scholarship to carry out this project. Other members of staff at Heriot-Watt I owe thanks to include Sara Medina-Lombardero and Dr. Laura Charlton, both of whom generously offered their time to help me with the cryogenically preserved porcine skin tissue experiments towards the end of my project, as well as Neil Ross, who trained me in the use of clean-room equipment, and the biological safety officer Paul Cyphus, who made our biological tissue experiments possible.

I also am extremely grateful for the collaborative efforts of the staff based at the Leeds Institute of Medical Research at St. James's. These include Thomas Maisey, without whom the histological images presented within this thesis could not have been obtained, as well as Prof. David Jayne and Dr. Nicholas West, who were also very generous with their time through providing incredibly insightful analysis of the observed features.

Additionally, I would like to thank my parents, my two brothers, and my partner Jennifer, who have always shown me unconditional love and support, and through doing so continue to motivate me, along with my many friends and family. Throughout my many years of study they have helped to appreciate what I have already achieved, yet understand why hopefully many years of further research lie ahead for me in order to fulfill my potential.

Finally, I would like to express my sincere debt of gratitude to the late Dr. Kevin Costello, Head of Science at Wick High School. Dr. Costello inspired me to pursue further education in physics courtesy of his charisma, sense of humour, humility, and genuine passion for both the subject itself and the craft of teaching. He inspired me to pursue physics as my chosen career.

Research Thesis Submission

Please note this form should be bound into the submitted thesis.

Name:	Donald Roddy Risbridger		
School:	Engineering and Physical Sciences		
Version: <i>(i.e. First, Resubmission, Final)</i>	Final	Degree Sought:	Doctor of Philosophy

Declaration

In accordance with the appropriate regulations I hereby submit my thesis and I declare that:

1. The thesis embodies the results of my own work and has been composed by myself
2. Where appropriate, I have made acknowledgement of the work of others
3. The thesis is the correct version for submission and is the same version as any electronic versions submitted*.
4. My thesis for the award referred to, deposited in the Heriot-Watt University Library, should be made available for loan or photocopying and be available via the Institutional Repository, subject to such conditions as the Librarian may require
5. I understand that as a student of the University I am required to abide by the Regulations of the University and to conform to its discipline.
6. I confirm that the thesis has been verified against plagiarism via an approved plagiarism detection application e.g. Turnitin.

ONLY for submissions including published works

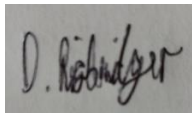
Please note you are only required to complete the Inclusion of Published Works Form (page 2) if your thesis contains published works)

7. Where the thesis contains published outputs under Regulation 6 (9.1.2) or Regulation 43 (9) these are accompanied by a critical review which accurately describes my contribution to the research and, for multi-author outputs, a signed declaration indicating the contribution of each author (complete)
8. Inclusion of published outputs under Regulation 6 (9.1.2) or Regulation 43 (9) shall not constitute plagiarism.

* Please note that it is the responsibility of the candidate to ensure that the correct version of the thesis is submitted.

Signature of Candidate:		Date:	
-------------------------	--	-------	--

Submission

Submitted By <i>(name in capitals):</i>	DONALD RODDY RISBRIDGER
Signature of Individual Submitting:	
Date Submitted:	30/9/22

For Completion in the Student Service Centre (SSC)

Limited Access	Requested	Yes	No	Approved	Yes	No
<i>E-thesis Submitted (mandatory for final theses)</i>						
Received in the SSC by <i>(name in capitals):</i>		Date:				

Contents

Chapter 1 – Introduction	1
1.1 Overview of minimally invasive laser surgery	1
1.2 Brief history of the medical applications of lasers	1
1.3 Bowel cancer	5
1.4 Motivation behind ultrafast laser-based resection processes	8
1.5 Thesis outline	15
1.6 References	16
Chapter 2 – Background	22
2.1 Laser-tissue interactions	22
2.1.1 Photochemical interactions	22
2.1.2 Photothermal interactions	23
2.1.3 Plasma-mediated ablation	26
2.1.4 Secondary effects of plasma-mediated ablation of tissue	30
2.1.5 Surgical applications of plasma-mediated ablation	34
2.1.6 Gaussian beams	36
2.1.7 Bessel beams	38
2.1.8 Alternative beam shaping techniques	45
2.2 Surgical devices	46
2.2.1 Non-laser-based surgical devices	46
2.2.1.1 Scalpel	46
2.2.1.2 Electrosurgery	47
2.2.1.3 Harmonic scalpel	51
2.2.2 Early laser-based surgical devices	52
2.3 Minimally invasive laser surgery	59
2.3.1 Brief history of minimally invasive procedures	59
2.3.2 Ultrashort laser pulses in minimally invasive surgery	62
2.4 Optical fibres for minimally invasive laser surgery	72
2.4.1 Negative curvature and photonic bandgap fibres	72
2.4.2 Kagome fibres	76
2.5 Bespoke endoscopic devices	77
2.6 Review summary	87
2.7 References	89

Chapter 3 – Bessel-Gauss beam modelling and characterisation, 106
experimental methodology and murine intestinal
tissue ablation trials

3.1 Theoretical modelling of Bessel-Gauss beams	106
3.1.1 Laser simulation methods within OpticStudio	106
3.1.2 Physical Optics Propagation (POP) modelling of axicons	108
– time-averaged total power model	
3.1.3 Physical Optics Propagation (POP) modelling of axicons	113
– peak irradiance model	
3.2 Bessel-Gauss beam characterisation	116
3.3 Physical axicon characterisation	122
3.4 Experimental methodology	124
3.4.1 Tissue ablation parameters	124
3.4.2 Tissue handling process for ablation trials	125
3.4.3 Histological and three-dimensional surface profilometry	126
post-ablation analysis of tissue samples	
3.5 Initial Bessel-Gauss beam material processing trials	129
3.6 Preserved porcine tissue ablation trials	129
3.7 Murine intestinal tissue ablation trials	131
3.8 References	137

Chapter 4 – Optical redesign for lower pulse repetition rate 139
porcine intestinal tissue ablation trials

4.1 Optical redesign	139
4.1.1 Design of reimaged Bessel-Gauss beam setup	139
4.1.2 Design of Gaussian beam setup	141
4.2 Spot size measurements	144
4.2.1 BP209-VIS/M profiler measurements	144
4.2.2 Stainless steel damage threshold test measurements	145
4.3 Initial ablation trials with redesigned setups	146
4.3.1 Ablation tests on preserved porcine tissue samples	146
4.3.2 Successive ablation trials on murine intestinal tissue	149
samples	
4.3.3 Initial low pulse repetition rate ablation trials on porcine	154
intestinal tissue samples	
4.3.4 Optical cage system orientation redesign	161

4.3.5 Successive low pulse repetition rate ablation trials on porcine intestinal tissue samples	163
4.4 References	179
Chapter 5 – Ablation of porcine intestinal tissue at higher pulse repetition rates	181
5.1 Characterisation of Carbide laser	181
5.2 Surface characterisation of porcine intestinal tissue samples	182
5.3 5 kHz ablation of porcine intestinal tissue samples with Bessel-Gauss beam	184
5.4 5 kHz ablation of porcine intestinal tissue samples with Gaussian beam	188
5.5 10 kHz ablation of porcine intestinal tissue samples with Bessel-Gauss beam	190
5.6 10 kHz ablation of porcine intestinal tissue samples with Gaussian beam	193
5.7 20 kHz ablation of porcine intestinal tissue samples with Bessel-Gauss beam	196
5.8 20 kHz ablation of porcine intestinal tissue samples with Gaussian beam	198
5.9 Summary of higher pulse repetition rate ablation trials	200
5.10 High-speed imaging of ablation process on cryogenically preserved porcine skin tissue samples	205
5.11 References	210
Chapter 6 – Conclusions and Future Work	212
6.1 Conclusions	212
6.2 Future work	214
6.3 References	218
Appendix 1a	220
Appendix 1b	220
Appendix 2a	221
Appendix 2b	221
Appendix 2c	221
Appendix 2d	222

List of Publications

Journal paper:

Donald R. Risbridger, Rainer J. Beck, Thomas I. Maisey, Nicholas P. West, David G. Jayne, Jonathan D. Shephard, *Comparison of Gaussian and Bessel-Gauss Beams for Surgical Resection of Soft Biological Tissues via Ultrafast Laser Ablation*, Manuscript circulated for internal comments prior to submission to Biomedical Optics Express.

Conference contributions:

Donald R. Risbridger, Rainer J. Beck, Thomas I. Maisey, Nicholas P. West, David G. Jayne, Jonathan D. Shephard, *Comparing Bessel-Gauss and Gaussian beams for ultrashort pulsed laser surgery*, Frontiers in Ultrafast Optics: Biomedical, Scientific, and Industrial Applications XXII, San Francisco, California, United States, SPIE Photonics West, 2022, Oral presentation.

Jonathan D. Shephard, Rainer J. Beck, Ioannis Bitharas, Katjana Ehrlich, Thomas I. Maisey, James Moor, Andrew J. Moore, **Donald R. Risbridger**, Robert R. Thomson, David G. Jayne, *Picosecond lasers for precision resection of soft tissues*, Frontiers in Ultrafast Optics: Biomedical, Scientific, and Industrial Applications XXII, San Francisco, California, United States, SPIE Photonics West, 2022, Invited Paper.

Donald R. Risbridger, Rainer J. Beck, Syam M. P. C. Mohanan, Jonathan D. Shephard, Aongus McCarthy, Mike Shires, David Jayne, *Novel optical technologies for ultrashort pulsed laser surgery*, Clinical and Preclinical Optical Diagnostics II, Vol. EB101 of SPIE Proceedings, paper 11075_57, SPIE/OSA European Conferences on Biomedical Optics (ECBO), 2019, Munich, Germany.

Syam M. P.C. Mohanan, Rainer J. Beck, **Donald R. Risbridger**, Sarah L. Perry, Mike Shires, David Jayne, Duncan P. Hand, Jonathan D. Shephard, *Preclinical evaluation of ultrashort pulsed laser surgery*, Health innovation and Technologies Festival, Edinburgh, UK, 2019, Poster Presentation.

Chapter 1

Introduction

1.1 Overview of minimally invasive laser surgery

Research into minimally invasive laser surgery is becoming increasingly important as cancer rates (including bowel cancer) within the UK continue to increase [1.1]. Globally, cancer is one of the leading causes of death worldwide [1.2]. With these trends in mind, it is easy to see why diagnosing various types of cancer as early as possible is such a prominent field of research within the global scientific community.

The particular research field of surgical applications of pulsed lasers dates back to 1960, with the invention of the pulsed Ruby laser by Theodore H. Maiman at Hughes Research Laboratories [1.3]. Soon after, it was accurately predicted that lasers would prove to be an invaluable tool within clinical environments [1.4]. This was even experimentally trialled in the same year [1.5].

The science behind this field is interdisciplinary, incorporating topics from physics, chemistry and biology. Aspects of physics include the consideration of laser systems, the various optical elements to be implemented and consequently the optimal imaging modality to use. Meanwhile, the primary aspects of chemistry and biology involved are centred around the characterisation and histology of numerous kinds of biological tissue based on their chemical and physical properties [1.6].

1.2 Brief history of the medical applications of lasers

The first recorded application of a laser within a medical context occurred in 1962, when a dermatologist named Leon Goldman used the pulsed ruby laser to remove unwanted tattoos [1.7]. Prior to this he had also showcased how the ruby laser could be used to remove melanomas and certain birthmarks from the skin. He also went on to carry out the first objective study of the effect of laser light on human skin [1.8].

Regarding ocular surgery, in 1961 it was observed that photocoagulation of retinal tissue was possible via the use of a laser, with experiments undertaken on rabbits [1.9]. Shortly after, ruby lasers were used to repair human retinal tissue and for ablating malignant melanomas and adenocarcinoma of human origin that were implanted in Syrian hamsters, as highlighted in figure 1.1 [1.10],[1.11]. Photocoagulation of the retina had been carried out previously using a xenon arc source, but this required exposure times of one second and consequently was painful for patients [1.12]. The ruby laser, despite having around a quarter of the power of the xenon arc source, was still able to achieve photocoagulation of the retina thanks to the temporal confinement provided by the one millisecond pulse length. However, the 694 nm wavelength of the ruby laser was suboptimal for absorption by the blood vessels and biological tissue in general (aside from melanin) [1.13].

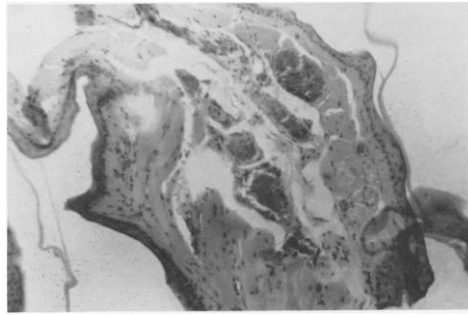


Figure 1.1 – Photomicrograph of excised Syrian hamster cheek pouch, with no tumour cells being observed after ruby laser treatment [1.11].

In the same year as the construction of the ruby laser by Maiman, the helium–neon (HeNe) laser was being developed by Javan *et al.* [1.14]. Following this, the neodymium doped yttrium–aluminium–garnet laser (Nd:YAG) was created by Johnson in 1961, the argon ion laser (Ar+) was designed by Bennett *et al.* in 1962, and the carbon dioxide (CO₂) laser was invented by Patel in 1964 [1.15],[1.16],[1.17]. This was later followed by the development of the erbium-doped yttrium aluminium garnet (Er:YAG) laser in 1975 [1.18]. The distinct emission wavelengths of each of these laser systems would be the subject of significant research interest. Staying within a medical context, the HeNe laser has been used to kill bacteria and for carrying out both blood analysis and intravenous therapy [1.19],[1.20]. The Nd:YAG laser is one of the most widely used in medicine, as despite water having a low absorption coefficient at its primary emission wavelength of 1064 nm (resulting in minimal damage for cell isolation studies), it is highly absorbed by various chromophores and haemoglobin, resulting in applications ranging from hair removal to oral surgery and the treatment of skin cancer [1.21],[1.22],[1.23]. Notably, it was also adopted by larger hospitals in the 1980s for the new field of laparoscopic surgery (also referred to as minimally invasive surgery), although being a continuous wave (CW) system these procedures suffered from heat accumulation, causing the tissue around the target sites to incur damage [1.24]. The argon laser, despite being inefficient due to losses from heat production, was found to be highly absorbed by haemoglobin, resulting in it being used for retina treatments as well as treating lesions found in both the skin and endometrium [1.25]. The CO₂ laser is of particular significance, as it is still one of the most commonly used in medical sciences to this day [1.26]. It owes this success to its infrared emission wavelength (10.6 µm) being highly absorbed by water, which is abundant in biological samples. This led to intense medical research interest across various fields, ranging from dermatology to gynaecology and general surgery [1.27]. The Er:YAG laser (wavelength of 2.94 µm) has similarly been subject to incorporation in various medical procedures for this same reason, including both soft-tissue cutting and bone surgery applications (such as laser dentistry), where the additional strong absorption of this wavelength by hydroxyapatite is beneficial [1.28].

Considerations of cancer tissue removal via laser surgery in both animals and humans were published in 1966 by Dr. Goldman [1.29]. While tests were initially done on mice, he supervised the first human cancer tissue laser resection surgery when Dr. Thomas Brown removed a tumour from a patient's thigh using a laser [1.30]. Following on from these considerations, in 1968 Dr. Endre Mester was the first to publish research showing low-power lasers stimulating tissues on a cellular level [1.31]. Again this involved a mouse model, albeit looking specifically at hair cells. He observed that those mice which underwent treatment with a low-powered ruby laser grew back the hair shaved off their backs faster than those that did not. Dr. Mester reviewed 20 years' worth of his experimental and clinical work involving lasers in his 1985

publication [1.32]. In this paper he coined the term “biostimulation”, originating from an overwhelming amount of data across 15 different biological systems showcasing stimulatory properties. He also noted, however, that high-energy radiation had an “inhibiting effect”. This propelled a significant amount of research interest into “photobioactivation” – a term which was later deemed more appropriate for the observed effects of low-level laser therapy (LLLT) [1.33]. A qualitative representation of this low-level and high-level laser therapy spectrum can be observed in figure 1.2. Inhibitory effects were observed in collagen synthesis depending on the dosage of incident light, due to the biphasic nature of laser light interacting with tissue (low doses causing stimulation of cells and high doses, as in high-level laser therapy, or HLLT, leading to bioinhibition). The encapsulating term “photobiomodulation” has also been coined within the scientific literature and used interchangeably with LLLT [1.34],[1.35].

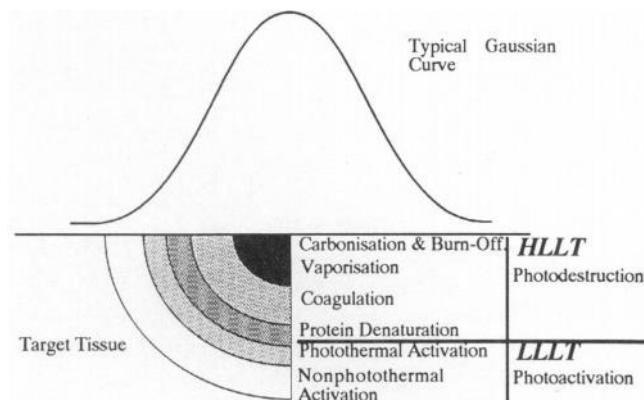


Figure 1.2 – Graphical illustration of Gaussian beam incident upon tissue, with the observed effects labelled respective to the gradually dropping intensity as it propagates through the medium [1.33].

For photobioactivation to occur, the incident light needs to be delivered to target tissue in the appropriate dose [1.36]. This is also true for applications that seek bioinhibition (or even cell death) such as photodynamic therapy (PDT) [1.37]. In PDT (which can be considered a type of LLLT), generally a photosensitiser (nontoxic chromophore) is injected. It localises in the target tissue and then a light source (conventionally a laser, although currently there is a range of both coherent and non-coherent compatible sources) is used to prompt photochemical reactions which incur cell death at the target site. This allows for selective eradication of malignant cells while leaving normal cells intact. As a result, it has primarily found applications in various disease and cancer treatments. In the case of cancerous tissue treatments, its ease of implementation allows for synergistic and/or intraoperative treatments to prevent recurrence within the original tumour margins [1.38]. This is significant, for example using glioblastoma as an example, recurrence rates around the peripheral local tumour volume can be as high as 70% [1.39].

The optical properties of light depend on the tissue it is propagating into (or through) and the wavelength of the incident light used. These are important factors as they determine the degree to which light can penetrate. For example, the absorption coefficient of human tissue is independent to the amplitude of the incident light. Although increasing the incident energy can lead to more energy being delivered to deeper parts of the body, it may also cause bioinhibitory effects in the superficial layer. Consequently, significant amounts of research has been carried out examining the optical window for various biological tissues [1.40].

Research into this topic continues to the present day, as the inhomogeneous, diverse, highly scattering and absorptive nature of biological tissue is still the primary challenge in medical imaging, with these properties

leading to scrambling of the spatial information, thus prohibiting direct imaging. With this in mind, there has been a surge of research interest in imaging modalities that can provide deep-tissue imaging such as surface-enhanced Raman scattering (SERS), optical coherence tomography (OCT), two- and three-photon microscopy and photoacoustic microscopy (PAM). SERS allows for high sensitivity, label-free imaging of cells and molecules but work is still ongoing to improve the reproducibility of label-free SERS [1.41]. OCT offers cellular resolution but suffers from image distortion upon stacking scans for widefield imaging which requires computational correction (as showcased in figure 1.3), making it difficult to achieve real-time imaging [1.42]. Two- and three-photon microscopy provides three dimensional optical sectioning capabilities and single neuron resolution (sub-micron spatial resolution) along with high temporal resolution, allowing it to keep up with neuronal activity but, similar to the other imaging modalities listed here, it still suffers from a small FOV [1.43]. PAM is able to comprehensively characterise microvascular function *in vivo* thanks to the high spatial resolution and contrast it offers, but still suffers from a degrading signal-to-noise ratio for greater depths via optical and acoustic attenuation, and it inherently struggles to provide real-time widefield imaging as it relies on relaying multiple one dimensional scans [1.44]. Complementary to the ongoing research of deep tissue imaging highlighted is the fundamental need to implement ultrafast lasers in various medical procedures.

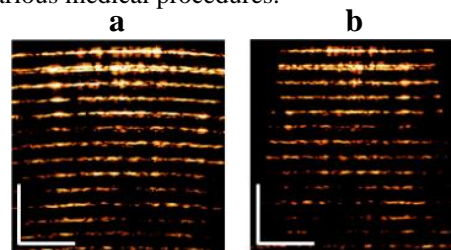


Figure 1.3 – OCT image of multilayer glass captured through a Micro-Electro-Mechanical System (MEMS) endoscopic probe a) before and b) after distortion correction [1.42].

In the existing literature, ultrafast lasers are typically considered to be lasers with pulse durations shorter than or in the order of picoseconds [1.45]. These lasers have led to improvements in all of the above imaging modalities, whether it is improving acquisition rates and depth-ranging (due to the broadband nature of ultrashort pulses) for OCT and PAM, increasing excitation efficiency in two- and three-photon microscopy, or improving nanostructure and/or substrate fabrication efficiency for SERS [1.46],[1.47],[1.48],[1.49],[1.50],[1.51]. Other imaging advancements enabled by these ultrafast lasers for medical and biological applications include time-resolved fluorescence spectroscopy (which has been used to localise skin tumours, shown in figure 1.4), optical mammography via time-resolved detection of transmitted light (which has been applied to human breast cancer screening) and white light propagation studies (which have been used for *in vivo* absorption spectroscopy of tumour seeking agents using mouse models) [1.52],[1.53],[1.54]. In addition to revolutionising the field of biomedical imaging, the continued development of ultrafast lasers has resulted in numerous advancements in resection-based surgical procedures.

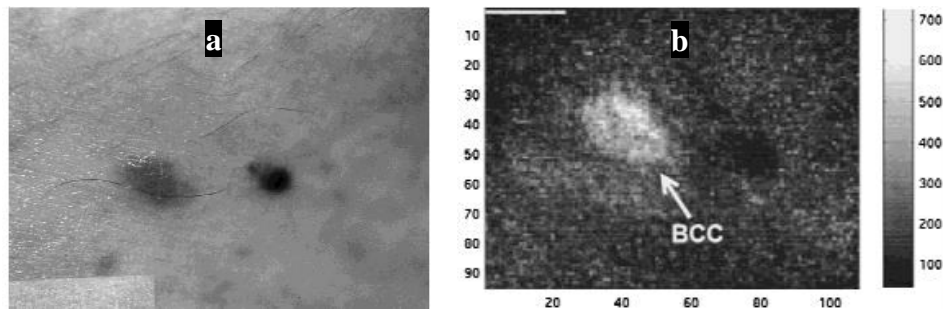


Figure 1.4 – a) Photograph of basal cell carcinoma (BCC, left side) in the skin and b) the corresponding fluorescence lifetime image of the BCC [1.52].

1.3 Bowel cancer

Bowel cancer is the third most common and second most fatal cancer globally [1.55]. However, with recent advances in medical screening it is now possible to detect these cancerous tumours earlier on in their development cycle [1.56],[1.57]. This cancer most commonly starts in the large bowel, which is primarily made up of colon tissue [1.58].

Early diagnosis and treatment (resection) of adenomatous polyps (tissue growth sites from which cancer can arise) is essential for reducing the high fatality rates associated with this type of cancer. The various stages of development for such polyps is illustrated in figure 1.5. The objective when treating early-stage bowel cancer cases is to resect such colonic polyps located within the mucosal (innermost lining) and submucosal layers.

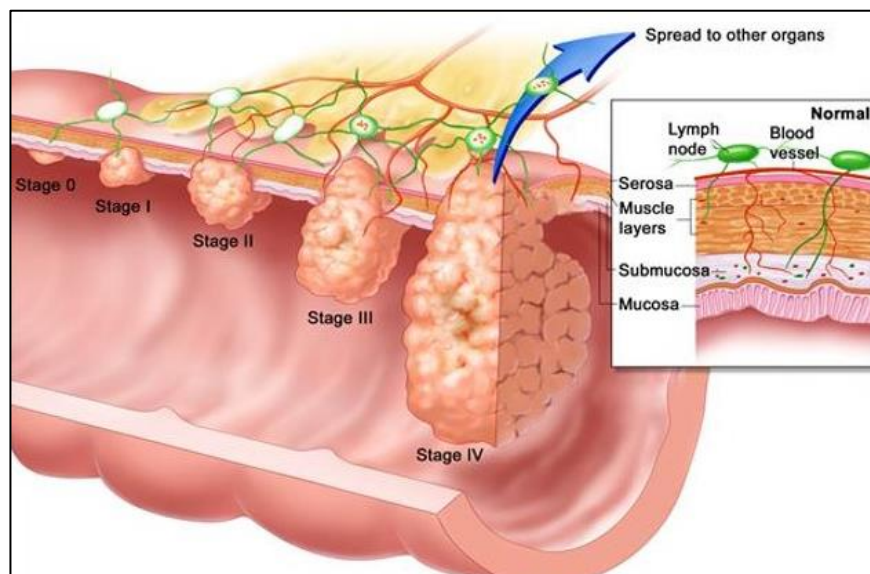


Figure 1.5 – Graphical depiction of the stages of colorectal cancer. The stages of colon cancer are categorised by the extent of spread through the layers of the bowel wall and whether the localized tumour has spread to lymph nodes or distant organs [1.59]. At stage 0 the cancer is still in the mucosa and at stage 1 it spreads through the mucosa to the submucosal and muscle layers. The cancer grows further into the muscle layers at stage 2, but it does not yet reach the lymph nodes. The cancer reaches these lymph nodes at stage 3 where all layers of the intestinal wall are invaded. Finally, at stage 4 it spreads to other organs from the lymph nodes and blood systems.

A more-detailed look at the anatomical structure of porcine colon tissue is shown in figure 1.6. While this is not human tissue, porcine models have been widely used in the existing literature for gastrointestinal systems courtesy of its remarkably similar physiological properties to human tissue [1.60].

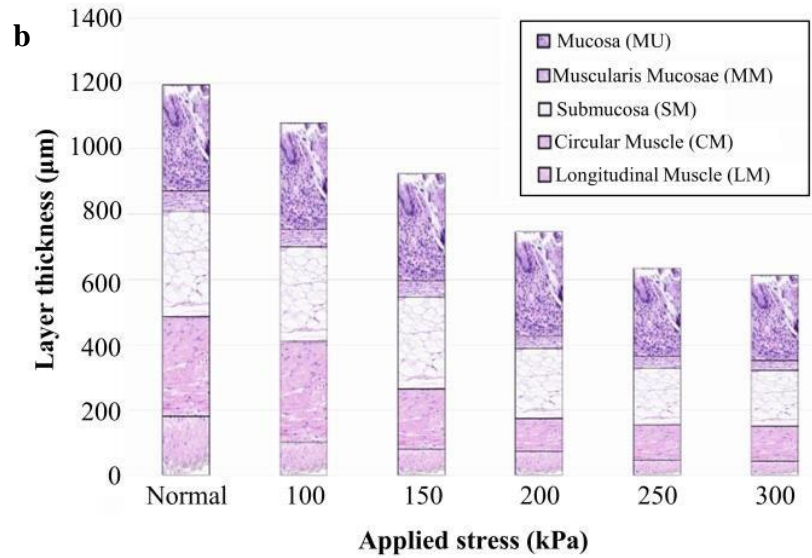
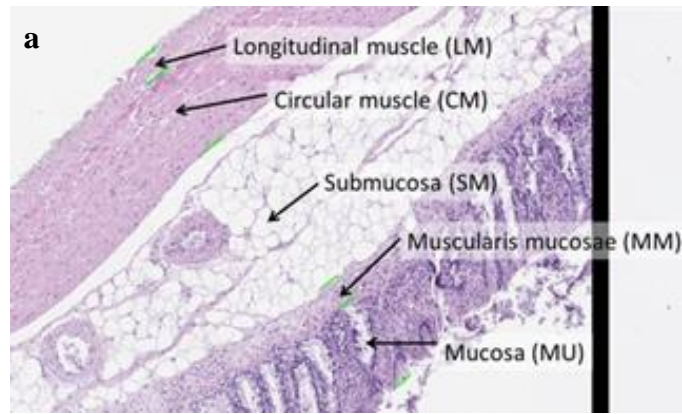


Figure 1.6 – Histology images showing a) the anatomical layers of porcine colon tissue and b) the typical thicknesses of these layers under various levels of axial stress applied by a bespoke grasper system [1.61]. From the applied stress chart it can be observed that the circular and longitudinal muscle layers of the muscularis propria were most prone to undergoing compression. These were followed by the submucosa and muscularis mucosae which only underwent significant compression at the higher applied stress levels. The mucosa did not appear to undergo any significant compression over the whole range of applied stresses. It is important to note however that the outer muscle layers were closest to the teeth of the grasp plates (used to simulate laparoscopic graspers), hence were the most impacted.

A comparison between human colon tissue and that of both porcine and murine (the two animal models used throughout this work) can be observed in figure 1.7. While porcine and human colonic tissues are similar in size and structure, murine colon is considerably smaller and more fragile. The murine samples were used as a cancerous tissue model as colorectal cancer is not observed within the porcine species.

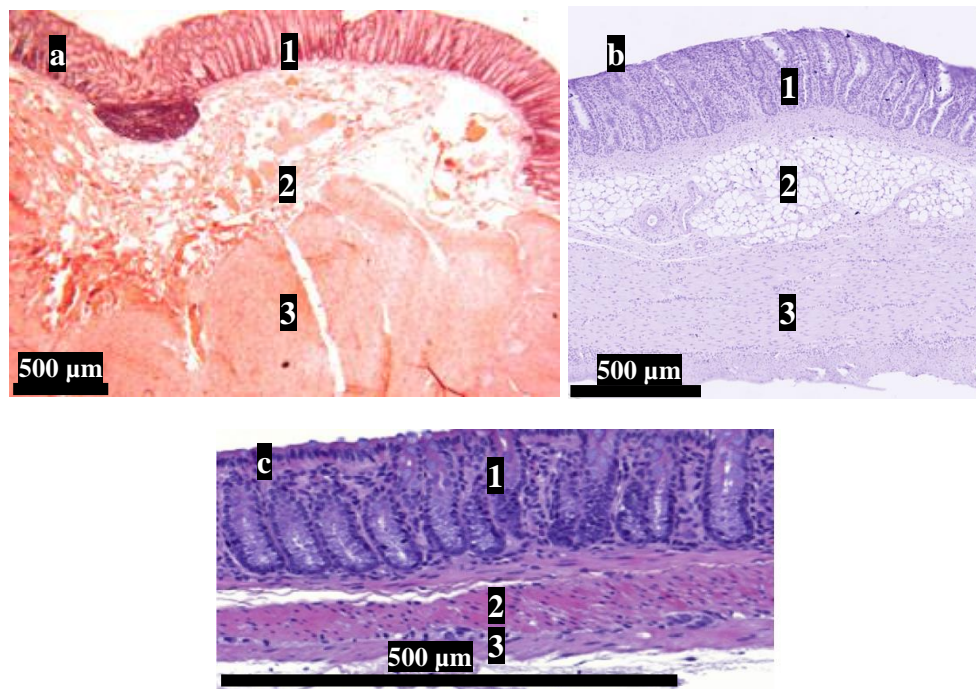


Figure 1.7 – Histology images of a) human b) porcine and c) murine intestinal tissue sample [1.62],[1.63]. The numbers 1,2 and 3 in each image represent the mucosal, submucosal and muscularis propria layers respectively.

The mucosa is the innermost layer of the colon. It consists of epithelial cells arranged into crypts, connective tissues and an underlying thin muscle layer, known as the muscularis mucosae. The mucosa has a thickness in the order of hundreds of microns in both fully grown humans and porcine [1.64]. The submucosa consists of loose connective tissue which contains nerves as well as both blood and lymphatic vessels. The muscularis propria is the primary layer of muscle within the bowel and is made up of both inner circular and outer longitudinal muscle layers. The outermost serosa layer is composed of a layer of mesothelium cells on a thin connective tissue membrane containing larger blood and lymphatic vessels, with the latter connecting to lymph nodes.

The overall mechanical strength of the colon wall is determined foremost by the submucosa and muscular layers. This is due to the smooth muscle layers containing colloid liquid, allowing them to tolerate significant stress (albeit only for a short duration), while the submucosa is primarily made up of collagen fibres that form a lattice structure, allowing it to undergo greater deformations than the muscularis can. The serosa and mucosa meanwhile do not contribute significantly to the total mechanical strength of the mechanical wall as the serosa does not usually exceed 50 μm in thickness and the cell mass of the mucosa is much greater than that of the stroma.

Consequently, the primary unmet clinical need seeking to be addressed within this project is the minimisation of thermal damage to the surrounding healthy tissue during resection of early-stage tumours within the gastrointestinal tract. It is worth noting however that the findings could be transferred to numerous other procedures as well due to the minimally invasive modality to be implemented. Current methods of performing these surgical procedures entail the use of electrocautery tools which lack the potential precision offered by ultrafast lasers, as indicated by the thermal damage margins being in the range of hundreds of microns [1.65]. A graphical depiction of such a procedure is shown in figure 1.8. This

limited precision can lead to recurrence due to incomplete resection of the cancerous tissue and/or bowel perforation, which leads to increased patient morbidity and possibly even mortality [1.66].

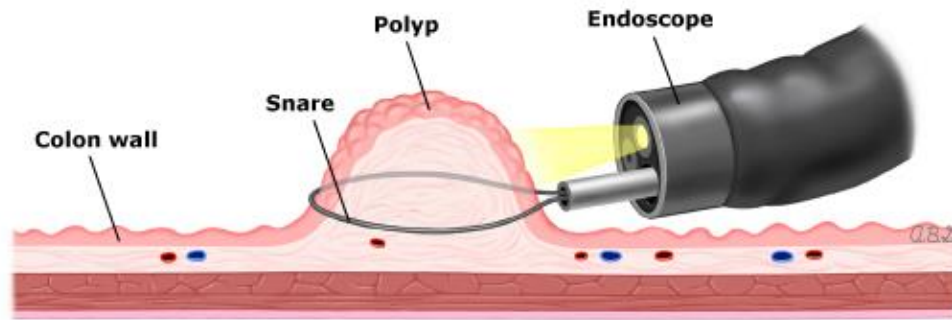


Figure 1.8 – Illustration of the removal of a polyp in the colon using an electrocautery snare implemented into an endoscope [1.67].

With regards to clinical specifications, intuitively the less thermal damage there is to the surrounding health tissue then the better the patient outcomes are likely to be. While sub-cellular precision would be ideal, and has been shown to be possible on neuronal and vascular systems with femtosecond laser pulses, this would be prone to suffering from increased operation times due to the reduced removal rates involved [1.68]. Upon considering this in conjunction with the previously discussed colon layer thicknesses, thermal damage zones on the order of tens of microns would enable improved patient recovery times and significantly reduced risk of bowel perforation by limiting the collateral damage to a few neighbouring cells while not increasing procedure times to the point of being both practically and economically infeasible.

Ultrafast lasers are ideally suited to tackle this problem due to the high precision they offer. This high level of precision is courtesy of the high energy intensities they can produce, leading to nonlinear plasma-mediated ablation as opposed to linear thermal-based processes. Additionally, early-stage tumours do not tend to significantly protrude from the colon wall, thus in the electrocautery technique depicted above an injection of saline is often necessary to ensnare and subsequently remove such polyps [1.69]. This in turn places further limitations on the maximum achievable precision, which ultrafast lasers are again well suited to mitigate through their non-contact surgical modality.

1.4 Motivation behind ultrafast laser-based resection processes

Lasers have been used for ablating biological tissue ever since their first medical applications in the fields of ophthalmology and dermatology, as mentioned previously. During the 1980s, in the field of endoscopic surgery, lasers were used for removing gastrointestinal malignant tumours, as well as neoplasm which showcased a high risk of developing malignancy [1.70],[1.71]. These procedures used a mixture of CW and long-pulsed (0.7s and 1s respectively) laser systems. The incorporation of lasers into endoscopic procedures occurred for treatment of tumours in other areas as well, such as the oesophagus [1.72]. However, older research comparing long-pulsed CO₂ and Nd:YAG (contact and non-contact) lasers to electrocautery tools on various murine tissues (stomach, small bowel, colon, liver and pancreas) showed similar levels of thermal damage (with the exception of non-contact Nd:YAG which caused noticeably more damage), to the point where an independent reviewer could not differentiate between the modality used in most of the tissue samples [1.73]. Further studies comparing these lasers to electrocautery and steel scalpel incisions on murine tongue tissue were also carried out shortly after [1.74]. While postoperative bleeding was observed with the steel scalpel and electrocautery (highlighting the better coagulation

properties of the lasers), there were no significant differences observed in the damage inflicted upon the tissue, with the exception of the contact Nd:YAG modality, which 7 days after the procedures showed slower healing than the scalpel. Any differences observed had subsided after 14 days post-surgery. With these studies both presenting incredibly similar wound healing characteristics between electrocautery devices and lasers, it becomes easy to see why the more conventional electrocautery method has remained the standard approach for tumour resection treatments in the gastrointestinal tract [1.75].

Again, the aim of this thesis is to further advance minimally invasive ultrafast laser-based resection procedures to reduce residual thermal damage to the healthy tissue that surrounds malignant and early-stage cancers. This is key for carrying out endoluminal gastrointestinal tract surgery, as this consequently minimises the risk of bowel perforation occurring, especially compared to electrocautery and CO₂ laser techniques which can both cause substantial damage, as indicated by figure 1.9 [1.76]. This is significant because perforation has high mortality rates and typically requires emergency surgery, as alluded to previously. Consequently, the best case outcome for the affected patients is a substantially increased recovery time, which in turn increases costs incurred by hospitals [1.77].

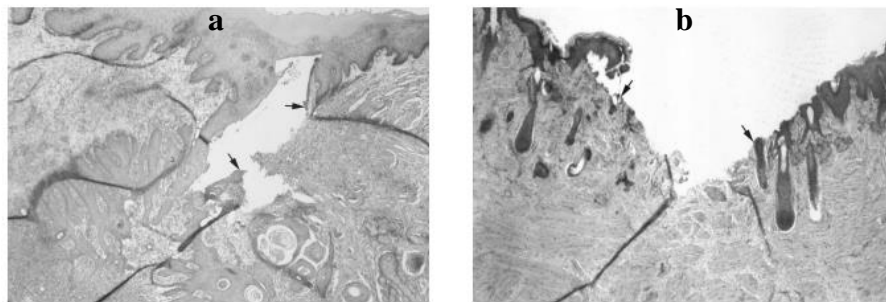


Figure 1.9 – Histopathological images of guinea pig oral mucosa 7 days after (a) bipolar electrosurgical treatment, showing incomplete epithelialisation, with epithelium covering just over half of the wound and (b) CO₂ laser treatment, showing epithelium present only at the edge of the wound. For both images there is no epithelium between the two arrows [1.76].

Regarding electrosurgical techniques, there are numerous potential sources that can cause excess tissue damage aside from the direct application of the electrical currents. In the context of bowel surgery, most of these injury sources (around 75%) go unnoticed at the instant they occur, with symptoms of bowel perforation only arising between 4 and 10 days post-surgery, while more severe cases can still take 12 to 36 hours [1.78],[1.79],[1.80]. These include direct coupling, where an electrode is activated whilst near another metal instrument (such as a laparoscope), causing the current to damage tissue structures in close proximity to these other instruments that are outwith the visual operating field [1.81]. This risk is illustrated in figure 1.10.

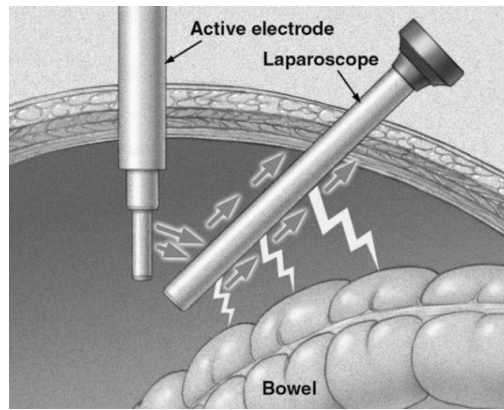


Figure 1.10 – Graphical depiction of direct coupling, where an active electrode is accidentally placed in close contact to another electrode or conductive instrument – in this case a laparoscope [1.81].

Other potential causes of damage from electrosurgical procedures include capacitive coupling, where electrical currents form in tissues and other conductive instruments running parallel to the active electrode through intact insulation, as well as insulation failure, where the coating around the active electrode element suffers from wear through repeated use (and therefore repeated sterilisations), causing defects to form in this layer [1.82]. This potential fault is shown in figure 1.11. Again, this can occur at the distal end, beyond the protective cannula and outside the field of view of the surgeon, meaning that catastrophic collateral damage can occur unknowingly to even the most experienced surgeons.

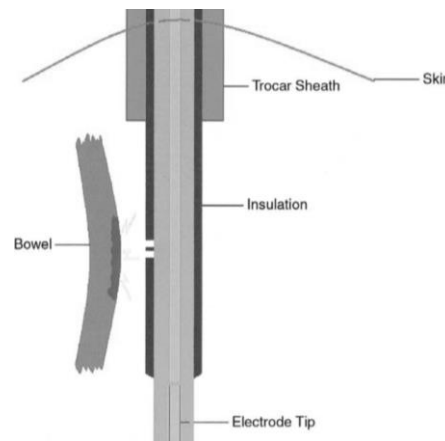


Figure 1.11 – Graphical representation of insulation failure, where a break in the insulation causes an additional path for the current to flow, which in turn damages healthy tissue outside of the target area of interest [1.81].

Despite the fact that lasers with picosecond pulse durations were developed shortly after the first laser was created, these have only recently been translated to clinical trials, primarily due to the instrumentation costs involved and the general availability of such systems [1.83]. Studies carried out by the group previously have shown the viability of ultrafast lasers in ablating ovine lung tissue and porcine intestinal and colon tissues [1.84],[1.85],[1.86]. These unanimously showed precise depth control in resection and minimal thermal damage margins around the ablated region. However, to translate these treatments to a clinical environment, incorporating an appropriate delivery mechanism is necessary. As a result, all the laser ablation trials performed on animal tissue models within this thesis were compatible with pulse delivery via hollow core negative curvature fibres (HC-NCFs).

These fibres enable delivery of pulse energies sufficient for ablation of biological tissues, which is an integral step towards realising these ultrafast laser-based endoscopic surgeries [1.87]. Prior to the

experimental realisation of these fibres, alternative delivery solutions such as conventional solid-core silica fibres or hollow core photonic crystal fibres suffered from low damage thresholds, fibre dispersion and/or non-linear losses such as self-phase modulation and weak Raman scattering, both of which lead to spectral broadening and thus transmission losses from exceeding the transmission band of the fibre [1.88],[1.89]. The light guidance mechanism in HC-NCFs is realised by the Antiresonant Reflecting Optical Waveguiding (ARROW) effect [1.90]. This means that the fibre core can guide light at wavelengths which are antiresonant to the core wall, as these rays destructively interfere and reflect back into the core. The antiresonant wavelength range is mainly dependent on the thickness of the core wall, with the resonant wavelengths outside of this range transmitting from the core to the cladding, resulting in attenuation. As a result, these fibres benefit from high damage thresholds, low attenuation (0.183 ± 0.050 dB/m), low nonlinearity, broad transmission and robustness to bending.

Due to this capacity for robust high power delivery, these fibres have been used in both micromachining and medical applications [1.91],[1.92]. Demonstrations in micromachining include laser cutting of aluminium sheets, marking titanium sheets and milling of fused silica - all commonly used materials in industry. Regarding medical applications, these fibres have been used for flexible delivery of ultrafast Er:YAG laser pulses to ablate porcine bone and muscle tissue [1.93].

More recently, these fibres have been used for ablating porcine colon tissue [1.94]. In this study the achieved ablated volumes were roughly equivalent to those of early-stage lesions which are found in the inner lining of the colon in early-stage bowel cancer patients, as highlighted in figure 1.12. While this study showcased a promising minimally invasive process using ultrafast lasers for carrying out precise colon tissue resection for early-stage cancer treatments with minimal damage, there is still further work required prior to adoption in clinical trials. Porcine tissue is also used for the work carried out in this thesis, as it has been previously established as an effective analogue to human tissue within the existing literature due to many similarities (anatomy, physiology, size, metabolic profile and significantly longer lifespans than species such as mice), while also being significantly easier to procure [1.95]. Murine tissue trials were also carried out, although these samples were significantly harder to handle and have less similarities with human tissue.

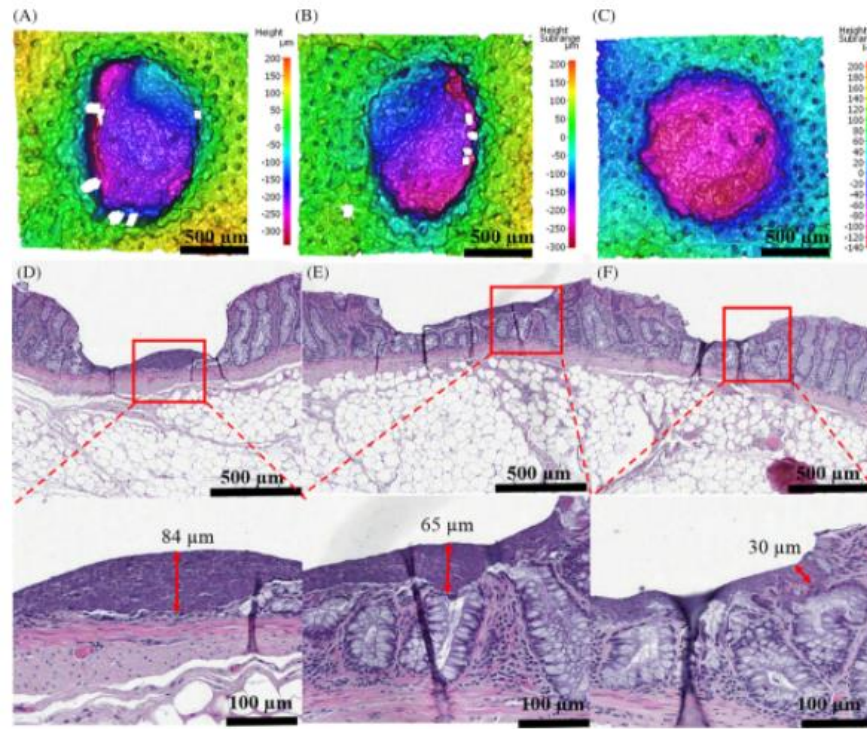


Figure 1.12 – Three-dimensional surface profiles of areas of porcine colon tissue samples ablated via HC-NCF-delivered 6 ps infrared laser pulses, captured using an Alicona Infinite Focus profilometer, alongside corresponding H&E stained histology images (albeit in separate tissue samples) of areas that were ablated using the same laser parameters. The laser fluence values are: (A) and (D) 21 J cm^{-2} , (B) and (E) 14 J cm^{-2} and (C) and (F) 7 J cm^{-2} . The dark lines present in the images are artefacts created during the histology preparation process. Magnified views showing the maximum thermal damage in each case are also presented [1.94].

In order to further illustrate the potential viability of ultrafast laser-based procedures, some of the current shortcomings need to be addressed. Primary among these are the comparatively low removal rates obtained compared to electrocautery techniques, where a tumour can be rapidly removed via diathermic snare [1.96]. While this is an inherent drawback of the increased precision and accuracy offered by these ultrafast laser-based procedures, this leads to longer operation times, which is clearly undesirable. These lower removal rates paired with higher instrumentation costs are the key reasons why electrocautery has remained the staple tool for tumour resection in the gastrointestinal tract, despite it being ill-suited for removing early-stage lesions due to it causing significantly higher levels of thermal necrosis in the surrounding healthy tissue [1.97]. Endoscopic mucosal resection via this modality has led to perforation rates in the gastrointestinal tract of between 4 and 6% [1.98],[1.99]. This is significant as it can lead to further corrective surgery being required. This lack of precision, paired with the flatter structure of these early-stage lesions compared to more developed cancerous tissue (*e.g.* polypoid lesions), creates a clear opportunity for ultrafast laser-based procedures to capitalise upon the increased level of control they offer the surgeon.

The comparatively low removal rates obtained from these ultrafast lasers is a consequence of the small spot sizes they are focussed down to. Although this offers them unmatched lateral precision, they are subject to short focal depths. Again, this offers incredible levels of depth control, but at the expense of processing time. There are also often issues regarding the sensitivity of the focal plane relative to the surface of the material to be ablated due to this tight focussing of the incident laser beam that is required to achieve the necessary energy intensities to realise plasma-mediated ablation processes. Also, to achieve greater resection depths, this would require either further manipulation of the endoscope by the surgeon or, perhaps

more practically for the level of accuracy that would be needed, some form of complex scanning mechanism that could vary the axial position of the focussing lens, in addition to the necessary implementation of lateral scanning capabilities. This in turn could lead to a relatively cumbersome endoscopic device design. To address this intrinsic issue, different beam types were tested.

Two different optical setups emitting different laser beam shapes were designed – one was a conventional transverse Gaussian mode, generated by a Gaussian beam input to a convex lens, and the other was a Bessel-Gauss (or quasi-Bessel) beam, created from a Gaussian beam input to an axicon. The term “quasi-Bessel” is commonly used within the existing scientific literature as an approximation of a theoretical non-diffracting Bessel beam can only be experimentally realised over a finite distance [1.100]. This is due to the fact that the Bessel zone range is limited by the finite aperture of the input beam, except for ultrafast laser sources, where the diffraction free beam diameter is instead limited by the finite pulse duration [1.101].

Despite this, Bessel-Gauss beams have shown great promise in additive manufacturing applications, where their capacity to offer high aspect ratios compared to the beams output from the traditionally used convex lenses (which, as previously mentioned, suffer from short focal depths for the small spot sizes needed) has been advantageous for modifying and drilling various materials [1.102],[1.103],[1.104],[1.105],[1.106]. Some of these results are presented in figures 1.13 and 1.14.

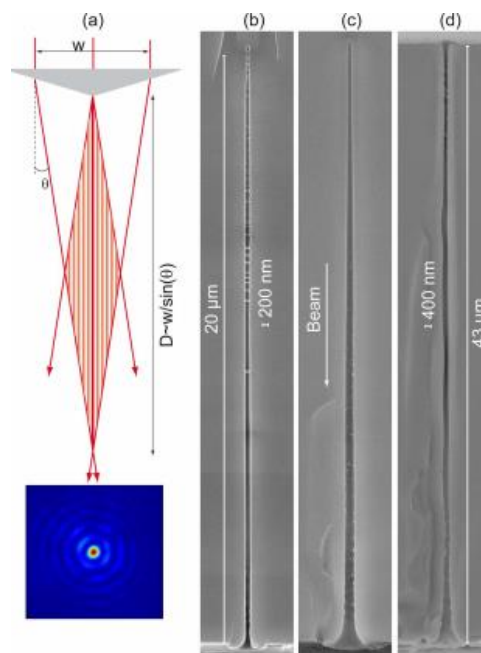


Figure 1.13 – (a) Geometrical ray structure of a Bessel-Gauss beam of conical angle θ created from an axicon being illuminated by a Gaussian beam of waist w . An experimental cross sectioned intensity profile of said beam is shown below this, with a central spot size of $0.7 \mu\text{m}$ FWHM in this case. (b) and (c) SEM images of nanochannels produced by single shot illumination at 0.65 and $0.85 \mu\text{J}$ in glass. (d) SEM image of the channel created by a single $3 \mu\text{J}$ pulse within a $43 \mu\text{m}$ thick glass slide [1.103].

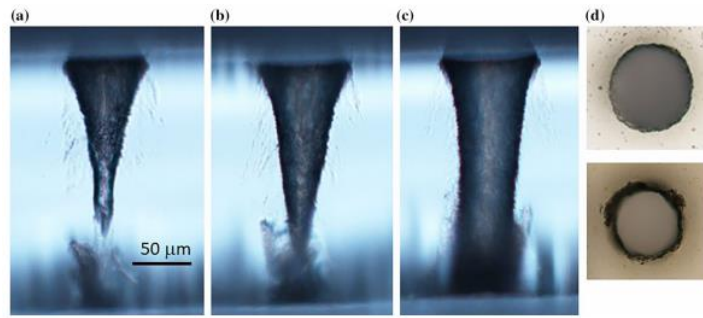


Figure 1.14 – (a) – (c) Lateral views captured using an optical microscope of the laser drilling process performed close to the side of an AF32 glass sample via a reimaged Bessel beam with a cone angle of around 12° , generated by an axicon of base angle 1° illuminated by a Ti:sapphire laser source operating at a repetition rate of 20 Hz and producing 40 fs long pulses of 140 μJ pulse energies at the sample surface. The first three images correspond to three progressive machining experiments: In (a) 20 circular writing trajectories were performed, while in (b) and (c) 30 and 40 writing rounds were applied respectively. A through-hole was generated exclusively in (c) as further highlighted in the corresponding top and bottom views depicted respectively in (d). The scale bar is the same across all the images [1.106].

There is an emphasis on lateral precision due to the medical context under consideration for the work carried out in this thesis, therefore the two optical setups were designed in such a way that they would provide roughly equivalent spot sizes at their respective “focus” regions (in the case of the Bessel-Gauss beam it does not focus down to a waist in a similar manner to the more conventional Gaussian beam). This was verified both via theoretical modelling performed using the OpticStudio software package and experimentally via both beam profiler measurements (BP209-VIS, Thorlabs) and damage threshold tests on stainless steel. Currently in the literature there is no standardised method for comparing these two beam geometries. This has been demonstrated by material processing research which drew comparisons between the axial ranges which contained an arbitrary percentage of the relative peak intensity values [1.107].

The primary outline of the work detailed in this thesis was to evaluate whether there was any potential merit to implementing an axicon into an endoscopic probe design as opposed to a conventional convex lens. Considerations for evaluating the two beam geometries included the achievable ablation depths, focussing efficiency (which is significant when considering fibre delivered surgical solutions), the level of thermal confinement and the relative insensitivity of the focal position, which is important for achieving uniformly sufficient energy densities for plasma-mediated ablation throughout scans across inhomogeneous surfaces. This is especially true in biological tissue structures which possess such varied characteristics between successive layers. The work carried out shows that the advantages observed in industrial materials processing applications could potentially be transferred to minimally invasive surgical procedures, although this would entail overcoming (or otherwise circumventing) a few existing experimental constraints.

1.5 Thesis outline

This thesis is structured as follows:

Chapter 2 consists of a comprehensive literature review covering various aspects related to minimally invasive surgery. This includes examinations of laser-tissue interactions, Bessel beams, conventional surgical tools, the history of laser-based and minimally invasive surgical procedures, optical fibres compatible with high-power beam delivery and current state-of-the-art endoscopic devices. Each of these is appraised under the context of aiming to increase the adoption rate of ultrafast lasers within clinical environments for performing minimally invasive procedures.

Chapter 3 covers the initial theoretical modelling undertaken for the range of axicons that are commercially available from Thorlabs. This was done within the OpticStudio software provided by Zemax, using the Physical Optics Propagation (POP) feature to plot the axial intensity profiles for each of the axicons. The Bessel beam produced by a 20° axicon (AX2520-B, Thorlabs) from the unmodified Carbide laser input beam and physical characterisation of the tip of the axicon are then characterised. This is followed up by the experimental methodology used for the tissue ablation tests and some initial ablation tests using the standalone 20° axicon on acrylic sheets and preserved porcine tissue (cooked ham). The chapter is then concluded by discussing the initial ablation tests performed on clinically relevant murine intestinal tissue.

Chapter 4 covers the development of the methodology outlined in the previous chapter by beginning with the optical design considerations involved for both reimaging the Bessel-Gauss beam produced by the 20° axicon and for producing a focussed Gaussian spot of roughly equivalent size to the Bessel core. This is followed by some characterisation of these beams, and further ablation trials on murine intestinal tissue samples with these new setups. The chapter is then concluded by discussing the initial sets of ablation trials performed on porcine intestinal tissue samples with lower pulse repetition rates applied, again using both setups. Both the murine and porcine intestinal tissues have corresponding histology data that is discussed.

Chapter 5 begins with some re-characterisation of the Carbide CB1-05 laser source (Light Conversion) following a firmware update, along with some characterisation of the surfaces of some porcine intestinal tissue samples. More porcine intestinal tissue ablation trials are then reviewed via histological analysis and surface profilometry, this time performed at increased pulse repetition rates for both the Bessel-Gauss and Gaussian beams. The chapter concludes with some high-speed imaging experiments performed on cryogenically preserved porcine skin samples to showcase the difference in the ablation characteristics between the two beams.

Chapter 6 covers the conclusions from the work carried out in this thesis, and some potential avenues for future work.

1.6 References

- [1.1] R. L. Siegel, K. D. Miller, and A. Jemal, “Cancer statistics, 2017,” *CA. Cancer J. Clin.*, vol. 67, no. 1, pp. 7–30, 2017, doi: 10.3322/caac.21387.
- [1.2] National Cancer Institute, “Cancer Statistics - National Cancer Institute,” *National Cancer Institute*, 2016. <https://www.cancer.gov/about-cancer/understanding/statistics>
- [1.3] T. H. Maiman, “Stimulated optical radiation in Ruby,” *Nature*, vol. 187, no. 4736, pp. 493–494, 1960, doi: 10.1038/187493a0.
- [1.4] L. R. Solon, R. Aronson, and G. Gould, “Physiological Implications of Laser Beams,” *Science (80-.)*, vol. 134, no. 3489, pp. 1506 LP – 1508, Nov. 1961, [Online]. Available: <http://science.sciencemag.org/content/134/3489/1506.abstract>
- [1.5] M. M. Zaret, G. M. Breinin, H. Schmidt, H. Ripps, I. M. Siegel, and L. R. Solon, “Ocular Lesions Produced by an Optical Maser (Laser),” *Science (80-.)*, vol. 134, no. 3489, pp. 1525 LP – 1526, Nov. 1961, [Online]. Available: <http://science.sciencemag.org/content/134/3489/1525.abstract>
- [1.6] C. Krafft, B. Dietzek, M. Schmitt, and J. Popp, “Raman and coherent anti-Stokes Raman scattering microspectroscopy for biomedical applications.,” *J. Biomed. Opt.*, vol. 17, no. 4, p. 040801, 2012, doi: 10.1117/1.JBO.17.4.040801.
- [1.7] D. S. Choy, “History of lasers in medicine.,” *Thorac. Cardiovasc. Surg.*, vol. 36 Suppl 2, no. S 2, pp. 114–117, Mar. 1988, doi: 10.1055/s-2007-1022985.
- [1.8] L. Goldman, D. J. Blaney, D. J. Kindel, D. Richfield, and E. K. Franke, “Pathology of the effect of the laser beam on the skin,” *Nature*, vol. 197, no. 4870, pp. 912–914, 1963, doi: 10.1038/197912b0.
- [1.9] M. M. Zaret, G. M. Breinin, H. Schmidt, H. Ripps, I. M. Siegel, and L. R. Solon, “Ocular lesions produced by an optical maser (laser),” *Science (80-.)*, vol. 134, no. 3489, pp. 1525–1526, Nov. 1961, doi: 10.1126/science.134.3489.1525.
- [1.10] N. S. Kapany, N. A. Peppers, H. C. Zweng, and M. Flocks, “Retinal photocoagulation by lasers,” *Nature*, vol. 199, no. 4889, pp. 146–149, 1963, doi: 10.1038/199146a0.
- [1.11] P. E. McGuff, D. Bushnell, H. S. Soroff, and R. A. Deterling, “Studies of the surgical applications of laser (light amplification by stimulated emission of radiation),” *Surg. Forum*, vol. 14, p. 143–145, 1963, [Online]. Available: <http://europepmc.org/abstract/MED/14064488>
- [1.12] D. P. Guerry and H. Wiesinger, “Light coagulation,” *Am. J. Ophthalmol.*, vol. 49, no. 1, pp. 87–96, Jan. 1960, doi: 10.1016/0002-9394(60)92668-4.
- [1.13] C. J. Campbell, M. C. Rittler, and C. J. Koester, “The optical maser as a retinal coagulator: an evaluation.,” *Trans. Am. Acad. Ophthalmol. Otolaryngol.*, vol. 67, pp. 58–67, Jan. 1963, Accessed: May 12, 2020. [Online]. Available: <http://www.ncbi.nlm.nih.gov/pubmed/14018113>
- [1.14] A. Javan, W. R. Bennett, and D. R. Herriott, “Population inversion and continuous optical maser oscillation in a gas discharge containing a He-Ne mixture,” *Phys. Rev. Lett.*, vol. 6, no. 3, pp. 106–110, Feb. 1961, doi: 10.1103/PhysRevLett.6.106.
- [1.15] L. F. Johnson, “Optical maser characteristics of rare-earth ions in crystals,” *J. Appl. Phys.*, vol. 34, no. 4, pp. 897–909, 1963, doi: 10.1063/1.1729557.
- [1.16] W. R. Bennett, W. L. Faust, R. A. McFarlane, and C. K. N. Patel, “Dissociative excitation transfer and optical maser oscillation in Ne-O₂ and Ar-O₂ rf discharges,” *Phys. Rev. Lett.*, vol. 8, no. 12, pp. 470–473, Jun. 1962, doi: 10.1103/PhysRevLett.8.470.
- [1.17] C. K. N. Patel, “Selective excitation through vibrational energy transfer and optical maser action in N₂-CO₂,” *Phys. Rev. Lett.*, vol. 13, no. 21, pp. 617–619, Nov. 1964, doi: 10.1103/PhysRevLett.13.617.
- [1.18] E. V Zharikov *et al.*, “ Stimulated emission from Er 3+ ions in yttrium aluminum garnet crystals at $\lambda = 2.94 \mu$,” *Sov. J. Quantum Electron.*, vol. 4, no. 8, pp. 1039–1040, Aug. 1975, doi: 10.1070/qe1975v004n08abeh011147.
- [1.19] T. Burns, M. Wilson, and G. J. Pearson, “Sensitisation of cariogenic bacteria to killing by light from a helium-neon laser,” *J. Med. Microbiol.*, vol. 38, no. 6, pp. 401–405, Jun. 1993, doi: 10.1099/00222615-38-6-401.

- [1.20] K. Pisula, W. Gaszynski, and D. Piotrowski, "Application of intravenous helium-neon (He-Ne) laser therapy to patients with respiratory insufficiency: introductory report," in *Lasers in Medicine*, Mar. 1996, vol. 2781, pp. 106–108. doi: 10.1117/12.236822.
- [1.21] C. A. Nanni and T. S. Alster, "A practical review of laser-assisted hair removal using the Q-switched Nd:YAG, long-pulsed ruby, and long-pulsed alexandrite lasers," *Dermatologic Surg.*, vol. 24, no. 12, pp. 1399–1405, 1998, doi: 10.1111/j.1524-4725.1998.tb00022.x.
- [1.22] P. F. Bradley, "A review of the use of the neodymium YAG laser in oral and maxillofacial surgery.," *Br. J. Oral Maxillofac. Surg.*, vol. 35, no. 1, pp. 26–35, Feb. 1997, doi: 10.1016/s0266-4356(97)90005-x.
- [1.23] K. Moskalik, A. Kozlov, E. Demin, and E. Boiko, "The Efficacy of Facial Skin Cancer Treatment with High-Energy Pulsed Neodymium and Nd:YAG Lasers," *Photomed. Laser Surg.*, vol. 27, no. 2, pp. 345–349, Apr. 2009, doi: 10.1089/pho.2008.2327.
- [1.24] S. L. Corson, M. Unger, D. Kwa, F. R. Batzer, and B. Gocial, "Laparoscopic laser treatment of endometriosis with the Nd: YAG sapphire probe," *Am. J. Obstet. Gynecol.*, vol. 160, no. 3, pp. 718–723, Mar. 1989, doi: 10.1016/S0002-9378(89)80067-5.
- [1.25] V. Knappe, F. Frank, and E. Rohde, "Principles of lasers and biophotonic effects," *Photomedicine and Laser Surgery*, vol. 22, no. 5. Mary Ann Liebert, Inc. 2 Madison Avenue Larchmont, NY 10538 USA , pp. 411–417, Oct. 18, 2004. doi: 10.1089/pho.2004.22.411.
- [1.26] T. Omi and K. Numano, "The role of the CO2 laser and fractional CO2 laser in dermatology," *Laser Therapy*, vol. 23, no. 1. Japan Medical Laser Laboratory, pp. 49–60, 2014. doi: 10.5978/islsm.14-RE-01.
- [1.27] I. Kaplan and S. Giler, "Carbon Dioxide Laser Surgery," in *CO2 Laser Surgery*, Berlin, Heidelberg: Springer Berlin Heidelberg, 1984, pp. 1–101. doi: 10.1007/978-3-642-82180-6_1.
- [1.28] J. Šulc and H. Jelínková, "Solid-state lasers for medical applications," in *Lasers for Medical Applications: Diagnostics, Therapy and Surgery*, Elsevier Ltd, 2013, pp. 127–176. doi: 10.1533/9780857097545.2.127.
- [1.29] L. Goldman, *Laser Cancer Research*. Springer Berlin Heidelberg, 1966. doi: 10.1007/978-3-642-87268-6.
- [1.30] "Leon Goldman, 71, Surgeon Was an Early User of Laser - The New York Times." <https://www.nytimes.com/1975/03/07/archives/leon-goldman-71-surgeon-was-an-early-user-of-laser.html> (accessed Jun. 04, 2020).
- [1.31] E. Mester, B. Szende, and P. Gärtner, "[The effect of laser beams on the growth of hair in mice].," *Radiobiol. Radiother. (Berl.)*, vol. 9, no. 5, pp. 621–6, 1968, Accessed: Jun. 08, 2020. [Online]. Available: <http://www.ncbi.nlm.nih.gov/pubmed/5732466>
- [1.32] E. Mester, A. F. Mester, and A. Mester, "The biomedical effects of laser application," *Lasers Surg. Med.*, vol. 5, no. 1, pp. 31–39, 1985, doi: 10.1002/lsm.1900050105.
- [1.33] T. Ohshiro and R. G. Caldenhead, "Development of Low Reactive-Level Laser Therapy and Its Present Status," *J. Clin. Laser Med. Surg.*, vol. 9, no. 4, pp. 267–275, 1991, doi: 10.1089/clm.1991.9.267.
- [1.34] W. Yu, J. O. Naim, M. McGowan, K. Ippolito, and R. J. Lanzafame, "Photomodulation of Oxidative Metabolism and Electron Chain Enzymes in Rat Liver Mitochondria," *Photochem. Photobiol.*, vol. 66, no. 6, pp. 866–871, 1997, doi: 10.1111/j.1751-1097.1997.tb03239.x.
- [1.35] J. J. Anders, R. J. Lanzafame, and P. R. Arany, "Low-level light/laser therapy versus photobiomodulation therapy," *Photomedicine and Laser Surgery*, vol. 33, no. 4. Mary Ann Liebert Inc., pp. 183–184, Apr. 01, 2015. doi: 10.1089/pho.2015.9848.
- [1.36] R. F. Labbe, K. J. Skogerboe, H. A. Davis, and R. L. Rettmer, "Laser photobioactivation mechanisms: In vitro studies using ascorbic acid uptake and hydroxyproline formation as biochemical markers of irradiation response," *Lasers Surg. Med.*, vol. 10, no. 2, pp. 201–207, Jan. 1990, doi: 10.1002/lsm.1900100215.
- [1.37] J. P. Celli *et al.*, "Imaging and photodynamic therapy: Mechanisms, monitoring, and optimization," *Chem. Rev.*, vol. 110, no. 5, pp. 2795–2838, May 2010, doi: 10.1021/cr900300p.
- [1.38] T. E. M. van Doeveren, M. B. Karakullukçu, R. L. P. van Veen, M. Lopez-Yurda, W. H. Schreuder, and I. B. Tan, "Adjuvant photodynamic therapy in head and neck cancer after tumor-

- positive resection margins,” *Laryngoscope*, vol. 128, no. 3, pp. 657–663, Mar. 2018, doi: 10.1002/lary.26792.
- [1.39] M. T. Milano *et al.*, “Patterns and timing of recurrence after temozolomide-based chemoradiation for glioblastoma,” *Int. J. Radiat. Oncol. Biol. Phys.*, vol. 78, no. 4, pp. 1147–1155, Nov. 2010, doi: 10.1016/j.ijrobp.2009.09.018.
- [1.40] S. L. Jacques, “Optical properties of biological tissues: A review,” *Physics in Medicine and Biology*. 2013. doi: 10.1088/0031-9155/58/11/R37.
- [1.41] X. S. Zheng, I. J. Jahn, K. Weber, D. Cialla-May, and J. Popp, “Label-free SERS in biological and biomedical applications: Recent progress, current challenges and opportunities,” *Spectrochim. Acta - Part A Mol. Biomol. Spectrosc.*, vol. 197, pp. 56–77, May 2018, doi: 10.1016/j.saa.2018.01.063.
- [1.42] D. Wang, P. Liang, S. Samuelson, H. Jia, J. Ma, and H. Xie, “Correction of image distortions in endoscopic optical coherence tomography based on two-axis scanning MEMS mirrors,” *Biomed. Opt. Express*, vol. 4, no. 10, p. 2066, Oct. 2013, doi: 10.1364/boe.4.002066.
- [1.43] T. Wang *et al.*, “Three-photon imaging of mouse brain structure and function through the intact skull,” *Nat. Methods*, vol. 15, no. 10, pp. 789–792, Oct. 2018, doi: 10.1038/s41592-018-0115-y.
- [1.44] S. Jeon, J. Kim, D. Lee, J. W. Baik, and C. Kim, “Review on practical photoacoustic microscopy,” *Photoacoustics*, vol. 15. Elsevier GmbH, p. 100141, Sep. 01, 2019. doi: 10.1016/j.pacs.2019.100141.
- [1.45] R. Ortega-Martinez, C. J. Roman-Moreno, A. A. Rodriguez-Rosales, and C. A. Juarez-Melchor, “Ultrashort laser pulses: a comparison between a mathematical model and experimental data,” in *Sixth International Conference on Education and Training in Optics and Photonics*, 2000, vol. 3831, p. 371. doi: 10.1117/12.388697.
- [1.46] H. M. Crespo and C. C. Rosa, “Femtosecond lasers for optical coherence tomography,” in *1st Canterbury Workshop on Optical Coherence Tomography and Adaptive Optics*, Sep. 2008, vol. 7139, p. 713902. doi: 10.1117/12.821852.
- [1.47] T. J. Allen *et al.*, “Ultrafast laser-scanning optical resolution photoacoustic microscopy at up to 2 million A-lines per second,” *J. Biomed. Opt.*, vol. 23, no. 12, p. 1, Dec. 2018, doi: 10.1117/1.jbo.23.12.126502.
- [1.48] Y. Andegeko, K. E. Sprague, D. Pestov, V. V. Lozovoy, and M. Dantus, “Advantages of Two-photon Microscopy with Ultrashort Pulses,” Springer, Berlin, Heidelberg, 2009, pp. 3012–3014. doi: 10.1007/978-3-540-95946-5_328.
- [1.49] K. Guesmi *et al.*, “Dual-color deep-tissue three-photon microscopy with a multiband infrared laser,” *Light Sci. Appl.*, vol. 7, no. 1, pp. 1–9, Dec. 2018, doi: 10.1038/s41377-018-0012-2.
- [1.50] Y. Yu, S. Bai, S. Wang, and A. Hu, “Ultra-Short Pulsed Laser Manufacturing and Surface Processing of Microdevices,” *Engineering*, vol. 4, no. 6. Elsevier Ltd, pp. 779–786, Dec. 01, 2018. doi: 10.1016/j.eng.2018.10.004.
- [1.51] T. K. Naqvi *et al.*, “Hierarchical Laser-Patterned Silver/Graphene Oxide Hybrid SERS Sensor for Explosive Detection,” *ACS Omega*, vol. 4, no. 18, pp. 17691–17701, Oct. 2019, doi: 10.1021/acsomega.9b01975.
- [1.52] A.-E. S *et al.*, “Preliminary Evaluation of Two Fluorescence Imaging Methods for the Detection and the Delineation of Basal Cell Carcinomas of the Skin,” *Lasers Surg. Med.*, vol. 26, no. 1, 2000, doi: 10.1002/(SICI)1096-9101(2000)26:1<76::AID-LSM11>3.0.CO;2-4.
- [1.53] R. Berg, O. Jarlman, and S. Svanberg, “Medical transillumination imaging using short-pulse diode lasers,” *Appl. Opt.*, vol. 32, no. 4, p. 574, Feb. 1993, doi: 10.1364/ao.32.000574.
- [1.54] C. A. Klinteberg, A. Pifferi, S. Andersson-Engels, R. Cubeddu, and S. Svanberg, “In vivo absorption spectroscopy of tumor sensitizers with femtosecond white light,” *Appl. Opt.*, vol. 44, no. 11, pp. 2213–2220, Apr. 2005, doi: 10.1364/AO.44.002213.
- [1.55] Y. Xi and P. Xu, “Global colorectal cancer burden in 2020 and projections to 2040,” *Translational Oncology*, vol. 14, no. 10. Elsevier, p. 101174, Oct. 01, 2021. doi: 10.1016/j.tranon.2021.101174.
- [1.56] J. S. Lin, L. A. Perdue, N. B. Henrikson, S. I. Bean, and P. R. Blasi, “Screening for Colorectal Cancer: Updated Evidence Report and Systematic Review for the US Preventive Services Task

- Force,” *JAMA - Journal of the American Medical Association*, vol. 325, no. 19. American Medical Association, pp. 1978–1997, May 18, 2021. doi: 10.1001/jama.2021.4417.
- [1.57] R. Bevan and M. D. Rutter, “Colorectal Cancer Screening—Who, How, and When?,” *Clin. Endosc.*, vol. 51, no. 1, p. 37, Jan. 2018, doi: 10.5946/CE.2017.141.
- [1.58] T. Tan, “Colorectal polyps and bowel cancer: So which are the risky ones and how do we deal with them? | Day Surgery Australia,” *Day Surg. Aust.*, vol. 19, no. 1, pp. 18–20, Sep. 2020, doi: 10.3316.
- [1.59] “Colorectal Cancer Stages | Colorectal Cancer Alliance.” <https://www.ccalliance.org/colorectal-cancer-information/stage-of-diagnosis> (accessed Jun. 12, 2022).
- [1.60] M. M. Swindle, A. Makin, A. J. Herron, F. J. Clubb, and K. S. Frazier, “Swine as Models in Biomedical Research and Toxicology Testing,” *Vet. Pathol.*, vol. 49, no. 2, pp. 344–356, 2012, doi: 10.1177/0300985811402846.
- [1.61] J. H. Chandler, F. Mushtaq, B. Moxley-Wyles, N. P. West, G. W. Taylor, and P. R. Culmer, “Real-Time Assessment of Mechanical Tissue Trauma in Surgery,” *IEEE Trans. Biomed. Eng.*, vol. 64, no. 10, pp. 2384–2393, Oct. 2017, doi: 10.1109/TBME.2017.2664668.
- [1.62] “Histology Guide: Digestive - Large Intestine.” https://www.histology.leeds.ac.uk/digestive/large_intestine.php (accessed May 30, 2022).
- [1.63] S. Vidal-Lletjós *et al.*, “Mucosal healing progression after acute colitis in,” *World J. Gastroenterol.*, vol. 25, no. 27, pp. 3572–3589, Jul. 2019, doi: 10.3748/wjg.v25.i27.3572.
- [1.64] V. I. Egorov, I. V. Schastlivtsev, E. V. Prut, A. O. Baranov, and R. A. Turusov, “Mechanical properties of the human gastrointestinal tract,” *J. Biomech.*, vol. 35, no. 10, pp. 1417–1425, Oct. 2002, doi: 10.1016/S0021-9290(02)00084-2.
- [1.65] A. Fetz, D. Farnell, S. Irani, and S. I. Gan, “Spray coagulation with snare-tip versus argon plasma coagulation: An ex vivo study evaluating tissue effects,” *Endosc. Int. Open*, vol. 9, no. 6, pp. 790–795, Jun. 2021, doi: 10.1055/a-1373-4162.
- [1.66] I. Barouhas, Y. Mouhayar, and J. M. Stephan, “Intraoperative Bowel Injury during Hysterectomy,” *Journal of Gynecologic Surgery*, vol. 37, no. 3. Mary Ann Liebert, Inc., publishers 140 Huguenot Street, 3rd Floor New Rochelle, NY 10801 USA, pp. 197–199, May 31, 2021. doi: 10.1089/gyn.2020.0230.
- [1.67] “UpToDate - Removing a colon polyp.” https://www.uptodate.com/contents/image?imageKey=PI%2F63967&topicKey=PI%2F2019&source=see_link (accessed May 30, 2022).
- [1.68] P. S. Tsai *et al.*, “Plasma-mediated ablation: an optical tool for submicrometer surgery on neuronal and vascular systems,” *Current Opinion in Biotechnology*, vol. 20, no. 1. pp. 90–99, 2009. doi: 10.1016/j.copbio.2009.02.003.
- [1.69] T. Kaltenbach *et al.*, “Endoscopic Removal of Colorectal Lesions—Recommendations by the US Multi-Society Task Force on Colorectal Cancer,” *Gastroenterology*, vol. 158, no. 4, pp. 1095–1129, Mar. 2020, doi: 10.1053/j.gastro.2019.12.018.
- [1.70] J. M. Brunetaud *et al.*, “Villous adenomas of the rectum. Results of endoscopic treatment with argon and Nd:YAG lasers,” *Gastroenterology*, vol. 89, no. 4, pp. 832–837, Oct. 1985, doi: 10.1016/0016-5085(85)90580-3.
- [1.71] E. M. H. Mathus-Vliegen and G. N. J. Tytgat, “Nd:YAG laser photocoagulation in colorectal adenoma. Evaluation of its safety, usefulness, and efficacy,” *Gastroenterology*, vol. 90, no. 6, pp. 1865–1873, 1986, doi: 10.1016/0016-5085(86)90254-4.
- [1.72] D. Fleischer and F. Kessler, “Endoscopic Nd:YAG laser therapy for carcinoma of the esophagus: A new form of palliative treatment,” *Gastroenterology*, 1983, doi: 10.1016/0016-5085(83)90014-8.
- [1.73] T. Schroder, K. Brackett, and S. N. Joffe, “An experimental study of the effects of electrocautery and various lasers on gastrointestinal tissue,” *Surgery*, vol. 101, no. 6, pp. 691–697, Jun. 1987, doi: 10.5555/uri:pii:0039606087900821.
- [1.74] J. Hukki, M. Castren, S. Nordling, and T. Schröder, “An experimental study on the effects of the steel scalpel, electrocautery and various lasers on oral tissue,” *Lasers Med. Sci.*, vol. 4, no. 2, pp. 103–110, Jun. 1989, doi: 10.1007/BF02032606.

- [1.75] G. Nelson and M. L. Morris, "Electrosurgery in the Gastrointestinal Suite," *Gastroenterol. Nurs.*, vol. 38, no. 6, pp. 430–439, 2015, doi: 10.1097/SGA.000000000000167.
- [1.76] U. K. Sinha and L. A. Gallagher, "Effects of steel scalpel, ultrasonic scalpel, CO2 laser, and monopolar and bipolar electrosurgery on wound healing in guinea pig oral mucosa," *Laryngoscope*, vol. 113, no. 2, pp. 228–236, 2003, doi: 10.1097/00005537-200302000-00007.
- [1.77] J. T. Langell and S. J. Mulvihill, "Gastrointestinal Perforation and the Acute Abdomen," *Medical Clinics of North America*, vol. 92, no. 3. Elsevier, pp. 599–625, May 01, 2008. doi: 10.1016/j.mcna.2007.12.004.
- [1.78] R. D. Tucker and C. R. Voyles, "Laparoscopic Electrosurgical Complications and Their Prevention," *AORN J.*, vol. 62, no. 1, pp. 49–71, Jul. 1995, doi: 10.1016/S0001-2092(06)63683-1.
- [1.79] B. S. Levy, R. M. Soderstrom, and D. H. Dail, "Bowel injuries during laparoscopy. Gross anatomy and histology," *J. Reprod. Med. Obstet. Gynecol.*, vol. 30, no. 3, pp. 168–172, Mar. 1985, Accessed: Oct. 15, 2020. [Online]. Available: <https://europepmc.org/article/med/3158738>
- [1.80] M. Van Der Voort, E. A. M. Heijnsdijk, and D. J. Gouma, "Bowel injury as a complication of laparoscopy," *British Journal of Surgery*, vol. 91, no. 10. John Wiley & Sons, Ltd, pp. 1253–1258, Oct. 01, 2004. doi: 10.1002/bjs.4716.
- [1.81] I. Alkatout, T. Schollmeyer, N. A. Hawaldar, N. Sharma, and L. Mettler, "Principles and safety measures of electrosurgery in laparoscopy," *Journal of the Society of Laparoendoscopic Surgeons*, vol. 16, no. 1. Society of Laparoscopic & Robotic Surgeons, pp. 130–139, Jan. 2012. doi: 10.4293/108680812X13291597716348.
- [1.82] P. N. Montero, T. N. Robinson, J. S. Weaver, and G. V. Stiegmann, "Insulation failure in laparoscopic instruments," *Surg. Endosc.*, vol. 24, no. 2, pp. 462–465, 2010, doi: 10.1007/s00464-009-0601-5.
- [1.83] A. J. Demaria, D. A. Stetser, and H. Heynau, "Self mode-locking of lasers with saturable absorbers," *Appl. Phys. Lett.*, vol. 8, no. 7, pp. 174–176, Apr. 1966, doi: 10.1063/1.1754541.
- [1.84] R. J. Beck *et al.*, "Precision resection of lung cancer in a sheep model using ultrashort laser pulses," in *Frontiers in Ultrafast Optics: Biomedical, Scientific, and Industrial Applications XVII*, Feb. 2017, vol. 10094, p. 1009405. doi: 10.1117/12.2252215.
- [1.85] R. J. Beck *et al.*, "Precision machining of pig intestine using ultrafast laser pulses," in *Optics InfoBase Conference Papers*, Jul. 2015, vol. 9542, p. 95421B. doi: 10.1117/12.2197930.
- [1.86] S. M. P. C. Mohanan *et al.*, "Investigation of the efficacy of ultrafast laser in large bowel excision," in *Optical Interactions with Tissue and Cells XXVIII*, Feb. 2017, vol. 10062, p. 1006207. doi: 10.1117/12.2251956.
- [1.87] P. Jaworski *et al.*, "Delivery of high-power nanosecond and picosecond pulses through a hollow-core negative curvature fibre for micro-machining applications." Optical Society of America, 2013.
- [1.88] O. Boyraz, T. Indukuri, and B. Jalali, "Self-phase-modulation induced spectral broadening in silicon waveguides," *Opt. Express*, vol. 12, no. 5, p. 829, Mar. 2004, doi: 10.1364/opex.12.000829.
- [1.89] S. M. M Friis *et al.*, "Effects of Raman scattering and attenuation in silica fiber-based parametric frequency conversion References and links," vol. 18, pp. 2884–2893, 2010, doi: 10.1364/OE.25.007324.
- [1.90] N. M. Litchinitser, A. K. Abeeluck, C. Headley, and B. J. Eggleton, "Antiresonant reflecting photonic crystal optical waveguides," *Opt. Lett.*, vol. 27, no. 18, p. 1592, Sep. 2002, doi: 10.1364/ol.27.001592.
- [1.91] J. D. Shephard *et al.*, "Silica hollow core microstructured fibers for beam delivery in industrial and medical applications," *Front. Phys.*, vol. 3, p. 24, Apr. 2015, doi: 10.3389/fphy.2015.00024.
- [1.92] P. Jaworski *et al.*, "High peak power nanosecond and picosecond pulse delivery through a hollow-core Negative Curvature Fiber in the green spectral region for micro-machining," Jul. 2014. doi: 10.1364/sof.2014.som3b.5.
- [1.93] A. Urich, R. R. J. Maier, F. Yu, J. C. Knight, D. P. Hand, and J. D. Shephard, "Flexible delivery of Er:YAG radiation at 294 μm with negative curvature silica glass fibers: a new solution for minimally invasive surgical procedures," *Biomed. Opt. Express*, vol. 4, no. 2, p. 193, Feb. 2013,

doi: 10.1364/boe.4.000193.

- [1.94] S. M. P. C. Mohanan *et al.*, “Preclinical evaluation of porcine colon resection using hollow core negative curvature fibre delivered ultrafast laser pulses,” *J. Biophotonics*, vol. 12, no. 11, Nov. 2019, doi: 10.1002/jbio.201900055.
- [1.95] K. Gutierrez, N. Dicks, W. G. Glanzner, L. B. Agellon, and V. Bordignon, “Efficacy of the porcine species in biomedical research,” *Front. Genet.*, vol. 6, no. SEP, 2015, doi: 10.3389/fgene.2015.00293.
- [1.96] C.-W. Yang, H.-H. Yen, Y.-Y. Chen, M.-S. Soon, and C.-J. Chen, “Novel Use of the Tip of a Standard Diathermic Snare for Endoscopic Submucosal Dissection of a Large Gastric Adenomatous Polyp,” *J. Laparoendosc. Adv. Surg. Tech.*, vol. 22, no. 9, pp. 910–912, Nov. 2012, doi: 10.1089/lap.2012.0202.
- [1.97] C. Yu *et al.*, “Long-term outcomes of endoscopic resection of gastric GISTs,” *Surg. Endosc.*, vol. 31, no. 11, pp. 4799–4804, Nov. 2017, doi: 10.1007/s00464-017-5557-2.
- [1.98] M. Siddaiah-Subramanya, K. W. Tiang, and M. Nyandowe, “Complications, Implications, and Prevention of Electrosurgical Injuries: Corner Stone of Diathermy Use for Junior Surgical Trainees,” *Surg. J.*, vol. 03, no. 04, pp. e148–e153, Oct. 2017, doi: 10.1055/s-0037-1606547.
- [1.99] F. Schlottmann, M. G. Patti, and N. J. Shaheen, “Endoscopic Treatment of High-Grade Dysplasia and Early Esophageal Cancer,” *World J. Surg.*, vol. 41, no. 7, pp. 1705–1711, 2017, doi: 10.1007/s00268-017-3977-8.
- [1.100] J. Durnin, J. J. Miceli, and J. H. Eberly, “Diffraction-free beams,” *Phys. Rev. Lett.*, vol. 58, no. 15, pp. 1499–1501, Apr. 1987, doi: 10.1103/PhysRevLett.58.1499.
- [1.101] I. Alexeev, K. H. Leitz, A. Otto, and M. Schmidt, “Application of Bessel beams for ultrafast laser volume structuring of non transparent media,” in *Physics Procedia*, Jan. 2010, vol. 5, no. PART A, pp. 533–540. doi: 10.1016/j.phpro.2010.08.177.
- [1.102] A. Marcinkevicius, S. Juodkazis, S. Matsuo, V. Mizeikis, and H. Misawa, “Application of Bessel beams for microfabrication of dielectrics by femtosecond laser,” *Japanese Journal of Applied Physics, Part 2: Letters*, vol. 40, no. 11 A, Nov. 01, 2001. doi: 10.1143/jjap.40.11197.
- [1.103] F. Courvoisier, J. Zhang, M. K. Bhuyan, M. Jacquot, and J. M. Dudley, “Applications of femtosecond Bessel beams to laser ablation,” *Appl. Phys. A Mater. Sci. Process.*, vol. 112, no. 1, pp. 29–34, 2013, doi: 10.1007/s00339-012-7201-2.
- [1.104] F. He *et al.*, “Tailoring femtosecond 1.5- μm Bessel beams for manufacturing high-aspect-ratio through-silicon vias,” *Sci. Rep.*, vol. 7, no. 1, pp. 1–9, Jan. 2017, doi: 10.1038/srep40785.
- [1.105] R. et al. Meyer, “Beam Shaping Aids Transparent Materials Processing,” *The Laser User*, pp. 24–25, 2017.
- [1.106] O. Jedrkiewicz, D. Valetti, and P. Di Trapani, “Etching and drilling of through-holes in thin glass by means of picosecond Bessel beams,” *SN Appl. Sci.*, vol. 1, no. 10, pp. 1–7, Oct. 2019, doi: 10.1007/s42452-019-1328-0.
- [1.107] Y. Matsuoka, Y. Kizuka, and T. Inoue, “The characteristics of laser micro drilling using a Bessel beam,” *Appl. Phys. A Mater. Sci. Process.*, vol. 84, no. 4, pp. 423–430, Sep. 2006, doi: 10.1007/s00339-006-3629-6.

Chapter 2

Background

2.1 Laser-tissue interactions

The subject of laser-tissue interactions has been well documented since the early 1980s, when lasers were first becoming routinely used in a range of medical procedures [2.1]. Extensive reviews and texts exist on this subject already as a result, but worthy of highlighting in the context of minimally invasive surgery are the photochemical, photothermal, plasma-mediated ablation and photomechanical interactions [2.2].

2.1.1 Photochemical interactions

A photochemical process is one related to or caused by the chemical action of light. Perhaps the most prominent example of this is photosynthesis, although it also underpins eyesight through processes such as phototransduction (the capturing and conversion of incident photons to electrical signals that are subsequently transmitted to the brain) which occurs in photoreceptors found in the retina [2.3].

When light is incident upon tissue it is absorbed by chromophores found within the molecular structure. This leads to excitation of electrons in these molecules, promoting them to short lived, higher energy unstable states. From these states numerous chemical reactions can rapidly take place, as when the electrons decay back down to the lower energy states there is a chance that this excess energy generates a high-energy species which reacts with the molecules surrounding it [2.4]. These range from the formation of covalent bonds (which can bond protein molecules together to achieve tissue adhesion) to destroying target molecules by incurring phototoxicity (used in cancer treatments) [2.5]. For these photochemical reactions to take place there must be an incident light source of a specific wavelength (to provide photons at the desired energy level) and target molecules that react to the produced high-energy species. Additionally, there is often something that mediates these reactions (such as a photocrosslinker or photosensitiser). These processes are graphically summarised in figure 2.1.

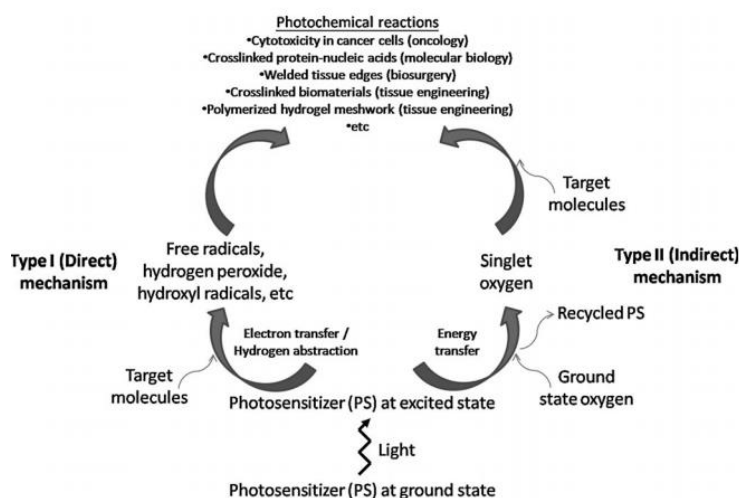


Figure 2.1 – Photochemical reactions - type 1 and type 2 pathways [2.6].

Photodynamic therapy (PDT) is the most established biomedical application of photochemistry, having been used in endoscopic cancer treatments for 60 years [2.7]. It is also the most relevant to the context of

minimally invasive surgery, with some state-of-the-art devices (covered at the end of this chapter) using it as a means of removing tumours [2.8]. It uses a photosensitiser (a nontoxic chromophore) to localise the desired photochemical reaction (in this case phototoxicity through oxidative stress to begin cell apoptosis) to the target, as illustrated in figure 2.2. It does this through both type 1 and type 2 (direct and indirect respectively) photochemical pathways [2.9].

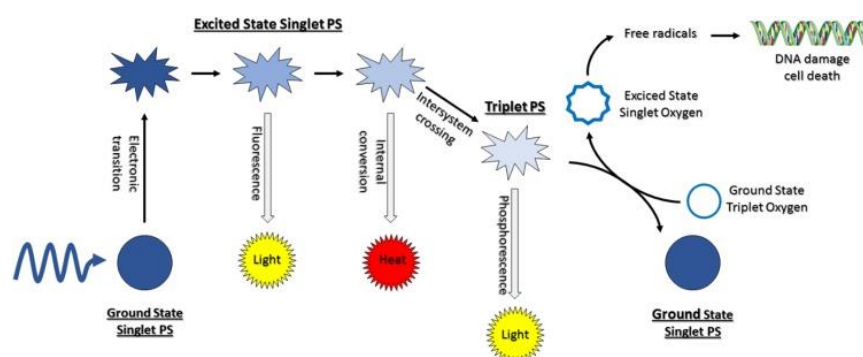


Figure 2.2 – Photodynamic reaction process [2.10].

While it can be performed intraoperatively, conventional PDT suffers from relying on the penetration depth of the light source used (which is normally in either the visible or ultraviolet range), meaning it is only suitable for superficial/early-stage tumours. While infrared wavelengths can provide high penetration depths in tissue, it is also highly absorbed by the water within the tissue, typically causing it to be highly attenuated by the time it reaches the target site, particularly for the low intensity laser light sources that are optimal for performing PDT [2.11]. Also, photosensitisers that are compatible with these wavelengths have typically suffered from poor yields of the triplet states needed for starting the underlying photochemical reactions responsible for PDT [2.12]. This has only started to be addressed within the relevant research relatively recently, meaning further development is still required prior to wider adoption for cancer treatments [2.13],[2.14]. For endo-laparoscopic PDT procedures in particular, the conventionally poor penetration depths of the photosensitisers have been improved through the incorporation of laser irradiation, with increased laser intensities (5 J cm^{-2}) improving cytotoxicity [2.15]. However numerous concerns remain, including off-target toxicity (particularly if using a light source with higher penetration depths), long treatment timelines and the heterogeneity of human disease meaning that multiple biomarkers must be targeted [2.16],[2.17]. The expressed biomarkers vary depending on the phenotypes (the observable properties) within the tumour, and with there being a continuum of phenotypes (that also evolve as the cancer treatment progresses) across these tumours this is not a trivial problem.

2.1.2 Photothermal interactions

When laser absorption occurs within tissue, heat is transferred to the tissue through the process of molecular excitation. The resultant production of heat from these excited molecules relaxing back down to lower energy states is referred to as the photothermal effect. This can be used in photothermal therapies, where incident light of a specified wavelength excites a photosensitiser (in a similar manner to the previously discussed PDT), which then releases this heat to either partially or completely ablate the target cells [2.18]. This photothermal interaction is listed alongside other processes in figure 2.3.

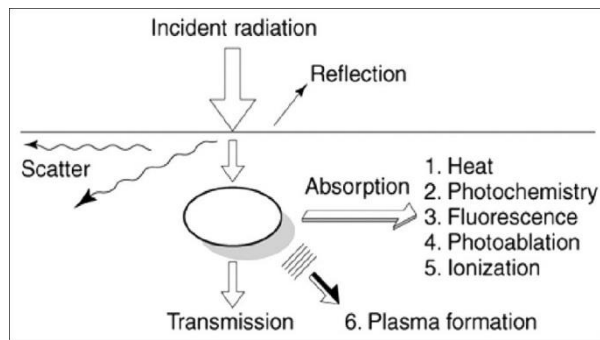


Figure 2.3 – Schematic of laser-tissue interactions [2.19].

When biological tissue is heated there are various observable effects which can occur. These depend on the extent to which its temperature rises and are summarised in table 2.1.

Temperature	Molecular and tissue reactions
42–45 °C	Hyperthermia leading to protein structural changes, hydrogen bond breaking, retraction
45–50 °C	More drastical conformational changes, enzyme inactivation, changes in membrane permeabilization, oedema
50–60 °C	Coagulation, protein denaturation
~80 °C	Collagen denaturation
80–100 °C	Dehydration
>100 °C	Boiling, steaming
100–300 °C	Vaporization, tissue ablation
>300 °C	Carbonization

Table 2.1 – Photothermal effects in tissue [2.20].

Less severe heating effects such as hyperthermia can be used for treating tumours, although in mouse models this has proven to be a less consistent method towards achieving complete tumour removal compared to ablation procedures (somewhat intuitively for the inevitably lower degree of damage inflicted), with only 50% of the mice that underwent hyperthermia treatment (via laser and gold-coated magnetic nanocomposites) showing full tumour regression over a period of 30 days [2.21]. Similar rates (53.09%) have since been reported in the inhibition of breast tumours transplanted into mice that were subsequently treated via laser hyperthermia, which again was enhanced by nanoparticles (single-walled carbon nanotubes in these trials) [2.22].

On the other end of the scale, carbonisation occurs at a temperature regime beyond that at which ablation of tissue is observed. During this excessive build-up of heat the surrounding tissue blackens and smoke is emitted. This is undesirable during surgical procedures as it inevitably leads to increased damage to the surrounding healthy tissue and can even obstruct the surgeon’s view.

Most significantly, this heat deposition can also lead to coagulation and vaporisation, enabling photocoagulation and photoablation respectively [2.23]. Photocoagulation is of interest as it has been used to prevent excessive bleeding during a range of procedures. It achieves this by inducing protein denaturation through increasing the tissue temperature to between 50 and 60 °C, which causes select blood cells to go through a state change that causes a blood clot to occur that in turn seals the vessels, effectively forming a barrier. This is highlighted in figure 2.4 along with other photothermally induced processes. In practice this is carried out using a series of pulses with radiant exposures just below that of the ablation threshold (the minimum pulse energy density at which material removal is achieved) of the targeted tissue. For example,

it has been shown that pulse fluences of $0.8 - 1.4 \text{ Jcm}^{-2}$, with a repetition rate of either 10 or 33 Hz, were able to achieve coagulation of collagen as deep as $300 \mu\text{m}$ beneath the epidermal-dermal junction [2.24].

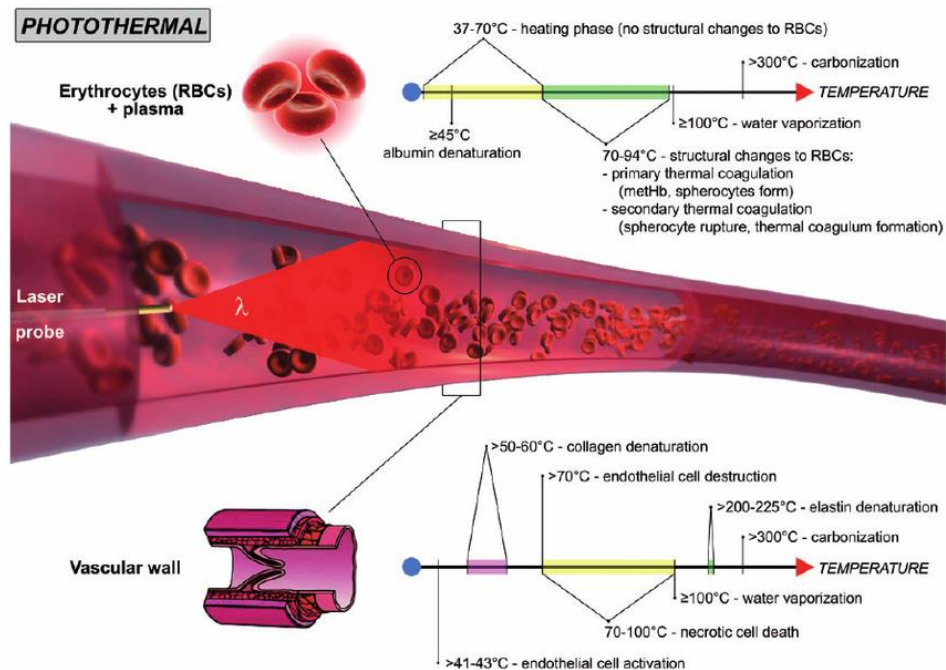


Figure 2.4 – Summary of photothermal processes in endovascular laser-tissue interactions [2.24].

Photoablation on the other hand occurs when higher intensity laser sources are applied to tissue [2.20]. The increase in incident energy upon the tissue leads to the cells within the tissue exceeding the boiling point of water. Upon this temperature increase the cells begin to evaporate and the tissue proceeds to melt accordingly due to the excessive heat [2.25]. For example, in excimer laser refractive surgery, the energy density must exceed $40\text{-}50 \text{ mJ cm}^{-2}$ to achieve this desired photoablation [2.26].

This laser-based tissue ablation has the advantage of being highly localised, particularly for shorter pulse durations, as these limit the spread of thermal energy to the surrounding tissue [2.27]. This is especially true for pulses with durations shorter than the thermal relaxation time of the tissue (such as ultrashort pulses in the picosecond regime or even shorter, which are discussed more in-depth later in this chapter), as the heat does not spread throughout the entire volume of the thermal penetration depth (a summation of the optical penetration depth and thermal diffusion length for dielectrics such as biological tissue) in these cases [2.28]. An example of this mechanism in action is the work done by Franjic *et al.* in 2009, where they achieved noticeably enhanced ablation efficiencies in healthy human enamel tissue using 55 ps infrared pulses of $2.95 \mu\text{m}$ wavelength (with peak intensities at least an order of magnitude below the plasma formation threshold) compared to nanosecond or microsecond pulses from a neodymium-doped yttrium aluminium garnet (Nd:YAG) laser [2.29]. The thermal relaxation time is a measure of the time taken for the directly heated (in this case irradiated) tissue to cool down as it diffuses heat to the adjacent areas [2.30]. It is important to note however that this variable has since been criticised within the literature as misleading (under the context of laser-based skin treatments), as the important parameter for determining the appropriate laser pulse widths is believed to actually be the time taken to induce protein denaturation at the target site [2.31]. Regardless of the underlying variable definition, ultrashort pulses in or shorter than the picosecond regime still offer improved localisation, as depicted in figure 2.5. Photocoagulation can even

be performed after photoablation by simply altering the working distance between the laser and the tissue, which reduces the irradiance by taking it out of focus.

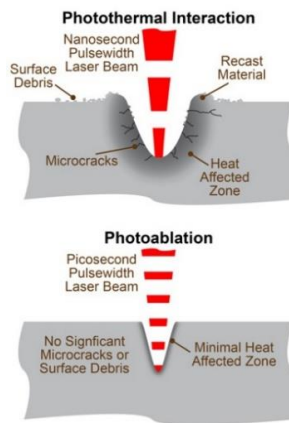


Figure 2.5 – Comparison between more conventional laser pulse widths and picosecond lasers for materials processing [2.32].

2.1.3 Plasma-mediated ablation

A relatively recent development in the field of laser-based surgery, plasma-mediated ablation offers a degree of precision that is 2 - 3 fold greater than that which can currently be obtained using conventional photoablation through continuous wave irradiation described previously [2.33]. Plasma is a state of matter with a high concentration of free electrons and positive ions. It can be thought of as an ionized region of gas which is highly conductive.

In order to induce photomechanical interactions (necessary for plasma formation to occur), lasers with pulse durations in the nanosecond regime (or shorter) are essential to obtain energy fluence values that are capable of rending molecules [2.34]. Purely plasma-induced ablation is observed for picosecond and shorter pulses. While photomechanical effects are observed for pulses in the nanosecond regime, pure plasma-mediated ablation is not, due to the optical breakdown threshold energy density being higher, as illustrated in figure 2.6. The electric field components of these tightly focused pulses have the power density values required for laser induced optical breakdown to occur (10^{10} - 10^{13} W cm⁻²), as these fields are greater than those which bind valence electrons ($\sim 10^9$ W cm⁻²). During this laser induced optical breakdown, the atoms within the tissue are ionized via a combination of multiphoton, impact and avalanche ionisation, resulting in plasma being formed.

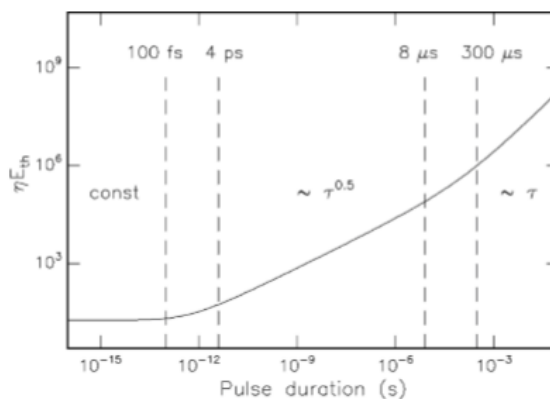


Figure 2.6 –Relationship between energy threshold density required for laser induced breakdown to occur and pulse duration. The ionisation probability, η , depends on the type of tissue and is expressed in units of (J/cm²)⁻¹ [2.35].

More thoroughly, multiphoton ionisation involves several photons being absorbed simultaneously by a bound valence electron (hence the need for a high energy density input, or equivalently a large number of incoming photons from ultrashort laser pulses, to increase the probability of this occurring), promoting it to a higher (free) energy state in the conduction band. These high energy (seed) electrons can then absorb further photons through the nonresonant process of Inverse Bremsstrahlung Absorption (IBA) as they collide with other charged particles (such as atomic nuclei or ions), which causes the electron to gain further energy as it is accelerated. Once it surpasses the bandgap energy it can produce another free electron through further collisions with surrounding charged particles – this is impact ionisation. These two electrons, now with lower kinetic energies, again gain energy through further IBA and repeat the process of impact ionisation – this is referred to as avalanche ionisation. As this cascade proceeds the number of free electrons increases exponentially, until the free electron density exceeds 10^{21} cm^{-2} (for picosecond and femtosecond pulses in water, the primary constituent of biological tissues) and the laser induced optical breakdown occurs, which is signalled by the formation of intense white plasma around the laser focus [2.36]. This process is shown in figure 2.7.

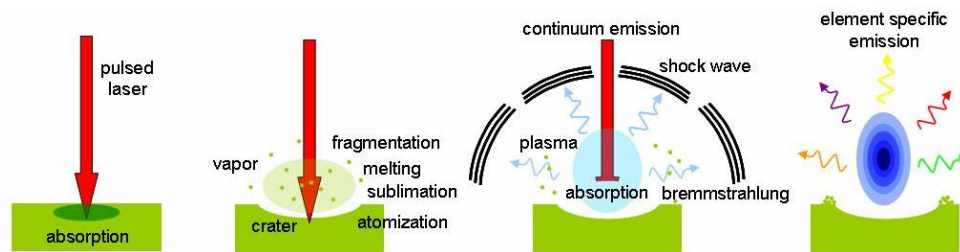


Figure 2.7 – Schematic of Laser Induced Breakdown [2.37].

This laser induced plasma proceeds to absorb the remaining laser energy (it is highly absorptive for various ultraviolet, visible and infrared wavelengths), coupling the light to the tissue in a precise and efficient manner, which leads to a non-thermal resection process [2.38]. As a result, this surgical modality offers excellent lateral precision and depth control. Figure 2.8 shows a graphical representation of this plasma cascade process with a plot of the laser power against time, with the numbers indicating the chronological steps in the formation of the plasma plume.

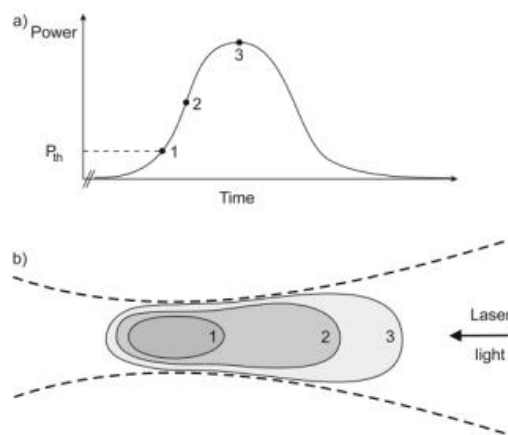


Figure 2.8 – a) Laser power evolving with time b) Plasma formation gradient [2.39].

Point 1 indicates the initial formation of plasma at and in the immediate vicinity of the beam waist of the laser beam, with points 2 and 3 corresponding to the times at which the free electron density is exceeded in

the respective larger peripheral volumes due to the initial plasma zone at point 1 absorbing the increasing incident laser energy. This plume stops extending upon the laser reaching its maximum power, indicated by point 3. Material is ejected after the development of this vapour plume with a subsequent crater being left in the material. In the case of soft biological tissue being ablated this plume consists of water (in the form of vapour and droplets) and/or minute tissue particles [2.38].

Ultrashort pulses on the order of picoseconds (or shorter) are again uniquely suited towards this plasma formation process, as multiphoton ionisation becomes the dominant mechanism by which seed electrons are produced and the energy from these seed electrons (which are the first to absorb the incident thermal energy) is transferred to the lattice of the target structure (tissue in this context) around the same timescale as, or prior to, electron cooling (~ 10 fs) and lattice heating ($\sim 1 - 10$ ps) [2.39],[2.40]. As the pulse ends before the heat is diffused throughout the lattice there is negligible thermal conduction. In the case of plasma formation, the high intensities provided by the incident ultrashort pulses lead to chemical bonds within the lattice structure being broken as ionisation occurs, with minimal excess energy transferring to adjacent lattices as heat. This is the underlying mechanism that lends these plasma-mediated ablation techniques their high degree of localisation, with the increase in temperature effectively being confined to the focal volume of the laser for these ultrashort pulses. This offers the potential to carry out ablation of tissue surfaces in a non-thermal regime.

When examining the fundamental mechanisms that underline plasma formation in biological tissues, it is vital to consider how it forms in water due to its abundance in these samples. Previous studies found that reducing the pulse duration from 100 ns to 100 fs results in an increase in the irradiance threshold at which laser induced optical breakdown, and thus plasma formation, occurs (from $\sim 10^{10}$ W cm⁻² to $\sim 10^{13}$ W cm⁻²) but a corresponding decrease in the radiant exposure threshold (from $\sim 10^3$ J cm⁻² to ~ 1 J cm⁻²) [2.41],[2.42]. They have also observed that the plasma energy density for nanosecond pulses is over ten times greater than that for femtosecond pulses and, perhaps most significantly for the experimental work carried out in this thesis (due to implications regarding the efficiency of high power laser delivery through novel hollow-core fibres discussed later), that the transmission efficiency of plasma in water is low for pulses in the nanosecond regime, high for picosecond pulses (peaking at around 3 ps) and decreases again as the pulse duration is reduced further down to the femtosecond regime [2.43]. This increased plasma transmission efficiency for picosecond pulses is observed through decreased “shielding” (mechanisms which limit the transfer of input energy through either reflection, absorption or scattering) [2.44]. For example, due to picosecond pulses resulting in greater lengths of plasma being formed in distilled water compared to nanosecond pulses, there are larger total volumes of plasma [2.45]. Due to the greater volume of plasma being formed, there is more energy required for ionisation and subsequent vaporisation of matter to occur, which results in less available energy for undesirable (in the context of minimally invasive surgery in the gastrointestinal tract) photomechanical effects to occur, such as the formation of shockwaves and cavitation bubbles – these are covered in depth in section 2.1.4.

This was observed by Alfred Vogel *et al.* using time resolved photography, where 30 ps pulses led to shockwaves of approximately 3 μ m width, while 6 ns pulses led to shockwaves that were roughly 10 μ m wide. Additionally, the pressure of the shockwaves formed via 30 ps pulses decayed to 1 kbar over a distance of 50 μ m, while the distance to drop to the same pressure value for the shockwaves formed via the 6 ns pulses was 200 μ m. If the focal volumes were equivalent, the energy density for the plasma induced

by the nanosecond pulses is much greater (due to greater energy densities being required to achieve an equivalent plasma electron density to the picosecond pulse induced plasma), which again results in this excess energy being dissipated into the surrounding tissue in the form of shockwaves, as well as the ensuing cavitation bubble and (potential) jet formation. This combination of a reduced optical breakdown fluence threshold (as depicted in figure 2.9) and lower energy deposition makes picosecond pulses (up to ~ 10 ps, with this being the upper end of the lattice heating timescale mentioned previously) optimal for ablating biological tissues. This has been confirmed by various papers, with surgical applications ranging from intraocular treatments, dental procedures and ear surgeries [2.46],[2.47].

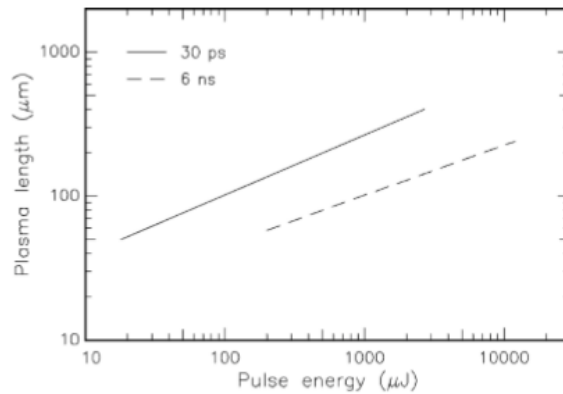


Figure 2.9 – Plasma length dependence on incident pulse energy for differing pulse durations in distilled water [2.35].

Additionally, it is worthwhile noting that the critical electron density (the free electron density at which the plasma oscillation and laser frequencies are equal, which is an important variable in determining the energy distribution between laser source-target coupling and laser source-plasma coupling) is most easily achieved (in an air medium, but transferrable to water as well) using infrared light compared to ultraviolet or visible sources, due to it being inversely proportional to the squared value of the incident wavelength [2.48]. However, when considering its applications in surgical contexts, it is important to consider the secondary effects of plasma formation in biological tissues as these correspond to additional damage mechanisms. These include the previously mentioned shock wave generation, as well as the potential formation of both cavitation bubbles and jets, with the latter depending on if the cavitation bubbles collapse in a fluid medium while in the vicinity of a solid boundary. An approximate timescale of these effects can be seen in figure 2.10.

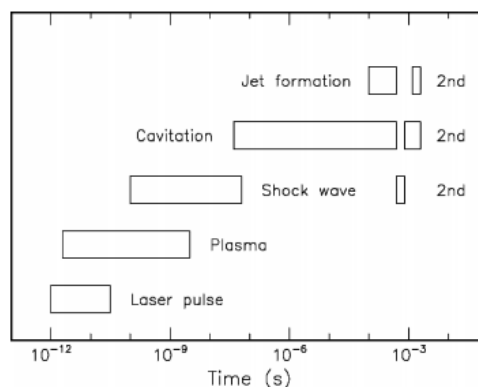


Figure 2.10 – Approximate timescale of the stages involved in plasma formation in a biological tissue sample. The “2nd” indicates the second incidences of the respective processes [2.35].

2.1.4 Secondary effects of plasma-mediated ablation of tissue

Supersonic shock waves are produced as the plasma expands from absorbing the incoming radiation (*i.e.* the incident laser light) immediately after it forms as previously described. These shock waves have a typical duration of 20 – 40 ns and are caused by the quick build-up of pressure that is associated with the rapidly increasing temperature within the focal volume of the incoming laser beam (and subsequent region of plasma) and they lead to photodisruption (disruption of the tissue structure as molecules are ionised upon interacting with the incident laser light) as they propagate outward from the plasma formation region across the surrounding tissue surface, reducing to the speed of sound in water (≈ 1500 m/s) as they do so [2.49]. The energy densities and pulse durations at which plasma-induced ablation or photodisruption processes occur are highlighted in figure 2.11. The mechanical process of photodisruption causes tissue separation and is ultimately one of the limiting factors regarding the otherwise impressive precision that is possible via plasma-mediated ablation of tissue, as while the plasma is confined around the focal region, these shockwaves and the resultant cavitation effects spread across the areas of adjacent tissue. However, these shockwaves are directly applied in other areas of medicine such as ophthalmology, where it enables minimally invasive intraocular surgeries (*e.g.* treatment of glaucoma).

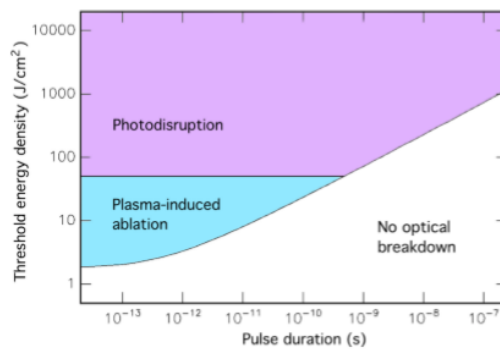


Figure 2.11 – Plot distinguishing the differences between pure plasma-induced ablation and photodisruption in terms of the applied energy density and pulse duration [2.35].

These photodisruption effects have been the favoured tool for performing various minimally invasive surgeries since first being reported in the scientific literature by Krasnov in 1972, and subsequently studied by Aron-Rosa *et al.* in 1980 and Fankhauser *et al.* in 1981, including posterior capsulotomy of lenses (most commonly required after performing cataract surgery) and laser induced lithotripsy of urinary calculi [2.50],[2.51],[2.52]. The relationship between photodisruption and both irradiance and exposure time is clearly illustrated in figure 2.12.

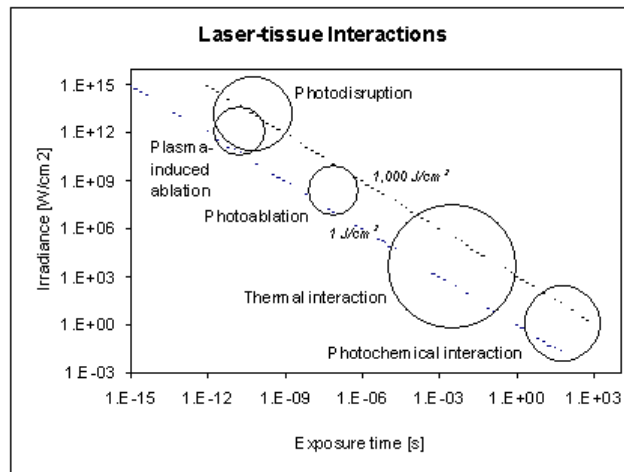


Figure 2.12 – Plot of irradiance versus pulse duration, highlighting the corresponding interaction mechanisms [2.53].

The rapid build-up of pressure can also cause cavitation bubbles to form within the fluid that is abundant in the tissue. The vapourisation within the focal volume causes work to be done against the surrounding medium, leading to the conversion of kinetic energy (from the shockwaves produced) to potential energy, which is then stored in these bubbles. These bubbles consist primarily of water vapour and carbon dioxide (both of which ultimately diffuse into the surrounding tissue upon the bubble collapsing) and are formed over nanosecond timescales, with the pressures inside these bubbles reaching as high as tens of megapascals [2.54]. The time taken to trigger these bubbles to begin forming ranges from nanoseconds to as short as femtoseconds, depending on the pulse duration of the incident laser source. These cavitation bubbles usually expand and collapse (in response to the outer static pressure of the surrounding fluid) several times over typical durations in the 100's of microseconds range (as illustrated in figure 2.10), although this duration is directly proportional to the applied pulse energy [2.55]. If operating close to the breakdown threshold (*i.e.* lower pulse energies) these bubbles typically collapse in the lower microsecond range. This entire sequence of events is also depicted in figure 2.13. As the pressure inside these bubbles increases with each collapse, the previously described shockwaves are emitted each time they reform. Additionally, jet formation can also ensue with each reformation of the bubble, but as stated previously this is dependent on the bubble collapsing while near a solid boundary.

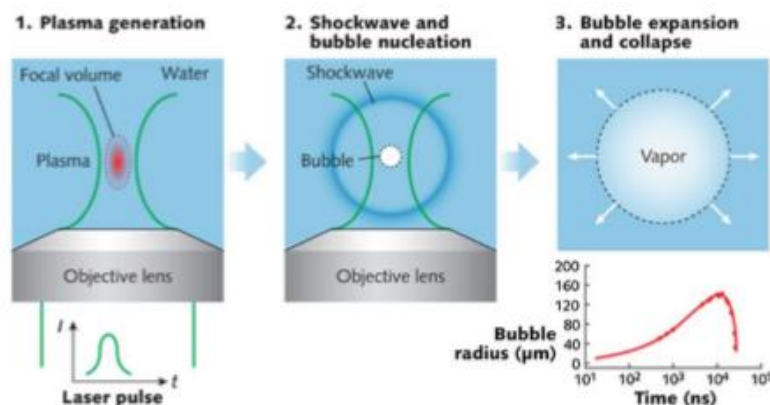


Figure 2.13 – Diagram depicting sequence of events that occur during laser induced optical breakdown in water (formation of a laser induced bubble) [2.54].

These jets are directed towards the solid boundary and can cause high-impact pressures if the bubble is in physical contact with the solid boundary as it collapses, leading to an increased potential for bubble induced

damage. These jets only form near a solid boundary as when a bubble collapses the surrounding fluid accelerates towards the centre of the bubble. However, when this occurs near a solid boundary, there is less fluid available on the side facing the boundary, which results in a slower collapsing process on this side and an asymmetric collapse. Fluid particles in the faster collapsing side proceed to gain more kinetic energy, as the decelerating force provided by the opposing side is consequently delayed. Counter jets may also be formed, but only if the jet is slow to the point where its speed is exceeded by that of the central part of the slower collapsing side.

Laser induced cavitation bubbles and jets have been studied using a variety of techniques. High-speed photographic methods were first used by Lauterborn in 1972, where framerates of 850000 pictures per second allowed for the bubble dynamics to be studied [2.56]. Shortly after this, in 1974 he was also the first to report on jet formation (instigated by the formation of single cavitation bubbles via Q-switched ruby laser), which was followed up by subsequent work with Bolle in 1975 further examining these high-speed liquid jets [2.57],[2.58]. Again, this was made possible through high-speed imaging, with framerates as high as 300000 frames per second being used for these examinations.

The high-speed imaging work published in 1972 led to further investigations of cavitation bubble dynamics by various researchers, including Alfred Vogel, who was previously mentioned regarding time resolved photography of cavitation bubble and shockwave formation. He was able to capture the formation and collapse of cavitation bubbles using a 20000 frames per second camera in 1989, with the bubbles again being generated by a Q-switched ruby laser, this time using pulse energies between 100 mJ and 400 mJ [2.59]. The results are shown in figures 2.14 and 2.15. In this study the maximum jet velocity observed was 156 m/s and the maximum bubble diameter was 2.05 mm. The 8th and 13th frames in figure 2.15 show the respective ends of the first and second collapsing processes of the cavitation bubble.

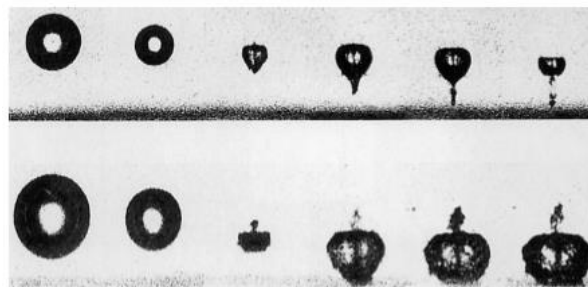


Figure 2.14 – Cavitation bubble collapse and ensuing jet formation from close proximity to brass block seen in the bottom of each frame, imaged at 20000 frames per second (individual frame size: 7.3 mm × 5.6 mm) [2.59].

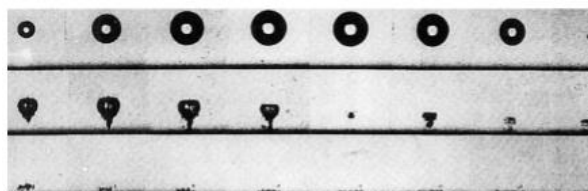


Figure 2.15 – Cavitation bubble formation and collapse, accompanied by corresponding jet formation, imaged via high-speed photography (individual frame size: 7.3 mm × 5.6 mm) [2.59].

Shortly after this in 1990, Vogel *et al.* observed that the tissue damage incurred is directly proportional to the cube root of the pulse energy, indicating that cavitation bubbles inflict more damage than

photomechanical shockwaves [2.60]. This was concluded by Markolf Niemz in his 1996 book “Laser-Tissue Interactions”, as the damage inflicted by these shockwaves scales with the square root of the pulse energy, while the extent of bubble induced damage scales with the cube root of the pulse energy [2.35].

In this same publication, Niemz was able to capture a cavitation bubble in human corneal tissue. This is shown in figure 2.16 and was achieved by fixating the tissue immediately after the laser exposure. It was produced by focusing a single 30 picosecond pulse from a Nd:YLF laser below the epithelium. This was done to preserve the cavitation bubble by preventing it from collapsing, which Niemz observed to occur after a lifetime of a few hundred microseconds, as indicated by figure 2.10. The cross-section of the cavitation is stretched out on an axis that is determined by the orientation of the collagen fibrils, because shear forces from the photomechanical effects can more easily split the tissue in this direction.

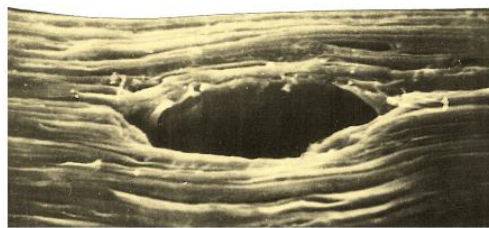


Figure 2.16 – Cavitation bubble formed within a human cornea, induced by a single 30 ps long pulse of 1 mJ energy from a Nd:YLF laser, focused just below the epithelium (scale bar: indicative of 30 μ m) [2.53].

The secondary effects of plasma generation within tissue covered in this section (shockwave generation, cavitation bubble and jet formation) have significant implications upon the extent of damage incurred by tissue during ultrafast laser surgery procedures, as a gas bubble left by a previous pulse may be hit by the resulting flow gradients that are produced by successive pulses. This can greatly impair the reliability and localisation of the ablation of the tissue itself (and hence the safety of the overall procedure) through various nonlinear interactions. For example, Vogel *et al.* reported damage dimensions of between 2 and 3.5 mm in diameter for 4 mJ pulses in instances where gas bubbles were attached to corneal tissue [2.60]. This was significant as the spot size of the Nd:YAG laser setup used was 20 μ m in fundamental mode operation and 50 μ m in multimode operation within the saline solution that the cornea samples were immersed in, showcasing that the damage incurred from these secondary effects was orders of magnitude greater in size than the spatial profile of the laser itself. Even when operating close to the optical breakdown threshold, where the cavitation bubbles are shorter lived (low microsecond regime) than at higher input energies, this remains an important consideration as the bubble left by the previous pulse may still oscillate (expand and collapse) in the temporal and spatial vicinity of the subsequently focussed pulse [2.61]. This is the principle that typically impairs performance for higher repetition rates in laser surgery applications. Also important to note however is that if these bubbles are sufficiently small (around micron scale) then they quickly dissipate, due to their small total volume and relatively high surface tension, resulting in certain laser repetition rates and scanning speeds providing more consistent ablation results with less damage being inflicted upon the surrounding tissue through providing increased temporal and spatial separation of the applied ultrafast laser pulses. This consideration is of paramount importance within the surgical contexts

of the work carried out in this thesis. A summary of these secondary effects that accompany plasma generation in biological tissues is illustrated in figure 2.17.

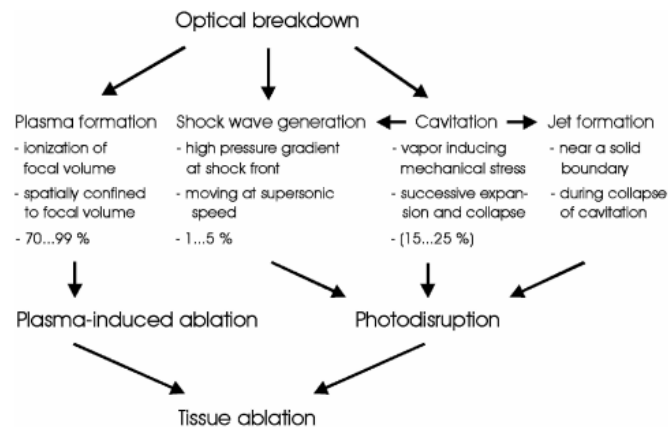


Figure 2.17 – Summary of the secondary effects caused by plasma generation within a biological tissue medium [2.53].

2.1.5 Surgical applications of plasma-mediated ablation

Collateral thermal damage is the primary driver for many complications in resection-based surgical procedures. The main cause of this is heat diffusion occurring within the tissue surrounding the surgical sites. This is a significant limiting factor in various procedures that utilise continuous-wave (CW) and/or long-pulsed (pulses with durations within or greater than the sub-microsecond regime) laser systems, despite such systems being ideal for general material processing applications for a multitude of reasons (including their capacity for contactless modalities, precise targeting via micron scale beam diameters, real-time process adjustability and a lack of tool deterioration).

While photothermal and photoablation processes fundamentally rely on linear thermal interactions occurring within the tissue structure, the comparatively recent research endeavour of plasma-mediated ablation shows great promise in various areas of medical practice, such as neurosurgery, due to the previously discussed high degree of localisation it offers, especially compared to electrical ablation or more conventional continuous wave laser photoablation, which both fundamentally function over longer timescales, leading to increased levels of thermal diffusion. This enables selective ablation on a sub-cellular level (*e.g.* micron scale) [2.62],[2.63]. This has been further realised experimentally through the implementation of simultaneous spatial temporal focusing [2.64]. Plasma-mediated ablation can target significantly more individual cells than what is currently possible through mechanical methods that utilize pipetted distribution of pharmaceutical compositions, resulting in higher throughputs. Yet, it is not without drawbacks.

In the context of neurological research, established techniques that use genetic and chemical manipulation methods to inactivate particular neuronal subclasses benefit from a higher extent of selectivity than plasma-mediated ablation, while also benefitting from the potential of reversibility [2.65]. Other complications surrounding plasma-mediated ablation include the potential for internal haemorrhaging and infections occurring in the local area of the treated region [2.66]. Also, the degree of precision it offers is offset by its comparatively slow ablation rate in some procedures [2.67]. An example of this is the calculated ablation rate for the Wyvern™ 1000-30 Ti:Sapphire regenerative amplifier (Kapteyn-Murnane Laboratories, Inc., Boulder) system, which can produce 1.6 mJ pulses at a repetition rate of 10 kHz. Although this is on the

higher end of commercially available amplified systems in terms of power output, it is calculated to only be able to achieve ablation rates of $\sim 0.033 \text{ mm}^3/\text{s}$, whilst a more conventional 523 nm continuous wave (CW) laser system has only recently been shown to achieve rates of $50 \text{ mm}^3/\text{s}$ on bovine liver tissue [2.68].

Despite these limitations, plasma-mediated ablation has proven key for advancements in numerous medical research endeavours. These include the treatment of lingual tonsil hypertrophy, which demonstrated the user friendliness of plasma-mediated ablation in tonsillectomy, courtesy of the excellent haemostasis it provides, albeit with a radiofrequency device [2.69]. Similarly, it has also been observed as a promising method for treating adult laryngotracheal stenosis, with lower grade stenosis cases in particular requiring fewer surgical interventions [2.70]. Plasma-mediated ablation has also found use in stripping thin slices from dry dermal tissue, which similarly required negligible thermal damage (in this instance less than $10 \mu\text{m}$ laterally, even after multiline ablation) and precise ablation on the scale of tens of microns [2.71]. This stripping of dry tissue layers has uses in the construction of skin allografts, which are used for treating burn wounds. The fact this was carried out on dry tissue is also significant, as previously studied wet dermis samples were prone to dehydration upon undergoing laser processing [2.72].

In dentistry it shows the potential for unmatched depth control in the production of high quality dental implant cavities, with fidelity again on the micron scale, while also offering higher pain relief through negligible thermal damage and not causing vibrations, which tooth nerves are very sensitive to, although this comes at the cost of reduced throughput compared to what mechanical drills can offer [2.73]. Recent work by Khosroshahi *et al.* has highlighted this, with fluences as high as 200 J cm^{-2} from 7ns Nd:YAG pulses providing removal rates of only around $45 \mu\text{m}$ per pulse in enamel tissue in the single shot regime [2.74].

This precision has been carried over to other hard biological tissues such as the nail, where the enhanced depth control of poration offered by plasma-mediated ablation is advantageous in aiding drug access to the target site [2.75]. Plasma-mediated ablation has also shown compatibility with laser induced breakdown spectroscopy-based feedback loops in laser osteotomy applications [2.76]. This was able to distinguish between fat, muscle and bone tissue in a porcine femur sample with 100% sensitivity and 99% specificity through discriminant function analysis of the respective peaks in the obtained spectra.

Recent plasma-mediated ablation studies have involved the precise resection of both tumours within ovine lung samples and of porcine intestinal tissue [2.77],[2.78],[2.79]. Both types of tissue exhibited minimal collateral damage (less than $50 \mu\text{m}$ in both cases) thanks to the utilisation of a non-thermal ablation regime – an illustration of this idea can be seen in figure 2.5, albeit not for biological tissue samples specifically. In addition, plasma-mediated ablation of porcine colon tissue via fibre delivered ultrafast pulses has been demonstrated [2.80]. Porcine vocal fold tissue has also been resected using 1.5 ps laser pulses (in this case delivered through a hollow-core Kagome lattice photonic crystal fibre, with the distal end being scanned in a Lissajous pattern) to generate plasma for simulating microsurgical procedures, although there was no histological analysis to review the extent of the thermal damage inflicted upon the tissue [2.81]. Due to the advantages it offers in terms of precision and minimising residual thermal damage, the underlying mechanisms of plasma-mediated ablation has been studied for various nanosecond pulsed laser wavelengths on porcine skin samples [2.82].

For ocular surgery in particular, the use of plasma formation dates back to 1977 [2.83]. Quantitative models for plasma-mediated ablation of corneal tissue have since been developed [2.84]. Additionally, studies examining the ablation of corneal tissue with various pulse durations have also been carried out, with the observations that more precise excisions were possible with shorter pulse lengths, and that these also benefitted from lower threshold energy requirements for ablation to occur [2.85]. The capacity for minimal collateral damage has led to this being a continued research interest to the present day, with patents being made for various devices [2.86],[2.87]. These bespoke setups combine a suitably short pulsed laser with either an optical coherence tomography imaging system to enable non-invasive targeting of floaters or scanning and delivery systems to treat astigmatism via repeated treatment patterns.

Yet, as it is a relatively recent research endeavour (primarily due to a previous lack of compatible delivery mechanisms for the high power ultrafast pulses required) longer term data on plasma-mediated ablation of soft tissues (such as organ structures) to draw comparisons with is inevitably lacking, indicating that there is ample room for more studies to be done that examine this method.

2.1.6 Gaussian beams

In previous laser ablation studies, obtaining the required energy intensities within the focal volume of the laser beam incident upon the tissue surface to achieve plasma formation has predominantly been done through the implementation of conventional convex lenses within the optical setups [2.88],[2.89],[2.90]. These lenses refract the constituent light rays of the input laser beams in a manner that forms a tight focal depth along both the transverse and propagation axes, courtesy of the Gaussian beam shape that is both typically input to and subsequently output from them. This refraction normally changes the shape of the wavefronts from planar (*e.g.* a collimated input beam) to spherical (*e.g.* a focussed output beam). These Gaussian beams have the distinct advantage of being the most widely used (particularly for material processing applications) and consequently the most well defined and established in terms of the theoretical modelling from mathematical expressions and experimental application respectively. They can also be the most strongly focussed of all electromagnetic beams (limited only by the diffraction limit of light), in turn offering the highest power densities (or highest potential resolutions for imaging applications). This is the primary reason why the majority of commercial laser systems are designed around operating via Gaussian beam generation, which also happens to be the lowest transverse mode. Additionally, Gaussian beams preserve their spatial intensity distribution through both propagation and focussing, further consolidating the relative ease of modelling their behaviour.

However, while the strongly confined focal regions provided by these focussed Gaussian beams are thus clearly well suited for reaching the aforementioned high energy densities required for plasma generation (or for exceeding the ablation threshold of the material in lower intensity photoablation processes), they inherently suffer from being highly divergent at either side of their respective focal regions. This is due to the well-established fact that the more tightly a Gaussian beam is focussed, the more divergent it becomes. This behaviour arises from the Rayleigh range characteristic of focussed Gaussian beams, which is expressed as follows:

$$z_R = \frac{\pi \omega_0^2}{\lambda}; \quad (2.1)$$

where Z_R is the Rayleigh range, ω_0 is the beam waist radius and λ is the wavelength of the laser source. The Rayleigh range is the parameter that defines the distance over which the beam waist radius (the minimum beam radius along the laser beams propagation) is increased by a factor of the square root of 2. For the conventional circular beam shapes considered here, this means that the area of the spot is doubled over this distance. It is the standard parameter for defining the distance over which the beam does not severely diverge. An illustration of the divergent nature of a typical Gaussian beam is shown in figure 2.18. As can be seen from equation 2.1, the smaller the beam waist radius is (*i.e.* the more strongly focussed the beam is), the shorter the corresponding Rayleigh range becomes. For spot sizes around the order of 10 μm the Rayleigh range can be as small as the 100 μm range, clearly indicating the potential for reduced maximum achievable removal depths within the material being ablated where increased levels of lateral precision are needed or desired.

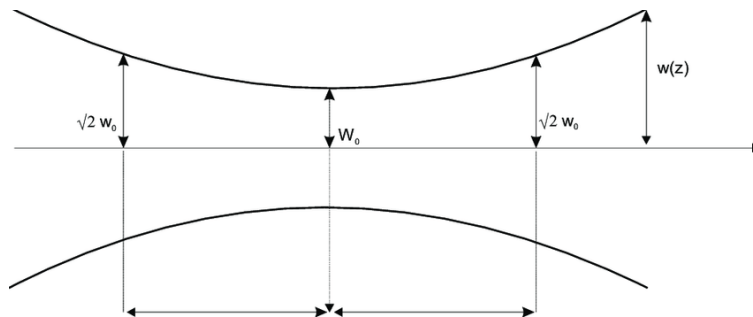


Figure 2.18 – Side profile of the waist area of a Gaussian beam [2.91].

Despite their prominence within industrial laser-based material processing applications, this divergent behaviour leads to numerous issues regarding limited throughputs in such processes. This is related to the finite volume over which plasma is formed (or again for lower intensity photoablation-based processes the finite volume over which the ablation threshold of the material is reached or exceeded) for these Gaussian beam geometries, as when the beam diverges there is a relatively drastic drop in the energy intensity contained within the consequently increased spot diameter. This also inevitably causes issues regarding focussing sensitivity, which is further exacerbated when the surface of the material to be ablated is inhomogeneous and/or difficult to accurately profile, as is the case for biological tissues. This is particularly true for procedures where high precision is desirable (which is the primary justification for the application of plasma-mediated ablation) as this inherently places additional demands upon the regularity/morphology of the sample surface. Additionally, while there exists an inherent tradeoff between removal/ablation rates and the level of depth control (vital for avoiding bowel perforation within the context of bowel surgery that is foremost among the considered applications for this thesis), there is clearly still ample room to further optimise laser-based ablation processing times (whether plasma-mediated or facilitated by photothermal effects) for increased cost-efficiency across various industries [2.92]. For the medical industry in particular the resulting reduction in operation times would prove mutually beneficial to both surgeons and patients.

These confining factors of limited throughputs and focussing sensitivity can be clearly observed in both transparent material processing (a significant industrial field, with applications including waveguide inscription and the manufacture of photonic and electronic devices) and laser drilling of opaque materials, as non-linear driven processes in both types of material depend not only on the cross-sectional focus area

at specific planes but also on the total focal volume of the incident laser beam [2.93]. For material drilling in particular this limits the achievable aspect ratios and leads to tapered crater walls for Gaussian beam inputs [2.94]. Techniques such as temporal focussing paired with a low numerical aperture have been used to try and address these issues in micromachining trials, including the sectioning of an excised mouse skull sample submersed in water [2.90]. While relatively high ablation rates of $25 \mu\text{m}^3$ per $80 \mu\text{J}$ pulse were achieved with a high degree of axial confinement, and this was subsequently taken further to permit *in vivo* imaging of mouse brain vasculature, it involved the use of femtosecond pulses to achieve the peak intensities required for plasma formation [2.95]. Despite the lateral and axial decoupling of the ablation process that was showcased through the consistent thickness of bone tissue removed, these shorter pulse durations are not suited towards fibre guided modalities, as discussed in more detail later in this chapter. In addition, the damage from the shockwaves produced during the plasma ablation process was not evaluated.

The hard-set limitations on both the productivity and robustness of the ablation process are clearly undesirable traits under the wider context of material processing, with the Gaussian beams not proving to be wholly ideal for various applications (particularly those involving materials with irregular/inconsistent morphologies, as is the case for tissue ablation) despite their established nature. As a result of this, there is an ongoing research interest in extending these ranges via various means of beam shaping to increase efficiency. These beam shaping techniques offer the potential to modify the way the energy from the laser source is deposited on the surface of and/or within the sample. This enables precise tailoring of the overall material ablation/modification process. However, most currently utilised beam-shaping techniques are limited as they only work in two dimensions at a given focal plane. This is due to the fact that they typically involve the use of a diffractive optical element to alter the phase front of the incident laser beam to match that of the Fourier transform of the desired output beam profile, which is subsequently formed at the focal region [2.96]. This causes the beam to be semi-randomised elsewhere along its propagation, which in turn inhibits the occurrence of non-linear phenomena such as plasma-mediated ablation, where the properties of the total focal volume are a significant factor, as opposed to the beam properties at a single focal plane.

2.1.7 Bessel beams

Another promising and recent development within the field of minimally invasive surgery is the application of Bessel beams towards tissue ablation. Bessel beams are of interest as they offer the potential for “non-diffracting” propagation. Durnin was the first to take note of these solutions to the Helmholtz equation [2.97]. He noticed that they were independent of the propagation direction and that they had the interesting property of being non-diffracting. Durnin *et al.* proceeded to showcase an experimentally realised approximation of this mathematical concept, with the important distinction that it was non-diffracting only over a finite distance [2.98]. This was a controversial idea upon its founding, with some publications questioning the legitimacy of this definition [2.99]. This was soon addressed by Durnin *et al.* by stating that what they had observed was that the “... central maxima are remarkably resistant to the diffractive spreading commonly associated with all wave propagation” [2.100]. In drawing this comparison between the Bessel beam and Gaussian beam geometries, they made it clear that it is the central core which remains propagation invariant. As a result, Bessel beams are able to remain focussed over distances that are orders of magnitude greater than the Rayleigh ranges offered by Gaussian beams [2.101]. This is significant as due to their comparatively low focal depths, Gaussian beams have suffered from low ablation

rates and restricted cutting depths as discussed in the previous section. Ablation with Gaussian beams has also been hindered by heightened non-uniformity in tissue, as the rapid variation in the focal spot size partnered with the inhomogeneous medium of tissue results in large alterations of the incident beam profile [2.102]. Meanwhile, Bessel beams appear to be ideal for treating tissue, as their inherent resistance to diffraction pairs well with inhomogeneous mediums. They are even able to self-heal, referring to the fact that they can reform further along their axis of propagation, even if partially obstructed at some point.

It has been well documented that the most efficient technique to generate a Bessel beam involves illuminating a conical lens (more commonly referred to as an axicon) with a conventional Gaussian beam, as opposed to using an annular slit, as it is able to use the majority of, if not the entirety of the incident Gaussian beam [2.103]. Axicons offer a potential solution to the previously discussed depth related issues within material processing studies through effectively decoupling the spot size/attainable resolution and the focal depth (which can be tailored via altering the physical angle of the conical side of the lens and/or the input beam diameter). In addition to being cheaper than high diffraction efficiency SLMs of roughly equivalent damage thresholds, they also offer the potential for miniaturisation by applying etching/polishing techniques to create either standalone micro-optics or integrated axicons at the output facets of optical fibres [2.104],[2.105],[2.106]. These lenses are the simplest example of three-dimensional beam shaping via interference, with the Bessel-Gauss beams that they generate from a Gaussian input beam providing the same order of lateral precision as a conventionally focussed (*i.e.* focussed via a convex lens) Gaussian beam while benefitting from much improved throughputs, increased tolerances with regards to focussing and the capacity for higher aspect ratio drilling. A diagram of a Bessel-Gauss beam being generated by an axicon from a Gaussian beam input is shown in figure 2.19.

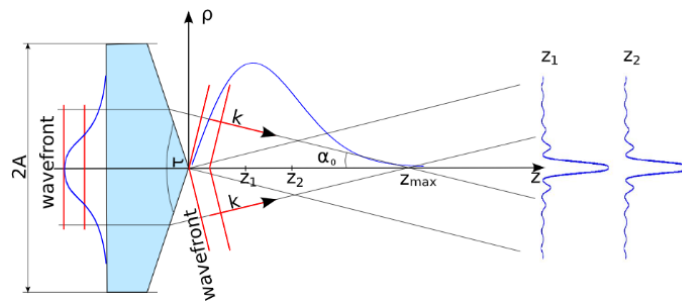


Figure 2.19 – Generation of a Bessel-Gauss beam by an ideal axicon illuminated by a Gaussian beam with the beam waist located on the front/plane surface of the axicon. The intensity profile along the propagation axis is illustrated along with the invariant radial intensity profile at two arbitrary axial positions, labelled Z_1 and Z_2 . Z_{max} is the maximum propagation distance up to which the Bessel-Gauss beam is maintained and τ is the apex angle of the axicon [2.107].

The more consistent intensity profile along the propagation of the beam has led to Bessel-Gauss beams earning some traction with researchers interested in materials processing [2.108],[2.109]. Following on from these recent nanofabrication trials, there have also been recent studies that have considered their potential applications in medical environments, as the numerous distinct advantages observed with Bessel-Gauss beams were of shared interest between the two industries. These have ranged from cosmetic surgery to the ablation of bone tissue, as well as targeted cell ablation [2.110],[2.111],[2.112].

Regarding the targeted cell ablation, the implementation of a Bessel-Gauss beam partnered with a selective plane illumination microscope enabled more precise and rapid targeting and subsequent ablation of cancerous cells found within zebrafish (signalled through the use of binding fluorescent proteins) compared

to more a conventional setup using a fluorescent microscope and Gaussian beam profile, which led to increased rates of fish survival [2.113]. These improvements in cell subset targeting at anatomical depths in live, developing zebrafish kidneys were primarily due to the low diffraction of the Bessel-Gauss beam and the incorporation of a compatible high numerical aperture (NA) lens. Other cell targeting studies have looked at cellular transfection using Bessel-Gauss beams, both through free space propagation and fibre delivery (generated via an axicon tip on the end of the fibre in the latter instance) [2.114],[2.115]. These studies benefitted from the reduction in the required precision of axial alignment that the Bessel-Gauss beam offers, due to the longer axial range it provides. This offered the potential for cellular transfection across axial ranges that were twenty times larger than the equivalently sized (1.8 μm spot diameter) Gaussian beam [2.116].

In the context of cosmetic surgery upon the skin (treatment of skin lesions in *ex vivo* human samples specifically), Bessel-Gauss beams benefitted from being able to penetrate deeper into the tissue, due to longer propagation distances, while also exhibiting a lesser extent of radial damage [2.110]. This again showcases their potential to provide improved depth-to-diameter ratios compared to Gaussian beams. Meanwhile, when considering tissue ablation as opposed to photothermolysis, Ashforth *et al.* were able to achieve a six to seven times lower ablation threshold in bovine and ovine cortical bone tissue using a zero-order Bessel-Gauss beam opposed to a Gaussian one, similar to the trends previously observed in both silicon and quartz [2.111],[2.117]. Some of the ablated features obtained with both beams are shown in figure 2.20. These ablation thresholds were found to be independent of the species, suggesting that ultrafast laser scalpels, whether utilising Gaussian or Bessel-Gauss beam shapes, would require minimal parameter modification between patients.

Both beam geometries also benefit from a lack of incubation effects while ablating bone, which was attributed to the inhomogeneity of the material. While these incubation effects can lead to more efficient ablation of materials such as metals and polymers when large numbers of pulses are applied, they hinder the consistency of the ablation rate, which would potentially be disadvantageous within surgical contexts where a high degree of precision is desirable. They also quoted ablation depths that were three times greater for the same number of pulses and pulse fluence, as well as ablation rates that were fourteen times greater, closing the sizable gap between the ablation rates that are possible with lasers and those achieved through mechanical tools, which in turn illustrates the potential for reduced laser-based surgical procedure durations. These greater ablation depths and rates can again be attributed to the lack of distortion experienced with a Bessel-Gauss beam profile when compared to a Gaussian, courtesy of its previously mentioned “self-healing” properties, which the authors theorise compensates for plasma shielding to some degree. This works synergistically with its previously mentioned ability to effectively remain focussed (thus possessing an intensity value above the ablation threshold) over distances that can be orders of magnitude greater than the Rayleigh ranges of Gaussian beams. A lack of heat-affected zones around the ablation sites within the bone tissue was confirmed via optical and single electron microscopy for both beams, but this lacks the more thorough insight that could be provided by histological evaluation. These studies are yet to be expanded to other forms of tissue, but it is thought that the more consistent intensity profile provided by Bessel-Gauss beams will be of significance in medical applications, as this could be invaluable when dealing with the various kinds of highly scattering tissue found within various animal species, including humans. In addition, the self-healing characteristics exhibited by Bessel-Gauss beams could prove to be

even more beneficial in cases where the tissue has a much higher degree of water within its composition, as this in turn places greater demands upon the robustness of the ablation process from the increased surface inhomogeneity and the fluid dynamics (such as the cavitation bubble formation covered previously) involved, whereas bone is a brittle and dry material by comparison [2.118].

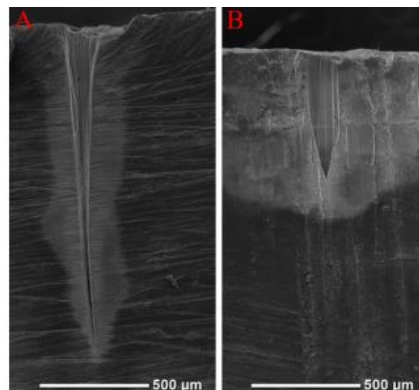


Figure 2.20 – SEM cross-sectional images of ablation features produced in bone after irradiation by 1000 pulses, each with a pulse fluence of 25.0 J cm^{-2} and pulse duration of 100 fs, operated at a pulse repetition rate of 1 kHz, with A) a zero-order Bessel-Gauss beam and B) a conventional Gaussian beam shape [2.111].

Also of note is that lasers have previously had their routine surgical applications limited to the treatment of soft tissues [2.119]. Still, these initial studies carried out by Ashforth *et al.* show promise, specifically with the markedly improved efficiency in ablation combined with both optical and scanning electron microscopy analysis indicating no thermal damage (specifically no charring, thermal induced cracking or molten debris). This would not only consolidate upon the currently established soft tissue procedures but also potentially open up routine hard tissue (*e.g.* bone) laser treatments. The authors even conclude this paper by stating that these axicons could be combined with Kagome type hollow-core photonic crystal fibres to deliver femtosecond laser sources with high peak powers. From these findings it becomes clear that there is further investigation to be carried out with these beams before any clinical applications can be realised. Validation of the lack of thermal damage while obtaining improved ablation properties is sought after, alongside evaluation of performance at pulse durations which are not inhibited by nonlinear effects while propagating through optical fibres.

The central lobes of Bessel-Gauss beams (albeit formed via a ring-shaped lens, as opposed to an axicon) have experimentally been shown to be very resistant to distortion upon propagation through water, with peak positional fluctuations of about 10% the FWHM of the central core in both the x- and y-axis [2.120]. This ability to penetrate deep within highly scattering media (such as biological tissues) has also been demonstrated in various imaging applications, including multiphoton microscopy of human gastric cancer and liver cancer samples performed through an axicon (AX255-C from Thorlabs), which showcased greater image acquisition rates without sacrificing lateral resolution [2.121]. This was achieved due to the greater depth of focus saving time in both capturing axial information across multiple tissue layers and the sample alignment process itself. Some of these microscope images can be observed in figure 2.21.

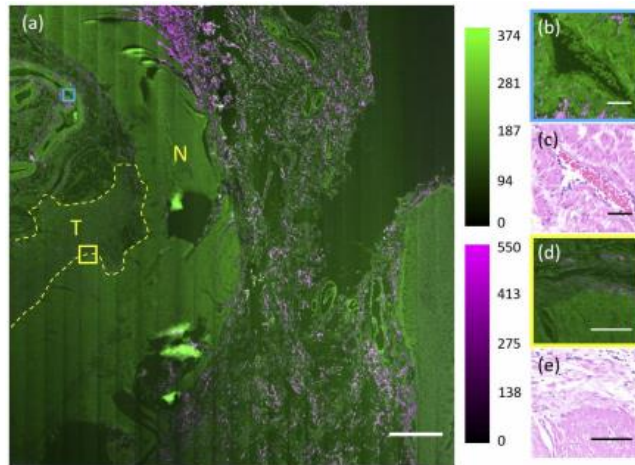


Figure 2.21 – Demonstration of rapid, high-resolution pathological imaging of a 3 μm thick human gastric tissue section via a reimaged 5° axicon, with a cancerous tumour region (T) being observed [2.121]. (a) Label-free image of the gastric tissue slice, with the yellow dashed line indicating the boundary between normal/healthy tissue (N) and the cancerous tumour tissue. The magenta and green areas represent second harmonic generation and two-photon auto-fluorescence signals respectively. The scale bar for (a) is 1 mm. (b) Magnified view of the area highlighted by the blue box in (a). The scale bar here is 50 μm . (c) Wide-field image of the corresponding area of (b) in the adjacent H&E stained slice. The scale bar here is again 50 μm . (d) Magnified view of the area highlighted by the yellow box in (a). The scale bar here is 100 μm . (e) Wide-field image of corresponding area of (d) in the adjacent H&E stained slice. Again, the scale bar here is 100 μm .

This potential for improved throughputs, increased tolerances to focal plane positioning and higher aspect ratio drilling from the increased focal depths Bessel-Gauss beams offer compared to more conventionally focussed Gaussian beams has also been experimentally demonstrated to greatly increase processing efficiency in the modification of glass, with this capability of highly precise and efficient dicing proving to be incredibly valuable towards endoscopic optics, as well as both the manufacturing of through-silicon-vias and cutting of quartz, both of which are vital to the semiconductor and consumer electronic industries [2.122],[2.123],[2.124],[2.125],[2.126],[2.127]. Figure 2.22 shows examples of high aspect ratio material modification in sapphire and glass obtained using a Bessel-Gauss beam.

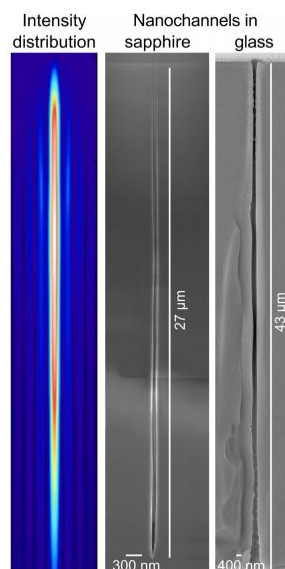


Figure 2.22 – Intensity distribution of Bessel-Gauss beam and the corresponding nanochannels produced in sapphire and glass samples via single shot ultrashort laser pulse illumination, with these images being captured using a Scanning Electron Microscope (SEM) [2.122].

These proof-of-concept material processing studies have been predominantly carried out on transparent materials, with limited publications on drilling more opaque materials like silicon carbide (SiC) [2.128],[2.129]. In this SiC processing research it was observed that the carbon-rich layers formed during ablation created a shielding effect which inhibited the propagation of the side lobes into the fabricated holes through strong absorption processes. This in turn limited the achievable ablation depths for the Bessel-Gauss beam, with the Gaussian drilling deeper. It is important to note however that a FWHM beam definition was used to define the beams, with the Gaussian spot (32 μm wide) being significantly larger than the Bessel-Gauss (1.5 μm wide), thus forming a wider lateral extent of plasma over a longer axial distance than if these spot sizes were more closely equated. Despite this, implications regarding the side lobes of the Bessel-Gauss profile leading to surface modifications upon the silicon carbide highlight the potential need for filtering out the surrounding concentric rings. Some publications have examined methods of suppressing these side lobes, but this comes at the expense of the axial extent over which propagation invariant behaviour is exhibited [2.130],[2.131].

Other limitations of the Bessel-Gauss beams produced by axicons include them not providing as high peak intensity values across their axial distributions compared to those produced by conventionally focussed Gaussian beams, as instead of propagating to a focus they rely on the occurrence of circularly symmetric interference mechanisms to form the central core and the equally spaced surrounding concentric rings. While this effectively provides them with a significantly greater depth of focus (while not being synonymous to a conventional focus) for equivalent lateral spot sizes, it comes at the expense of the irradiance contained within these quasi-focal regions. These Bessel-Gauss beam geometries also suffer from the potential drawback of having asymmetric energy distributions along their beam axis, as shown for both the ideal and oblate tip cases illustrated in figures 2.19 and 2.23 respectively. Compensation of this effect, similar to the experimental realisation of a beam with uniform axial intensity, would require bespoke, precise and technically demanding modulation of the field properties (*i.e.* phase), ideally paired with an aberration-free optical pathway [2.132]. These axicons also cost more to manufacture than typical convex lenses due to the geometrical demands that originate from the specifications of the conical surface.

Furthermore, while these axicons do offer the potential for miniaturisation, they will still potentially be the limiting factor for minimising the size of an endoscopic probe design. On-axis alignment of the incident beam could also be an area of concern for these axicons, particularly for the output facet of a fibre where a range of angles are produced by the guided light. However, the on-axis intensity for Bessel-Gauss beams has been shown to have a high tolerance to the relative tilt angle between the axicon and the input beam, with tilt angles of up to 10° leading to minimised ellipticity of the central core and increased intensities, as the added aberrations compensate for the distortions caused by the oblate tip while using a commercially available axicon (AX255-C from Thorlabs) [2.133].

This oblate (rounded) tip that arises during the manufacturing process is another practical limitation of these axicons. This rounding of the tip creates a refracted beam that interferes with the Bessel-Gauss beam generated by the axicon, causing noticeable modulation of the on-axis intensity distribution. This modification of the axial intensity distribution is depicted in figure 2.23. While this can be accounted for via the implementation of spatial filtering to remove the low frequency spatial frequency spectrum components generated by the oblate tip, this invariably reduces the efficiency/peak intensity of the output beam [2.107]. However, this effect can also potentially be accounted for to some degree via incorporating

a 4F optical setup comprising of two lenses of positive focal lengths. This acts as a reimaging telescope and reduces the central core diameter by a factor equal to the ratio of the focal lengths of the two lenses (which can also be helpful as the Bessel-Gauss beam formed from an axicon is often too wide for performing experiments with micro-level precision), while also compressing the Bessel zone length (Z_{\max} in figures 2.19 and 2.23) by the squared product of this demagnification factor [2.134],[2.124]. This leads to a significant increase in the intensity across this region, while still offering much greater focal depths (which can also be tailored via alteration of the input beam diameter and/or the demagnification factor) than a focussed Gaussian beam of an equivalent spot size. While this will consequently exacerbate these intensity fluctuations, for the application of plasma-mediated tissue ablation the primary interest is simply the portion of the total Bessel zone length that equals or exceeds the intensity regime necessary to maintain plasma formation.

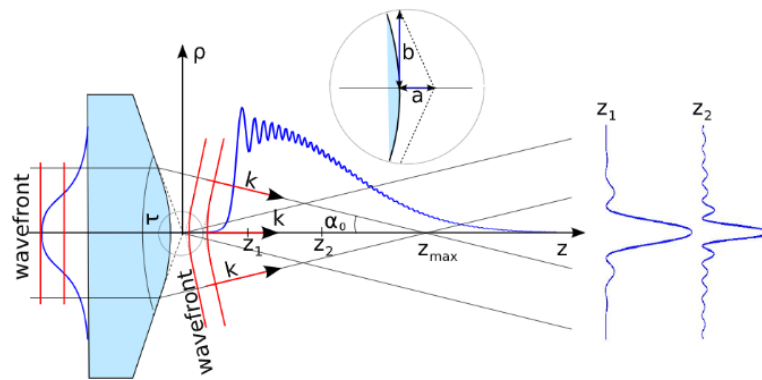


Figure 2.23 – Generation of a Bessel-Gauss beam by an oblate (rounded) tip axicon illuminated by a Gaussian beam with the beam waist located on the front/plane surface of the axicon [2.107]. Similar to figure 2.19, the intensity profile along the propagation axis is illustrated along with the radial intensity profile at two arbitrary axial positions, labelled Z_1 and Z_2 . Again, Z_{\max} is the maximum propagation distance up to which the Bessel-Gauss beam is maintained and τ is the apex angle of the axicon. The intensity modulating effect of the imperfect/rounded axicon tip is showcased here. This is caused by the wave that is refracted by the round tip propagating behind the axicon and subsequently interfering with the Bessel-Gauss beam. This interference also means that the radial intensity profile is no longer invariant (see examples at Z_1 and Z_2). The inset image shows an approximation of the round tip of the axicon via a two-sheet hyperboloid of revolution.

Even upon considering some of these practical limitations, it becomes conceptually clear that the ablation of tissue could benefit from reducing the need for specific focal plane positioning through the increased depth of focus offered by these Bessel-Gauss beams. This alone could significantly reduce the duration of various procedures, thus making the implementation of these more bespoke beam geometries economically beneficial, despite their less established nature.

The nonlinear ultrafast laser-based tissue ablation processes under consideration in this thesis could also potentially benefit from deeper removal of cancerous tissue, without being compromised via a linked increase in laterally induced thermal damage (as would be the case when using a Gaussian beam), as these Bessel-Gauss beams offer a more consistent cross-sectional intensity profile across these extended focal regions, as illustrated in figure 2.24. For this same reason, there is also the potential for reducing the number of passes required to achieve a specified depth of ablation compared to the relatively slow scanning techniques currently required by Gaussian beams. Both of these outcomes address a key issue regarding ultrafast laser ablation processes – improving throughput while maintaining the degree of localisation of

thermal damage around the surgical site which again is among the primary justifications for applying this specific surgical modality.

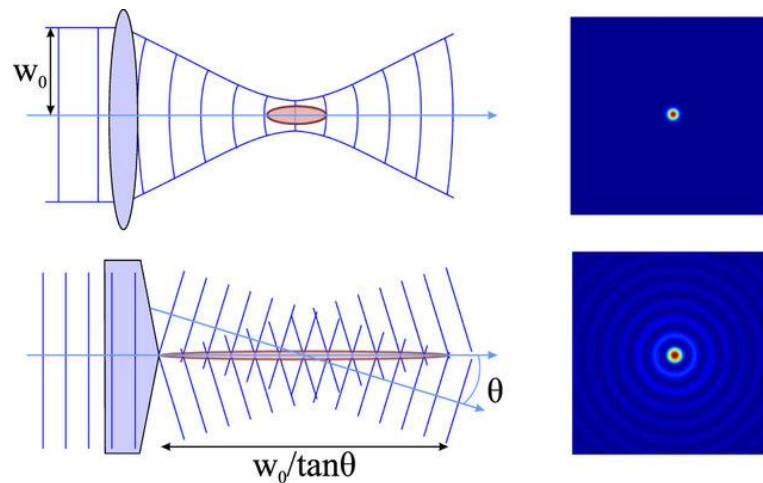


Figure 2.24 – A Gaussian beam focused by a convex lens generates a localised plasma in the focal region which is inherently of limited volume, while a Bessel-Gauss beam, obtained by focusing a Gaussian beam of width w_0 with an axicon, can generate a plasma channel over the Bessel zone, which by comparison can possess a significantly greater length [2.135].

Additionally, these laser-based tissue ablation processes could benefit from restrictions in the total achievable ablation depth that arise from the self-limiting behaviour of these Bessel-Gauss beams. This occurs due to the interference mechanisms that are responsible for their formation, as these create relatively sharp drop offs in the axial intensity distribution either side of the Bessel zone. However, as these Bessel-Gauss beams rely on these interference mechanisms for generation, various conventional assumptions in laser material interaction processes do not apply, hence experimental trials on clinically relevant tissue samples will need to be performed to observe the absorption and subsequent ablation characteristics.

While the comparative lack of focal depth from focussed Gaussian beams can be compensated via axial scanning, this introduces numerous endoscopic design implications. For changing the distance between the endoscope fibre and the objective lens, this entails the incorporation of moving components along the length of the endoscope, invariably adding to the total size of the device [2.92]. Alternatively, multiple fibres could be incorporated with slightly shifted axial positions, but this similarly increases the diameter of the endoscope for increased axial scan ranges. Lastly, a lens of varying refractive power, such as a tuneable acoustic gradient (TAG) index lens could be used, although the mismatch between the laser pulse repetition rate and the axial scanning leads to noticeable variation in both the depth and achievable resolution of material modification [2.136]. This method also presents challenges regarding miniaturisation.

2.1.8 Alternative beam shaping techniques

It is important to acknowledge that alternative beam shaping methods do exist. Simulations on Fundamental Beam Mode Shaper (FBS) techniques (a beam shaping method that uses binary phase information which is then converted into an optical component that acts as a phase plate via ion-beam-etching and reactive-ion-etching) offer some potential through showcasing a more uniform peak intensity around the focal plane compared to a conventional Gaussian beam [2.137]. These are yet to be experimentally showcased however and the Rayleigh length was only increased up to a maximum of 40% (from 327 μm to 470 μm for a given beam waist radius of 7.44 μm) by superimposing two FBS phase distributions.

Spatial light modulators (SLMs) offer another means of beam shaping [2.138]. While being a powerful research tool due to the flexibility that these devices provide through the ability to dynamically modify the amplitude and/or phase of the laser beam input to them (as opposed to being a fixed optical element), they are inherently not suited for incorporation into endoscopic applications due to requiring a well-defined laser beam input at a specific angle of incidence to the SLM surface, whereas a fibre guided laser would produce an array of incident angles if the SLM were to be placed at the output facet (increasing the already significant computational demands for high resolution outputs) [2.139]. Alternatively, if placed prior to the input facet of the fibre, the beam shape would not be preserved upon guidance through said fibre. Additionally, while recently developed SLMs exhibit higher damage thresholds and are therefore compatible with high power laser sources which are capable of material processing, they are intrinsically ill-suited towards the level of miniaturisation required for endoscopic applications, particularly with issues of shaping inefficiencies arising from speckle noise and discrepancies between the sizes of the geometric mask displayed on the SLM and the input beam itself [2.140],[2.141],[2.142].

2.2 Surgical devices

2.2.1 Non-laser-based surgical devices

2.2.1.1 Scalpel

The most rudimentary and widely used medical tool that could be viewed as competition against the laser in a range of procedures is the scalpel. Flint knives (which can be considered the predecessor to the scalpel) were the first surgical tool to be developed, with evidence of them being used in medical applications (cutting through the skull) dating as far back as the Mesolithic period during the Middle Stone Age [2.143]. The first incarnation of the surgical knife (or scalpel) was described by Hippocrates, with it maintaining the same general shape to this day (a sharp, curved blade that comes to a straight point) [2.144]. The modern concept of the scalpel was conceived by Morgan Parker, who received a patent for his two-piece design (blade and handle, held together by overlapping metal sections) in 1915 [2.145].

Scalpels are used to make incisions in various tissues where precision is important, with the width of the cut being determined by the type of blade used. Bleeding is highlighted as being the primary concern with scalpel-based procedures among medical staff, as unlike the other tools highlighted here it lacks haemostatic capabilities [2.146]. Bleeding can obstruct points of interest, consequently increasing surgery time, which is clearly undesirable. Other significant factors in surgical procedures that utilize the scalpel include low-initial setup costs and more consistently documented wound recovery compared to alternative methods like electrosurgery, although there is also potentially significant scarring of the tissue post-surgery [2.147]. Other drawbacks compared to electrosurgical and harmonic scalpel-based procedures include longer incision times (particularly with both meticulous planning and an experienced user being necessary for maximising the potential precision), more severe post-operative pain and a higher demand for pain-killers as a result [2.148],[2.149]. The typical damage zones formed by scalpel incisions are illustrated in figure 2.25 alongside those generated by conventional and picosecond infrared lasers.

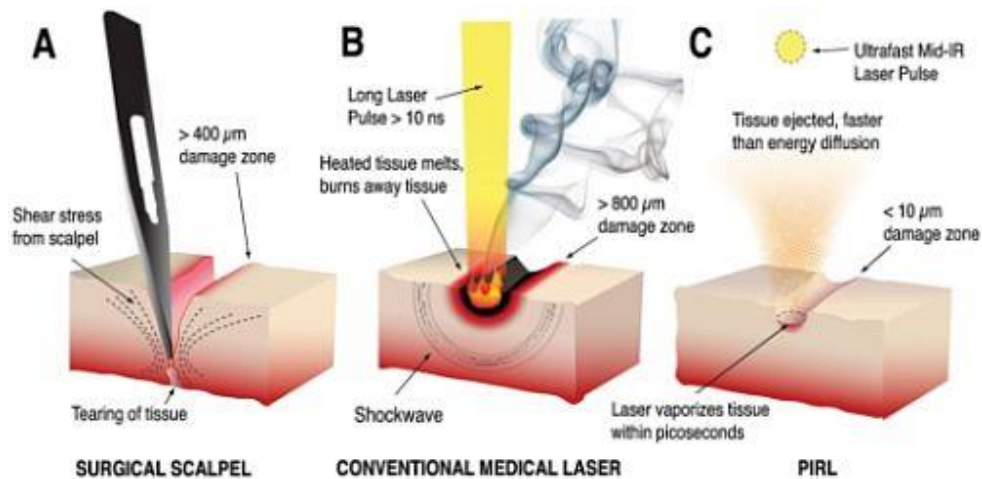


Figure 2.25 – Comparison between a) scalpel, b) conventional surgical laser and c) picosecond infrared laser (PIRL) [2.150].

2.2.1.2 Electrosurgery

The first record of electricity being applied to medicine was a treatment carried out on a patient by physician Johann Gottlob Krüger in 1743 [2.151]. The modern electrosurgical unit (a cutting loop) was initially designed by William T. Bovie and this design was implemented into clinical practice for the first time by Dr. Harvey Cushing on October 1st 1926 at the Peter Bent Brigham Hospital in Boston [2.152]. This operation involved the removal of a vascular myeloma from the head of a patient [2.153].

Electrosurgery is based on applying high frequency electrical currents (typically 100 kHz to 5 MHz) through tissue in various forms of clinical procedures [2.154]. These high frequencies are used as nerve and muscle stimulation are hindered at around 100 kHz, ensuring these electrosurgical procedures are as safe as possible [2.155]. Undesirable tissue is heated through these high frequency electrical currents, as energy is dissipated when these currents encounter resistance imposed by the biological structures within the human body (with typical tissue resistances lying between 100 and 1000 ohms) [2.156]. This elevation in temperature (potentially heating the water molecules within the tissue to such an extent that they can exceed boiling point) is what causes the desired ablation and/or sealing of blood cells. Figure 2.26 is a photograph of an electrosurgical device in use during an operative procedure.



Figure 2.26 – Use of a monopolar electrosurgical instrument to coagulate tissue during the excision of a lipoma [2.157].

There is a distinction made between electrosurgery and electrocautery. The latter uses a direct current which does not enter the body of the patient (only the heated wire end occasionally makes physical contact with the tissue), while the former uses an alternating radio frequency (RF) current which does.

The electrosurgical generators which produce the high frequencies required for these procedures can produce a variety of waveforms. The effects observed on the tissue change upon altering these waveforms through modulation, with the primary applications being the cutting or coagulation of tissue. Various waveforms are showcased in figure 2.27.

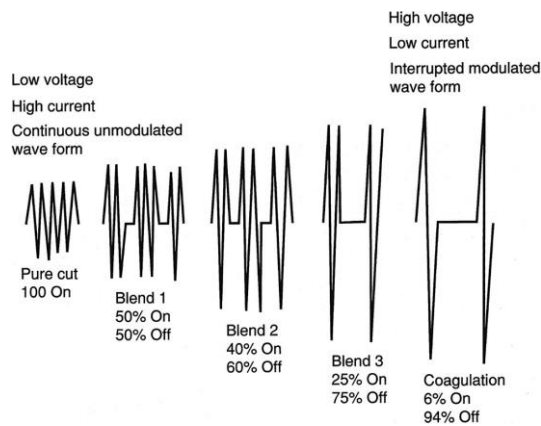


Figure 2.27 – Various electrosurgical waveforms [2.158].

Cutting current uses a constant, unmodulated sinusoidal waveform to ablate tissue in a non-contact manner [2.158]. The cutting of tissue is achieved as this waveform attains a higher average power than any other (assuming equivalent peak voltages). This can be attributed to the fact that the duty cycle with this waveform is 100% (*i.e.* the current is on with no lapses for the complete duration of the procedure, producing the greatest amount of heat out of all the waveforms), allowing sparks to form between the active electrode and the tissue.

Coagulating current uses a modulated waveform which reduces the duty cycle (typically to around 6%). This waveform consists of numerous intermittent damped sinusoidal waves, which use high peak voltages to achieve a lower transmission of heat to the tissue than the cutting current. As less heat is produced this makes it the ideal waveform to produce a coagulum within blood vessels. There are two types of coagulation that can be performed – desiccation and fulguration [2.159]. Desiccation uses an active electrode which makes physical contact with the skin (either the surface of the skin or inserted into the skin), while fulguration is a non-contact method. In desiccation a coagulum is formed when the electrode touches the skin. While it allows deeper coagulation, it comes at the expense of increased thermal damage. Fulguration coagulates the tissue by spraying electric sparks over the tissue, allowing treatment over a wide area. However, it suffers from requiring higher voltages than the cutting current (to overcome the high impedance of the air between the electrode and the tissue), which is a potential source of numerous complications in minimally invasive contexts.

A blending current enables both cutting and coagulating of tissue. However, it is important to note that this is not simply a combination of the two waveforms, but instead relies on an altered duty cycle, or “blends”. Switching progressively from a 50% to 25% duty cycle causes less efficient tissue ablation but more efficient haemostasis, which causes this apparent switch of operating modalities. Examples of the thermal damage caused by cutting, blending and coagulating currents are highlighted in figure 2.28.

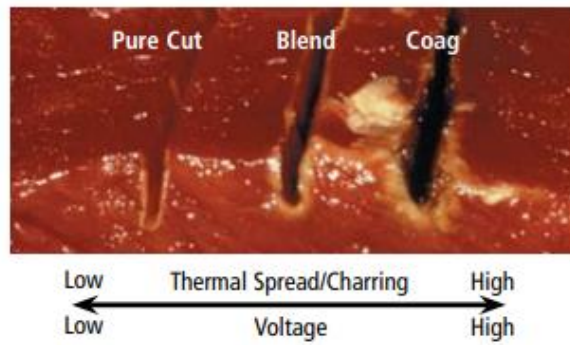


Figure 2.28 – Thermal spread in tissue from various electro-surgical procedures using different waveforms [2.160].

The current density is the other (and perhaps more significant) electrical property that determines the application of the applied currents, with higher current densities leading to the necessary energy levels for water molecules within the cells to vaporise (causing the tissue to separate), which effectively cuts the tissue [2.161]. Meanwhile, lower current densities lead to coagulation as the generated heat is spread over a larger area, preventing the cells from reaching their vaporisation temperatures but still heating them to the point where protein denaturation occurs. This starts the forming of a coagulum that inhibits blood flow.

It is important to note that, regardless of the intended application, the power required to reach the necessary temperatures depends on both the thermal and electrical conductivity properties of the tissue. The bioheat equation has been used previously for calculating the temperature of tissue subjected to electro-surgical procedures, through the pairing of thermodynamic variables such as specific heat capacity with electrical properties such as electrical conductivity and current density [2.162],[2.163]. While earlier theoretical models (such as the ETherm3 simulation software) were able to take changes in the radiofrequency field solution into consideration (originating from changes in the tissue properties from ongoing thermal effects) and various transition temperatures, they lacked comprehensive characterisation of the various physical processes which occur at these high temperature induced phase transitions during electro-surgical dissection [2.164],[2.165].

These include the evaporation of water and the transport of water vapor within the tissue. These are of significance as they prevent continued linear trends in the calculated temperatures as they exceed the boiling point – something which is not observed experimentally. While these have been factored into a recent model developed at the Rensselaer Polytechnic Institute, and have even been experimentally validated through electro-surgical ablation trials carried out on *ex vivo* porcine liver samples, this model still lacks consideration of some potentially important factors regarding tissue damage [2.166]. These include the rapid transport of fluids within the tissue, mechanical deformation and/or dissection of the tissue and friction arising from physical contact between the electrode and the tissue surface.

Electrosurgery relies on dipole circuit setups, with the two respective electrodes being in contact with the human tissue (a dielectric substance) [2.167]. This constitutes the complete circuit necessary for an electrical current to flow. The two types of dipole circuit are monopolar and bipolar. Monopolar utilises one active electrode (the surgical instrument end) and one return electrode (a dispersive electrode pad, attached to the patient). It typically requires much greater power input than bipolar, as the increased distance between the two electrodes means there are many more possible paths for the applied currents to travel through the tissue. This does lead to improved haemostatic performance however, due to the deeper heating

of the tissue that occurs which leads to more blood vessels being coagulated. Bipolar has both the active and return electrode functionalities being carried out at the site of surgery (*i.e.* electrical forceps), which results in higher current densities and improved localisation of tissue damage compared to monopolar modes. Diagrams of monopolar and bipolar electro-surgery are shown in figure 2.29.

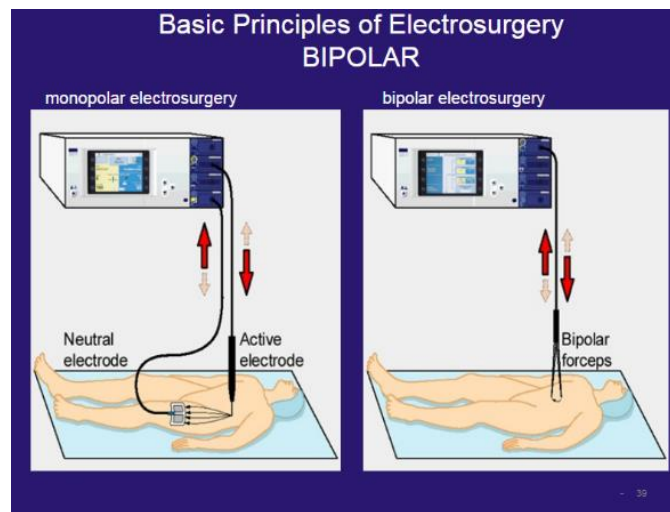


Figure 2.29 – Monopolar vs bipolar electro-surgical circuits [2.168].

Advantages of electro-surgery compared to conventional scalpel procedures include improved haemostasis/reduced blood loss and even the potential for simultaneous cutting and coagulation via blending current operation as described previously [2.169]. However, postoperative pain for both techniques has been reported in numerous papers to be roughly equivalent and there was no clinically significant difference in the time taken to make major abdominal incisions [2.170],[2.171].

However, conflicting studies comparing electro-surgery with laser surgery have emerged with regards to collateral thermally induced damage and overall suitability for a range of procedures. Some older papers have stated that both methods result in fairly even magnitudes of thermal damage in the context of infertility surgery, while more recent publications state that postoperative wound infection rates were found to not have improved from scalpel procedures after carrying out electro-surgery, indicating that laser-based procedures would potentially be preferable [2.172],[2.173],[2.174]. Additionally, in orthodontic tissue surgery, electro-surgical and conventional scalpel techniques require anaesthesia, whereas this is not mandatory for diode laser treatments, due to reduced intraoperative and postoperative discomfort [2.175],[2.176]. Electro-surgery currently benefits from lower equipment costs, and higher ablation rates, while also showing a similar capacity for haemostasis as a CO₂ laser, but it suffers from a greater degree of surgical smoke and tissue debris being produced (as it causes significantly more carbonisation, whereas this is more easily avoided with laser-based surgical modalities), offering lower precision from the endoscope being obscured, making it less suitable for minimally invasive procedures [2.177],[2.178]. This is particularly true for cases where thin structures are being operated on, which intrinsically carry a high risk of perforation (*e.g.* vocal folds and bowel lining).

2.2.1.3 Harmonic scalpel

The harmonic scalpel functions via ultrasonic vibrations [2.179]. These vibrations drive the primary component of the scalpel - the active blade. Other components include a generator, a hand-piece which contains piezoelectric transducers (these convert the electrical energy supplied by the generator to the ultrasonic vibrations), and a foot pedal for tailoring the power supplied to the instrument in real-time. A harmonic scalpel hand-piece is illustrated in figure 2.30.



Figure 2.30 – Harmonic scalpel hand-piece (with the active blade component magnified) [2.180].

Like both laser and electrosurgical devices, it allows for simultaneous cutting and cauterising of tissue through mechanical friction between the tissue and the active blade. This friction transfers between the cells within the tissue, causing protein denaturation by disrupting the hydrogen bonding, leading to coagulation and/or dissection of the tissue. Advantages of the harmonic scalpel over electrosurgery include less smoke generation (thus less visual obstruction), increased precision in tissue dissection and improved haemostasis/less blood loss [2.181]. Additionally, it also benefits from reduced lateral thermal damage, with clinical trials on the human peritoneum showing average damage zones on the order of 100 μm [2.182]. In some earlier work it even outperformed both CO_2 and Nd:YAG lasers in this regard, achieving lateral thermal injury spread of less than 1.5 mm in porcine small bowel mesentery samples, compared to 4 mm and 4.2 mm respectively [2.183].

In randomised controlled studies of haemorrhoidectomy techniques the harmonic scalpel again showcased maximum lateral thermal damage zones of less than 1.5 mm, leading to reduced levels of postoperative pain, higher levels of patient satisfaction and reduced hospital stay periods, whereas bipolar and monopolar electrocautery exhibited thermal damage zones as large as 9 mm and 15 mm respectively in resection of small bowel mesentery tissue in a porcine model [2.184],[2.185]. Older laparoscopic trials comparing bipolar electrocautery to the harmonic scalpel reaffirm these results, with the harmonic scalpel causing lateral thermal injuries varying from 1 to 3 mm, which was reported as being around half of the mucosal damage that is observed using bipolar electrocautery [2.186],[2.187]. Similar findings were also published in previous randomised controlled studies of haemorrhoidectomy techniques that compared monopolar electrocautery to the harmonic scalpel (which displayed peak thermal spread measurements of less than 2 mm in this instance), as would be expected from the increased thermal damage zone that is created using a monopolar device as opposed to a dipolar one [2.188]. These significant reductions of the thermal damage zones originate from the harmonic scalpel using ultrasonic mechanisms to drive dissection and/or coagulation, as opposed to relying primarily on thermal diffusion as is the case for electrocautery. As a

result of these advantages, harmonic scalpels have even made cost efficient laparoscopic appendectomies in children a reality, with an example of this procedure being shown in figure 2.31 [2.189].

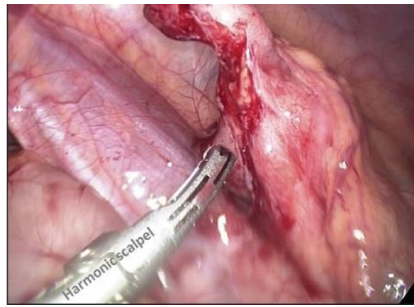


Figure 2.31 – Harmonic scalpel hand-piece coagulating and dividing the mesoappendix in laparoscopic appendectomy [2.189].

However, there are conflicting studies on operative time, with older studies indicating that harmonic scalpel-based procedures were shorter in duration than electrosurgical ones and more recent ones claiming the contrary [2.190],[2.191]. There are also relatively recent patient reports pointing towards more intense post-operative pain being experienced after the use of a harmonic scalpel compared to an electric scalpel [2.192]. This in turn creates demand for researching alternative methods (with laser-based procedures having precedence).

The harmonic scalpel has only recently been reported to be capable of sealing blood vessels up to 7 mm in diameter (through the formation of coagulum from the protein denaturation process described previously), whereas laser-based instruments have been able to achieve this for quite some time while also causing a lower extent of thermal damage in relatively recent trials [2.193],[2.194]. These studies reinforce the initial trials which showed that a CO₂ fibre laser led to less than half of the thermal damage compared to that caused by a harmonic scalpel (mean depths of thermal damages of 0.30 mm and 0.69 mm respectively, despite the harmonic scalpel operating at 5 W and the CO₂ laser operating between 13 and 18 W) in human cadaver heads [2.195].

2.2.2 Early laser-based surgical devices

Lasers have been established as an alternative surgical tool to the previously covered electrosurgical devices, as well as both the conventional and harmonic scalpels. They offer minimal bleeding, reduced swelling, improved haemostasis, higher precision and improved process control in both tissue ablation and coagulation procedures [2.196],[2.197],[2.198]. This section focuses on long-pulsed (pulse duration equal to or greater than the sub-microsecond regime) and CW lasers and their applications in surgical contexts.

As discussed in the photothermal interactions section, these types of lasers rely on linear photon absorption processes within the cells that cause molecular excitation. Upon the relaxation of electrons from these excited states, heat is produced within the tissue. Depending on the extent of heat that is generated various effects are observed, including ablation, coagulation and carbonisation [2.199]. While this offers a high degree of localisation, coagulated damage zones are still present as this damage occurs prior to the tissue reaching the vaporisation point (*i.e.* prior to ablation being observed).

The laser that was used for initial surgical trials was the carbon dioxide-nitrogen-helium laser, commonly referred to as the CO₂ gas laser. This laser system was the most powerful CW laser available during the 1960s, when these initial trials were being carried out [2.200]. Despite the primary drive for the

development of this laser system being based around advances in communication, it was soon being used for surgical applications. This was primarily attributed to it having a wavelength that was highly absorbed by water [2.201]. The other laser system developed around the same period that propelled the use of infrared radiation in surgical applications was the erbium-doped yttrium aluminium garnet laser, also referred to as the erbium YAG laser (typically abbreviated to Er:YAG) [2.202]. The water absorption spectrum is shown in figure 2.32, highlighting both of these laser systems and 808 – 980 nm diode lasers.

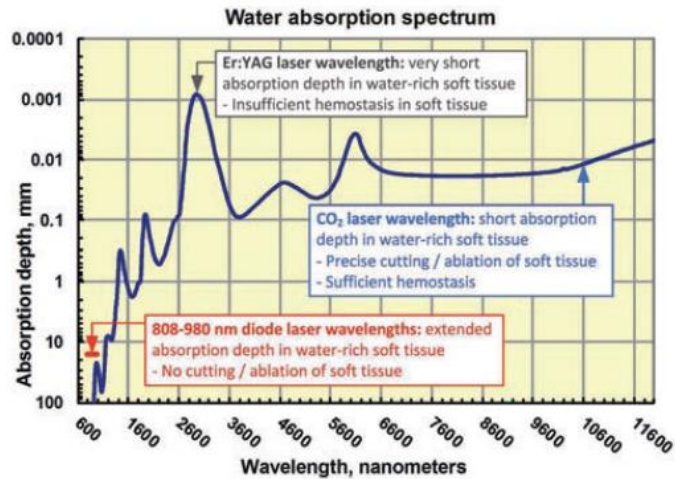


Figure 2.32 – Plot showcasing wavelength dependence of laser light interaction with water [2.203].

The first human tissue reconstruction laser surgery trials were carried out by Yahr and Strully in 1964 using a neodymium laser [2.204]. They later noted that using a CO₂ laser allowed them to make incisions on dry skin that healed as well as, if not better than those made with scalpels. They also noted that various kinds of tissue could be neatly divided, including bone, liver, kidney and lung tissues. They predicted that flexible bundles could be used to deliver laser beams to destroy various obstructions (*e.g.* kidney stones) that could clog up vital biological duct systems within the human body. They also went on to predict that the CO₂ laser would end up being used in medicine to make rapid incisions in the skin and ablate numerous kinds of organ without blood loss, once again showing foresight that was impressively accurate. Soon after these predictions were published, Yako used a CO₂ laser to surgically treat lesions located in the vocal cords of canines, the setup for which is shown in figure 2.33 [2.205]. This method of ablation proved to be fast, accurate and almost bloodless.

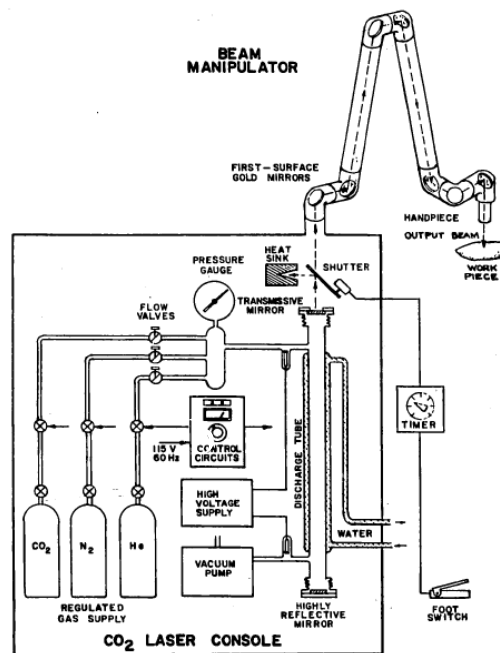


Figure 2.33 – Schematic of CO₂ continuous wave laser system used for targeted ablation of canine vocal cord tissue [2.205].

This vocal cord treatment was translated to human treatments only a few years later, as Yako, along with Strong, went on to elaborate how the CO₂ laser could be used for microscopic laryngoscopy [2.206]. Since then, other lasers have been incorporated into laryngeal surgical procedures, including pulsed dye lasers (PDLs), for which some results can be observed in figure 2.34 [2.207]. These offered better haemostatic effects than CO₂ lasers, but they could not be focused down as well.



Figure 2.34 – a) Microlaryngoscopic image of vocal fold capillary ectasia pre-operation b) Image captured post ablation with pulsed dye laser (PDL), showcasing the obliteration of vascular lesions while preserving overlying epithelium [2.207].

Only a year after being implemented in microscopic laryngoscopy, a CO₂ laser was used to treat a reproductive organ. Erosions of the uterine cervix were irradiated with a CO₂ laser, which was delivered through an endoscope [2.208]. Erosions within this region of the body were previously treated using either electrocautery or cryosurgery, but both methods led to potential haemorrhaging and resultant discomfort. Meanwhile, carrying out this treatment with a CO₂ laser was reported to be totally painless. This gynecological work was followed up by Staffl, who used the CO₂ laser to treat cervical intraepithelial neoplasia, as shown in figure 2.35 [2.209]. Comprehensive discussions on this topic were later formed by Bellina [2.210].

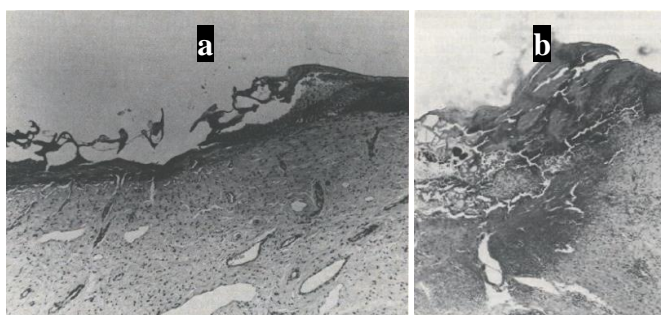


Figure 2.35 – Comparison between a) 1 s exposure CO₂ laser treatment of ectocervix at 3 watts and b) treatment of the cervix by electrocautery. The CO₂ laser enabled intraepithelial vaporisation (the separation between epithelium and stroma is apparent), useful for treating vaginal lesions with minimal or no collateral scarring. The electrocautery method of ablation showed a relatively large extent of leftover eschar and necrotic tissue in the treated area [2.210].

As previously mentioned, the Er:YAG laser has also been widely used in medicine due to the high absorption coefficient of water (approximately 12000 cm⁻¹) at the 2.94 μm wavelength that it emits [2.211]. A 1989 comparative study by Walsh Jr. *et al.* examined the thermal damage caused by 200 μs long normal-spiking-mode pulses and 90 ns Q-switched pulses from an Er:YAG laser on guinea pig skin and bone, as well as bovine cornea and aorta models [2.212]. The results for the bovine cornea model are shown in figure 2.36. The normal-spiking pulses were found to leave damaged zones of 10 – 50 μm to the collagen present around the incisions made, although the higher fluence values of around 80 J cm⁻² that were tested led to occasional tears being observed in the cornea and aorta samples, leading to collagen damage zones as large as 100 μm around the incision edges. The Q-switched pulses benefitted from higher localisation and more consistent ablation, leaving only 5 – 10 μm across the various types of tissue.

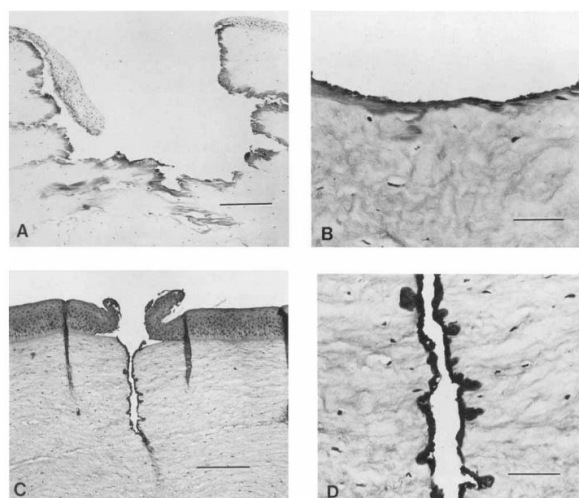


Figure 2.36 – Photomicrographs showing bovine cornea ablated by the normal-spiking-mode Er:YAG laser at A) high and B) low fluences respectively. At high fluences the tissue appears torn at the ablation crater edge. The damage zone around the crater is 20 – 60 μm wide, with sections of corneal epithelium dipping into the ablated crater being a common observation. Ablation parameters for a) were: 80 J cm⁻², 3 pulses, 2 Hz. Scale. bar = 200 μm. Contrary to high-fluence irradiations, at lower fluences the damage zone is somewhat intuitively much thinner, in this case 15 - 25 μm wide, and tears are not observed. Ablation parameters for b) were 22 J cm⁻², 3 pulses, 2 Hz. Scale bar = 50 μm. C) and D) are photomicrographs of bovine cornea ablated by the Q-switched Er:YAG laser; the damage zone is less than 10 μm wide. Ablation parameters used here were 1 J cm⁻², 60 pulses, 1Hz. Scale bars = 200 μm and 50 μm for c) and d) respectively [2.212].

This work was followed up by Hohenleutner *et al.*, who published work in 1997 examining the efficacy of Er:YAG laser ablation of both *in vivo* and *in vitro* human skin samples using 250 μs pulses with high pulse energies (up to 500 mJ) and repetition rates of between 7 and 10 Hz [2.213]. The extent of thermal damage

was also evaluated microscopically. They intuitively observed a linear trend between the applied fluence and ablation rate, as well as diminishing returns for the volume removed per pulse upon increasing the number of pulses applied to a single spot on the skin samples. Thermal damage zones in the region of 25 μm were observed when less than 10 pulses had been used to irradiate the tissue, with maximums of approximately 100 μm for 40 applied pulses, indicating that the thermal damage inflicted upon the samples increased directly with an increasing number of applied pulses, with this effect being exacerbated further by the limited precision that was possible for the 3 mm spot size. Higher fluences meanwhile were found to only cause slight increases on the order of a few microns in the dimensions of the thermal damage zones. While they found that overlapping pulses with fluences of around 4 J cm^{-2} applied in a sweeping scanning pattern could provide effective skin ablation, achieving smooth surface finishes and thermal damage zone dimensions below 50 μm , they also found that ablation was limited strictly to the superficial dermis layer due to haemostasis not being observed through a lack of coagulation, offering self-limiting depth control but only achieving maximum ablation depths equivalent to superficial exfoliation techniques like dermabrasion or a moderate depth chemical peel.

Despite some mixed findings from these older studies, advantages offered by lasers include tuneable coagulation and cutting efficiencies that are defined by the wavelength and the type of tissue (both defining traits in determining the penetration depth), as well as the ability to reduce bacteria (particularly in the context of oral soft tissue treatments) [2.214],[2.215],[2.216]. Figure 2.37 showcases the ablation of rat brain tissue captured using optical coherence tomography (OCT). There is still ongoing research towards investigating various feedback imaging modalities compatible with laser surgery due to these perks [2.217].

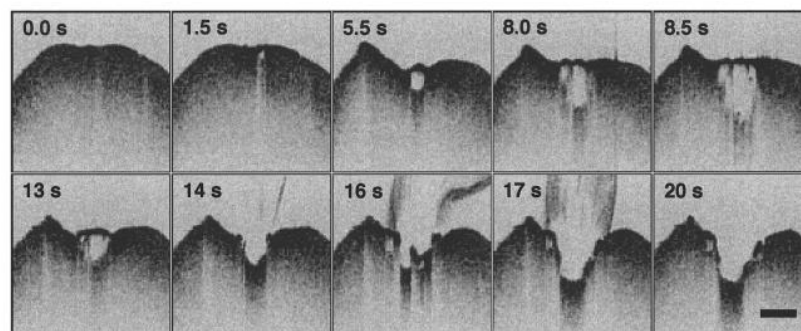


Figure 2.37 – Ablation of rat brain tissue carried out over 20 seconds using a CW argon laser. Brain tissue has a lower absorption coefficient compared to hemoglobin-rich tissue (*e.g.* liver and kidney), resulting in longer exposure times being necessary to achieve equivalent tissue ablation. The scale bar denotes 1 mm [2.215].

The Er:YAG laser has also been applied to urology, similar to the CO_2 laser, with a 2005 study by Varkarakis *et al.* examining wound healing characteristics of 1 cm long incisions made by Er:YAG (70 μs pulse duration, 20 mJ pulse energy, 10 Hz repetition rate) and holmium yttrium-aluminum-garnet (Ho:YAG, 300 μs pulse duration, 500 mJ pulse energy, 3 Hz repetition rate) lasers on *in vivo* porcine urethra and bladder neck samples, with 9 pigs used for each laser being tested [2.218]. The seemingly large discrepancy between the pulse energies was specifically chosen as the Er:YAG laser is absorbed approximately twenty five times more strongly by the tissue than the Ho:YAG. The collateral thermal damage was evaluated through histologic analysis performed by a trained pathologist, with quantitative measurements of both this and the incision depth being made by a transmission light microscope. Some of the captured histology images can be observed in figure 2.38. The Er:YAG laser was focussed by a 20 mm

focal length calcium fluoride lens into a 250 μm core sapphire optical fibre of 2 m length, while the Ho:YAG laser was focused by a 20 mm focal length quartz lens into a 300- μm -core silica optical fibre of 3 m length.

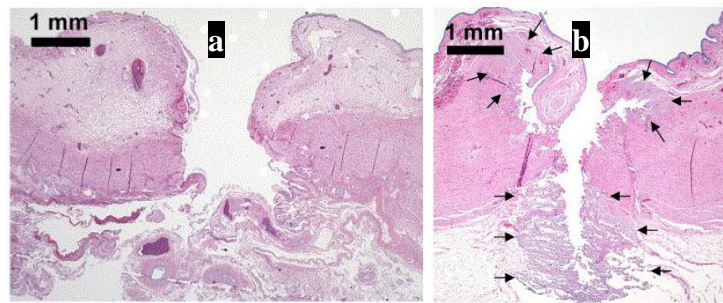


Figure 2.38 – Hematoxylin-eosin-stained histologic cross-sections of incisions made with a) Er:YAG and b) Ho:YAG laser (with the arrows indicating the border between native and thermally coagulated tissue) on postoperative day 0. No discernible thermal damage zone is observed in the tissue ablated via the Er:YAG laser [2.218].

The observable collateral thermal damage on postoperative days 0, 6, and 14 induced by the Er:YAG laser was 20 ± 5 , 900 ± 100 , and 430 ± 100 μm respectively, while for the Ho:YAG laser it was 660 ± 110 , 2280 ± 700 , and 1580 ± 250 μm , with the Er:YAG also benefitting from significantly lower widths of granulation tissue at the base of the laser incisions throughout the 14 day postoperative observation period, as indicated by figure 2.39. The incision depths followed a similar trend, with the Er:YAG and Ho:YAG lasers showcasing incised depths of 1100 ± 200 μm and 1500 ± 300 μm on postoperative day 6, while on day 14 these reduced down to 670 ± 140 μm versus 1240 ± 140 μm respectively, indicating that the Er:YAG profited from faster healing of the wound created.



Figure 2.39 – Microscopic images of incisions approximately 1 cm long made with a) Er:YAG and b) Ho:YAG lasers on postoperative day 14, with the former clearly displaying much faster wound healing capabilities [2.218].

Historical context of particular significance in relation to the work detailed in this thesis is the previous use of longer pulsed lasers for gastric tumour treatments. In 1986, Kiefhaber *et al.* used an Nd:YAG laser to treat obstructive colon cancers, with preoperative recanalisation treatments relieving symptoms of intestinal build-up and allowing for further preoperative treatment in the form of washing out the bowels [2.219]. This led to a reduced mortality rate of 8.8%, compared to the 24% for patients that underwent staged operations (which involved temporary colostomies) who did not undergo any laser treatments. The following year they also published work confirming that this laser treatment could also be applied to ulcerated bleeding cancerous tissues [2.220]. That same year, Sugoru *et al.* published a six-year study (1980 to 1986) on using Nd:YAG laser therapy through a gastroscop to treat gastric tumours in 123 patients, with particularly promising results in those who had gastric mucosa and polyps with unusual epithelial structures, as well as adenocarcinoma which did not exceed 2 cm and was limited to the mucosal volume, although it proved less effective in treating more depressed types of gastric cancer tissue (where argon-dye laser therapy proved more effective) [2.221]. As mentioned in chapter 1, Schroder *et al.* also published work looking at colon tissue ablation (albeit in mouse models as opposed to human patient trials) via

Nd:YAG laser in 1987, with their work comparing 2 s Nd:YAG pulses (contact and non-contact modalities) to CO₂ lasers and electrocautery techniques [2.222]. They observed similar thermal damage effects between these methods, aside from non-contact Nd:YAG which exhibited considerably more thermal damage. Low *et al.* followed this up with a 1989 publication, presenting a four-year study looking at 115 patients that underwent Nd:YAG laser treatments in either the rectum or the colon (the two sides of the peritoneal reflection) [2.223]. In line with the previous studies they found that the Nd:YAG laser proved to be a safe and effective tool in treating various lesions, including malignant tumours, large villous adenomas and carcinoid tumours, as well as treating inflammation and abnormal tangles of blood vessels. A further two-year study was published in 1991 by Daneker *et al.*, where they also reaffirmed the stance that endoscopic laser therapy provides a safe and effective method of removing obstructive distal cancers [2.224]. However, despite this trend of favourable findings, later work by Gevers *et al.* published in 2000 looked at long-term outcomes of palliative endoscopic laser therapy across 219 patients with colorectal adenocarcinoma [2.225]. They found that while long-term effective palliation was achieved across 75% of the patients, there were numerous potential complications, including local spreading of the tumour in cases of obstruction and possible perforation, further highlighting the need for enhanced depth control in these laser treatments. Additionally, while they achieved an improved quality of life for most of the patients in these trials, they also highlighted survival rates of only 44.4% at 1 year and 20.4% at 2 years, stressing the clinical need for further advancements in these cancerous tissue resection procedures, particularly the ability to remove larger tumour volumes safely.

As per Yahr and Strully's earlier predictions, delivery systems consisting of fibre-optic bundles were developed for CO₂ lasers, which enabled a wider range of surgical procedures to be carried out. This led to the CO₂ laser being used regularly in medical practices to carry out a wide range of procedures [2.226],[2.227],[2.228]. This increased capacity for minimally invasive procedures is perhaps the most significant advantage that lasers have over the previously covered surgical methods, although smaller fibre diameters that allow for smaller mechanical bend radii also tend to suffer from reduced damage thresholds [2.229].

Contrarily, the lack of suitably flexible optical fibres that are compatible with Er:YAG laser systems has previously inhibited their clinical indications. While there had been some previous work examining their incorporation into various medical procedures, such as work by Neubaur *et al.* published in 1999 looking at cataract removal via Er:YAG laser delivered through both zirconium-fluoride-based and sapphire fibres, they concluded that an optimal delivery system for this wavelength had yet to be found, with posterior capsule rupture occurring for 3 of the 32 patients [2.230]. Fried *et al.* noted the potential of Er:YAG lasers for cutting urethral and ureteral tissues for endourology applications in a 2001 publication, as it benefitted from significantly more precision compared to Ho:YAG lasers, with thermal damage zones of $30 \pm 10 \mu\text{m}$ compared to $290 \pm 30 \mu\text{m}$ [2.231]. The group then followed this up with a 2003 publication which was able to reduce the thermal damage zones obtained from Er:YAG laser incision of *ex vivo* porcine ureteral and canine urethral tissues from as low as $30 \mu\text{m}$ down to between 10 and $20 \mu\text{m}$ by reducing the pulse duration from 220 μs to 8 μs , with these pulses being delivered through 250 μm and 425 μm core germanium oxide optical fibres placed in direct physical contact with the tissue samples [2.232]. This work was followed up by Raif *et al.* who published research in 2006 looking at delivering an Er:YAG laser for lithotripsy of salivary stones through metal hollow waveguides sealed with polished sapphire rods [2.233]. While 15 of the 18 glands treated in these trials returned to normal function without any adverse symptoms, showing

some clinical viability and even cost-effectiveness to these waveguides, they lacked the flexibility for incorporation into fully fledged endoscopes. Work from Scott *et al.* published in 2007 showcased germanium oxide fibres with sapphire tips which were able to deliver Er:YAG laser light with pulse energies as high as 850 mJ before damage to the germanium oxide - sapphire interface was observed [2.234]. This was a marked improvement over previous studies showing that germanium oxide fibres without these sapphire end tips were damaged with pulse energies as low as 9 mJ when tested in previous contact tissue ablation trials [2.235].

However, as commented on in later review papers, the incompatibility of these Er:YAG with silica fibres hindered their clinical adoption as the alternative materials required for guidance were noticeably more expensive [2.236]. There is a current research drive to further reduce the invasiveness and cost of these laser setups, as this will allow for their implementation into increasingly delicate procedures, with recent work by Bernal *et al.* even comparing various types of optical fibre for Er:YAG laser delivery, including hollow-core, fluoride, sapphire and germanium oxide fibres with core sizes of 500, 450, 425 and 450 μm respectively [2.237]. High coupling efficiencies (between 70 and 81%) were obtained for each of these, indicating that they each show potential towards the intended aim of performing minimally invasive laser surgery upon bone tissue through an endoscopic device. Additionally, while laser transmission at wavelengths beyond 3.5 μm is inhibited for silica fibres due to material absorption, silver-coated capillaries have been shown to be capable of delivering wavelengths beyond this limit, as indicated by figure 2.40 [2.238].

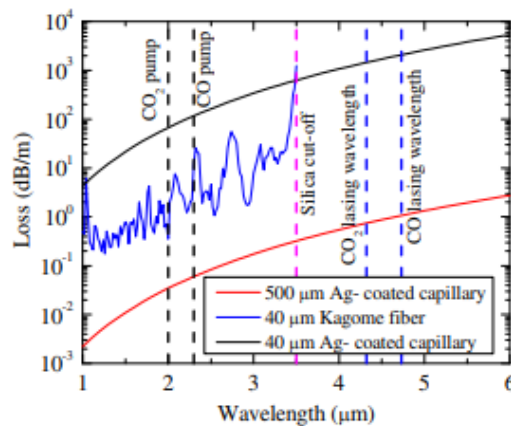


Figure 2.40 – Propagation losses for silver coated capillaries of varying diameters and the calculated losses for 40 μm diameter silica Kagome fibre. In addition, corresponding pump and lasing wavelengths for CO and CO₂ active media are displayed [2.238].

2.3 Minimally invasive laser surgery

2.3.1 Brief history of minimally invasive procedures

Laser-based surgical procedures can be divided into two main categories: invasive and non-invasive. Invasive procedures entail breaching of the skin - most commonly via some form of incision being made [2.239]. Non-invasive procedures contrarily do not involve the skin being breached in order to enter the body. The most common non-invasive procedures are those used in diagnosis, such as x-rays, computerised tomography (CT) scans, magnetic resonance imaging (MRI) scans and ultrasound scans [2.240],[2.241]. Radiotherapy meanwhile is an example of a non-invasive procedure that is used in treatment, as it can be used to target tumours without breaking the skin [2.242]. A sub-category of invasive procedures, referred

to as minimally invasive (or laparoscopic surgery), has risen to prominence over the past couple of decades, even establishing itself as the exemplary method in numerous fields on a global scale [2.243],[2.244].

These types of procedure have previously been defined loosely in the literature as one that benefits from a greatly reduced morbidity rate in patients post-surgery. They typically involve numerous incisions being made, all of which are much smaller (usually on the order of a few millimetres in length) than the opening required for more conventional open surgery [2.245]. An endoscope is then inserted into the patient through one of these small incisions, allowing for the surgeon(s) to view the problematic areas within the body and deliver laser light to the targets of interest. Optical fibres were first used in such devices in 1954 by Harold Hopkins and Narinder Kapany (who is accredited for first coining the term “fibre optics”, highlighting it as its own research field), with the flexibility that the glass fibre bundle offered (particularly compared to previous rigid endoscope designs which relied on trains of copying positive lenses, including cytosopes, bronchoscopes and gastroscopes) proving ideal for such applications [2.246]. These procedures benefit from reduced recovery times, less scarring, shorter stay periods for patients and less pain-inhibiting medication being required post-surgery, all courtesy of the smaller operation sites, resulting in a significant decrease in the cost of postoperative care [2.247],[2.248],[2.249]. The advantages listed here are responsible for these minimally invasive procedures being adopted in some form within practically every surgical field, from obesity surgery to orthodontics, as well as various kinds of cancer treatment [2.250].

With regards to delivering lasers through these endoscopic devices, similar to the previously covered CO₂ gas laser, these optical fibres were initially applied to communications-based research before gaining significant interest in the medical field. While conventional silica fibres (both single and multimode) allow flexible delivery of wavelengths below 2 μm (which includes the visible region, making them suitable for medical imaging) via total internal reflection from the core and cladding having different refractive indexes and are chemically inert (which is ideal for processes where they may come into contact with biological tissues), the previously covered Er:YAG and CO₂ lasers were initially adopted in medical practices courtesy of their wavelengths being highly absorbed by water, leading to efficient photoablation and/or photocoagulation. Unfortunately, these wavelengths are highly absorbed by silica, rendering it an unsuitable medium for the delivery of these medical lasers. This generated research interest in developing solid core fibres made from different materials (such as sapphire), with the primary aim being efficient transmission of these longer infrared wavelengths, to further capitalise on the promise they had already established across medical literature [2.251]. As a result, the CO₂ and Er:YAG lasers examined earlier are still widely used due to the range of compatible and cost-effective delivery systems available, as opposed to being solely justified from the inherent properties of the lasers themselves [2.252],[2.237]. While many of these fibre materials (such as fluoride glass and polycrystalline silver halide) are not as convenient to work with as silica, they offer much more efficient delivery of these specific wavelengths [2.253]. The development of hollow-core silica fibres (both negative curvature and photonic bandgap designs) by Urich *et al.* was a relatively recent innovation which benefits from both the convenience offered by silica and compatibility with these infrared wavelengths [2.254]. These are covered in more detail in a later section on optical fibres specifically tailored for minimally invasive surgery applications.

Over time these minimally invasive procedures have been proven to provide equal, if not better results than previous conventional methods, while also inflicting less surgical trauma and consequently being of lower risk to the patient. Recently, they have been demonstrated as being an ideal technique for treating hepatic

tumours, where the precision offered by endoscopic ultrasonography (EUS) guided laser ablation allowed for tumour removal to be carried out, even in cases where these hepatic tumours were in close proximity to relatively delicate gastrointestinal structures [2.255]. The alternative method of percutaneous ultrasonography guided laser ablation, while still benefitting from low surgical complication rates, was not able to distinguish the tumour margins as clearly [2.256],[2.257]. These minimally invasive procedures have even enabled surgeries which aim to simply improve quality of life, such as in the treatment of benign prostatic hyperplasia (which can lead to erectile dysfunction) through endoscopic enucleation of the prostate via fibre lasers [2.258].

However, since their general conception in 1931, these minimally invasive procedures had suffered from two primary flaws when compared to the conventional procedures they were replacing – a steeper learning curve for surgeons and increased costs from sourcing the more sophisticated instrumentation required [2.239],[2.259],[2.260]. Yet, in the numerous years since these particular publications, the ongoing research within this field has addressed these factors, whether it is through the implementation of imaging techniques that allow for clearer visualisation of the areas of interest, or through continuous improvements upon the ablation rates of tissue that can be achieved [2.261],[2.262],[2.111].

Despite these ongoing advances, the ablation rates attainable with Gaussian laser beams (54 mm min^{-1} in ovine and bovine skull and cortical samples using a Ti:Sapphire femtosecond laser with 3.5 W maximum average power at a repetition rate of 1 kHz) are still vastly lower than practical values from conventional mechanical cutting tools such as saws and drills (6.53 m min^{-1} in porcine cortical bone using a standard surgical drill), although these ultrashort pulses do benefit from much lower levels of thermally and mechanically induced damage [2.111],[2.263]. This was illustrated in work carried out by McCaughey *et al.*, where using 700 fs long pulses of 10 μJ energy at 1053 nm they were able to ablate both porcine otic capsule and human stapes bones while observing no damage to the surrounding bone structure, with the latter being highlighted in figure 2.41 [2.264]. This lack of residual damage was confirmed via light microscopy, optical coherence tomography (OCT) and a scanning electron microscope. More recent work by Zhang *et al.* has achieved removal rates of $0.99 \text{ mm}^3/\text{s}$ in sheepshank bone with 230 fs pulses from a 20 W neodymium doped potassium-gadolinium tungstate (Yb:KGW) laser – twenty times higher than the 0.05 mm^3 obtained from previous work by Kerse *et al.* for drilling millimetre sized holes in human dentine via 800 fs pulses of 3 μJ energy, while also exhibiting thermal damage depths of only 200 μm through histological evaluation [2.265],[2.266]. This is significant as this is much lower than the damage induced by mechanical drilling (with the latter being primarily driven by brittle fracture, while femtosecond laser ablation relies on thermal vaporisation) and the thermal conductivity of human bone is relatively low, with the thermal effect caused by conventional CW laser drilling altering the properties of alkaline phosphatase in said bone, causing thermal necrosis and the resultant death of bone cells. Combining this localisation potential with the possibility for minimally invasive procedures to be carried out with ultrafast lasers, it is easy to see that there is still significant clinical interest in implementing optical fibres capable of delivering higher pulse energies to regions within the body that exhibit characteristics indicative of early-stage cancer development.

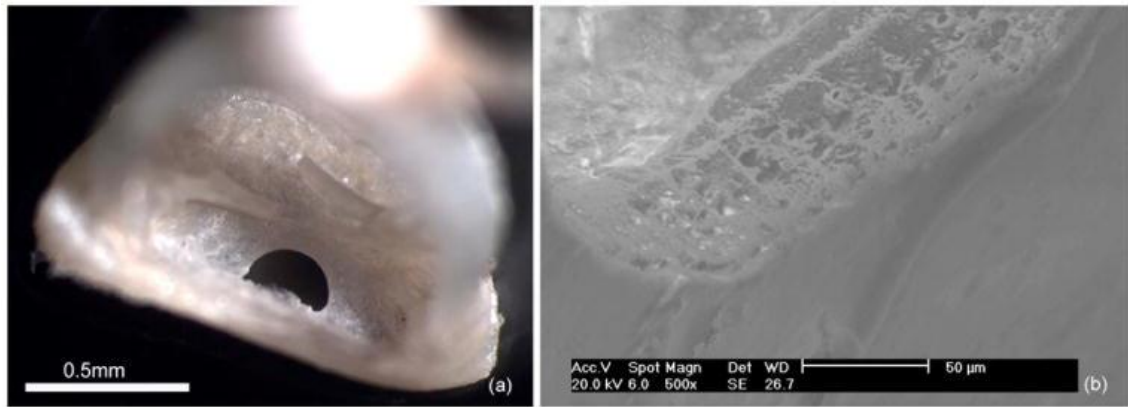


Figure 2.41 – Human stapes bone after femtosecond laser ablation, where (a) is a light microscope image of the whole stapes and (b) is an SEM×500 image of the perforation wall [2.264].

2.3.2 Ultrashort laser pulses in minimally invasive surgery

As discussed earlier under the consideration of the various kinds of laser-tissue interactions that have been studied, the generation of ultrashort laser pulses has been of utmost importance in advancing the field of laser surgery. Laser surgery using mid-infrared ultrafast picosecond and femtosecond lasers can greatly enhance both the precision and effectiveness of treatment for a wide range of diseases [2.267]. Laser ablation carried out with CW or longer pulsed lasers relies on thermal build up from local thermolysis and the subsequent formation of vapor bubbles, both of which are staggered single-photon absorption processes which therefore highly depend on the absorption characteristics of the biological samples. However, tissue ablation performed using high peak power picosecond (or shorter) lasers is achieved by the sequential effects of multiphoton ionisation and plasma-mediated absorption, which are nonlinear processes.

These pulses have proved invaluable in this field due to the higher energy density outputs that they have made possible, particularly when partnered with the smaller areas of collateral damage observed in the surrounding tissue courtesy of the smaller spot sizes that have been attained with these shorter pulse durations [2.268],[2.269],[2.95]. Recent studies have even demonstrated excellent compatibility with well-established *in vivo* tissue imaging techniques for carrying out microsurgery [2.270]. These inherent characteristics are clearly advantageous when considering ablation of tissue.

As a result, the application of ultrashort pulses has created new forms of widely adopted procedures. Foremost among these is femtosecond laser-assisted in situ keratomileusis (femto-LASIK), where the cornea is reshaped [2.271]. This is typically labelled as laser eye surgery or laser vision correction. The steps involved in this procedure are shown in figure 2.42. The first published clinical test results date back to 2003 [2.272]. Since then it has risen to prominence to the point where the incorporation of femtosecond lasers is now widely considered the most important recent advancement in the field of ophthalmology [2.273].

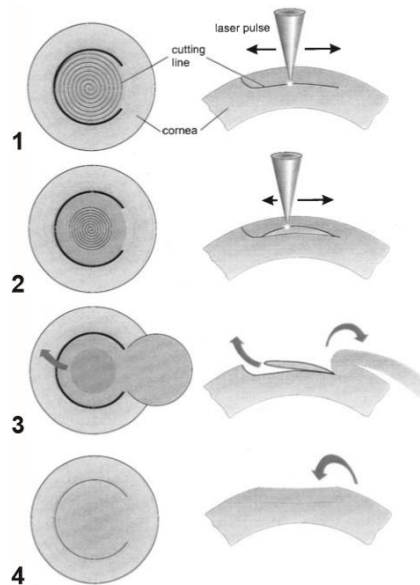


Figure 2.42 – Steps of femtosecond laser-assisted in situ keratomileusis (femto-LASIK). Step 1 shows the laser being scanned in a spiral pattern to perform a lamellar intrastromal cut. Step 2 shows a lenticule being prepared via another cut being made, which is dependent on the specific refractive error of the eye. Step 3 depicts the front corneal flap being opened for extracting the prepared lenticule. Step 4 illustrates the repositioning of the flap. This fits to the removed volume of the lenticule, causing a change in the refractive power of the eye [2.273].

As touched upon in section 2.1.4, the photodisruptive effects that suitably intense ultrashort pulses can create are directly applied in various eye-based surgeries, establishing them as the optimal means of treating conditions such as presbyopia and cataracts [2.274]. The use of femtosecond lasers for these treatments is significant as it allows for lower pulse energies to be used to achieve photodisruption, which lowers residual thermal damage to the surrounding tissue. The higher peak intensities that are possible with femtosecond pulses can also lead to smaller cavitation bubbles. This was showcased in a comparison to a CW Nd:YAG laser in corneal ablation trials published in 1989, where the collateral damage from using a femtosecond laser was over one hundred times smaller [2.85]. They also enable greater degrees of control over the depth of ablation, further increasing the precision, safety and reliability of these procedures.

This potential is still being showcased in current research as well. Recently published trials by Gros-Otero *et al.* showed impressive root-mean-square (RMS) and standard deviation values in the nanometre range for the surface roughness of corneal stromal beds after LASIK flap creation procedures in porcine models using two different femtosecond laser platforms [2.275]. Using atomic force microscopy, they found RMS values of 430 ± 150 nm for the corneal femtosecond laser platform (IntraLase iFS 150 kHz, the results from which are highlighted in figure 2.43) and 370 ± 100 nm for the dual femtosecond laser platform (LenSx). The former platform had a spot size of less than $3 \mu\text{m}$ with a spot separation of $6 \mu\text{m}$ and a pulse energy of $0.8 \mu\text{J}$, while the latter had a spot size of $5 \mu\text{m}$ with a spot separation of $7 \mu\text{m}$ and a pulse energy of $0.9 \mu\text{J}$. Both illustrate the incredible precision made possible by the application of femtosecond lasers, while also benefitting from short ablation times (18 and 19 seconds respectively).

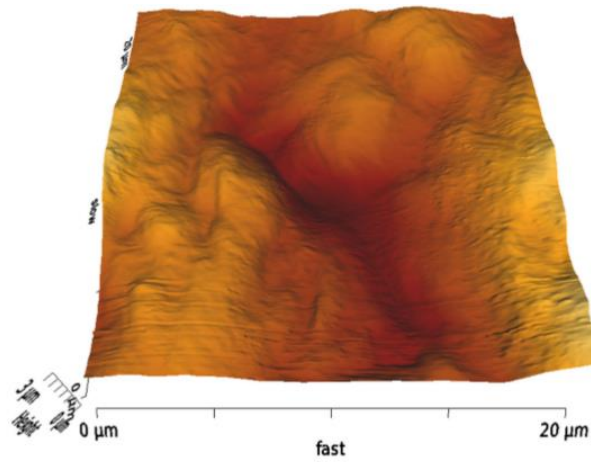


Figure 2.43 –Three-dimensional image of corneal surface treated with iFS 150 kHz captured using atomic force microscopy topography [2.275].

The implementation of femtosecond lasers has enabled other advancements upon LASIK too, such as the induction of femtosecond lenticule extraction (FLEX) procedures, where a thin lenticule is effectively cleaved from the stroma to then be manually extracted before the flap is created, contrary to LASIK where it is done afterwards [2.276]. The results from the first trials of this new procedure were published in 2008. Subsequent studies with larger patient samples have reaffirmed advantages of this method over LASIK performed with pulsed excimer lasers by addressing issues encountered with the latter [2.277]. These include increased stability in environmental conditions such as corneal hydration levels, temperature and humidity, although it did suffer from slower visual recovery times [2.278],[2.279]. Femtosecond lasers have also improved corneal astigmatism and transplantation treatments through the increased precision they offer [2.280].

As mentioned in section 2.1.5, plasma-mediated ablation has shown great promise in the field of neurosurgery. Ultrafast lasers are ideal for performing these procedures, particularly with increased research interest in the flexible delivery systems that are necessary to realise their full potential. An earlier study carried out by Goetz *et al.* that was published in 1999 focussed on the design of a probe attached to a stereotactic frame shown in figures 2.44 and 2.45 [2.281]. While this was able to ablate deep-seated sections of porcine brain tissue (forming a model for deep-seated brain tumours in human patients) with 30 ps pulses, it did so in an invasive manner, with the invasive part of the probe consisting of three coaxial tubes. The system also used focussing lenses of between 35 mm and 45 mm focal lengths. As a result of this design it lacked the overall flexibility and miniaturisation necessary for performing minimally invasive procedures. This has since been addressed in more recent research, with smaller probes having since been developed for various clinical procedures, including neurosurgery [2.282].

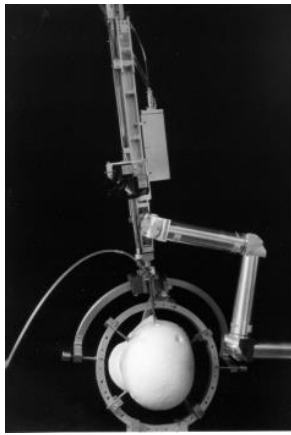


Figure 2.44 – Invasive laser probe with integrated laser scanning microscope mounted to stereostatic frame [2.281].

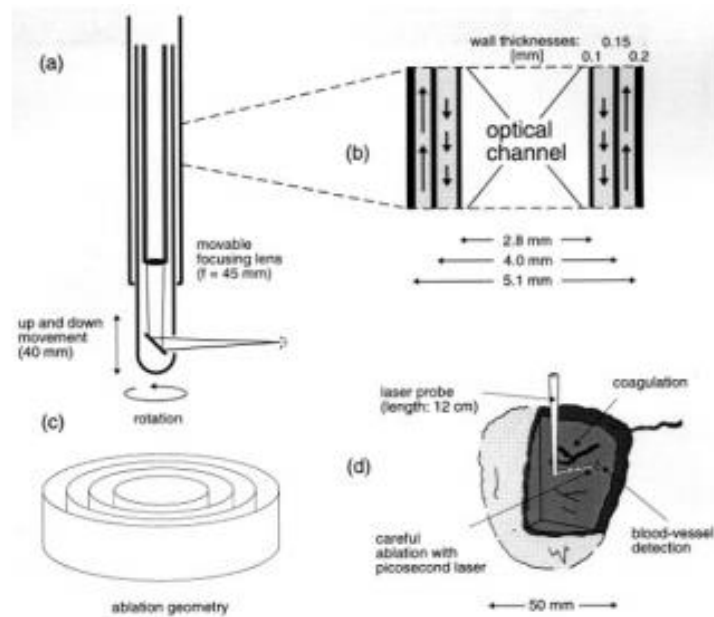


Figure 2.45 – a) Optical design of invasive laser probe b) Cross-section highlighting the optical, irrigation and suction channels (respectively when moving outward from central axis) c) Scanning pattern for tumour ablation d) Schematic overview of laser probe in operation [2.281].

Similarly, vocal fold plasma-mediated ablation surgery was also briefly covered in section 2.1.5. Ultrafast lasers are again ideal for performing minimally invasive procedures in this field. Wisweh *et al.* were the first to showcase femtosecond laser ablation on porcine vocal fold tissue (and the potential for these ultrashort pulses to perform sub-epithelial ablation with negligible residual damage to the surrounding tissue) in work that was published in 2007 [2.283]. In this work they highlighted a new computer-guided laser probe design which achieved maximum resected depths of approximately 185 μm , with lateral thermal damage of roughly 1 μm , from square scanning patterns that were performed using a galvoscaner over a 400x400 μm area. The dimension measurements of the ablated area were taken using optical coherence tomography and the thermal damage was evaluated from histological images. They obtained these ablation results using a 5 μm Gaussian spot with a 10% spatial overlap in both the laser line separation and scanning axes, operating at a pulse repetition rate of 5 kHz.

Following on from this, 750 fs pulses from a 500 kHz fibre laser were used to ablate sub-epithelial voids in *ex vivo* porcine focal folds by Hoy *et al.* in 2012, with the aim being to illustrate the validity of the

ablation parameters used to then incorporate them into a minimally invasive probe [2.284]. The tested pulse energies included 50, 100, 500 and 750 nJ, corresponding to fluences of 3, 6, 30 and 45 J/cm² respectively with the focused laser spot size of 1.47 μm (measured inside an agar phantom at equivalent depths to those used in the experimental trials on the porcine tissue). No tissue modification was observed for 50 nJ pulses but the 100 nJ pulses were able to ablate very thin planes and create some small near-threshold voids. This was verified using the multiphoton imaging capabilities of the laser. The 500 nJ and 750 nJ pulses were able to create voids that extended both above and below the ablation plane across the entire scan. These were theorised to originate from bubbles with relatively long lifetimes (from more molecules being vaporised at higher pulse energies, leading to longer diffusion times) that form at the ablation plane. These then expand beyond the focal volume and combine, leading to tissue displacement both above and below the ablation plane. This aligns with the mechanisms of femtosecond laser ablation of tissue that is carried out at power densities much higher than those of the optical breakdown threshold. A peak depth of 116 μm was reported for these voids with negligible thermal damage being confirmed through histological evaluation (from which some of the captured images are showcased in figure 2.46), although the authors conclude that further examinations into the maximum possible ablation depths are required.

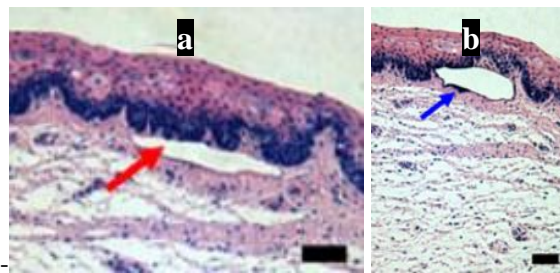


Figure 2.46 – Histology images of voids in porcine vocal fold tissue made using 500 nJ pulses at a) 100 μm beneath the tissue surface, with the void indicated by the red arrow and b) slightly closer to the tissue surface, with the blue arrow highlighting a section of epithelial nuclei that was displaced from the epithelium during the ultrafast laser ablation process. Both scale bars are 50 μm [2.284].

In these trials a raster scan over an area of approximately 235 x 235 μm was performed, with a 75% spatial overlap of the laser pulses in both the laser line separation (achieved by translating the sample stage) and scanning (via a pair of galvanometric scanning mirrors) axes. This high overlap was chosen to increase pulse-to-pulse accumulation effects, which allowed for the desired extent of tissue ablation to occur for the low pulse energies required to cause ablation while operating in the femtosecond pulse duration regime. Correspondingly, these low energy femtosecond pulses are also promising for parallel nonlinear imaging, particularly second harmonic generation (SHG) and multi-photon-excited fluorescence modalities, due to the lower energies required for signal generation and the non-linear interaction of high intensity light with tissue leading to focal volume confinement. This high level of confinement enables submicron resolution and the potential for depth sectioning, which allowed for accurate visualisation of the microsurgical zone with the same resolution and field-of-view as the laser itself. This group has followed up this work with publications detailing a new microsurgical probe design based on pulse delivery through hollow-core Kagome lattice photonic crystal fibres – this was briefly touched upon in section 2.1.5 and is covered in more detail in section 2.5 [2.81].

More applicable to the work carried out in this thesis is the research carried out by Lanvin *et al.* which used 1.5 ps laser pulses to achieve subsurface ablation of atherosclerotic plaque beneath the endothelium of

excised mouse aortas [2.285]. 1.5 ps was chosen for the pulse duration to avoid non-linear self-focusing effects encountered with shorter pulses in the femtosecond regime when the peak power exceeds a critical threshold (which limits the precision and maximum obtainable ablation depths as the pulse proceeds to collapse, causing it to focus prior to the expected spot along its propagation axis) while also benefitting from similarly low ablation thresholds. Additionally, while femtosecond pulses benefit from higher peak intensities for equivalent pulse energies compared to those in the picosecond regime due to there being a greater degree of temporal confinement placed upon each pulse, they suffer from self-phase modulation and pulse broadening when delivered through multicore fibres. This was shown by Conkey *et al.* (with this research also being very applicable to the work carried out in this thesis due to the use of a 1030 nm Satsuma laser, produced by Amplitude), resulting in lower focussing efficiencies when comparing 500 fs pulses to 2 ps pulses, particularly for pulse energies above 0.3 μJ in a 4400 core system and pulse energies above 2 μJ in a 10000 core system, as shown in figure 2.47 [2.286]. Evaluation of the plaque ablation was performed through OCT imaging and histological analysis, confirming axial thermal damage on the order of roughly 10 μm . A focussed Gaussian spot of approximately 1 μm diameter was used to ablate the tissue samples which were translated in a serpentine pattern via a 3-axis piezo mechanical stage to provide scanning of the laser beam.

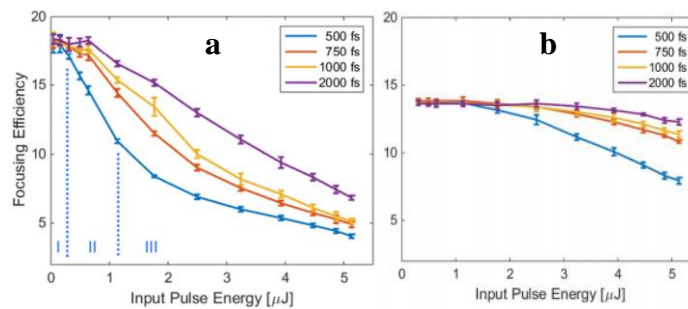


Figure 2.47 – Focusing efficiencies against input pulse energy plots obtained when focusing ultrashort pulses of various durations through multicore fibres of a) 4400 cores (with “I”, “II” and “III” indicating the three different behavioural regimes observed for 500 fs pulses) b) 10000 cores [2.286].

The primary finding of this research was that these picosecond pulses were able to ablate plaque that was just beneath the artery surface without inflicting damage to the surface itself, highlighting their promise in microsurgical applications. Additionally, they were able to confirm that the percentage of ablated craters showing signs of surface damage at various depths within the tissue typically increased for increasing pulse energy, with optimal results in terms of localised ablation volumes being observed at depths of greater than 15 μm within the tissue while operating with pulse energies of less than 4 μJ . These results are depicted in figure 2.48.

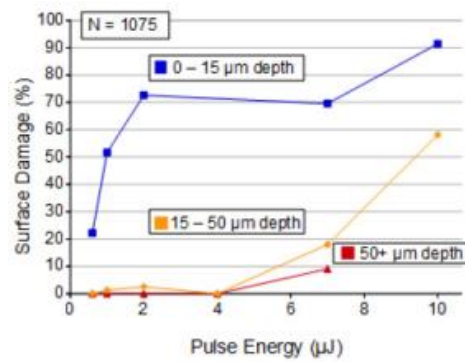


Figure 2.48 –Percentage of ablated craters exhibiting surface damage for various applied pulse energies at several depth ranges [2.286].

Another important takeaway, particularly for the research carried out in this thesis, is that while femtosecond pulses are able to achieve optical breakdown at lower input powers, they are also more prone to various non-linear interactions when transmitted by fibres. Consequently, it is worthwhile considering how equivalent peak intensities can be achieved using picosecond pulses. This can be done by either increasing the input power and thus the pulse energy or by reducing the spot size. While the former is simpler in terms of optical design, the requirement of remote delivery via optical fibre to carry out these minimally invasive procedures prohibits indefinite increases in the input power. Incorporating the latter into the optical design considerations avoids damage to the fibres and further limits the possible thermal damage to the surrounding tissue – both desirable outcomes. The reduction in the required power also has the benefit of further avoiding the previously touched upon self-focusing phenomena, albeit at the inevitable expense of some efficiency in the ablation process due to having a smaller interaction volume and thus slower scanning speeds for equivalent spatial pulse overlaps upon the tissue surface. This can be compensated for however by optimising the other ablation parameters, including the scanning pattern used, the pulse repetition rate, pulse duration and applied pulse energy.

More recent research in the field of minimally invasive surgery has shown the potential for imaging methods to provide visual feedback for ultrafast laser ablation procedures. Schlüter *et al.* have showcased optical coherence tomography (OCT) as a guidance mechanism in picosecond infrared laser ablation trials on porcine tissue (consisting of both muscle and fat) [2.287]. In this work 400 ps pulses of 1064 nm wavelength from a HP3 1064 OPA 3000 Nd:YAG laser system (made by Attodyne Inc.) were guided down a multimode sapphire fibre (produced by MicroMaterials Inc.) of 1 metre length and 200 μm core diameter at a repetition rate of 1 kHz. This gave averaged output powers between 107 and 130 μJ. Using the commercially available Telesto I spectral-domain OCT system from Thorlabs they obtained morphological (for scanning trajectory planning) and sub-surface (for target identification) information to a micron scale for the tissue samples. This data was obtained both before and after ablation, as shown in figure 2.49. Additionally, the ablation process was automated by calibrating the coordinates of the OCT images (in which targets were identified) to those of the hexapod robot that the sapphire fibre was mounted to (enabling fibre scanning).

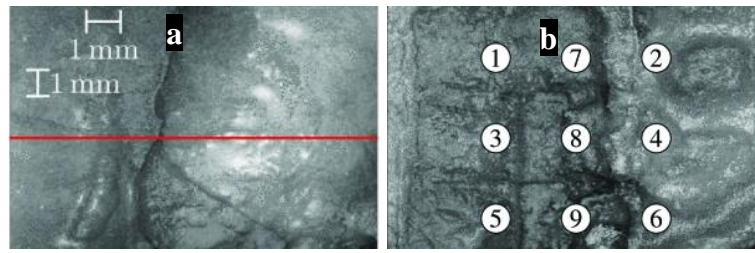


Figure 2.49 – OCT images of porcine sample surface a) before and b) after picosecond laser ablation, with the numbers simply indicating the sequencing of the 3 x 3 mm ablated areas [2.287].

Kakkava *et al.* achieved femtosecond laser ablation of the organ of Corti in extracted murine cochlea samples with their dual-modality endoscopic probe, capable of both high energy femtosecond pulse delivery and two-photon fluorescence (TPF) imaging [2.288]. Gradient-index (GRIN) multimode fibres of 200 μm and 400 μm core diameters were used to deliver femtosecond pulses from a Satsuma laser system (the same one that was used in the previously mentioned atherosclerotic plaque ablation studies), with the former suffering from spectral and temporal broadening from nonlinearities, causing the maximum deliverable intensity to saturate within the range of $2.5 - 3 \times 10^{13} \text{ W cm}^{-2}$, while the latter achieved peak intensities of $1.5 \times 10^{13} \text{ W cm}^{-2}$ at the 2.3 μm full width half maximum focal spot. Both of these achieved peak focusing efficiencies of roughly 28% (with sources of loss including polarisation selectivity and coherence gating of the fibre output), which is still significantly higher than the approximate 18% obtained for multicore fibres in the previously highlighted femtosecond pulse delivery efficiency examination [2.286]. Like that prior work, this paper is again highly applicable to the research carried out in this thesis due to the same 1030 nm laser source being used. Both show promise for tissue ablation applications, as both reached the necessary tissue ablation threshold of around 10^{12} W/cm^2 (close to that of water), with potential for increased deliverable intensities through prechirping of the pulses to account for pulse broadening through both group velocity dispersion and nonlinearities.

The 200 μm core diameter GRIN fibre suffered from decreased focusing efficiencies for pulse energies of around 1 μJ and higher for all the tested pulse widths (500 fs, 700 fs and 1 ps), while the 400 μm core diameter GRIN fibre exhibited noticeable drops in the focusing efficiency for 500 and 700 fs pulses at pulse energies beyond approximately 5 μJ , while 1 ps pulses showed relatively linear behavior up to 10 μJ . These trends are highlighted in figure 2.50.

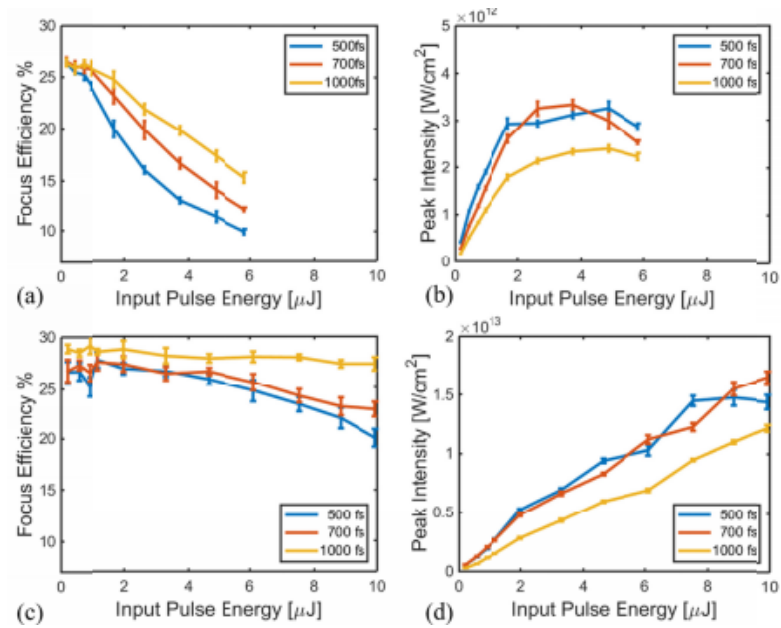


Figure 2.50 – a) + b) Focusing efficiency and peak intensity as functions of the input pulse energy for the 200 μm core diameter GRIN fibre c) + d) Focusing efficiency and peak intensity as functions of the input pulse energy for the 400 μm core diameter GRIN fibre [2.288].

The authors comment that these fibres show comparable performance to Kagome hollow-core photonic crystal fibres, which have delivered peak intensities of $4 \times 10^{13} \text{ W/cm}^2$. However, in micromachining trials carried out on silicon, glass and aluminum using the fundamental mode of these Kagome fibres (with no distal component), the feature size depended on the mode diameter (50 μm for 19-cell design) [2.289]. Despite the lower peak intensities obtained, the GRIN fibre probes benefitted from improved spatial resolution over previous Kagome fibre probe designs (which are discussed in section 2.5), while also having a smaller final probe diameter of less than 1 mm due to the lack of distal components and piezo-based scanning mechanism, instead relying on wavefront shaping, although this suffers from potential distortion of the calculated transmission matrix from bending and/or misalignment. They also managed to maintain its spatial resolution over a depth of 300 μm, with the 400 μm core diameter design having a 200 μm field of view.

The capacity of TPF imaging also enabled high depth imaging of the scattering tissue courtesy of the infrared photons from the 1030 nm laser used for excitation. This allowed for visual confirmation of the selective ablation of cochlea hair cells, although further work is required to evaluate the residual damage. It also allowed for imaging of a cavitation bubble during the ablation of a hair cell within an organ of Corti sample, as shown in figure 2.51. As these samples were placed in a water-based solution the produced bubbles were trapped, resulting in unpredictable bubble lifetimes, varying from a few seconds to a few minutes in the same samples. This inhibited immediate TPF imaging after ablation in some cases, as the bubbles prevent the light from the distal end of the fibre from focusing on the sample surface, meaning this will need to be addressed in future work.

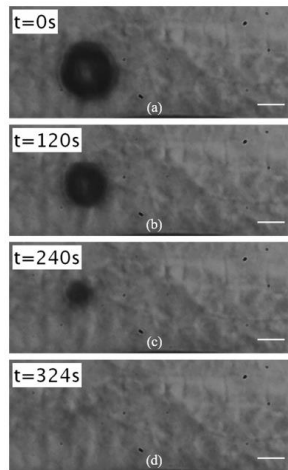


Figure 2.51 – Bright-field images of cavitation bubble generated from femtosecond laser ablation of a hair cell within an organ of Corti sample. Scale bar indicates 10 μm and 0 s timestamp indicates moment after ablation is finished [2.288].

Ultrashort pulses have also been applied to dentistry. Work carried out by Konorov *et al.* in 2004 presented 40 ps pulse delivery from an Nd:YAG laser through a hydrogen gas filled hollow-core photonic crystal fibre of 14 μm core diameter [2.290]. While they were able to ablate enamel material from dental tissue with high precision by focusing the fibre delivered laser light down to a 15 μm spot via a 0.2 NA lens (achieving a calculated fluence of 60 GW cm^{-2}), filling the fibre with hydrogen gas to increase the optical breakdown threshold within the fibre itself and reduce optical nonlinearities presents numerous challenges that currently prevent this technique being implemented into minimally invasive surgeries targeting regions within the body that are harder to access.

Current research in this area carried out by Petrov *et al.* has shown that 310 fs pulses at a repetition rate of 100 kHz from a 1030 nm wavelength laser were able to ablate dentin and enamel at rates of 3.33 $\text{mm}^3 \text{s}^{-1}$ and 2.85 $\text{mm}^3 \text{s}^{-1}$ respectively by performing a hatch scan with no overlap of the lines, giving square cavities of 1 mm^2 area [2.291]. These cavities are shown in figure 2.52. While this is on the same order of magnitude as the dental drilling times achievable with conventional tools, it does not yet exceed them. In addition, the fluences used were in the photoablation regime, as opposed to it being a plasma-mediated process. However, it did lead to increased surface roughness (advantageous for bonding dental fillings to the tooth cavity) and removal of contaminants.

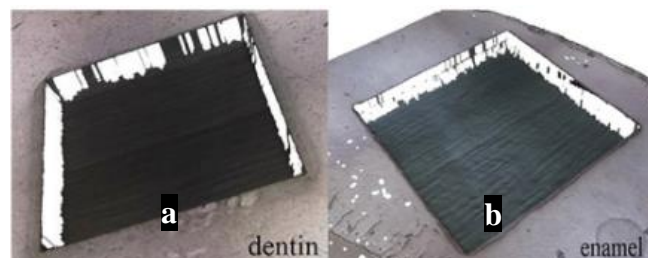


Figure 2.52 – Microscopy images of ablated a) dentin and b) enamel surfaces via femtosecond pulses showing minimal collateral damage and no crack formation [2.291].

Other recent work done by Friedrich *et al.* has examined using picosecond infrared lasers for ablating the roots of extracted human teeth, as amputating an inflamed tooth root is a well-established procedure in this field, with the aim being to preserve both the function and appearance of an unnecessary tooth [2.292]. Histological evaluation showed that they were able to achieve a high level of localisation, with average

thermal damage zones in the dentin between 10.87 and 15.18 μm . A histology image of one of these highly localised ablated features is shown in figure 2.53. The laser setup used in this work was not fibre delivered however, which is stated by the authors to be the next step towards clinical translation. Previously, a lack of compatible, low-loss delivery systems has inhibited the inclusion of these ultrashort pulses to a range of procedures [2.293].



Figure 2.53 – Histology image of incision made via picosecond infrared laser in root of tooth sample [2.292].

2.4 Optical fibres for minimally invasive laser surgery

2.4.1 Negative curvature and photonic bandgap fibres

Until recently, fibres capable of guiding appropriate pulse energies and wavelengths of light for tissue ablation have suffered from large mechanical bend radii (primarily due to the large core diameters required for multimode fibres), clearly making them unsuitable for navigating the various complex structures within the human body, where bend diameters as low as 10's of mm may be required. Similarly, sapphire fibres have been demonstrated to be capable of delivering high power laser beams, and have been used to deliver Er:YAG laser beams at 2.94 μm in dental and cosmetic skin treatments, but to overcome the laser induced damage threshold they have required relatively large total diameters of 200 – 500 μm , meaning they are not currently flexible enough to be suited towards minimally invasive procedures [2.294]. While some research groups are developing alternative guidance tools such as hollow arm-based devices, there are also various types of hollow core fibre which can overcome these limitations, with intelligent structural design mitigating the various limitations of conventional optical fibres [2.96]. The hollow cores benefit from low modal overlaps with the surrounding cladding structures (typically made from silica), resulting in comparatively low loss delivery of light in wavelength ranges that otherwise suffer high levels of attenuation in bulk materials through various absorption mechanisms taking place.

This has been shown for some time within the literature, such as the work published by Temelkuran *et al.* in 2002 highlighting a hollow core fibre design that used an omnidirectional dielectric mirror to line the interior of the fibre, with confinement being achieved through large photonic bandgaps being created via multiple alternating submicrometre thick layers of a low refractive index polymer (polyether sulphone or PES, $n = 1.55$) and a chalcogenide glass of higher refractive index (arsenic triselenide, $n = 2.8$) [2.295]. A cross-sectional image of this fibre is shown in figure 2.54. This fibre was able to achieve transmission losses of around 1 dB m^{-1} for CO_2 laser light, which is considerably lower than that for the fibre material itself, showing the significance of implementing these structural design considerations. Additionally, it was able to transmit power densities of 300 W cm^{-2} without any damage being caused to the fibre. As a result of these traits a polymeric photonic bandgap fibre based on this design was later used by Koufman *et al.* to perform upper aerodigestive tract un-sedated office-based laser surgery across 443 laryngotracheal cases

[2.296]. However, while this design was impressive, it was still clearly limited in its capability to handle sufficient powers for performing plasma-mediated ablation.

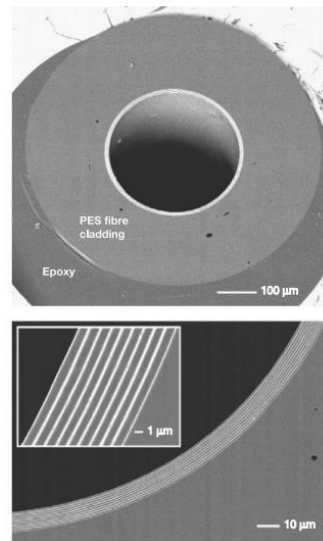


Figure 2.54 – SEM image of hollow core cylindrical multilayer fibre mounted in epoxy, with the hollow core appearing black, the polyether sulphone (PES) cladding layers appearing grey, and the arsenic triselenide layers appearing white [2.295].

One of the potential solutions for this is the highly flexible anti-resonant microstructured fibres (also referred to as negative curvature fibres, or NCFs). These guide light through the principle of being an anti-resonant reflecting optical waveguide (ARROW), where wavelengths that are resonant with the core wall are unable to be confined within the core, resulting in them being highly attenuated [2.297]. Conversely, wavelengths that are anti-resonant to the core wall are highly confined within the core itself, experiencing only low levels of leakage into the wall structure (from a small degree of coupling of the core modes occurring, causing formation of modes that are able to propagate within the walls) and thus lower overall attenuation [2.298]. The wavelengths that are confined within this core can be tailored by varying the thickness of the surrounding wall.

Another potential solution to high energy laser pulse delivery is offered by photonic bandgap fibres (PBFs), also referred to as hollow-core photonic crystal fibres (HC-PCFs). More widely, PCFs is a term within the literature that covers a class of optical fibre, including holey, Bragg and photonic bandgap fibres. These designs all guide light in a similar manner to conventional fibres, with the silica core and the differing surrounding microstructures having different refractive indexes, albeit with the variations in these microstructures offering certain advantages over the standard fibre in each case. The PBF design will be discussed here, as it benefits from higher transmission efficiencies and damage thresholds compared to the other PCFs. With the PBF design the transmission-limiting factors of material absorption and low damage thresholds that are observed with more conventional fibres are quelled through the implementation of a photonic bandgap structure [2.299],[2.300]. This restricts the radiation to lower order modes, which are then delivered through a small diameter air core, which increases the damage threshold [2.301],[2.302]. With this design the wavelength that is guided through the core is determined by the separation of the air holes of the surrounding structure (referred to as the pitch). Cross-sectional images of both NCFs and photonic bandgap fibres can be observed in figure 2.55.

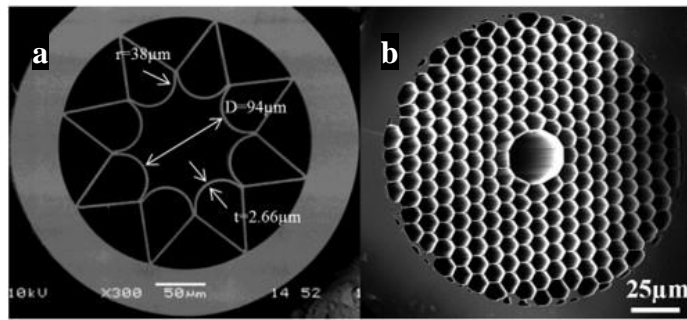


Figure 2.55 – SEM cross-sectional images of a) negative curvature fibre and b) photonic bandgap fibre [2.254].

The guidance mechanisms for both designs are significant as they allow for the delivery of higher pulse energies without severe degradation of the fibre occurring. Both structures also have the desirable effect of making the overall fibre diameter smaller as well, as they possess only one cladding layer, which in turn helps to address the issue with previously large bend radii.

Yet, these fibres both have limitations of their own, including the hollow-cores present in both designs leading to potential contamination issues, which would inhibit their implementation into clinical environments [2.303]. This contamination could also lead to reductions in the damage thresholds of the fibres. A bespoke end cap will therefore be required to prevent contamination occurring. However, these end caps also offer an immense opportunity for advancement through the implementation of various optical components.

Both fibres have shown great promise in initial experimental trials. Urich *et al.* used them to carry out ablation on hard and soft porcine tissue (bone and muscle respectively, as captured in figures 2.56 and 2.57), proving that both designs had the capacity to deliver sufficient fluences for surgical applications [2.303],[2.254]. This highlighted these fibres as being a noteworthy solution in relatively efficient and flexible delivery of these higher wavelength laser sources.

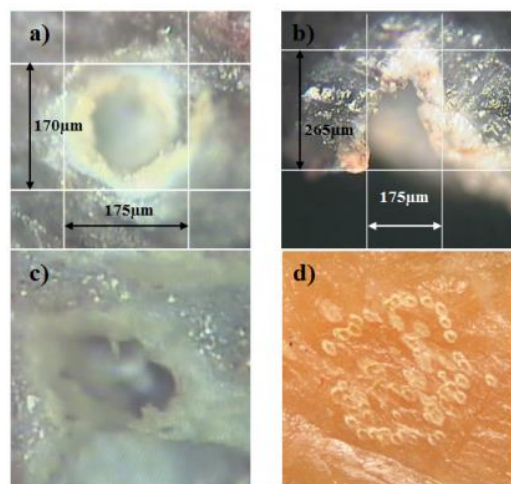


Figure 2.56 – Tissue ablation results from using Er:YAG laser light delivered by NCF a) Microscope image of ablated porcine bone b) Cross-section of ablated porcine bone, showing ablated depth of 265 µm obtained from a single shot c) Microscope image of ablated porcine muscle d) Porcine muscle ablated with varying number of shots applied over its surface [2.211].

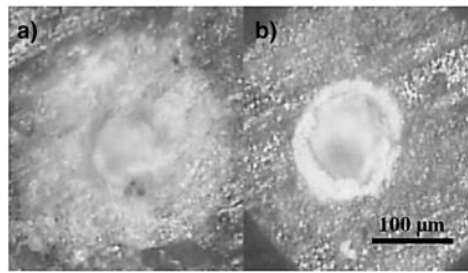


Figure 2.57 – Microscope images of single shot porcine bone ablation in a) air and b) water [2.254].

They found that the output for both types of fibre were akin to that of single-mode fibres, which is particularly advantageous for the intended surgical applications, courtesy of the increased precision the smaller spot sizes offer compared to the multimodal outputs of the larger diameter fibres previously required for efficient delivery of laser light within this 3 μm range. This was noteworthy, as while single-mode fibres are not hindered by modal interference upon bending of the fibres, they do limit the NA of the system. This increase in precision is significant as these Er:YAG lasers emitting wavelengths of 2.94 μm are widely used in medicine courtesy of their high absorption rate in water, which as discussed previously is vital in achieving efficient ablation [2.304]. These lasers are currently delivered in operating theatres through the implementation of articulated arms, which although it intuitively contains focusing optics within the handpiece, it also requires specialist knowledge and is inherently restrictive with regards to minimally invasive procedures due to its size and inflexibility. They also addressed the contamination issue highlighted earlier through the successful incorporation of a sapphire end-tip. This was particularly impressive, as they were able to exceed the required energy density values for ablating various types of tissue ($> 500 \text{ J cm}^{-2}$), even with a maximum coupling efficiency of only around 35% (originating from a mismatch between the laser mode and the fibre mode field profile upon focussing the Er:YAG laser into the core of the negative curvature fibre using a 100 mm focal length lens), while also maintaining the structural integrity of this end-tip. However, further work is required regarding both the robustness of the end tips (particularly at the interfaces between them and the fibres) and the coupling of Er:YAG laser light to the cores of these negative curvature fibres prior to wider clinical adoption.

Jaworski *et al.* have also since shown the ability of NCFs to deliver 0.57 mJ nanosecond and 30 μJ picosecond pulses for micromachining fused-silica glass and metals (aluminium and titanium), albeit with 1030 nm picosecond pulses in particular being limited by the non-optimised structure of the fibre, leading to instability in the form of multimode behaviour for delivery of such pulses [2.305]. This is significant as modal interference occurs upon bending of the fibre but without the same extent of statistical averaging observed in highly multimode fibres, which otherwise helps to mitigate this modal noise. This inhibited the spatial profile of the delivered pulses and thus both the potential precision and efficiency of the ablation process. More recent work from the group within Heriot-Watt University has shown that these fibres are capable of delivering 6 ps pulses for removing volumes from a porcine colon tissue model corresponding to those of early stage lesions found in cancer patients [2.80]. This was achieved after obtaining coupling efficiencies of around 70%.

The fabrication of the NCFs is carried out using a fairly standard stack and draw technique upon fused silica, similar to that carried out for the more conventional PBFs [2.306]. The use of silica is worth noting as it is both biologically inert and is capable of withstanding very high temperatures, making it ideal for

medical applications [2.307]. Also, low bend radii were tested for both fibres. As low as 5 cm was tested for the NCFs, with only slight additional losses occurring, as shown by the ability to still observe ablation of porcine bone tissue. For the PBFs bend diameters as low as 5 mm were shown to have no effect on the output power. The sufficient output energy densities achieved with both designs makes these fibres worthy of consideration in a great number of medical applications (with typical bend diameters for endoscopy applications being in the range of 15 cm). However, the potential for further improvements in the coupling efficiency and the current lack of suitable (*i.e.* minimally invasive) beam scanning and steering mechanisms mean that there is more work needed in examining these fibres prior to them being adopted in various operating theatres [2.308].

2.4.2 Kagome fibres

The Kagome fibre is another promising potential solution to the ongoing challenge of obtaining truly flexible delivery of ultrashort laser pulses. These fibres guide light through inhibited coupling between the respective modes in the cladding and the core, owing their name to the Kagome lattice structure that surrounds the hollow core [2.309]. This in turn leads to a reduction in the spatial overlap between the core mode and the silica walls, enabling much greater pulse energies to be delivered, albeit with higher attenuation occurring.

Kagome fibres share numerous similarities with the NCFs and PBFs described previously, including comparable core sizes (10's of μm), low transmission losses ($\sim 180 \text{ dB km}^{-1}$), broadband transmission, high damage thresholds and primarily single-mode guidance (when kept straight) [2.310],[2.311]. Energies as high as 100 μJ have been delivered with Kagome fibres, albeit filled with helium to avoid nonlinear effects [2.312],[2.313]. The geometry of the core wall has been studied in these Kagome fibres by Wang *et al.*, with hypocycloid shaped cores providing lower attenuation (150 dB km^{-1} from 1050 nm to 1400 nm) than circular shaped cores, although this low attenuation did increase for a widening transmission bandwidth via decreasing both the glass thickness and the pitch within the fibre structure (average of 300 dB km^{-1} for 900 nm to 1200 nm) [2.314]. Cross-sections of differing Kagome fibre geometries are shown in figure 2.58.

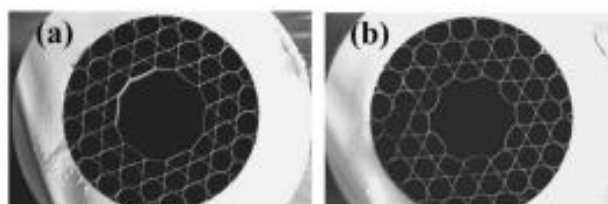


Figure 2.58 – SEM images of seven-cell core and three-ring Kagome cladding HC-PCF with (a) circular core and (b) hypocycloid core [2.310].

Kagome fibres have also been used to achieve much smaller spot sizes compared to the NCFs (4.5 μm diameter as opposed to 67 μm) and they have been successfully incorporated into an ultrafast laser scalpel [2.81]. The fibres used in this case (hypocycloid core Kagome fibre, 0.018 NA, PMC-PL-780-UP, GLOphotonics) had a mode field diameter of 31 μm , which is also smaller than that of the NCFs, allowing for more localised ablation.

While this initially sounds promising, the Kagome hollow-core fibres still possess large core sizes compared to other hollow-core fibres. This leads to them being comparatively inflexible, with bend losses only being improved upon after the implementation of more cladding layers, which is not ideal for

minimally invasive applications [2.315]. A bend radius of 5 cm was tested for these Kagome fibres, and the previously significant bend losses measured with 3 cladding layers were only improved upon by adding another cladding layer. This led to a relatively large outer diameter of around 300 μm , and based on the prediction that bend diameters on the order of 10 mm are required for truly novel minimally invasive procedures, it becomes clear that these fibres also require further investigation prior to adoption in clinical environments. The increased complexity in the structure of these fibres also translates to a more difficult (and thus more expensive) fabrication process compared to the NCFs described earlier, which incorporate only a single row of capillaries. Figure 2.59 shows a cross-section of a nodeless hollow core anti-resonant fibre design which was able to somewhat address this bending loss issue.



Figure 2.59 – Optical microscope image of free boundary anti-resonant hollow-core fibre [2.315].

Additionally, with recent studies carried out on NCFs exhibiting low loss, broad bandwidth single-mode guidance in a bent state (upon varying the pressure within the capillaries, altering their size to form a free boundary core surround), it would appear that these fibre geometries hold more immediate promise, although they too have previously suffered from significant bending losses. Further examination of these NCFs has been able to decrease the minimum bend diameter from >160 mm to ~ 15 mm [2.316]. This improvement in bend diameter was achieved through reducing the ratio of the cladding capillary diameter: core diameter from 0.70 to 0.43, further highlighting the problem with simply incorporating more cladding layers to reduce measured bend loss, as was carried out with the Kagome fibres discussed previously. A comparative study by Kolyadin *et al.* from 2015 also concluded that compared to all the other HC-PCFs, NCFs benefitted from stronger light localisation within their cores and thus lower dispersion [2.317].

2.5 Bespoke endoscopic devices

Due to all the advances made possible in minimally invasive surgery through the application of ultrashort laser pulses that have been previously highlighted, numerous research groups are currently developing bespoke endoscopic devices towards practical implementation in the operating theatre.

One of particular interest is the raster scanning two-photon multimodal endomicroscope that was developed at the Korea Advanced Institute of Science and Technology [2.318]. A schematic of this device can be observed in figure 2.60. The raster scanning was carried out using a quarter-tubular piezoelectric (PZT) actuator, which reduces the overall volume of the endoscopic probe when compared to more traditional microelectromechanical system (MEMS) mirrors [2.319]. In this instance, the probe diameter achieved was 3.5 mm, whereas previous endoscopic probes utilising MEMS mirrors or trimorph PZT actuators had a diameter of ~ 5 mm, while still benefitting from the scanning mechanism being incorporated into the probe itself [2.320]. The probe has a rigid distal length of 30 mm, which includes the high NA GRIN lens. This was incorporated into the probe to increase the efficiency of the two-photon effect at the focal spot.

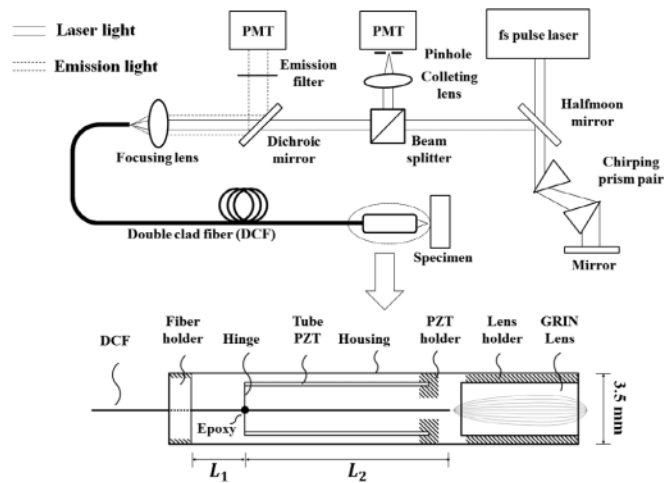


Figure 2.60 – System Configuration of the Raster Scanning Two-Photon Endomicroscope [2.318].

A raster scanning method was chosen as the previously commonplace spiral and Lissajous scanning patterns with tubular PZT actuators have noticeable non-uniformity between the inner and outer scan regions [2.321],[2.322]. Meanwhile, the raster scanning method with MEMS mirrors requires high voltage for slow axis actuation, but the raster scanning via bimorph PZT actuators is not without any drawbacks of its own, as it leads to an increase in rigid length of the endoscopic probe [2.323].

Using this design, they were able to carry out two-photon imaging of a mouse kidney. While a flexible field of view was successfully obtained, there were some issues with displacement of the fibre tip in the fast axis, image distortion occurring around the boundaries of the obtained images and overall light collection efficiency, suggesting that there is still room for improvement before this is incorporated into commercial devices for *in vivo* imaging. Additionally, as this was purely an imaging probe, it lacks the power handling capability for carrying out laser-based resection procedures.

Another device of interest is the Varifocal Micro-Opto-Electro-Mechanical-System (MOEMS) fibre scanner developed at the University of Freiburg [2.324]. A diagram of this device is shown in figure 2.61. The Microsystems Engineering Department there were able to form an endoscope probe capable of confocal imaging (thus greater depth discrimination and noise filtering while also benefitting from a simpler design and lower minimum bend radius due to a combined illumination and collection pathway), which is particularly impressive considering that it had an outer diameter of only 2.5 mm. This was achieved through the integration of a varifocal membrane lens into a piezo-driven fibre scanner setup, based on a silicon micro-bench. This enabled three-dimensional scanning, while also forgoing the need for any movable components, allowing this design to benefit from a reduced rigid tip length compared to the multimodal two-photon endomicroscope (which incorporated a lever mechanism at the epoxy-filled hinge joint highlighted in figure 2.60) covered previously.

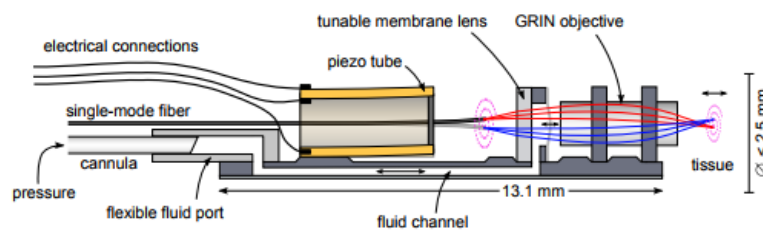


Figure 2.61 –Concept of the Varifocal MOEMS Fibre Scanner [2.324].

Although the lateral and axial resolutions achieved were impressive (1.7 μm and 19 μm respectively) and a multitude of possible scanning modes were possible courtesy of the pairing of the single-mode fibre and piezo tube, issues with image distortion were once again encountered (despite the higher pixel density offered by the single-mode fibre compared to coherent fibre bundles of approximately the same size), along with a relatively limited field-of-view (320 μm at a working distance of 0.5 mm) as the NA of the system is limited by the single-mode fibre (creating a trade-off between resolution and field-of-view). The confocal imaging technique used also suffers from reduced collection efficiency compared to implementing an independent illumination channel. This shows that further work remains to be carried out to fine-tune this instrument for clinical applications. The image distortion issue appears in a number of earlier publications as well, with feedback control being highlighted as a potential solution [2.325],[2.326]. Again, as this device is purely intended for imaging, it does not have the damage thresholds necessary for ultrafast high power laser pulse delivery.

A bespoke endoscopic probe capable of nonlinear spectroscopic imaging was developed at the Leibniz Institute of Photonic Technology [2.327]. A diagram of this probe design is shown in figure 2.62. This is the first fibre probe capable of carrying out various nonlinear imaging modalities simultaneously, in this case through a multimodal imaging fibre of 500 μm . These include coherent anti-stokes Raman scattering (CARS) (which involves 2 laser pulses of differing excitation wavelengths being collinearly guided into the laser scanning microscope, hence requires more than one fibre), second harmonic generation (SHG) and two-photon excited auto-fluorescence (TPEF) [2.328],[2.329].

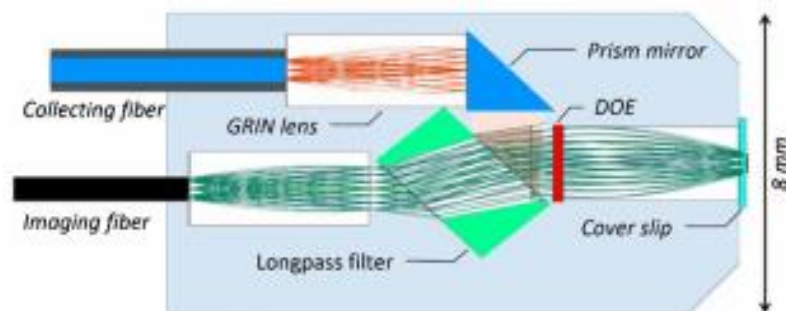


Figure 2.62 – Imaging fibre probe design [2.327].

The design of this probe is based around GRIN lenses, which allows for flexible lens parameters without the high research and development costs typically associated with such versatility. While the lack of electricity and moving parts makes the design philosophies behind this endoscope safe to apply to *in vivo* tissue applications, the collecting efficiency was comparatively low for the SHG and TPEF imaging modalities. This was due to a filter and various diffractive optical elements that had been incorporated into the probe to compensate for chromatic and spherical aberrations. While solutions were proposed to solve these issues, these all affected the inherent properties of the GRIN lenses.

Furthermore, while an overall diameter of 8 mm makes this device potentially suitable for use within the colon, there is still an opportunity for further miniaturisation. Image distortion was also once again encountered (originating from the fibre structure, particularly from under sampling caused by the inter-core spacing of the coherent fibre bundles), yet again suggesting that further investigation is mandatory before any further clinical considerations can be conclusively drawn. There are however ongoing research endeavours examining and correcting for such artefacts [2.330]. This probe, like the other devices

previously highlighted here, is purely intended for imaging. As a result, it too lacks the capability of delivering laser pulses of sufficient energy for ablating cancerous tissue sites.

Magnetic scanning mechanisms have also been proposed for implementation into the distal end of an endoscope [2.331],[2.332]. At the Department of Advanced Robotics in the Center for Convergent Technologies based in Italy they designed a novel miniaturised magnetic laser scanner device with transoral laser microsurgery in mind. In this context the use of lasers delivered via endoscopes is advantageous as this avoids the complications involved in conventional open neck surgeries using cold steel instruments and it removes the requirement of direct line of site to the target area [2.333]. The use of magnetic fields enables the high frequencies required for the scanning processes involved and bypasses the issue of hand stability/fatigue in existing fibre-based systems that rely on manual control of the fibre [2.334]. The incorporation of focusing lenses mitigates the issue of the fibre end requiring extremely close proximity to the tissue for incisions due to a high degree of light divergence. This prevents tissue residue sticking to and resultingly damaging the fibre tip, which otherwise significantly degrades the quality of any incisions made. Figure 2.63 shows both a photograph and schematic of this device.

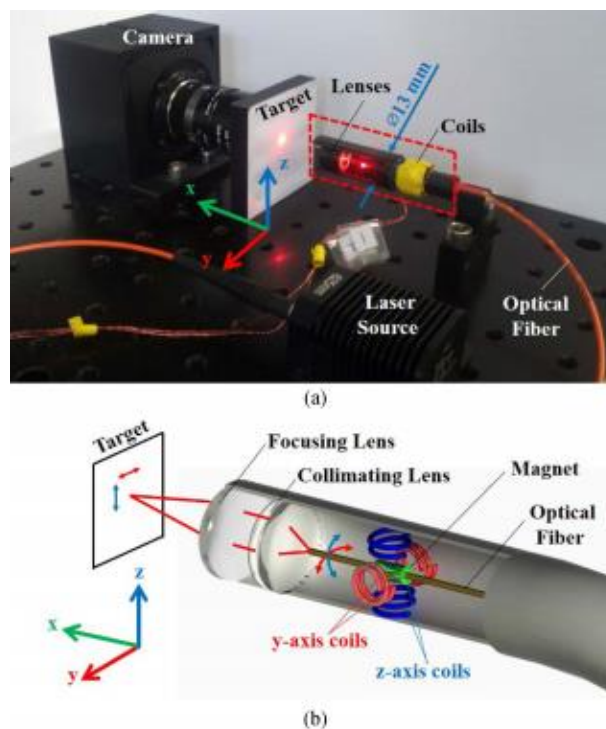


Figure 2.63 – Endoscopic magnetic laser scanner a) Experimental setup b) Schematic of scanning mechanisms and the focussing and collimation of the beam via two plano-convex lenses [2.332].

This magnetic scanning endoscope tip was also paired with a CO₂ laser, where it showed lower levels of thermally induced damage around the ablation sites compared to the same CO₂ laser (with the same laser parameters) delivered via bare flexible waveguide [2.335]. This is as expected, as without any focusing optics the laser diverged from the fibre end, creating a spot diameter of > 750 μm, as opposed to the 400 μm wide spot focused by the zinc selenide coated 20 mm focal length plano-convex lens (LA7733-F from Thorlabs) that was incorporated into the magnetic laser scanner, along with another zinc selenide coated plano-convex lens of 15 mm focal length (LA7477-G from Thorlabs) which collimates the beam prior to this focusing lens. Further improvements in the lateral confinement of ablation were observed upon

switching on the actuation and comparing it to the non-actuated process, showing a reduction in tissue carbonisation when the high-speed laser scanning (scanning frequency of 15 Hz) was enabled.

A repeatability assessment on the high-speed scanning controlled by a computer showcased high repeatability with a precision of $21 \pm 10 \mu\text{m}$. A questionnaire further solidified this, with the surgeons stating that they found it easy to use, accurate and precise. However, it is noted that although the workspace of the prototype magnetic scanner ($4 \times 4 \text{ mm}^2$) is comparable to the 5 mm lines obtained via mirror-based scanning state of the art systems, and that this could be increased further by using either longer focal length focusing optics or coupling it with a robotic endoscope, the maximum attainable volumes of resection would remain a concern [2.336]. Additional challenges limiting the efficiency of the ablation process that are highlighted include keeping the laser in focus across the whole scan (which is exacerbated further by the inhomogeneous nature of the tissue to be ablated) and maintaining the perpendicularity of the magnetic scanner to the tissue, which reduces potential reflections from the tissue surface. A suggested solution from the researchers for these two latter issues involves incorporating a continuum robot or flexible robot arm to increase the level of control over the working distance and orientation of the magnetic scanner, but this is yet to be fully realised and could further inhibit the potential compatibility with more spatially restricted regions of the body, such as the gastrointestinal tract. Finally, with an outer diameter of approximately 15 mm (from the two zinc selenide coated plano-convex lenses incorporated into the magnetic laser scanner) there is room for further miniaturisation to be implemented (especially once compared to the imaging endoscope tips covered previously), particularly if it is to be used for procedures carried out in the gastrointestinal tract.

More recently published work from this group has involved transoral laser microsurgery trials on *ex vivo* pig larynxes using a motorised laser micromanipulator controlled in real-time via a tablet instead, which includes a spherical orienting mechanism that uses anti-backlash gears and operates via high-resolution encoders [2.337]. Figure 2.64 is a photograph of the experimental setup used for these trials. While the subjective assessments of the system from the 57 surgeons in the trial were again generally favourable in terms of intuitiveness and safety, it lacks the flexibility and degree of miniaturisation required for endoscopic resection procedures in hard-to-reach surgical sites like the gastrointestinal tract.

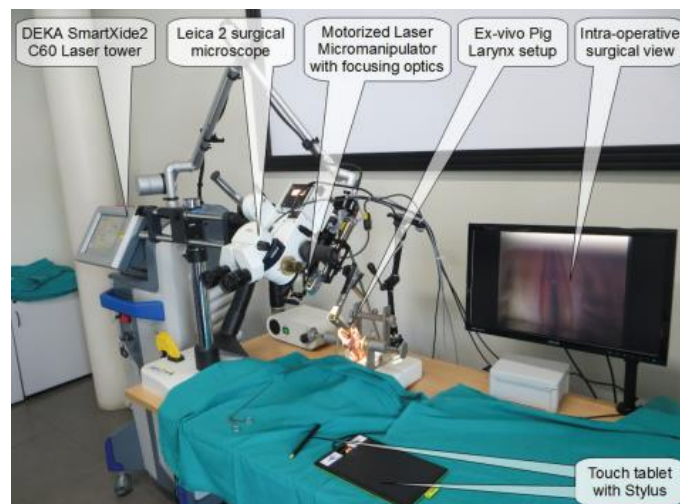


Figure 2.64 – Computer assisted transoral laser microsurgery setup for *ex vivo* pig larynx trials [2.337].

More appropriate for this task is the ultrafast laser scalpel developed for carrying out microsurgery between the Departments of Mechanical and Biomedical Engineering at the University of Texas at Austin and the Biomedical Engineering Department at Rice University based in Houston [2.81]. A schematic of this device is shown in figure 2.65. This probe has a cross-sectional outer diameter of 5.15 mm, reduced down from 9.6 mm and 18 mm in prior work, in large part due to the replacement of bulky MEMS mirrors with a piezo-scanning mechanism [2.338],[2.339]. This device achieved delivery of pulse energies on the order of microjoules through the implementation of Kagome lattice hollow-core photonic crystal fibres. These fibres did not suffer from as large a spatial overlap between the core mode and the silica walls as the small hollow-core photonic bandgap fibres used in previous probe designs, allowing for higher pulse energies to be delivered through the guidance mechanism of inhibited coupling, although this does lead to increased attenuation (> 0.5 dB/m). The Kagome fibres also benefitted from a higher tolerance to cladding damage at the input face of the fibre compared to the small hollow-core photonic bandgap fibres previously used. Additionally, it achieved peak intensities of 5×10^{12} W/cm².

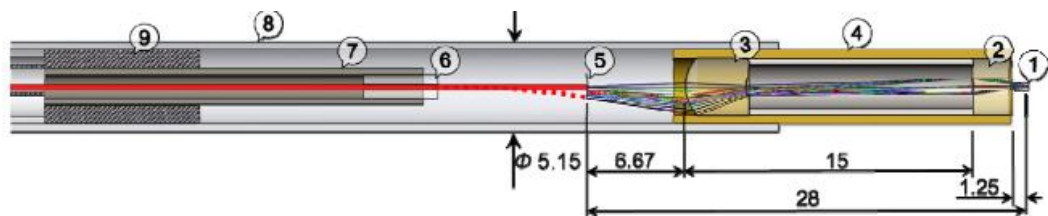


Figure 2.65 – Cross-sectional view of the optical design of hypocycloid Kagome fibre-based endoscopic ultrafast laser scalpel, developed using Solidworks with ray tracing inserted imported from Zemax, with 1) miniaturised objective piece made from 2) a coverslip and 3) + 4) two zinc sulphide lenses 5) Tip of optical fibre was modelled in Zemax to observe the ray paths as they propagate from the focal plane to the objective piece 6) Polymethyl methacrylate insert holds the fibre in the inner cavity of 7) PZT actuator, which is centred in 8) a hypodermic tube, which forms the outer casing, of 6X gauge size made of type 304 stainless steel using 9) an accurately turned plug made from epoxy glue, which electrically isolates the PZT connections [2.81].

However, the probe is only capable of scanning over a $75 \times 75 \mu\text{m}^2$ area with a focused spot $1/e^2$ diameter of $4.52 \pm 0.17 \mu\text{m}$. While such a small focal spot offers excellent precision, the maximum scan area is limited, and this would lead to increases in the duration of surgical procedures for polyps with larger lateral dimensions. Also, while the probe was able to transmit laser energies capable of ablating tissue and achieved surgery speeds of 5 mm/s, with a measured transmission efficiency of 62% and an inherently limited focal depth from using a tightly focused Gaussian beam, it was only able to ablate as deep as approximately 40 μm in porcine vocal fold tissue with a single pass at the maximum operating fluence of 7.8 J cm^{-2} . Additionally, while the larger core diameters enabled by the Kagome lattice structure allowed for higher pulse energies to be delivered, this will ultimately lead to larger mechanical bend radii, potentially limiting its use in navigating the gastrointestinal tract. Finally, while the probe design was able to deliver pulse energies of 1.2 μJ , and the use of zinc sulfide (ZnS) crystal for the focusing optics allowed the low NA fibre output to be converted to a high NA focal spot due to its high refractive index, the high non-linear susceptibility of this ZnS crystal led to three-photon absorption processes taking over when operating at pulse energies $> 1.4 \mu\text{J}$. In the conclusion the authors mention that using calcium fluoride instead may help mitigate this in future designs, albeit at the expense of the higher refractive index and greater degree of aberration correction offered by ZnS crystals.

An additional example of a laser endoscope device is the one designed at the Automatic Control and Micro-Mechatronic Systems Department based at the Franche-Comté Electronics Mechanics Thermal Science and

Optics–Sciences and Technologies Institute, with some added clinical insight provided by an ear, nose and throat surgeon based at the University Hospital of Besançon [2.340]. A cross-sectional photograph of this device is highlighted in figure 2.66. This microrobotic device consists of two linear piezoelectrical motors (enabling two degrees-of-freedom), combined with a microfabricated deformable silicon mirror. It uses a stylus and tablet to create a Surgeon-Robot Interface, which controls the scanning pattern of the laser spot upon the vocal fold tissue at a user defined speed. Although the primary application under consideration for this device is microphonosurgery (vocal fold microsurgery, targeting cysts and cancerous tissues), it is stated that this device could be used in other types of surgeries such as laparoscopy and gastroesophageal procedures (particularly with the device being compatible with endoscopes that have outer diameters just below 18 mm). This endoluminal endoscopy device benefits from not requiring a direct line of sight from the laser source to the target site, contrary to current vocal fold surgical instruments which typically consist of a stereomicroscope and a laser device. As a result, these more conventional setups require the patient to be positioned with an extreme extension of the neck throughout the surgery, which inhibits patient recovery more than the vocal fold laser surgery itself [2.341]. Also, with the laser source inherently suffering from positional inaccuracies due to having a long working distance from being positioned outside the larynx, these laser vocal fold surgical procedures require significant expertise from the surgeons performing it, especially upon considering the delicate nature of the tissue being resected [2.342].

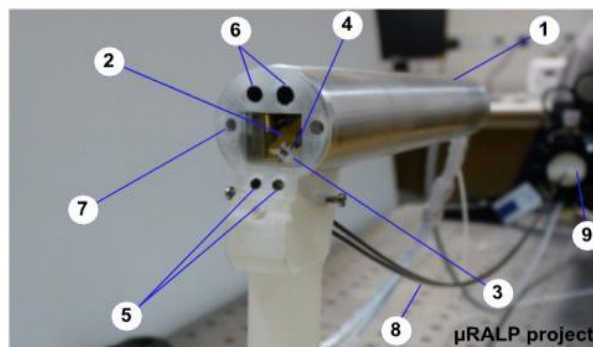


Figure 2.66 –Endoscopic tip of microrobotic laser endoscope device with 1) endoscopic tube 2) silicon on insulator mirror 3) 20° inclined millimetric right angle prism 4) laser fibre 5) GRIN lens that connects the two fibre bundles 6) two 25 fps RGB MISUMI cameras 7) lighting guide 8) two fibre bundles 9) 10000 fps Mikrotron EoSens camera [2.340].

This device was able to achieve a smaller form factor ($9 \times 11 \times 42 \text{ mm}^3$) compared to previous device designs which used bulky galvanometric mirrors, as well as suitable scanning areas ($20 \times 20 \text{ mm}^2$) for the intended vocal fold laser microsurgery applications. The piezoelectric actuators used to effectively scan the laser (Squiggle motors, New Scale Technologies, Inc.) offer a high positional resolution of $0.5 \text{ }\mu\text{m}$, which translated to a Root Mean Square (RMS) value for positional error of the laser spot of $80.50 \text{ }\mu\text{m}$ in path-following validation trials. These were carried out using a testbench setup consisting of two fibre bundles (FUJIKURA FIGH-50-1100N), connected at their distal ends to a GRIN lens (GRINTECH GT-IFRL-180-inf-50-C1). The device is also easily made bio-compatible, as the only part to come into contact with human tissue is the outer shell made of thermoplastic elastomer. This was useful for the preclinical human cadaver trials that were carried out over four days by the surgeon from the University Hospital of Besançon, which were able to achieve an RMS value in the laser spot positional error of $88.35 \text{ }\mu\text{m}$. Figure 2.67 consists of a pair of photographs taken from these trials.

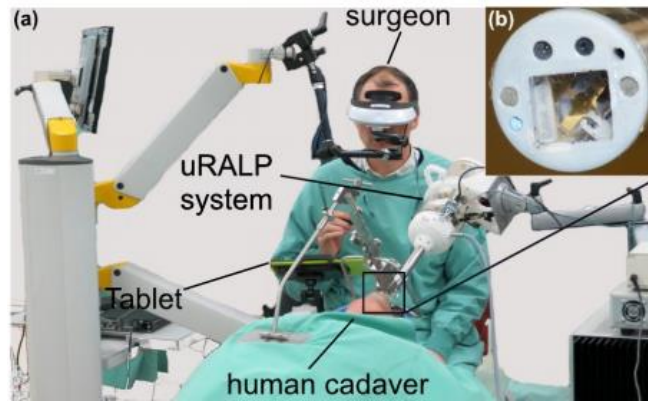


Figure 2.67 – a) Image captured during cadaver trial as part of the μ RALP project b) Zoomed view of endoscopic tip [2.340].

However, there are further preclinical trials required for this device. While the testbench trials were carried out at 40 Hz, the cadaver trials were only carried out at 17 Hz due to a framerate limitation of the RGB camera used in the setup. Also, while the RMS value of the laser spot positional error in both cases lay within the predetermined specifications for vocal fold laser microsurgery ($\leq 100 \mu\text{m}$), in the case of the testbench trials 30% of the thirty trials carried out were above this range, with an average maximum deviance value (between the position of the laser spot and the scanning path defined by the surgeon via the tablet) of $335.07 \mu\text{m}$. The working distance of 20 mm between the endoscope tip and the vocal folds could also be improved, as this causes the laser spot to undergo significant divergence (particularly with it being on the order of tens of microns), limiting the lateral accuracy. While the cadaver trials were thorough in testing various aspects of the endoscopic system (ease of insertion into larynx, robustness of micromechatronic components, extent of waterproofing and the functionality of both the laser steering and visual feedback mechanisms), unfortunately there was no investigation into the efficacy of ablating the vocal fold tissue (and thus the power output required for ablating said tissue) with this device. Consequently, the transmission efficiencies and damage threshold of the device are also not discussed in this publication, or in previous work by the group [2.343],[2.344],[2.345]. Also, once again there is potential for further miniaturisation (which is emphasised by the imaging probes discussed previously), as the primary constraint in the optical design continues to be the total diameter of the endoscopic device. This is particularly important if applications to the gastrointestinal tract are to be considered.

Another device designed for removing cancerous tissue (in this case neuroendocrine tumours from the gastrointestinal tract) in an endoscopically deployable manner is the EUSRA™ electrode designed at Taewoong Medical Co. based in Gyeonggi-do in South Korea [2.346]. This device functions via endoscopic ultrasound-guided radiofrequency ablation (EUS-guided RA) electrode needle of either 1.1 or 1.27 mm diameter (depending on the product model) and has been used for the treatment of both adenocarcinoma and tumours in the pancreas in various patient trials carried out in Asia, Europe and America (after preclinical trials were carried out to test ablation parameters on porcine models) [2.347],[2.348],[2.349],[2.350]. While there are other EUS-guided RA devices available, the EUSRA™ electrode is the only current product line which varies in active segment length (length of the needle) from as small as 5 mm to as large as 20 mm [2.351]. Figure 2.68 shows an image of the probe alongside corresponding images of EUS-guided ablation of pancreatic tissue and an operative view of this procedure.

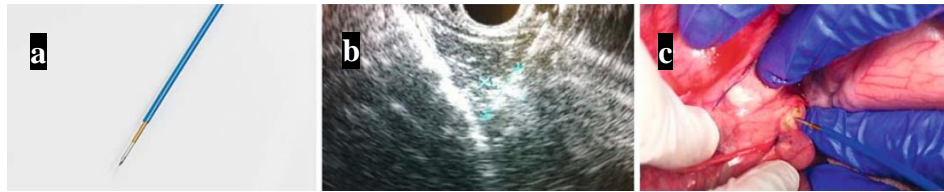


Figure 2.68 – a) Profile of EUSRA probe b) EUS-guided radiofrequency ablation performed with the EUSRA probe in healthy pancreatic tissue, with a visible echogenic cloud around the electrode c) Operative view of per-laparotomy radiofrequency ablation carried out in the pancreas using the EUSRA probe [2.346].

While these do show promise, particularly with them achieving ablation depths on the order of millimetres in 15 seconds or less, this inevitably comes at the expense of the neighbouring healthy tissue, with damage zones also being on the order of millimetres (despite the incorporation of an internal cooling mechanism via chilled saline solution to prevent charring/damage of the electrode surface). This will inevitably lead to longer patient recovery times, while also increasing the risk of further complications such as pancreatic leakage and chronic pancreatitis (complication rates for treating both pancreatic neuroendocrine tumours and cystic neoplasms in recent trials were around 10%). As a result, the studies referenced here unanimously state that further work is required in larger study populations for evaluating both the safety and long-term efficacy of these radiofrequency ablation procedures. It is also noted that tumour recurrence remains a concern and for removing larger lesions the position of the electrode may have to be varied for repeat procedures, as opposed to simply varying the ablation parameters used.

Another alternative method for achieving tumour removal in a minimally invasive manner involves the incorporation of photodynamic therapy (PDT) into an endoscope. Such a device was designed and tested via in-vitro experiments on the gelatin found in porcine skin in a collaborative effort between researchers based at the Graduate School of Information Science and Technology at the University of Tokyo and the Institute of Advanced Biomedical Engineering and Science at Tokyo Women’s Medical University [2.8]. This is the first endoscope which can simultaneously realise PDT alongside photodynamic diagnosis (PDD), which allows for tumours to be distinguished from the surrounding healthy tissue through variations in fluorescent properties. This is ideal as this imaging modality is intraoperatively compatible. After these tumour sites are located, PDT is used to destroy them without destroying the tissue. While it benefits from a small objective lens system diameter of 3 mm, is capable of localising malignant cells and is linked to reductions in the recurrence rates of these tumours, as discussed at the beginning of this chapter it is only suited for dealing with those in the very early stages of their development cycle (even more so than ablation-based procedures) due to the limited penetration depths of the appropriate light sources, as well as the increased costs and procedure timescales involved [2.352]. Figure 2.69 highlights a schematic and photograph of this device.

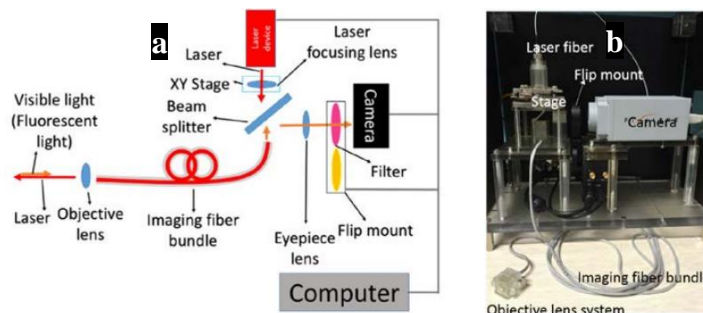


Figure 2.69 – Flexible PDD and PDT compatible laser steering endoscope a) schematic and b) photograph [2.8].

An additional shortcoming of this endoscope is the low transmission efficiency ($\sim 2.44\%$) from the endoscope due to the inclusion of a pinhole to obtain a parallel focus and the use of a laser beam diameter (1.663 to 1.723 mm horizontal, 2.277 and 2.584 mm vertical at 20 mm and 50 mm from the endoscope tip respectively) which is larger than that of one of the fibres in the fibre bundle (active diameter of the bundle was 1.4 mm). Also, despite the significantly lower power densities required for PDT compared to laser ablation-based procedures, damage of the fibre bundle (from Sumita Optical Glass) was still observed after testing the highest power setting of the laser used (Wavespectrum Laser Group, WSLP-635-400m-M), which was only 375 mW, as the light was focused down to a 64 μm diameter spot into the imaging fibre bundle using an objective lens system, to then be collected by the camera sensor after further focusing from the eyepiece lens. Other issues include a portion of the laser spot being outside of the selected tumour area during scanning due to only the central region of the laser spot being considered as the target, the illumination source and blue laser (used as the excitation source for carrying out diagnosis imaging) not yet being integrated into the laser endoscope and the use of a vector scanning pattern that was not fully optimised. Furthermore, this endoscope currently lacks three-dimensional imaging capabilities and the authors state that for tumours of dimensions $> 10 - 15$ mm the integration of a device capable of removing tissue would be necessary.

2.6 Review summary

The application of ultrafast laser pulses to minimally invasive surgical procedures shows much promise through the increased precision in ablating tissue (minimising collateral damage of surrounding tissue as a result). This has led to a wide range of surgical applications as shown in table 2.2, which summarises some of the key research looking at ultrafast laser ablation of biological tissues highlighted in this review.

Reference number	Tissue type	Laser used, pulse duration	Type of surgery
2.29	Human teeth	Neodymium-doped yttrium lithium fluoride, 55 ps	Dental
2.71	Human skin (freeze-dried)	Erbium-doped fibre laser, 900 fs	Tissue reconstruction (skin grafts)
2.77	Ovine lung	Ytterbium-doped yttrium aluminum garnet, 6 ps	Cancer
2.78	Porcine intestine		Numerous (flexible delivery of beam)
2.80		Carbide, 6 ps	
2.81	Porcine vocal fold	Erbium-doped fibre laser, 1.5 ps	
2.85	Bovine eyes	Ring dye, 8 ns – 65 fs	Ocular
2.111	Ovine and bovine bone	Ti:Sapphire, 100 fs	Orthopedic
2.264	Porcine bone	Model I Intralase, 700 fs	Stapedotomy
2.265	Ovine bone	Neodymium doped potassium-gadolinium tungstate, 230 fs	Orthopedic
2.275	Porcine eyes	iFS 150 and LenSx, 600 – 800 fs	Ocular
2.281	Porcine brain	Neodymium-doped yttrium lithium fluoride, 30 ps	Neurosurgery
2.284	Porcine vocal fold	Erbium-doped fibre laser	Laryngeal
2.290	Human teeth	Neodymium-doped yttrium aluminum garnet, 40 ps	Dental

Table 2.2 – Summary of key ultrafast laser-tissue interaction studies

Furthermore, through the high aspect ratios offered by interference generated Bessel-Gauss beams via the effective decoupling of the tightly confined lateral spots and extended focal depths, it is possible that applying these to ultrafast laser-based procedures could improve both the aspect ratio/depth of ablation and the focussing tolerance for generating plasma on the tissue surface.

The experimental realisation of either (or both) of these traits would be hugely advantageous when performing these surgeries, especially upon considering the inherent inhomogeneity of biological tissue, as this would enable more consistent, more efficient and deeper ablation/drilling of cancerous tissue, while further minimising the extent of induced lateral damage, which otherwise impairs and/or removes the surrounding healthy tissue. Additionally, due to the “self-healing” and propagation invariant (albeit over a finite range experimentally) properties of these Bessel-Gauss beams, they are potentially less affected by uneven surface morphologies compared to conventional Gaussian beam generated by traditional convex lenses, meaning it is possible that they could offer new levels of precision to these procedures, perhaps even down to the cellular level upon combination with some the novel technologies previously discussed.

With the fibres and bespoke devices highlighted, it is apparent that there is still room in this field for combining the flexibility offered by new innovative fibre geometries with the precision offered by ultrafast laser systems. This could enable full exploitation of the advantages offered by each towards medical applications.

2.7 References

- [2.1] J. M. Krauss, C. A. Puliafito, and R. F. Steinert, "Laser interactions with the cornea," *Surv. Ophthalmol.*, vol. 31, no. 1, pp. 37–53, 1986, doi: 10.1016/0039-6257(86)90050-0.
- [2.2] R. W. Waynant, *Lasers in medicine*. CRC Press, 2001. doi: 10.1088/0031-9112/35/10/030.
- [2.3] K. W. Yau and R. C. Hardie, "Phototransduction Motifs and Variations," *Cell*, vol. 139, no. 2. Cell Press, pp. 246–264, Oct. 16, 2009. doi: 10.1016/j.cell.2009.09.029.
- [2.4] J. A. Parrish, "New concepts in therapeutic photomedicine: Photochemistry, optical targeting and the therapeutic window," *J. Invest. Dermatol.*, vol. 77, no. 1, pp. 45–50, 1981, doi: 10.1111/1523-1747.ep12479235.
- [2.5] C. Gu, T. Ni, E. E. Verter, R. W. Redmond, I. E. Kochevar, and M. Yao, "Photochemical tissue bonding: A potential strategy for treating limbal stem cell deficiency," *Lasers Surg. Med.*, vol. 43, no. 5, pp. 433–442, Jul. 2011, doi: 10.1002/ism.21066.
- [2.6] B. P. Chan, "Biomedical applications of photochemistry," *Tissue Engineering - Part B: Reviews*, vol. 16, no. 5. pp. 509–522, 2010. doi: 10.1089/ten.teb.2009.0797.
- [2.7] R. L. Lipson, E. J. Baldes, and A. M. Olsen, "Hematoporphyrin derivative: a new aid for endoscopic detection of malignant disease," *J. Thorac. Cardiovasc. Surg.*, vol. 42, no. 5, pp. 623–629, Nov. 1961, doi: 10.1016/s0022-5223(19)32560-7.
- [2.8] Y. Hu and K. Masamune, "Flexible laser endoscope for minimally invasive photodynamic diagnosis (PDD) and therapy (PDT) toward efficient tumor removal," *Opt. Express*, vol. 25, no. 14, p. 16795, Jul. 2017, doi: 10.1364/oe.25.016795.
- [2.9] K. Plaetzer, B. Krammer, J. Berlanda, F. Berr, and T. Kiesslich, "Photophysics and photochemistry of photodynamic therapy: Fundamental aspects," *Lasers in Medical Science*, vol. 24, no. 2. Lasers Med Sci, pp. 259–268, Mar. 2009. doi: 10.1007/s10103-008-0539-1.
- [2.10] S. Kwiatkowski *et al.*, "Photodynamic therapy – mechanisms, photosensitizers and combinations," *Biomedicine and Pharmacotherapy*, vol. 106. Elsevier Masson SAS, pp. 1098–1107, Oct. 01, 2018. doi: 10.1016/j.biopha.2018.07.049.
- [2.11] M. R. Detty, S. L. Gibson, and S. J. Wagner, "Current clinical and preclinical photosensitizers for use in photodynamic therapy," *Journal of Medicinal Chemistry*, vol. 47, no. 16. J Med Chem, pp. 3897–3915, Jul. 29, 2004. doi: 10.1021/jm040074b.
- [2.12] W. Bäumlner *et al.*, "Photo-oxidative killing of human colonic cancer cells using indocyanine green and infrared light," *Br. J. Cancer*, vol. 80, no. 3–4, pp. 360–363, 1999, doi: 10.1038/sj.bjc.6690363.
- [2.13] Q. Q. Dou, C. P. Teng, E. Ye, and X. J. Loh, "Effective near-infrared photodynamic therapy assisted by upconversion nanoparticles conjugated with photosensitizers," *Int. J. Nanomedicine*, vol. 10, pp. 419–432, Jan. 2015, doi: 10.2147/IJN.S74891.
- [2.14] G. S. Omar, M. Wilson, and S. P. Nair, "Lethal photosensitization of wound-associated microbes using indocyanine green and near-infrared light," *BMC Microbiol.*, vol. 8, p. 111, 2008, doi: 10.1186/1471-2180-8-111.
- [2.15] J. Kim *et al.*, "Tumor-Specific Aptamer-Conjugated Polymeric Photosensitizer for Effective Endo-Laparoscopic Photodynamic Therapy," *Adv. Funct. Mater.*, vol. 29, no. 23, p. 1900084, Jun. 2019, doi: 10.1002/adfm.201900084.
- [2.16] R. Tang, L. M. M. Habimana-Griffin, D. D. Lane, C. Egbulefu, and S. Achilefu, "Nanophotosensitive drugs for light-based cancer therapy: What does the future hold?," *Nanomedicine*, vol. 12, no. 10. Future Medicine Ltd., pp. 1101–1105, May 01, 2017. doi: 10.2217/nmm-2017-0077.
- [2.17] E. C. Anigo, B. Plackal Adimuriyil George, and H. Abrahamse, "The role of photodynamic therapy on multidrug resistant breast cancer," *Cancer Cell International*, vol. 19, no. 1. BioMed Central Ltd., Apr. 11, 2019. doi: 10.1186/s12935-019-0815-0.
- [2.18] A. C. V. Doughty, A. R. Hoover, E. Layton, C. K. Murray, E. W. Howard, and W. R. Chen, "Nanomaterial applications in photothermal therapy for cancer," *Materials*, vol. 12, no. 5. MDPI AG, Mar. 01, 2019. doi: 10.3390/ma12050779.
- [2.19] D. Khemasuwan, A. C. Mehta, and K. P. Wang, "Past, present, and future of endobronchial laser photoresection," *Journal of Thoracic Disease*, vol. 7, no. 4. Pioneer Bioscience Publishing, pp. S380–S388, 2015. doi: 10.3978/j.issn.2072-1439.2015.12.55.
- [2.20] Q. Peng *et al.*, "Lasers in medicine," *Reports Prog. Phys.*, vol. 71, no. 5, May 2008, doi: 10.1088/0034-4885/71/5/056701.
- [2.21] A. A. M. Elsherbini, M. Saber, M. Aggag, A. El-Shahawy, and H. A. A. Shokier, "Laser and radiofrequency-induced hyperthermia treatment via gold-coated magnetic nanocomposites.," *Int. J. Nanomedicine*, vol. 6, pp. 2155–2165, 2011, doi: 10.2147/ijn.s23952.
- [2.22] F. Tang, Y. Zhang, J. Zhang, J. Guo, and R. Liu, "Assessment of the efficacy of laser hyperthermia and nanoparticle-enhanced therapies by heat shock protein analysis," *AIP Adv.*, vol.

- 4, no. 3, p. 031334, Mar. 2014, doi: 10.1063/1.4869095.
- [2.23] K. M. McNally, B. S. Sorg, A. J. Weich, J. M. Dawes, and E. R. Owen, “Photothermal effects of laser tissue soldering,” *Phys. Med. Biol.*, vol. 44, no. 4, pp. 983–1002, Apr. 1999, doi: 10.1088/0031-9155/44/4/013.
- [2.24] M. Heger, “Thrombosis versus thermal coagulum formation as a result of endovenous laser treatment: Biochemistry versus photophysics,” *Phlebology*, vol. 29, no. 10. SAGE Publications Ltd, pp. 701–705, Dec. 20, 2014. doi: 10.1177/0268355513505507.
- [2.25] S. Arba-Mosquera and S. Verma, “Analytical optimization of the ablation efficiency at normal and non-normal incidence for generic super Gaussian beam profiles,” *Biomed. Opt. Express*, vol. 4, no. 8, pp. 1422–1433, 2013, doi: 10.1364/boe.4.001422.
- [2.26] V. Venugopalan, N. S. Nishioka, and B. B. Mikić, “The effect of laser parameters on the zone of thermal injury produced by laser ablation of biological tissue,” *J. Biomech. Eng.*, vol. 116, no. 1, pp. 62–70, Feb. 1994, doi: 10.1115/1.2895706.
- [2.27] F. Dausinger, “Femtosecond technology for precision manufacturing: fundamental and technical aspects,” in *Third International Symposium on Laser Precision Microfabrication*, Feb. 2003, vol. 4830, p. 471. doi: 10.1117/12.486506.
- [2.28] C. Gabriel, “The Dielectric Properties of Tissues,” in *Radio Frequency Radiation Dosimetry and Its Relationship to the Biological Effects of Electromagnetic Fields*, Springer Netherlands, 2000, pp. 75–84. doi: 10.1007/978-94-011-4191-8_10.
- [2.29] K. Franjic, M. L. Cowan, D. Kraemer, and R. J. D. Miller, “Laser selective cutting of biological tissues by impulsive heat deposition through ultrafast vibrational excitations,” *Opt. Express*, vol. 17, no. 25, p. 22937, Dec. 2009, doi: 10.1364/oe.17.022937.
- [2.30] B. Choi and A. J. Welch, “Analysis of thermal relaxation during laser irradiation of tissue,” *Lasers Surg. Med.*, vol. 29, no. 4, pp. 351–359, Nov. 2001, doi: 10.1002/lsm.1128.
- [2.31] M. J. Murphy and P. A. Torstensson, “Thermal relaxation times: An outdated concept in photothermal treatments,” *Lasers Med. Sci.*, vol. 29, no. 3, pp. 973–978, 2014, doi: 10.1007/s10103-013-1445-8.
- [2.32] K. J. Kasunic and K. J. Kasunic, “Laser Selection,” in *Laser Systems Engineering*, SPIE PRESS, 2017, pp. 35–98. doi: 10.1117/3.2247601.ch2.
- [2.33] A. Vogel, J. Noack, G. Hüttman, and G. Paltauf, “Mechanisms of femtosecond laser nanosurgery of cells and tissues,” *Appl. Phys. B*, vol. 81, no. 8, pp. 1015–1047, Dec. 2005, doi: 10.1007/s00340-005-2036-6.
- [2.34] P. S. Tsai *et al.*, “Plasma-mediated ablation: an optical tool for submicrometer surgery on neuronal and vascular systems,” *Curr. Opin. Biotechnol.*, vol. 20, no. 1, pp. 90–9, Feb. 2009, doi: 10.1016/j.copbio.2009.02.003.
- [2.35] M. H. Niemz, “Light Acting on Matter,” in *Laser-Tissue Interactions*, Springer International Publishing, 2019, pp. 45–152. doi: 10.1007/978-3-030-11917-1_3.
- [2.36] J. Noack and A. Vogel, “Laser-induced plasma formation in water at nanosecond to femtosecond time scales: calculation of thresholds, absorption coefficients, and energy density,” *IEEE J. Quantum Electron.*, vol. 35, no. 8, pp. 1156–1167, Aug. 1999, doi: 10.1109/3.777215.
- [2.37] “What is LIBS? | Dr. Steven J. Rehse - University of Windsor.” <http://www1.uwindsor.ca/people/rehse/15/what-is-libs> (accessed Mar. 12, 2018).
- [2.38] A. Vogel and V. Venugopalan, “Mechanisms of pulsed laser ablation of biological tissues,” *Chem. Rev.*, vol. 103, no. 2, pp. 577–644, Feb. 2003, doi: 10.1021/cr010379n.
- [2.39] A. A. Oraevsky *et al.*, “Plasma-mediated ablation of biological tissues with ultrashort laser pulses,” in *Laser-Tissue Interaction VI*, 1995, vol. 2391, p. 423. doi: 10.1117/12.209943.
- [2.40] R. R. Letfullin, T. F. George, G. C. Duree, and B. M. Bollinger, “Ultrashort laser pulse heating of nanoparticles: Comparison of theoretical approaches,” *Adv. Opt. Technol.*, 2008, doi: 10.1155/2008/251718.
- [2.41] P. K. Kennedy, S. A. Boppart, D. X. Hammer, B. A. Rockwell, G. D. Noojin, and W. P. Roach, “A First-Order Model for Computation of Laser-Induced Breakdown Thresholds in Ocular and Aqueous Media: Part II—Comparison to Experiment,” *IEEE J. Quantum Electron.*, vol. 31, no. 12, pp. 2250–2257, 1995, doi: 10.1109/3.477754.
- [2.42] A. Vogel *et al.*, “Energy balance of optical breakdown in water at nanosecond to femtosecond time scales,” *Appl. Phys. B Lasers Opt.*, vol. 68, no. 2, pp. 271–280, Apr. 1999, doi: 10.1007/s003400050617.
- [2.43] J. Noack, D. X. Hammer, G. D. Noojin, B. A. Rockwell, and A. Vogel, “Influence of pulse duration on mechanical effects after laser-induced breakdown in water,” *J. Appl. Phys.*, vol. 83, no. 12, pp. 7488–7495, Jun. 1998, doi: 10.1063/1.367512.
- [2.44] D. X. Hammer *et al.*, “Shielding properties of laser-induced breakdown in water for pulse durations from 5 ns to 125 fs,” *Appl. Opt.*, vol. 36, no. 22, p. 5630, Aug. 1997, doi: 10.1364/ao.36.005630.

- [2.45] K. Nahen and A. Vogel, "Plasma formation in water by picosecond and nanosecond Nd:YAG laser pulses - Part II: Transmission, scattering, and reflection," *IEEE J. Sel. Top. Quantum Electron.*, vol. 2, no. 4, pp. 861–871, 1996, doi: 10.1109/2944.577308.
- [2.46] A. Vogel, S. Busch, K. Jungnickel, and R. Birngruber, "Mechanisms of intraocular photodisruption with picosecond and nanosecond laser pulses," *Lasers Surg. Med.*, vol. 15, no. 1, pp. 32–43, Jan. 1994, doi: 10.1002/lsm.1900150106.
- [2.47] H. Petersen *et al.*, "Picosecond Infrared Laser (PIRL) Application in Stapes Surgery-First Experience in Human Temporal Bones," *Otol. Neurotol.*, vol. 39, no. 4, pp. e224–e230, Apr. 2018, doi: 10.1097/MAO.0000000000001753.
- [2.48] A. E. Hussein, P. K. Diwakar, S. S. Harilal, and A. Hassanein, "The role of laser wavelength on plasma generation and expansion of ablation plumes in air," *J. Appl. Phys.*, vol. 113, no. 14, 2013, doi: 10.1063/1.4800925.
- [2.49] R. Yadav, "Photodisruption," in *Encyclopedia of Ophthalmology*, Springer Berlin Heidelberg, 2015, pp. 1–2. doi: 10.1007/978-3-642-35951-4_651-1.
- [2.50] M. M. Krasnov, "Laser puncture of the anterior chamber angle in glaucoma (a preliminary report)," *Vestn. Oftalmol.*, vol. 3, pp. 27–31, Jan. 1972, Accessed: Aug. 25, 2020. [Online]. Available: <https://europepmc.org/article/med/5078295>
- [2.51] D. Aron-Rosa, J. J. Aron, M. Griesemann, and R. Thyzel, "Use of the neodymium-yag laser to open the posterior capsule after lens implant surgery: A preliminary report," *Am. Intra-Ocular Implant Soc. J.*, vol. 6, no. 4, pp. 352–354, 1980, doi: 10.1016/S0146-2776(80)80036-X.
- [2.52] F. Fankhauser, P. Roussel, J. Steffen, E. Van Der Zypen, and A. Chrenkova, "Clinical studies on the efficiency of high power laser radiation upon some structures of the anterior segment of the eye - First experiences of the treatment of some pathological conditions of the anterior segment of the human eye by means of a Q-switched," *Int. Ophthalmol.*, vol. 3, no. 3, pp. 129–139, 1981, doi: 10.1007/BF00130696.
- [2.53] M. H. Niemz, "Interaction Mechanisms," in *Laser-Tissue Interactions: Fundamentals and Applications*, Springer, Berlin, Heidelberg, 2007, pp. 45–150. doi: 10.1007/978-3-540-72192-5_3.
- [2.54] Y. Feng, D. Qin, and M. Wan, "Laser-Induced Cavitation and Photoacoustic Cavitation," in *Cavitation in Biomedicine*, Springer Netherlands, 2015, pp. 401–455. doi: 10.1007/978-94-017-7255-6_8.
- [2.55] A. Vogel, N. Linz, S. Freidank, and G. Paltauf, "Femtosecond-laser-induced nanocavitation in water: Implications for optical breakdown threshold and cell surgery," *Phys. Rev. Lett.*, vol. 100, no. 3, p. 038102, Jan. 2008, doi: 10.1103/PhysRevLett.100.038102.
- [2.56] W. Lauterborn, "High-speed photography of laser-induced breakdown in liquids," *Appl. Phys. Lett.*, vol. 21, no. 1, pp. 27–29, Jul. 1972, doi: 10.1063/1.1654204.
- [2.57] W. Lauterborn, "Cavitation by laser light," *Acustica*, 1974.
- [2.58] W. Lauterborn and H. Bolle, "Experimental investigations of cavitation-bubble collapse in the neighbourhood of a solid boundary," *J. Fluid Mech.*, vol. 72, no. 2, pp. 391–399, Nov. 1975, doi: 10.1017/S0022112075003448.
- [2.59] A. Vogel, W. Lauterborn, and R. Timm, "Optical and acoustic investigations of the dynamics of laser-produced cavitation bubbles near a solid boundary," *J. Fluid Mech.*, vol. 206, pp. 299–338, 1989, doi: 10.1017/S0022112089002314.
- [2.60] A. Vogel, P. Schweiger, A. Frieser, M. N. Asiyo, and R. Birngruber, "Intraocular Nd: YAG Laser Surgery: Light-Tissue Interaction, Damage Range, and Reduction of Collateral Effects," *IEEE J. Quantum Electron.*, vol. 26, no. 12, pp. 2240–2260, 1990, doi: 10.1109/3.64361.
- [2.61] N. Tinne, B. Kaune, A. Krüger, and T. Ripken, "Interaction mechanisms of cavitation bubbles induced by spatially and temporally separated fs-laser pulses," *PLoS One*, vol. 9, no. 12, p. e114437, Dec. 2014, doi: 10.1371/journal.pone.0114437.
- [2.62] M. F. Yanik, H. Cinar, H. N. Cinar, A. D. Chisholm, Y. Jin, and A. Ben-Yakar, "Neurosurgery: Functional regeneration after laser axotomy," *Nature*, vol. 432, no. 7019, pp. 822–822, Dec. 2004, doi: 10.1038/432822a.
- [2.63] A. Heisterkamp *et al.*, "Pulse energy dependence of subcellular dissection by femtosecond laser pulses," *Opt. Express*, vol. 13, no. 10, pp. 3690–6, May 2005, Accessed: Dec. 05, 2017. [Online]. Available: <http://www.ncbi.nlm.nih.gov/pubmed/16035172>
- [2.64] E. Block *et al.*, "Simultaneous spatial and temporal focusing for tissue ablation," *Biomed. Opt. Express*, vol. 4, no. 6, pp. 831–41, Jun. 2013, doi: 10.1364/BOE.4.000831.
- [2.65] D. Tervo and A. Y. Karpova, "Rapidly inducible, genetically targeted inactivation of neural and synaptic activity in vivo," *Curr. Opin. Neurobiol.*, vol. 17, no. 5, pp. 581–586, Oct. 2007, doi: 10.1016/j.conb.2007.10.002.
- [2.66] K. Katsanos, "Overview of thermal ablation: Plasma-mediated ablation," in *Interventional Radiology Techniques in Ablation*, London: Springer London, 2013, pp. 43–49. doi: 10.1007/978-

- 0-85729-094-6_6.
- [2.67] D. C. Jeong, P. S. Tsai, and D. Kleinfeld, "Prospect for feedback guided surgery with ultra-short pulsed laser light," *Curr. Opin. Neurobiol.*, vol. 22, no. 1, pp. 24–33, Feb. 2012, doi: 10.1016/j.conb.2011.10.020.
- [2.68] S. Park and H. W. Kang, "Multivariate analysis of laser-induced tissue ablation: Ex vivo liver testing," *Appl. Sci.*, vol. 7, no. 10, p. 974, Sep. 2017, doi: 10.3390/app7100974.
- [2.69] S. E. Mowry, M. Ament, and N. L. Shapiro, "Lingual tonsil hypertrophy causing severe dysphagia: Treatment with plasma-mediated radiofrequency-based ablation (Coblation)," *Ear, Nose Throat J.*, vol. 89, no. 3, pp. 134–136, Mar. 2010, doi: 10.1177/014556131008900312.
- [2.70] R. S. Virk, S. Bansal, G. Nayak, and L. P., "Plasma Ablation-Assisted Endoscopic Management of Postintubation Laryngotracheal Stenosis: An Alternate Tool for Management," *Otolaryngol. - Head Neck Surg. (United States)*, vol. 161, no. 6, pp. 993–995, Dec. 2019, doi: 10.1177/0194599819881439.
- [2.71] H. Huang and Z. Guo, "Ultrashort pulsed laser ablation and stripping of freeze-dried dermis," *Lasers Med. Sci.*, vol. 25, no. 4, pp. 517–524, 2010, doi: 10.1007/s10103-009-0741-9.
- [2.72] H. Huang and Z. Guo, "Human dermis separation via ultra-short pulsed laser plasma-mediated ablation," *J. Phys. D: Appl. Phys.*, vol. 42, no. 16, pp. 165204–9, 2009, doi: 10.1088/0022-3727/42/16/165204.
- [2.73] S. Liang, P. Lyu, and F. Yuan, "Method for Accurately Preparing Cavities on Cortical Bones Using Picosecond Laser," *Photobiomodulation, Photomedicine, Laser Surg.*, vol. 38, no. 5, pp. 301–307, May 2020, doi: 10.1089/photob.2019.4724.
- [2.74] M. E. Khosroshahi and S. Valizadeh, "Measurement of pulse Nd: YAG laser-induced stress and analysis of dental tissue and amalgam plume using uniaxial polyvinylidene fluoride-based photoacoustic sensor and plasma spectroscopy," *Opt. Laser Technol.*, vol. 128, p. 106239, Aug. 2020, doi: 10.1016/j.optlastec.2020.106239.
- [2.75] S. Vanstone, J. M. Stone, S. N. Gordeev, and R. H. Guy, "Mechanism of human nail poration by high-repetition-rate, femtosecond laser ablation," *Drug Deliv. Transl. Res.*, vol. 9, no. 5, pp. 956–967, Oct. 2019, doi: 10.1007/s13346-019-00638-x.
- [2.76] H. Abbasi, R. Guzman, P. C. Cattin, G. Rauter, and A. Zam, "Differentiation of femur bone from surrounding soft tissue using laser-induced breakdown spectroscopy as a feedback system for smart laserosteotomy," in *Biophotonics: Photonic Solutions for Better Health Care VI*, May 2018, vol. 10685, p. 60. doi: 10.1117/12.2309473.
- [2.77] R. J. Beck *et al.*, "Precision resection of lung cancer in a sheep model using ultrashort laser pulses," in *Frontiers in Ultrafast Optics: Biomedical, Scientific, and Industrial Applications XVII*, Feb. 2017, vol. 10094, p. 1009405. doi: 10.1117/12.2252215.
- [2.78] R. J. Beck *et al.*, "Precision machining of pig intestine using ultrafast laser pulses," Jul. 2015, p. 95421B. doi: 10.1117/12.2197930.
- [2.79] R. J. Beck, W. S. Gora, D. Jayne, D. P. Hand, and J. D. Shephard, "Precision resection of intestine using ultrashort laser pulses," Mar. 2016, vol. 9706, p. 97060P. doi: 10.1117/12.2209589.
- [2.80] S. M. P. C. Mohanan *et al.*, "Preclinical evaluation of porcine colon resection using hollow core negative curvature fibre delivered ultrafast laser pulses," *J. Biophotonics*, vol. 12, no. 11, Nov. 2019, doi: 10.1002/jbio.201900055.
- [2.81] K. Subramanian *et al.*, "Kagome fiber based ultrafast laser microsurgery probe delivering micro-Joule pulse energies," *Biomed. Opt. Express*, vol. 7, no. 11, p. 4639, Nov. 2016, doi: 10.1364/boe.7.004639.
- [2.82] X. H. Hu, Q. Fang, M. J. Cariveau, X. Pan, and G. W. Kalmus, "Mechanism study of porcine skin ablation by nanosecond laser pulses at 1064, 532, 266, and 213 nm," *IEEE J. Quantum Electron.*, vol. 37, no. 3, pp. 322–328, 2001, doi: 10.1109/3.910440.
- [2.83] M. M. Krasnov, "Q-switched laser iridectomy and Q-switched laser goniopuncture.," *Adv. Ophthalmol.*, vol. 34, pp. 192–196, Jan. 1977, Accessed: Jun. 24, 2020. [Online]. Available: <http://www.ncbi.nlm.nih.gov/pubmed/868692>
- [2.84] M. H. Niemz, E. G. Klancnik, and J. F. Bille, "Plasma-mediated ablation of corneal tissue at 1053 nm using a Nd:YLF oscillator/regenerative amplifier laser," *Lasers Surg. Med.*, vol. 11, no. 5, pp. 426–431, 1991, doi: 10.1002/lsm.1900110507.
- [2.85] D. Stern, C. A. Puliafito, E. T. Dobi, R. W. Schoenlein, J. G. Fujimoto, and R. Birngruber, "Corneal Ablation by Nanosecond, Picosecond, and Femtosecond Lasers At 532 And 625 nm," *Arch. Ophthalmol.*, vol. 107, no. 4, pp. 587–592, 1989, doi: 10.1001/archopht.1989.01070010601038.
- [2.86] D. V. et. al. Palanker, "Apparatus for patterned plasma-mediated laser ophthalmic surgery," Aug. 2016, Accessed: Apr. 27, 2018. [Online]. Available: <https://patents.google.com/patent/US9750640B2/en>

- [2.87] W. et. al. Culbertson, “Method and Apparatus for Creating Ocular Surgical and Relaxing Incisions,” Nov. 2015, Accessed: Apr. 27, 2018. [Online]. Available: <https://patents.google.com/patent/US20160074228A1/en>
- [2.88] U. Sarma and S. N. Joshi, “Machining of micro-channels on polycarbonate by using Laser-Induced Plasma Assisted Ablation (LIPAA),” *Opt. Laser Technol.*, vol. 128, p. 106257, Aug. 2020, doi: 10.1016/j.optlastec.2020.106257.
- [2.89] Y. Li, H. Liu, and M. Hong, “High-quality sapphire microprocessing by dual-beam laser induced plasma assisted ablation,” *Opt. Express*, vol. 28, no. 5, p. 6242, Mar. 2020, doi: 10.1364/oe.381268.
- [2.90] D. N. Vitek *et al.*, “Temporally focused femtosecond laser pulses for low numerical aperture micromachining through optically transparent materials,” *Opt. Express*, vol. 18, no. 17, p. 18086, Aug. 2010, doi: 10.1364/oe.18.018086.
- [2.91] P. Arias, J. Jaeckel, J. Redondo, and A. Ringwald, “Optimizing light-shining-through-a-wall experiments for axion and other weakly interacting slim particle searches,” *Phys. Rev. D - Part. Fields, Gravit. Cosmol.*, vol. 82, no. 11, Dec. 2010, doi: 10.1103/PhysRevD.82.115018.
- [2.92] H. Wu, P. Zou, J. Cao, and K. F. Ehmann, “Vibrating-lens-assisted laser drilling,” *J. Manuf. Process.*, vol. 55, pp. 389–398, Jul. 2020, doi: 10.1016/j.jmapro.2020.03.005.
- [2.93] Z. Ouyang, Y. Okamoto, Y. Ogino, T. Sakagawa, and A. Okada, “Influence of numerical aperture on molten area formation in fusion micro-welding of glass by picosecond pulsed laser,” *Appl. Sci.*, vol. 9, no. 7, p. 1412, Apr. 2019, doi: 10.3390/app9071412.
- [2.94] V. Nasrollahi, P. Penchev, A. Batal, H. Le, S. Dimov, and K. Kim, “Laser drilling with a top-hat beam of micro-scale high aspect ratio holes in silicon nitride,” *J. Mater. Process. Technol.*, vol. 281, p. 116636, Jul. 2020, doi: 10.1016/j.jmatprotec.2020.116636.
- [2.95] D. C. Jeong, P. S. Tsai, and D. Kleinfeld, “All-optical osteotomy to create windows for transcranial imaging in mice,” *Opt. Express*, vol. 21, no. 20, p. 23160, Oct. 2013, doi: 10.1364/oe.21.023160.
- [2.96] K. Akimoto *et al.*, “Development of local therapy device using laser-inducing plasma,” *Proc. JSME Annu. Conf. Robot. Mechatronics*, vol. 2020, pp. 2A2-D03, May 2020, doi: 10.1299/jsmermd.2020.2a2-d03.
- [2.97] J. Durnin, “Exact solutions for nondiffracting beams I The scalar theory,” *J. Opt. Soc. Am. A*, vol. 4, no. 4, p. 651, Apr. 1987, doi: 10.1364/josaa.4.000651.
- [2.98] J. Durnin, J. Miceli, and J. H. Eberly, “Diffraction-free beams,” *Phys. Rev. Lett.*, vol. 58, no. 15, pp. 1499–1501, 1987, doi: 10.1103/PhysRevLett.58.1499.
- [2.99] P. Sprangle and B. Hafizi, “Comment on nondiffracting beams,” *Phys. Rev. Lett.*, vol. 66, no. 6, pp. 837–837, Feb. 1991, doi: 10.1103/PhysRevLett.66.837.
- [2.100] J. Durnin, J. J. Miceli, and J. H. Eberly, “Durnin, Miceli, and Eberly reply,” *Phys. Rev. Lett.*, vol. 66, no. 6, pp. 838–838, Feb. 1991, doi: 10.1103/PhysRevLett.66.838.
- [2.101] R. et al. Meyer, “Beam Shaping Aids Transparent Matierals Processing,” *The Laser User*, pp. 28–29, 2017. Accessed: Apr. 30, 2018. [Online]. Available: www.ailu.org.uk
- [2.102] Y. Chen and J. T. C. Liu, “Characterizing the beam steering and distortion of Gaussian and Bessel beams focused in tissues with microscopic heterogeneities,” *Biomed. Opt. Express*, vol. 6, no. 4, pp. 1318–30, Apr. 2015, doi: 10.1364/boe.6.001318.
- [2.103] D. Mcgloin and K. Dholakia, “Bessel beams: Diffraction in a new light,” *Contemp. Phys.*, vol. 46, no. 1, pp. 15–28, 2005, doi: 10.1080/0010751042000275259.
- [2.104] C. Chen and S. W. Huang, “The generation of non-conventional beam in a nonlinear electro-optic photonic crystal,” *Jpn. J. Appl. Phys.*, vol. 59, no. 9, p. 092003, Sep. 2020, doi: 10.35848/1347-4065/ababbb.
- [2.105] K. M. Tan *et al.*, “In-fiber common-path optical coherence tomography using a conical-tip fiber,” *Opt. Express*, vol. 17, no. 4, pp. 2375–2384, Feb. 2009, doi: 10.1364/oe.17.002375.
- [2.106] Y. Zhang, X. Xu, J. Cao, F. Wu, A. Dun, and J. Shao, “Precision manufacturing technology of axicon,” in *9th International Symposium on Advanced Optical Manufacturing and Testing Technologies: Subdiffraction-limited Plasmonic Lithography and Innovative Manufacturing Technology*, Feb. 2019, vol. 10842, p. 120. doi: 10.1117/12.2505900.
- [2.107] O. Brzobohatý, T. Cizmar, and P. Zemánek, “High quality quasi-Bessel beam generated by round-tip axicon,” *Opt. Express*, vol. 16, no. 17, pp. 12688–12700, Aug. 2008, doi: 10.1364/oe.16.012688.
- [2.108] F. Courvoisier, J. Zhang, M. K. Bhuyan, M. Jacquot, and J. M. Dudley, “Applications of femtosecond Bessel beams to laser ablation,” *Appl. Phys. A Mater. Sci. Process.*, vol. 112, no. 1, pp. 29–34, 2013, doi: 10.1007/s00339-012-7201-2.
- [2.109] P. Wu, C. Sui, and W. Huang, “Theoretical analysis of a quasi-Bessel beam for laser ablation,” *Photonics Res.*, vol. 2, no. 3, pp. 82–86, 2014, doi: 10.1364/prj.2.000082.
- [2.110] C. Mignon, A. H. Rodriguez, J. A. Palero, B. Varghese, and M. Jurna, “Fractional laser

- photothermolysis using Bessel beams.,” *Biomed. Opt. Express*, vol. 7, no. 12, pp. 4974–4981, Dec. 2016, doi: 10.1364/BOE.7.004974.
- [2.111] S. A. Ashforth, R. N. Oosterbeek, and M. C. Simpson, “Ultrafast pulsed Bessel beams for enhanced laser ablation of bone tissue for applications in LASSOS,” *Proc. SPIE*, vol. 10094, pp. 100941O–100941O–9, 2017. doi: 10.1117/12.2250068.
- [2.112] C. Buckley *et al.*, “Precise spatio-temporal control of rapid optogenetic cell ablation with mem-KillerRed in Zebrafish,” *Sci. Rep.*, vol. 7, no. 1, p. 5096, Dec. 2017, doi: 10.1038/s41598-017-05028-2.
- [2.113] C. Teh *et al.*, “Optogenetic in vivo cell manipulation in KillerRed-expressing zebrafish transgenics,” *BMC Dev. Biol.*, vol. 10, no. 1, p. 110, Nov. 2010, doi: 10.1186/1471-213X-10-110.
- [2.114] T. Čižmár *et al.*, “Generation of multiple Bessel beams for a biophotonics workstation,” *Opt. Express*, vol. 16, no. 18, p. 14024, 2008, doi: 10.1364/oe.16.014024.
- [2.115] X. Tsampoula *et al.*, “Fibre based cellular transfection; Optical force field mapping in microdevices,” *Opt. EXPRESS Lab a Chip*, vol. 16, no. 6, pp. 1545–1547, 2008, Accessed: Dec. 06, 2017. [Online]. Available: https://www.osapublishing.org/DirectPDFAccess/BE2AEFA7-E7DE-0E30-E0FF7B9C8F8C1328_172603/oe-16-21-17007.pdf?da=1&id=172603&seq=0&mobile=no
- [2.116] X. Tsampoula *et al.*, “Femtosecond cellular transfection using a nondiffracting light beam,” *Appl. Phys. Lett.*, vol. 91, no. 5, p. 053902, Jul. 2007, doi: 10.1063/1.2766835.
- [2.117] R. N. Oosterbeek, S. Ashforth, O. Bodley, and M. C. Simpson, “Measuring the ablation threshold fluence in femtosecond laser micromachining with vortex and Bessel pulses,” *Opt. Express*, vol. 26, no. 26, pp. 34558–34568, Dec. 2018, doi: 10.1364/oe.26.034558.
- [2.118] S. N. Khonina, N. L. Kazanskiy, S. V. Karpeev, and M. A. Butt, “Bessel beam: Significance and applications —A progressive review,” *Micromachines*, vol. 11, no. 11, MDPI AG, p. 997, Nov. 11, 2020. doi: 10.3390/mi11110997.
- [2.119] S. A. Ashforth, R. N. Oosterbeek, O. L. C. Bodley, and M. C. Simpson, “Investigating ultrashort laser pulses as a LASer scalpel for orthopedic surgery (LASSOS),” in *2016 Conference on Lasers and Electro-Optics, CLEO 2016*, Jun. 2016, p. AW4O.1. doi: 10.1364/cleo_at.2016.aw4o.1.
- [2.120] C. Vetter *et al.*, “Realization of Free-Space Long-Distance Self-Healing Bessel Beams,” *Laser Photon. Rev.*, vol. 13, no. 10, p. 1900103, Oct. 2019, doi: 10.1002/lpor.201900103.
- [2.121] C. Liu *et al.*, “High-speed, multi-modal, label-free imaging of pathological slices with a Bessel beam,” *Biomed. Opt. Express*, vol. 11, no. 5, p. 2694, May 2020, doi: 10.1364/boe.391143.
- [2.122] R. Meyer, “Beam Shaping Aids Transparent Materials Processing,” *The Laser User*, pp. 28–29, Mar. 2017. Accessed: Jun. 18, 2021. [Online]. Available: https://www.ailu.org.uk/assets/document/issue_84_low_res.pdf
- [2.123] J. Dudutis *et al.*, “Laser-fabricated axicons challenging the conventional optics in glass processing applications,” *Opt. Express*, vol. 28, no. 4, pp. 5715–5730, Feb. 2020, doi: 10.1364/oe.377108.
- [2.124] J. Dudutis, P. Gečys, and G. Račiukaitis, “Non-ideal axicon-generated Bessel beam application for intra-volume glass modification,” *Opt. Express*, vol. 24, no. 25, pp. 28433–28443, Dec. 2016, doi: 10.1364/oe.24.028433.
- [2.125] Z. Ali, C. Zakian, and V. Ntziachristos, “Ultra-broadband axicon transducer for optoacoustic endoscopy,” *Sci. Rep.*, vol. 11, no. 1, p. 1654, Dec. 2021, doi: 10.1038/s41598-021-81117-7.
- [2.126] Z. Q. Li *et al.*, “Debris-free cutting of quartz with zero kerf width and ultra-low surface roughness using femtosecond Bessel laser beam filamentation,” *Lasers Eng.*, vol. 46, no. 5–6, pp. 343–357, 2020.
- [2.127] R. N. Oosterbeek, S. Ashforth, O. Bodley, and M. C. Simpson, “Spatial shaping of femtosecond laser pulses for improved micromachining efficiency,” in *2016 Conference on Lasers and Electro-Optics, CLEO 2016*, Dec. 2016, p. Ath1K.3. doi: 10.1364/cleo_at.2016.ath1k.3.
- [2.128] B. Kim, R. Iida, S. Kiyokawa, and K. Fushinobu, “Effect of beam profile on nanosecond laser drilling of 4H-SiC,” *J. Laser Appl.*, vol. 30, no. 3, p. 032207, Aug. 2018, doi: 10.2351/1.5040597.
- [2.129] B. Kim, R. Iida, D. H. Doan, and K. Fushinobu, “Mechanism of nanosecond laser drilling process of 4H-SiC for through substrate vias,” *Appl. Phys. A Mater. Sci. Process.*, vol. 123, no. 6, pp. 1–9, Jun. 2017, doi: 10.1007/s00339-017-0986-2.
- [2.130] S. Mori, “Side lobe suppression of a Bessel beam for high aspect ratio laser processing,” *Precis. Eng.*, vol. 39, pp. 79–85, Jan. 2015, doi: 10.1016/j.precisioneng.2014.07.008.
- [2.131] F. He *et al.*, “Tailoring femtosecond 1.5- μm Bessel beams for manufacturing high-aspect-ratio through-silicon vias,” *Sci. Rep.*, vol. 7, no. 1, pp. 1–9, Jan. 2017, doi: 10.1038/srep40785.
- [2.132] T. Čižmár and K. Dholakia, “Axial intensity shaping of a Bessel beam,” in *Optical Trapping and Optical Micromanipulation VI*, Aug. 2009, vol. 7400, p. 74001Q. doi: 10.1117/12.826297.
- [2.133] J. Dudutis, R. Stonys, G. Račiukaitis, and P. Gečys, “Aberration-controlled Bessel beam processing of glass,” *Opt. Express*, vol. 26, no. 3, p. 3627, Feb. 2018, doi: 10.1364/oe.26.003627.

- [2.134] O. Brzobohatý, T. Cižmár, and P. Zemánek, “Quasi-Bessel beam generated by oblate-tip axicon,” in *16th Polish-Slovak-Czech Optical Conference on Wave and Quantum Aspects of Contemporary Optics*, Dec. 2008, vol. 7141, p. 714126. doi: 10.1117/12.822425.
- [2.135] C. L. Arnold *et al.*, “Nonlinear Bessel vortex beams for applications,” *J. Phys. B At. Mol. Opt. Phys.*, vol. 48, no. 9, May 2015, doi: 10.1088/0953-4075/48/9/094006.
- [2.136] X. Du, S. Y. Kang, and C. B. Arnold, “Optimization of ultrafast axial scanning parameters for efficient pulsed laser micro-machining,” *J. Mater. Process. Technol.*, vol. 288, p. 116850, Feb. 2021, doi: 10.1016/j.jmatprotec.2020.116850.
- [2.137] C. Bischoff, E. Jäger, U. Umhofer, A. F. Lasagni, and F. Völklein, “Homogeneous Intensity within The Rayleigh Length and Enhanced Depth of Focus for Gaussian Beams,” *J. Laser Micro Nanoeng.*, vol. 15, no. 3, pp. 178–185, 2020, doi: 10.2961/JLMN.2020.03.2004.
- [2.138] C. Song, X. J. Yang, W. Zhao, and Y. F. Duan, “Depth-micro Laser Drilling Methods Based on Spatial Light Modulator,” *Guangzi Xuebao/Acta Photonica Sin.*, vol. 49, no. 8, p. 814001, Aug. 2020, doi: 10.3788/gzxb20204908.0814001.
- [2.139] A. D. Chandra and A. Banerjee, “Rapid phase calibration of a spatial light modulator using novel phase masks and optimization of its efficiency using an iterative algorithm,” *J. Mod. Opt.*, vol. 67, no. 7, pp. 628–637, 2020, doi: 10.1080/09500340.2020.1760954.
- [2.140] Z. Xing, W. Fan, D. Huang, H. Cheng, and G. Xia, “High laser damage threshold liquid crystal optical switch based on a gallium nitride transparent electrode,” *Opt. Lett.*, vol. 45, no. 13, p. 3537, Jul. 2020, doi: 10.1364/ol.390440.
- [2.141] L. Xin, D. Xiao, and Q. H. Wang, “Method to suppress speckle noise using time multiplexing in phase-only holographic display,” *J. Soc. Inf. Disp.*, vol. 28, no. 7, pp. 641–647, Jul. 2020, doi: 10.1002/jsid.861.
- [2.142] Z. Kuang, J. Li, S. Edwardson, W. Perrie, D. Liu, and G. Dearden, “Ultrafast laser beam shaping for material processing at imaging plane by geometric masks using a spatial light modulator,” *Opt. Lasers Eng.*, vol. 70, pp. 1–5, 2015, doi: 10.1016/j.optlaseng.2015.02.004.
- [2.143] J. Ochsner, “Surgical knife,” in *Texas Heart Institute Journal*, 2009, vol. 36, no. 5, pp. 441–443. Accessed: Jul. 29, 2020. [Online]. Available: <http://www.ncbi.nlm.nih.gov/pubmed/19876423>
- [2.144] “The Medical Works of Hippocrates: A New Translation from the Original Greek Made Especially for English Readers,” *J. Am. Med. Assoc.*, vol. 147, no. 15, p. 1506, Dec. 1951, doi: 10.1001/jama.1951.03670320106045.
- [2.145] M. Parker, “Detachable-blade knife..” May 18, 1915 Accessed: Jul. 29, 2020. [Online]. Available: <https://patents.google.com/patent/US1139796A/en>
- [2.146] A. E. S. El Askary, *Fundamentals of Esthetic Implant Dentistry*. John Wiley & Sons, 2008. doi: 10.1002/9780470376423.
- [2.147] N. Sharma and S. Dev Sachdeva, “A Comparative Study of Electro-Surgery & Scalpel Surgery,” vol. 05, 2012, Accessed: Nov. 01, 2017. [Online]. Available: <http://oaji.net/articles/2014/1143-1412673099.pdf>
- [2.148] B. Kadyan, S. Chavan, M. Mann, P. Punia, and S. Tekade, “A prospective study comparing diathermy and steel scalpel in abdominal incisions,” *Med. J. Dr. D.Y. Patil Univ.*, vol. 7, no. 5, pp. 558–563, 2014, doi: 10.4103/0975-2870.140382.
- [2.149] S. R. Kearns, E. M. Connolly, S. McNally, D. A. McNamara, and J. Deasy, “Randomized clinical trial of diathermy versus scalpel incision in elective midline laparotomy,” *Br. J. Surg.*, vol. 88, no. 1, pp. 41–44, Jan. 2001, doi: 10.1046/j.1365-2168.2001.01625.x.
- [2.150] “Ultrafast Mid-IR Laser Scalpel Leaves Tiny Scars | Research Technology | Oct 2010 | Photonics.com.” https://www.photonics.com/a44468/Ultrafast_Mid-IR_Laser_Scalpel_Leaves_Tiny_Scars_ (accessed May 16, 2018).
- [2.151] W. Kaiser, “Johann Gottlieb Krüger (1715-1759) and Christian Gottlieb Kratzenstein (1723-1795) as originators of modern electrotherapy.,” *Zahn. Mund. Kieferheilkd. Zentralbl.*, vol. 65, no. 5, pp. 539–54, Jan. 1977, Accessed: Jul. 29, 2020. [Online]. Available: <http://www.ncbi.nlm.nih.gov/pubmed/143842>
- [2.152] J. L. O’Connor and D. A. Bloom, “William T. Bovie and electrosurgery.,” *Surgery*, vol. 119, no. 4, pp. 390–396, Apr. 1996, doi: 10.1016/S0039-6060(96)80137-1.
- [2.153] H. Cushing, W. T. Bovie, and S. P. C. of Chicago, *Electro-surgery as an Aid to the Removal of Intracranial Tumors: With a Preliminary Note on a New Surgical Current Generator*, vol. 47. Chicago: Surgical Pub. Co., 1928. Accessed: Jul. 29, 2020. [Online]. Available: <http://books.google.com/books?id=cX3XGwAACAAJ>
- [2.154] B. L. Hainer, “Fundamentals of electrosurgery.,” *J. Am. Board Fam. Pract.*, vol. 4, no. 6, pp. 419–426, 1991, doi: 10.3122/jabfm.4.6.419.
- [2.155] C. J. Slager, J. C. H. Schuurbijs, J. A. F. Oomen, and N. Bom, “Electrical nerve and muscle stimulation by radio frequency surgery: role of direct current loops around the active electrode,” *Biomed. Eng. IEEE Trans.*, vol. 40, no. 2, pp. 182–187, 1993.

- [2.156] I. Alkatout, T. Schollmeyer, N. A. Hawaldar, N. Sharma, and L. Mettler, "Principles and safety measures of electrosurgery in laparoscopy," *Journal of the Society of Laparoendoscopic Surgeons*, vol. 16, no. 1. Society of Laparoscopic & Robotic Surgeons, pp. 130–139, Jan. 2012. doi: 10.4293/108680812X13291597716348.
- [2.157] "XcelLance Medical Technologies Pvt. Ltd. Leader in Manufacturing of SHALYA Brand Electro Surgery, Vessel Sealing, Saline Plasma Bipolar Resection units." <http://www.xcellancetech.com/ClinicalEducation.html> (accessed May 16, 2018).
- [2.158] J. M. Davison and N. M. Zamah, "Electrosurgery: Principles, Biologic Effects and Results in Female Reproductive Surgery," *Glob. Libr. Women's Med.*, 2009, doi: 10.3843/ glowm.10021.
- [2.159] B. L. Hainer and R. B. Usatine, "Electrosurgery for the skin," *Am. Fam. Physician*, vol. 66, no. 7, pp. 1259–1266, Oct. 2002, Accessed: Aug. 06, 2020. [Online]. Available: www.aafp.org/afp/AMERICANFAMILYPHYSICIAN1259
- [2.160] D. L. Carr-Locke and J. Day, "Principles of Electrosurgery," in *Successful Training in Gastrointestinal Endoscopy*, 2011, pp. 125–134. doi: 10.1002/9781444397772.ch11.
- [2.161] A. Taheri, P. Mansoori, L. F. Sandoval, S. R. Feldman, D. Pearce, and P. M. Williford, "Electrosurgery: Part II. Technology, applications, and safety of electrosurgical devices," *Journal of the American Academy of Dermatology*, vol. 70, no. 4. Mosby Inc., pp. 607.e1-607.e12, Apr. 01, 2014. doi: 10.1016/j.jaad.2013.09.055.
- [2.162] S. Humphries, R. C. Platt, and T. P. Ryan, "Finite-element codes to model electrical heating and non-linear thermal transport in biological media," *Am. Soc. Mech. Eng. Bioeng. Div. BED*, vol. 37, pp. 131–134, 1997.
- [2.163] S. Humphries, K. Johnson, K. Rick, Z. Liu, and S. N. Goldberg, "Three-dimensional finite-element code for electrosurgery and thermal ablation simulations (Invited Paper)," in *Thermal Treatment of Tissue: Energy Delivery and Assessment III*, Apr. 2005, vol. 5698, p. 181. doi: 10.1117/12.591055.
- [2.164] Z. Liu, M. Ahmed, Y. Weinstein, M. Yi, R. L. Mahajan, and S. N. Goldberg, "Characterization of the RF ablation-induced 'oven effect': The importance of background tissue thermal conductivity on tissue heating," *Int. J. Hyperth.*, vol. 22, no. 4, pp. 327–342, Jan. 2006, doi: 10.1080/02656730600609122.
- [2.165] Z. Liu, M. Ahmed, A. Sabir, S. Humphries, and S. N. Goldberg, "Computer modeling of the effect of perfusion on heating patterns in radiofrequency tumor ablation," *Int. J. Hyperth.*, vol. 23, no. 1, pp. 49–58, Jan. 2007, doi: 10.1080/02656730601094415.
- [2.166] A. Taheri, P. Mansoori, L. F. Sandoval, S. R. Feldman, D. Pearce, and P. M. Williford, "Electrosurgery: Part I. Basics and principles," *Journal of the American Academy of Dermatology*, vol. 70, no. 4. Mosby, pp. 591.e1-591.e14, Apr. 01, 2014. doi: 10.1016/j.jaad.2013.09.056.
- [2.167] C. C. Nduka, P. A. Super, J. R. T. Monson, and A. W. Darzi, "Cause and prevention of electrosurgical injuries in laparoscopy," *J. Am. Coll. Surg.*, vol. 179, no. 2, pp. 161–170, Aug. 1994, Accessed: Jul. 29, 2020. [Online]. Available: <https://europepmc.org/article/med/8044385>
- [2.168] "Electrosurgery Intervention in Flexible Endoscopy ---Managing Safety." <http://slideplayer.com/slide/6057467/> (accessed May 16, 2018).
- [2.169] S. A. Loh, G. A. Carlson, E. I. Chang, E. Huang, D. Palanker, and G. C. Gurtner, "Comparative Healing of Surgical Incisions Created by the PEAK PlasmaBlade, Conventional Electrosurgery, and a Scalpel," *Plast. Reconstr. Surg.*, vol. 124, no. 6, pp. 1849–1859, Dec. 2009, doi: 10.1097/PRS.0b013e3181bcee87.
- [2.170] L. D. Prakash, N. Balaji, S. S. Kumar, and V. Kate, "Comparison of electrocautery incision with scalpel incision in midline abdominal surgery - A double blind randomized controlled trial," *Int. J. Surg.*, vol. 19, pp. 78–82, Jul. 2015, doi: 10.1016/j.ijso.2015.04.085.
- [2.171] K. Charoenkwan, Z. Iheozor-Ejiofor, K. Rerkasem, and E. Matovinovic, "Scalpel versus electrosurgery for major abdominal incisions," *Cochrane Database Syst. Rev.*, vol. 2017, no. 6, p. CD005987, Jun. 2017, doi: 10.1002/14651858.CD005987.pub3.
- [2.172] A. A. Luciano, J. Randolph, G. Whitman, R. Maenza, and D. B. Maier, "A comparison of thermal injury, healing patterns, and postoperative adhesion formation following CO2 laser and electromicrosurgery," *Fertil. Steril.*, vol. 48, no. 6, pp. 1025–1029, Dec. 1987, doi: 10.1016/S0015-0282(16)59603-4.
- [2.173] M. P. Goldman, R. A. Weiss, H. J. Brody, W. P. Coleman, and R. E. Fitzpatrick, "Treatment of Facial Telangiectasia with Sclerotherapy, Laser Surgery, and/or Electrodesiccation: A Review," *J. Dermatol. Surg. Oncol.*, vol. 19, no. 10, pp. 899–906, Oct. 1993, doi: 10.1111/j.1524-4725.1993.tb00976.x.
- [2.174] S. M. Shapshay, *Endoscopic Laser Surgery Handbook*. Dekker, 2020. doi: 10.1201/9781003065753.
- [2.175] I. N. Ize-Iyamu, B. D. Saheeb, and B. E. Edetanlen, "Comparing the 810nm diode laser with

- conventional surgery in orthodontic soft tissue procedures.,” *Ghana Med. J.*, vol. 47, no. 3, pp. 107–111, 2013, Accessed: Aug. 07, 2020. [Online]. Available: [/pmc/articles/PMC3875278/?report=abstract](https://pubmed.ncbi.nlm.nih.gov/3875278/)
- [2.176] M. Garashi, “Comparing the Efficacy of Scalpel, Electrosurgical, and Laser Gingivectomies for the Management of Gingival Enlargement Following Orthodontic Therapy,” *Student Theses, Diss. Capstones*, Jan. 2018, Accessed: Aug. 07, 2020. [Online]. Available: https://nsuworks.nova.edu/hpd_cdm_stuetd/83
- [2.177] E. B. Silverman, R. W. Read, C. R. Boyle, R. Cooper, W. W. Miller, and R. M. McLaughlin, “Histologic Comparison of Canine Skin Biopsies Collected Using Monopolar Electrosurgery, CO₂ Laser, Radiowave Radiosurgery, Skin Biopsy Punch, and Scalpel,” *Vet. Surg.*, vol. 36, no. 1, pp. 50–56, Jan. 2007, doi: 10.1111/j.1532-950X.2007.00234.x.
- [2.178] G. J. Christensen, “Soft-tissue cutting with laser versus electrosurgery.,” *J. Am. Dent. Assoc.*, vol. 139, no. 7, pp. 981–4, Jul. 2008, doi: 10.14219/JADA.ARCHIVE.2008.0286.
- [2.179] B. J. Wiatrak and J. P. Willging, “Harmonic scalpel for tonsillectomy,” *Laryngoscope*, vol. 112, no. 8, pp. 14–16, Oct. 2002, doi: 10.1002/lary.5541121406.
- [2.180] “Bloodless medicine glossary | Baltimore Washington Medical Center.” <https://www.mybwmc.org/library/28/000205> (accessed Oct. 24, 2017).
- [2.181] Rahul and S. De, “A multi-physics model for ultrasonically activated soft tissue,” *Comput. Methods Appl. Mech. Eng.*, vol. 314, pp. 71–84, Feb. 2017, doi: 10.1016/j.cma.2016.07.026.
- [2.182] N. Družijanić, Z. Pogorelić, Z. Perko, I. Mrklič, and S. Tomić, “Comparison of lateral thermal damage of the human peritoneum using monopolar diathermy, Harmonic scalpel and LigaSure,” *Can. J. Surg.*, vol. 55, no. 5, pp. 317–321, 2012, doi: 10.1503/cjs.000711.
- [2.183] S. D. McCarus, “Physiologic mechanism of the ultrasonically activated scalpel,” *J. Am. Assoc. Gynecol. Laparosc.*, vol. 3, no. 4, pp. 601–608, Aug. 1996, doi: 10.1016/S1074-3804(05)80174-4.
- [2.184] A. Sarkar, D. B. Choksi, A. Sutaria, and M. Sindhal, “Harmonic scalpel versus bipolar diathermy in Milligan-Morgan haemorrhoidectomy: a randomized controlled study,” *Int. Surg. J.*, vol. 5, no. 7, p. 2507, Jun. 2018, doi: 10.18203/2349-2902.isj20182763.
- [2.185] A. A. Abo-hashem, A. Sarhan, and A. M. Aly, “Harmonic Scalpel® compared with bipolar electro-cautery hemorrhoidectomy: A randomized controlled trial,” *Int. J. Surg.*, vol. 8, no. 3, pp. 243–247, Jan. 2010, doi: 10.1016/j.ijisu.2010.01.010.
- [2.186] D. M. Hoenig, C. A. Chrostek, and J. F. Amaral, “Laparoscopic Coagulating Shears: Alternative Method of Hemostatic Control of Unsupported Tissue,” *J. Endourol.*, vol. 10, no. 5, pp. 431–433, Oct. 1996, doi: 10.1089/end.1996.10.431.
- [2.187] H. Bulus, A. Tas, A. Coskun, and M. Kucukazman, “Evaluation of two hemorrhoidectomy techniques: Harmonic scalpel and Ferguson’s with electrocautery,” *Asian J. Surg.*, vol. 37, no. 1, pp. 20–23, Jan. 2014, doi: 10.1016/j.asjsur.2013.04.002.
- [2.188] D. R. Lim, D. H. Cho, J. H. Lee, and J. H. Moon, “Comparison of a hemorrhoidectomy with ultrasonic scalpel versus a conventional hemorrhoidectomy,” *Ann. Coloproctol.*, vol. 32, no. 3, pp. 111–116, Jun. 2016, doi: 10.3393/ac.2016.32.3.111.
- [2.189] M. Bajpai, “Technique of ‘suture less’ appendicectomy by laparoscopy in children: Preliminary communication,” *J. Indian Assoc. Pediatr. Surg.*, vol. 19, no. 1, pp. 28–30, 2014, doi: 10.4103/0971-9261.125956.
- [2.190] “A randomized controlled study comparing harmonic versus electrosurgery in laparoscopic myomectomy,” *Fertil. Steril.*, vol. 94, no. 5, pp. 1882–1886, Oct. 2010, doi: 10.1016/J.FERTNSTERT.2009.08.049.
- [2.191] P. Mittal, A. Kumar, S. Kaur, P. Pandove, R. Singla, and J. Singh, “A comparative study of the use of harmonic scalpel versus unipolar cautery in modified radical mastectomy,” *Niger. J. Surg.*, vol. 23, no. 1, pp. 20–25, 2017, doi: 10.4103/1117-6806.199962.
- [2.192] I. Kuhajda *et al.*, “Electric vs. harmonic scalpel in treatment of primary focal hyperhidrosis with thoracoscopic sympathectomy,” *Ann. Transl. Med.*, vol. 3, no. 15, 2015, doi: 10.3978/j.issn.2305-5839.2015.09.01.
- [2.193] D. K. Dutta and I. Dutta, “The Harmonic Scalpel.,” *J. Obstet. Gynaecol. India*, vol. 66, no. 3, pp. 209–10, Jun. 2016, doi: 10.1007/s13224-016-0850-x.
- [2.194] C. M. Cilip *et al.*, “Infrared laser thermal fusion of blood vessels: preliminary ex vivo tissue studies,” *J. Biomed. Opt.*, vol. 18, no. 5, p. 058001, May 2013, doi: 10.1117/1.JBO.18.5.058001.
- [2.195] D. F. Hanby *et al.*, “Harmonic scalpel versus flexible CO₂ laser for tongue resection: A histopathological analysis of thermal damage in human cadavers,” *World J. Surg. Oncol.*, vol. 9, no. 1, p. 83, Aug. 2011, doi: 10.1186/1477-7819-9-83.
- [2.196] C. Patil, N. Srinath, U. DN, and M. Kumar, “Comparative Study of Diode Laser versus Diathermy in Soft Tissue Surgical Procedures of Oral Cavity,” *J. Adv. Med. Med. Res.*, vol. 32, no. 4, pp. 104–111, Mar. 2020, doi: 10.9734/jammr/2020/v32i430406.

- [2.197] L. Kotlow, "Laser ankyloglossia release: Implications for maxillomandibular growth," *Semin. Orthod.*, Jun. 2020, doi: 10.1053/j.sodo.2020.06.004.
- [2.198] R. J. Lanzafame, "Laser/light applications in general surgery," in *Lasers in Dermatology and Medicine*, vol. 9780857292810, Springer-Verlag London Ltd, 2012, pp. 539–559. doi: 10.1007/978-0-85729-281-0_43.
- [2.199] P. Janda, R. Sroka, C. S. Betz, R. Baumgartner, and A. Leunig, "Comparison of laser induced effects on hyperplastic inferior nasal turbinates by means of scanning electron microscopy," *Lasers Surg. Med.*, vol. 30, no. 1, pp. 31–39, Jan. 2002, doi: 10.1002/lsm.10020.
- [2.200] V. C. Wright, "Laser surgery: using the carbon dioxide laser," *Can. Med. Assoc. J.*, vol. 126, no. 9, pp. 1035–1039, May 1982, [Online]. Available: <http://www.cmaj.ca/content/126/9/1035.abstract>
- [2.201] B. Wozniak and J. Dera, *Light absorption in sea water*, vol. 33. 2007. doi: 10.1007/978-0-387-49560-6.
- [2.202] E. V Zharikov *et al.*, "Stimulated emission from Er 3+ ions in yttrium aluminum garnet crystals at $\lambda = 2.94 \mu$," *Sov. J. Quantum Electron.*, vol. 4, no. 8, pp. 1039–1040, Aug. 1975, doi: 10.1070/qe1975v004n08abeh011147.
- [2.203] "Soft Tissue Cutting with CO2, Diode Lasers." <https://www.aesculight.com/case-studies/soft-tissue-cutting-with-co2-diode-lasers/> (accessed May 24, 2018).
- [2.204] R. E. Windsor, "Arthroscopic Laser Surgery.," *J. Bone Jt. Surg.*, vol. 77, no. 9, p. 1469, 1995, doi: 10.2106/00004623-199509000-00027.
- [2.205] G. J. Jako, "Laser surgery of the vocal cords: An experimental study with carbon dioxide lasers on dogs," *Laryngoscope*, vol. 82, no. 12, pp. 2204–2216, Dec. 1972, doi: 10.1288/00005537-197212000-00009.
- [2.206] M. S. Strong and G. J. Jako, "Laser surgery in the larynx. Early clinical experience with continuous CO 2 laser.," *Ann. Otol. Rhinol. Laryngol.*, vol. 81, no. 6, pp. 791–798, 1972.
- [2.207] R. H. Ossoff, J. A. Coleman, M. S. Courey, J. A. Duncavage, J. A. Werkhaven, and L. Reinisch, "Clinical applications of lasers in otolaryngology--head and neck surgery.," *Lasers Surg. Med.*, vol. 15, no. 3, pp. 217–48, 1994, Accessed: May 21, 2018. [Online]. Available: <http://www.ncbi.nlm.nih.gov/pubmed/7830468>
- [2.208] I. Kaplan, J. Goldman, and R. Ger, "The treatment of erosions of the uterine cervix," *Obstet. Gynecol.*, vol. 41, no. 5, pp. 795–796, 1973, Accessed: Oct. 19, 2017. [Online]. Available: http://journals.lww.com/greenjournal/Citation/1973/05000/THE_TREATMENT_OF_EROSION_S_OF_THE_UTERINE_CERVIX_BY.29.aspx
- [2.209] A. Staffl, E. J. Wilkinson, and R. F. Mattingly, "Laser treatment of cervical and vaginal neoplasia.," *Am. J. Obstet. Gynecol.*, vol. 128, no. 2, pp. 128–36, May 1977, doi: 10.1016/0002-9378(77)90676-7.
- [2.210] J. H. Bellina and G. Bandieramonte, "Principles and Practice of Gynecologic Laser Surgery.," 1984, Accessed: Oct. 19, 2017. [Online]. Available: <https://books.google.co.uk/books?id=QEnTBwAAQBAJ&pg=PA109&lpg=PA109&dq=Gynecology+and+the+laser+1974&source=bl&ots=U1toG8kszJ&sig=hgAVJgwudR-53Yjr7gZc0vnoG6I&hl=en&sa=X&ved=0ahUKEwj87fzl5fzWAhV11xoKHejEAdwQ6AEIKDAB#v=onepage&q=Gynecology and the laser 197>
- [2.211] A. Urich, R. R. J. Maier, F. Yu, J. C. Knight, D. P. Hand, and J. D. Shephard, "Flexible delivery of Er:YAG radiation at 2.94 μ m with negative curvature silica glass fibers: a new solution for minimally invasive surgical procedures.," *Biomed. Opt. Express*, vol. 4, no. 2, pp. 193–205, Feb. 2013, doi: 10.1364/BOE.4.000193.
- [2.212] J. T. Walsh, T. J. Flotte, and T. F. Deutsch, "Er:YAG laser ablation of tissue: Effect of pulse duration and tissue type on thermal damage," *Lasers Surg. Med.*, vol. 9, no. 4, pp. 314–326, 1989, doi: 10.1002/lsm.1900090403.
- [2.213] U. Hohenleutner, S. Hohenleutner, W. Bäuml, and M. Landthaler, "Fast and effective skin ablation with an Er:YAG laser: Determination of ablation rates and thermal damage zones," *Lasers Surg. Med.*, vol. 20, no. 3, pp. 242–247, Jan. 1997, doi: 10.1002/(SICI)1096-9101(1997)20:3<242::AID-LSM2>3.0.CO;2-Q.
- [2.214] J. P. Minton, "The laser in surgery. A 23 year perspective," *Am. J. Surg.*, vol. 151, no. 6, pp. 725–729, Jun. 1986, doi: 10.1016/0002-9610(86)90052-8.
- [2.215] S. A. Boppart, J. Herrmann, C. Pitris, D. L. Stamper, M. E. Brezinski, and J. G. Fujimoto, "High-resolution optical coherence tomography-guided laser ablation of surgical tissue," *J. Surg. Res.*, vol. 82, no. 2, pp. 275–284, Apr. 1999, doi: 10.1006/jsre.1998.5555.
- [2.216] S. Andreana DDS *et al.*, "Laser Energy in Oral Soft Tissue Applications," *J. Laser Dent. J Laser Dent*, vol. 2018, no. 23, pp. 123–131, 2012, Accessed: Dec. 06, 2017. [Online]. Available: https://www.laserdentistry.org/uploads/files/members/jld/JLD_20_2/JLD_20_2_PositionPaper_Soft_Tissue_Applications.pdf

- [2.217] F. Stelzle *et al.*, “The impact of laser ablation on optical soft tissue differentiation for tissue specific laser surgery-an experimental ex vivo study,” *J. Transl. Med.*, vol. 10, no. 1, 2012, doi: 10.1186/1479-5876-10-123.
- [2.218] I. M. Varkarakis *et al.*, “Comparison of erbium:yttrium-aluminum-garnet and holmium:yttrium-aluminum-garnet lasers for incision of urethra and bladder neck in an in vivo Porcine model,” *Urology*, vol. 65, no. 1, pp. 191–195, Jan. 2005, doi: 10.1016/j.urology.2004.09.020.
- [2.219] P. Kiefhaber, K. Kiefhaber, and F. Huber, “Preoperative neodymium-YAG laser treatment of obstructive colon cancer,” *Endoscopy*, vol. 18, no. SUPPL. 1, pp. 44–46, 1986, doi: 10.1055/s-2007-1018408.
- [2.220] P. Kiefhaber, F. Huber, and K. Kiefhaber, “Palliative and pre-operative endoscopic neodymium-YAG laser treatment of colorectal carcinoma,” *Endoscopy*, vol. 19, no. SUPPL. 1, pp. 43–46, 1987, doi: 10.1055/s-2007-1018308.
- [2.221] M. Suguro, T. Hasegawa, S. Suzuki, and F. Hanyu, “Clinical evaluation of laser endoscopy for the treatment of gastric tumors,” *Surg. Endosc.*, vol. 1, no. 3, pp. 131–138, Sep. 1987, doi: 10.1007/BF00590917.
- [2.222] T. Schroder, K. Brackett, and S. N. Joffe, “An experimental study of the effects of electrocautery and various lasers on gastrointestinal tissue,” *Surgery*, vol. 101, no. 6, pp. 691–697, Jun. 1987, doi: 10.5555/uri:pii:0039606087900821.
- [2.223] D. E. Low, R. A. Kozarek, T. J. Ball, D. J. Patterson, and L. D. Hill, “Colorectal Neodymium-YAG Photoablative Therapy: Comparing Applications and Complications on Both Sides of the Peritoneal Reflection,” *Arch. Surg.*, vol. 124, no. 6, pp. 684–688, Jun. 1989, doi: 10.1001/archsurg.1989.01410060046010.
- [2.224] G. W. Daneker, G. W. Carlson, D. C. Hohn, P. Lynch, L. Roubein, and B. Levin, “Endoscopic Laser Recanalization Is Effective for Prevention and Treatment of Obstruction in Sigmoid and Rectal Cancer,” *Arch. Surg.*, vol. 126, no. 11, pp. 1348–1352, Nov. 1991, doi: 10.1001/archsurg.1991.01410350038006.
- [2.225] A. M. Gevers, E. Macken, M. Hiele, and P. Rutgeerts, “Endoscopic laser therapy for palliation of patients with distal colorectal carcinoma: Analysis of factors influencing long-term outcome,” *Gastrointest. Endosc.*, vol. 51, no. 5, pp. 580–585, May 2000, doi: 10.1016/S0016-5107(00)70294-X.
- [2.226] H.-S. Oh and J.-S. Kim, “Clinical Application of CO₂ Laser,” *CO₂ Laser - Optim. Appl.*, Mar. 2012, doi: 10.5772/38469.
- [2.227] Q. Peng *et al.*, “Laser light delivery systems for medical applications,” *Phys. Med. Biol. Phys. Med. Biol.*, vol. 42, no. 42, pp. 869–869, 1997, Accessed: Oct. 19, 2017. [Online]. Available: <http://iopscience.iop.org/article/10.1088/0031-9155/42/5/010/pdf>
- [2.228] I. Kaplan and S. Giler, *CO₂ Laser Surgery*. Springer Berlin Heidelberg, 1984. Accessed: Oct. 19, 2017. [Online]. Available: https://books.google.co.uk/books?id=ZDQrBAAAQBAJ&pg=PP3&lpg=PP3&dq=Kaplan+1984+CO2+laser+surgery&source=bl&ots=nMUyOg8SDh&sig=0jTL_gwCVA4o9g8JPBPss4X-PFA&hl=en&sa=X&ved=0ahUKEwjtxYn3jP3WAhUsDMAKHVr_BRcQ6AEINTAE#v=onepage&q=Kaplan+1984+CO2+laser+surgery&f=false
- [2.229] Tichindelean Teodor, “Novel Optical Fiber Applications: Hollow glass fiber for CO₂ laser surgery has coincident aiming beam - Laser Focus World,” 2015. <https://www.laserfocusworld.com/articles/2015/07/novel-optical-fiber-applications-hollow-glass-fiber-for-co2-laser-surgery-has-coincident-aiming-beam.html> (accessed Jul. 23, 2018).
- [2.230] G. Stevens, “Erbium:YAG laser cataract removal: Role of fiber-optic delivery system,” *J. Cataract Refract. Surg.*, vol. 25, no. 4, pp. 514–520, 1999, doi: 10.1016/s0886-3350(99)80048-0.
- [2.231] N. M. Fried, “New technologies in endourology: Potential applications of the erbium:YAG laser in endourology,” *J. Endourol.*, vol. 15, no. 9, pp. 889–894, Nov. 2001, doi: 10.1089/089277901753284080.
- [2.232] N. M. Fried, Z. Tesfaye, A. M. Ong, K. H. Rha, and P. Hejazi, “Optimization of the Erbium:YAG laser for precise incision of ureteral and urethral tissues: In vitro and in vivo results,” *Lasers Surg. Med.*, vol. 33, no. 2, pp. 108–114, Aug. 2003, doi: 10.1002/lsm.10205.
- [2.233] J. Raif, M. Vardi, O. Nahlieli, and I. Gannot, “An Er:YAG laser endoscopic fiber delivery system for lithotripsy of salivary stones,” *Lasers Surg. Med.*, vol. 38, no. 6, pp. 580–587, Jul. 2006, doi: 10.1002/lsm.20344.
- [2.234] N. J. Scott *et al.*, “Mid-IR Germanium oxide fibers for contact erbium laser tissue ablation in endoscopic surgery,” *IEEE J. Sel. Top. Quantum Electron.*, vol. 13, no. 6, pp. 1709–1714, Nov. 2007, doi: 10.1109/JSTQE.2007.910557.
- [2.235] C. A. Chaney, Y. Yang, and N. M. Fried, “Hybrid Germanium/Silica Optical Fibers for Endoscopic Delivery of Erbium:YAG Laser Radiation,” *Lasers Surg. Med.*, vol. 34, no. 1, pp. 5–11, 2004, doi: 10.1002/lsm.10249.

- [2.236] A. Zarrabi and A. J. Gross, "The evolution of lasers in urology," *Therapeutic Advances in Urology*, vol. 3, no. 2. pp. 81–89, 2011. doi: 10.1177/1756287211400494.
- [2.237] L. M. Beltran Bernal, F. Canbaz, N. Friederich, P. Cattin, and A. Zam, "Measurements of coupling efficiency of high power Er:YAG laser in different types of optical fibers," in *Optical Fibers and Sensors for Medical Diagnostics and Treatment Applications XX*, Feb. 2020, vol. 11233, p. 52. doi: 10.1117/12.2546048.
- [2.238] A. V. V. Nampoothiri *et al.*, "Hollow-core Optical Fiber Gas Lasers (HOFGLAS): a review [Invited]," *Opt. Mater. Express*, vol. 2, no. 7, p. 948, 2012, doi: 10.1364/ome.2.000948.
- [2.239] J. L. Ochsner, "Minimally invasive surgical procedures.," *Ochsner J.*, vol. 2, no. 3, pp. 135–6, Jul. 2000, Accessed: Nov. 28, 2017. [Online]. Available: <http://www.ncbi.nlm.nih.gov/pubmed/21765681>
- [2.240] H. Hu, "Multi-slice helical CT: scan and reconstruction.," *Med. Phys.*, vol. 26, no. 1, pp. 5–18, 1999, doi: 10.1118/1.598470.
- [2.241] D. Le Bihan, C. Poupon, A. Amadon, and F. Lethimonnier, "Artifacts and pitfalls in diffusion MRI," *Journal of Magnetic Resonance Imaging*, vol. 24, no. 3. pp. 478–488, 2006. doi: 10.1002/jmri.20683.
- [2.242] N. MacLeod, *Practical Radiotherapy Planning*, vol. 55, no. 1. 2010. doi: 10.1258/rsmmj.55.1.29.
- [2.243] T. A. Gaskin, J. H. Isobe, J. L. Mathews, S. B. Winchester, and R. J. Smith, "Laparoscopy and the general surgeon," *Surg. Clin. North Am.*, vol. 71, no. 5, pp. 1085–1097, Oct. 1991, doi: 10.1016/S0039-6109(16)45536-2.
- [2.244] J. H. Peters *et al.*, "Safety and efficacy of laparoscopic cholecystectomy: A Prospective analysis of 100 initial patients," *Ann. Surg.*, vol. 213, no. 1, pp. 3–12, 1991, doi: 10.1097/00000658-199101000-00002.
- [2.245] S. A. Darzi and Y. Munz, "The impact of minimally invasive surgical techniques.," *Annu. Rev. Med.*, vol. 55, pp. 223–237, 2004, doi: 10.1146/annurev.med.55.091902.105248.
- [2.246] H. H. Hopkins and N. S. Kapany, "A flexible fibrescope, using static scanning," *Nature*, vol. 173, no. 4392. Nature Publishing Group, pp. 39–41, 1954. doi: 10.1038/173039b0.
- [2.247] R. Glasgow, K. Adamson, and S. Mulvihill, "The benefits of a dedicated minimally invasive surgery program to academic general surgery practice," *J. Gastrointest. Surg.*, vol. 8, no. 7, pp. 869–873, Nov. 2004, doi: 10.1016/j.gassur.2004.08.002.
- [2.248] A. Sood *et al.*, "Minimally invasive surgery and its impact on 30-day postoperative complications, unplanned readmissions and mortality," *Br. J. Surg.*, vol. 104, no. 10, pp. 1372–1381, Sep. 2017, doi: 10.1002/bjs.10561.
- [2.249] J. E. Brazier and A. G. Johnson, "Economics of surgery.," *Lancet (London, England)*, vol. 358, no. 9287, pp. 1077–81, Sep. 2001, doi: 10.1016/S0140-6736(01)06185-2.
- [2.250] A. M. H. Alfawal, M. Y. Hajeer, M. A. Ajaj, O. Hamadah, and B. Brad, "Effectiveness of minimally invasive surgical procedures in the acceleration of tooth movement: a systematic review and meta-analysis," *Progress in Orthodontics*, vol. 17, no. 1. 2016. doi: 10.1186/s40510-016-0146-9.
- [2.251] R. W. Waynant, I. K. Ilev, and I. Gannot, "Mid-infrared laser applications in medicine and biology," *Philos. Trans. R. Soc. London. Ser. A Math. Phys. Eng. Sci.*, vol. 359, no. 1780, pp. 635–644, Mar. 2001, doi: 10.1098/rsta.2000.0747.
- [2.252] A. Frega *et al.*, "Feasibility of office CO2 laser surgery in patients affected by benign pathologies and congenital malformations of female lower genital tract," *Eur. Rev. Med. Pharmacol. Sci.*, vol. 19, no. 14, pp. 2528–2536, 2015, Accessed: Nov. 21, 2017. [Online]. Available: <http://www.ncbi.nlm.nih.gov/pubmed/26221878>
- [2.253] G. N. Merberg, "Current status of infrared fiber optics for medical laser power delivery," *Lasers Surg. Med.*, vol. 13, no. 5, pp. 572–576, Jan. 1993, doi: 10.1002/lsm.1900130513.
- [2.254] A. Urich, R. R. J. Maier, F. Yu, J. C. Knight, D. P. Hand, and J. D. Shephard, "Silica hollow core microstructured fibres for mid-infrared surgical applications," *J. Non. Cryst. Solids*, vol. 377, pp. 236–239, Oct. 2013, doi: 10.1016/j.jnoncrsol.2013.01.055.
- [2.255] W. Chai, Q. Zhao, H. Song, C. Cheng, G. Tian, and T. Jiang, "Treatment response and preliminary efficacy of hepatic tumour laser ablation under the guidance of percutaneous and endoscopic ultrasonography," *World J. Surg. Oncol.*, vol. 17, no. 1, Aug. 2019, doi: 10.1186/s12957-019-1677-6.
- [2.256] T. Jiang *et al.*, "EUS dating with laser ablation against the caudate lobe or left liver tumors: a win-win proposition?," *Cancer Biol. Ther.*, vol. 19, no. 3, pp. 145–152, Mar. 2018, doi: 10.1080/15384047.2017.1414760.
- [2.257] F. Di Matteo *et al.*, "EUS-guided Nd:YAG laser ablation of a hepatocellular carcinoma in the caudate lobe," *Gastrointest. Endosc.*, vol. 73, no. 3, pp. 632–636, Mar. 2011, doi: 10.1016/j.gie.2010.08.019.

- [2.258] D. Enikeev *et al.*, “Impact of endoscopic enucleation of the prostate with thulium fiber laser on the erectile function,” *BMC Urol.*, vol. 18, no. 1, p. 87, Oct. 2018, doi: 10.1186/s12894-018-0400-1.
- [2.259] G. G. Hamad and M. Curet, “Minimally invasive surgery,” *American Journal of Surgery*, vol. 199, no. 2. Elsevier, pp. 263–265, Feb. 01, 2010. doi: 10.1016/j.amjsurg.2009.05.008.
- [2.260] K. H. Fuchs, “Minimally Invasive Surgery,” *Endoscopy*, vol. 34, no. 2, pp. 154–159, Feb. 2002, doi: 10.1055/s-2002-19857.
- [2.261] T. Lee, N. Mendhiratta, D. Sperling, and H. Lepor, “Focal laser ablation for localized prostate cancer: principles, clinical trials, and our initial experience.,” *Rev. Urol.*, vol. 16, no. 2, pp. 55–66, 2014, Accessed: Nov. 28, 2017. [Online]. Available: <http://www.ncbi.nlm.nih.gov/pubmed/25009445>
- [2.262] H. G. Je, D. J. Shuman, and N. Ad, “A systematic review of minimally invasive surgical treatment for atrial fibrillation: a comparison of the Cox-Maze procedure, beating-heart epicardial ablation, and the hybrid procedure on safety and efficacy,” *Eur. J. Cardio-Thoracic Surg.*, vol. 48, no. 4, pp. 531–541, Oct. 2015, doi: 10.1093/ejcts/ezu536.
- [2.263] T. ; Udiljak, D. & Ciglar, and S. Skoric, “Investigation Into Bone Drilling and Thermal Bone Necrosis,” *Adv. Prod. Eng. Manag.*, vol. 2, no. 3, pp. 103–112, 2007, Accessed: May 25, 2018. [Online]. Available: http://apem-journal.org/Archives/2007/APEM2-3_103-112.pdf
- [2.264] R. G. McCaughey, H. Sun, V. S. Rothholtz, T. Juhasz, and B. J. F. Wong, “Femtosecond laser ablation of the stapes,” *J. Biomed. Opt.*, vol. 14, no. 2, p. 024040, 2009, doi: 10.1117/1.3120490.
- [2.265] J. Zhang, K. Guan, Z. Zhang, and Y. Guan, “In vitro evaluation of ultrafast laser drilling large-size holes on sheepshank bone,” *Opt. Express*, vol. 28, no. 17, p. 25528, Aug. 2020, doi: 10.1364/oe.396727.
- [2.266] C. Kerse *et al.*, “Ablation-cooled material removal with ultrafast bursts of pulses,” *Nature*, vol. 537, no. 7618, pp. 84–88, Jul. 2016, doi: 10.1038/nature18619.
- [2.267] S. Antipov, D. D. Hudson, A. Fuerbach, and S. D. Jackson, “High-power mid-infrared femtosecond fiber laser in the water vapor transmission window,” *Optica*, vol. 3, no. 12, p. 1373, 2016, doi: 10.1364/optica.3.001373.
- [2.268] K. E. Donaldson *et al.*, “Femtosecond laser-assisted cataract surgery for the ASCRS Refractive Cataract Surgery Subcommittee,” *J. Cart. Refract. Surg.*, vol. 39, pp. 1753–1763, 2013, doi: 10.1016/j.jcrs.2013.09.002.
- [2.269] W. S. Góra *et al.*, “High precision laser sclerostomy,” Mar. 2015, p. 93071Y. doi: 10.1117/12.2079146.
- [2.270] Q. Sun *et al.*, “In vivo imaging-guided microsurgery based on femtosecond laser produced new fluorescent compounds in biological tissues,” *Biomed. Opt. Express*, vol. 9, no. 2, p. 581, Feb. 2018, doi: 10.1364/boe.9.000581.
- [2.271] H. Lubatschowski, “Ultrafast lasers in ophthalmology,” in *Physics Procedia*, 2010, vol. 5, no. PART 2, pp. 637–640. doi: 10.1016/j.phpro.2010.08.092.
- [2.272] I. Ratkay-Traub, I. E. Ferincz, T. Juhasz, R. M. Kurtz, and R. R. Krueger, “First clinical results with the femtosecond neodymium-glass laser in refractive surgery,” *J. Refract. Surg.*, vol. 19, no. 2, pp. 94–103, Mar. 2003, doi: 10.3928/1081-597X-20030301-03.
- [2.273] H. Lubatschowski *et al.*, “Application of ultrashort laser pulses for intrastromal refractive surgery,” *Graefe’s Arch. Clin. Exp. Ophthalmol.*, vol. 238, no. 1, pp. 33–39, 2000, doi: 10.1007/s004170050006.
- [2.274] E. Chlasta-Twardzik, A. Nowińska, E. Wylęgała, and S. Demircan, “Comparison of the selected parameters of the anterior segment of the eye between femtosecond laser-assisted cataract surgery, microincision cataract surgery, and conventional phacoemulsification: A case-control study,” *Med. (United States)*, vol. 98, no. 52, p. e18340, Dec. 2019, doi: 10.1097/MD.00000000000018340.
- [2.275] J. Gros-Otero *et al.*, “Analysis of corneal stromal roughness after iFS 150 kHz and LenSx femtosecond LASIK flap creation in porcine eyes,” *Graefe’s Arch. Clin. Exp. Ophthalmol.*, vol. 257, no. 12, pp. 2665–2670, 2019, doi: 10.1007/s00417-019-04497-7.
- [2.276] W. Sekundo *et al.*, “First efficacy and safety study of femtosecond lenticule extraction for the correction of myopia. Six-month results,” *J. Cataract Refract. Surg.*, vol. 34, no. 9, pp. 1513–1520, 2008, doi: 10.1016/j.jcrs.2008.05.033.
- [2.277] M. Blum, K. S. Kunert, C. Engelbrecht, J. Dawczynski, and W. Sekundo, “Femtosekunden-Lentikel-Extraktion (FLEX) - Ergebnisse nach 12 Monaten bei myopen Astigmatismus,” *Klin. Monbl. Augenheilkd.*, vol. 227, no. 12, pp. 961–965, 2010, doi: 10.1055/s-0029-1245894.
- [2.278] P. J. Dougherty, K. L. Wellish, and R. K. Maloney, “Excimer laser ablation rate and corneal hydration,” *Am. J. Ophthalmol.*, vol. 118, no. 2, pp. 169–176, 1994, doi: 10.1016/S0002-9394(14)72896-X.
- [2.279] E. Schena, S. Silvestri, G. T. Franzesi, G. Cupo, P. Carito, and E. Ghinelli, “Theoretical model

- and design of a device to reduce the influence of environmental factors on refractive surgery outcomes,” in *Annual International Conference of the IEEE Engineering in Medicine and Biology - Proceedings*, 2006, vol. 2006, pp. 343–346. doi: 10.1109/IEMBS.2006.260184.
- [2.280] V. P. Kankariya, I. Pallikaris, G. Kymionis, and T. Singh, “Newer Technologies for Refractive Surgery: Femtosecond Laser,” in *Current Advances in Ophthalmic Technology*, 2020, pp. 57–68. doi: 10.1007/978-981-13-9795-0_3.
- [2.281] M. H. Goetz, S. K. Fischer, A. Velten, J. F. Bille, and V. Sturm, “Computer-guided laser probe for ablation of brain tumours with ultrashort laser pulses,” *Phys. Med. Biol.*, vol. 44, no. 6, pp. 119–127, 1999, doi: 10.1088/0031-9155/44/6/407.
- [2.282] C. L. Hoy *et al.*, “Clinical ultrafast laser surgery: Recent advances and future directions,” *IEEE J. Sel. Top. Quantum Electron.*, vol. 20, no. 2, 2014, doi: 10.1109/JSTQE.2013.2287098.
- [2.283] H. Wisweh, U. Merkel, A. K. Hurler, K. LiierBen, and H. Lubatschowski, “Optical coherence tomography monitoring of vocal fold femtosecond laser microsurgery,” in *Optics InfoBase Conference Papers*, Jun. 2007, p. 6632_6. doi: 10.1117/12.728139.
- [2.284] C. L. Hoy, W. N. Everett, M. Yildirim, J. Kobler, S. M. Zeitels, and A. Ben-Yakar, “Towards endoscopic ultrafast laser microsurgery of vocal folds,” *J. Biomed. Opt.*, vol. 17, no. 3, p. 038002, 2012, doi: 10.1117/1.jbo.17.3.038002.
- [2.285] T. Lanvin *et al.*, “Subsurface ablation of atherosclerotic plaque using ultrafast laser pulses,” *Biomed. Opt. Express*, vol. 6, no. 7, p. 2552, Jul. 2015, doi: 10.1364/boe.6.002552.
- [2.286] D. B. Conkey *et al.*, “High power, ultrashort pulse control through a multi-core fiber for ablation,” *Opt. Express*, vol. 25, no. 10, p. 11491, May 2017, doi: 10.1364/oe.25.011491.
- [2.287] M. Schluter *et al.*, “Towards OCT-Navigated Tissue Ablation with a Picosecond Infrared Laser (PIRL) and Mass-Spectrometric Analysis,” in *Proceedings of the Annual International Conference of the IEEE Engineering in Medicine and Biology Society, EMBS*, Jul. 2019, pp. 158–161. doi: 10.1109/EMBC.2019.8856808.
- [2.288] E. Kakkava *et al.*, “Selective femtosecond laser ablation via two-photon fluorescence imaging through a multimode fiber,” *Biomed. Opt. Express*, vol. 10, no. 2, p. 423, 2019, doi: 10.1364/boe.10.000423.
- [2.289] B. Debord *et al.*, “Multi-meter fiber-delivery and pulse self-compression of milli-Joule femtosecond laser and fiber-aided laser-micromachining,” *Opt. Express*, vol. 22, no. 9, p. 10735, May 2014, doi: 10.1364/oe.22.010735.
- [2.290] S. O. Konorov *et al.*, “Hollow-core photonic-crystal fibres for laser dentistry,” *Phys. Med. Biol.*, vol. 49, no. 7, pp. 1359–1368, 2004, doi: 10.1088/0031-9155/49/7/021.
- [2.291] T. Petrov, E. Pecheva, A. D. Walmsley, and S. Dimov, “Femtosecond laser ablation of dentin and enamel for fast and more precise dental cavity preparation,” *Mater. Sci. Eng. C*, vol. 90, pp. 433–438, Sep. 2018, doi: 10.1016/j.msec.2018.04.070.
- [2.292] R. E. Friedrich *et al.*, “Ablation Precision and Thermal Effects of a Picosecond Infrared Laser (PIRL) on Roots of Human Teeth: A Pilot Study Ex Vivo,” *In Vivo (Brooklyn)*, vol. 34, no. 5, pp. 2325–2336, Aug. 2020, doi: 10.21873/invivo.12045.
- [2.293] A. Urich, T. Delmonte, R. R. J. Maier, D. P. Hand, and J. D. Shephard, “Towards implementation of hollow core fibres for surgical applications,” in *Optical Fibers, Sensors, and Devices for Biomedical Diagnostics and Treatment XI*, Feb. 2011, vol. 7894, p. 78940W. doi: 10.1117/12.876109.
- [2.294] M. Klejch, M. Němec, J. Kubát, and J. Polák, “Preparation, properties and application of sapphire single-crystal fibers grown by the EFG method,” in *EPJ Web of Conferences*, 2013, vol. 48. doi: 10.1051/epjconf/20134800007.
- [2.295] B. Temelkuran, S. D. Hart, G. Benoit, J. D. Joannopoulos, and Y. Fink, “Wavelength-scalable hollow optical fibres with large photonic bandgaps for CO₂ laser transmission,” *Nature*, vol. 420, no. 6916, pp. 650–653, Dec. 2002, doi: 10.1038/nature01275.
- [2.296] J. A. Koufman *et al.*, “Office-based laryngeal laser surgery: A review of 443 cases using three wavelengths,” *Otolaryngol. - Head Neck Surg.*, vol. 137, no. 1, pp. 146–151, Jul. 2007, doi: 10.1016/j.otohns.2007.02.041.
- [2.297] N. M. Litchinitser, A. K. Abeeluck, C. Headley, and B. J. Eggleton, “Antiresonant reflecting photonic crystal optical waveguides,” *Opt. Lett.*, vol. 27, no. 18, p. 1592, Sep. 2002, doi: 10.1364/ol.27.001592.
- [2.298] S. Février, B. Beaudou, and P. Viale, “Understanding origin of loss in large pitch hollow-core photonic crystal fibers and their design simplification,” *Opt. Express*, vol. 18, no. 5, p. 5142, Mar. 2010, doi: 10.1364/oe.18.005142.
- [2.299] J. D. Shephard, J. D. C. Jones, D. P. Hand, and J. C. Knight, “Delivery of nanosecond pulses through hollow core photonic crystal fibres and the associated damage limitations,” in *Laser-Induced Damage in Optical Materials: 2005*, Oct. 2005, vol. 5991, p. 59911Y. doi: 10.1117/12.637674.

- [2.300] W. Belardi, "Design and Properties of Hollow Antiresonant Fibers for the Visible and Near Infrared Spectral Range," *J. Light. Technol.* Vol. 33, Issue 21, pp. 4497–4503, vol. 33, no. 21, pp. 4497–4503, Nov. 2015, Accessed: Dec. 11, 2017. [Online]. Available: <https://www.osapublishing.org/jlt/abstract.cfm?uri=jlt-33-21-4497>
- [2.301] P. Steinvurzel, B. T. Kuhlmeier, T. P. White, M. J. Steel, C. M. de Sterke, and B. J. Eggleton, "Long wavelength anti-resonant guidance in high index inclusion microstructured fibers," *Opt. Express*, vol. 12, no. 22, pp. 4–66, 2004, doi: 10.1364/opex.12.005424.
- [2.302] J. D. Shephard *et al.*, "Single-mode mid-IR guidance in a hollow-core photonic crystal fiber," *Opt. Express*, vol. 13, no. 18, p. 7139, Sep. 2005, doi: 10.1364/opex.13.007139.
- [2.303] A. Urich *et al.*, "Fabrication of silica hollow core photonic crystal fibres for Er:YAG surgical applications," in *Optical Fibers and Sensors for Medical Diagnostics and Treatment Applications XII*, Feb. 2012, vol. 8218, p. 821805. doi: 10.1117/12.906171.
- [2.304] Robertson CW and Williams D, "Lambert absorption coefficients of water in the infrared," *J Opt Soc Amer*, vol. 61, no. 10, pp. 1316–1320, Oct. 1971, doi: 10.1364/josa.61.001316.
- [2.305] P. Jaworski, F. Yu, R. M. Carter, J. C. Knight, J. D. Shephard, and D. P. Hand, "High energy green nanosecond and picosecond pulse delivery through a negative curvature fiber for precision micro-machining," *Opt. Express*, vol. 23, no. 7, p. 8498, Apr. 2015, doi: 10.1364/oe.23.008498.
- [2.306] F. Yu, W. J. Wadsworth, and J. C. Knight, "Low loss silica hollow core fibers for 3–4 μm spectral region," *Opt. Express*, vol. 20, no. 10, p. 11153, May 2012, doi: 10.1364/oe.20.011153.
- [2.307] T. Toyoda and M. Yabe, "The temperature dependence of the refractive indices of fused silica and crystal quartz," *J. Phys. D. Appl. Phys.*, vol. 16, no. 5, pp. L97–L100, May 1983, doi: 10.1088/0022-3727/16/5/002.
- [2.308] Z. Huang, F. Fu, Z. Zhong, L. Zhang, R. Xu, and X. Zhao, "Flexible Ureteroscopy and Laser Lithotripsy for Bilateral Multiple Intrarenal Stones: Is This a Valuable Choice?," *Urology*, vol. 80, no. 4, pp. 800–804, Oct. 2012, doi: 10.1016/j.urology.2012.05.013.
- [2.309] F. Couny, F. Benabid, P. J. Roberts, P. S. Light, and M. G. Raymer, "Generation and photonic guidance of multi-octave optical-frequency combs," *Science (80-.)*, vol. 318, no. 5853, pp. 1118–1121, 2007, doi: 10.1126/science.1149091.
- [2.310] Y. Y. Wang, N. V. Wheeler, F. Couny, P. J. Roberts, and F. Benabid, "Low loss broadband transmission in hypocycloid-core Kagome hollow-core photonic crystal fiber," *Opt. Lett.*, vol. 36, no. 5, p. 669, Mar. 2011, doi: 10.1364/ol.36.000669.
- [2.311] F. Emaury *et al.*, "Beam delivery and pulse compression to sub-50 fs of a modelocked thin-disk laser in a gas-filled Kagome-type HC-PCF fiber," *Opt. Express*, vol. 21, no. 4, p. 4986, Feb. 2013, doi: 10.1364/oe.21.004986.
- [2.312] B. Beaudou *et al.*, "Millijoule laser pulse delivery for spark ignition through kagome hollow-core fiber," *Opt. Lett.*, vol. 37, no. 9, p. 1430, May 2012, doi: 10.1364/ol.37.001430.
- [2.313] Y. Y. Wang *et al.*, "Design and fabrication of hollow-core photonic crystal fibers for high-power ultrashort pulse transportation and pulse compression," *Opt. Lett.*, vol. 37, no. 15, p. 3111, Aug. 2012, doi: 10.1364/ol.37.003111.
- [2.314] Y. Y. Wang, F. Couny, P. J. Roberts, and F. Benabid, "Low loss broadband transmission in optimized core-shape Kagome hollow-core PCF," 2010. doi: 10.1364/cleo.2010.cpdb4.
- [2.315] S. Gao, Y. Wang, X. Liu, and P. Wang, "Low bending loss nodeless hollow-core anti-resonant fiber," in *2016 Conference on Lasers and Electro-Optics, CLEO 2016*, Jun. 2016, p. SW11.4. doi: 10.1364/cleo_si.2016.sw11.4.
- [2.316] R. M. Carter *et al.*, "Measurement of resonant bend loss in anti-resonant hollow core optical fiber," *Opt. Express*, vol. 25, no. 17, p. 20612, 2017, doi: 10.1364/oe.25.020612.
- [2.317] A. N. Kolyadin *et al.*, "Negative Curvature Hollow-core Fibers: Dispersion Properties and Femtosecond Pulse Delivery," in *Physics Procedia*, 2015, vol. 73, pp. 59–66. doi: 10.1016/j.phpro.2015.09.122.
- [2.318] D. Do, H. Yoo, and D.-G. Gweon, "Fiber-optic raster scanning two-photon endomicroscope using a tubular piezoelectric actuator," *J. Biomed. Opt.*, vol. 19, no. 6, p. 066010, Jun. 2014, doi: 10.1117/1.JBO.19.6.066010.
- [2.319] D. T. McCormick, W. Jung, Y.-C. Ahn, Z. Chen, and N. C. Tien, "A Three Dimensional Real-Time MEMS Based Optical Biopsy System for In-Vivo Clinical Imaging," in *TRANSDUCERS 2007 - 2007 International Solid-State Sensors, Actuators and Microsystems Conference*, 2007, pp. 203–208. doi: 10.1109/SENSOR.2007.4300106.
- [2.320] A. D. Aguirre, J. Sawinski, S.-W. Huang, C. Zhou, W. Denk, and J. G. Fujimoto, "High speed optical coherence microscopy with autofocus adjustment and a miniaturized endoscopic imaging probe," *Opt. Express*, vol. 18, no. 5, pp. 4222–4239, Mar. 2010, doi: 10.1364/oe.18.004222.
- [2.321] Y. Zhao, H. Nakamura, and R. J. Gordon, "Development of a versatile two-photon endoscope for biological imaging," *Biomed. Opt. Express*, vol. 1, no. 4, p. 1159, Nov. 2010, doi: 10.1364/BOE.1.001159.

- [2.322] N. Zhang *et al.*, “Compact piezoelectric transducer fiber scanning probe for optical coherence tomography,” *Opt. Lett.*, vol. 39, no. 2, p. 186, Jan. 2014, doi: 10.1364/OL.39.000186.
- [2.323] V. Milanovic, G. A. Matus, and D. T. McCormick, “Gimbal-Less Monolithic Silicon Actuators for Tip-Tilt-Piston Micromirror Applications,” *IEEE J. Sel. Top. Quantum Electron.*, vol. 10, no. 3, pp. 462–471, May 2004, doi: 10.1109/JSTQE.2004.829205.
- [2.324] T. Meinert, N. Weber, H. Zappe, and A. Seifert, “Varifocal MOEMS fiber scanner for confocal endomicroscopy,” *Opt. Express*, vol. 22, no. 25, p. 31529, Dec. 2014, doi: 10.1364/OE.22.031529.
- [2.325] E. J. Seibel, R. S. Johnston, and C. D. Melville, “A full-color scanning fiber endoscope,” Feb. 2006, vol. 6083, p. 608303. doi: 10.1117/12.648030.
- [2.326] D. R. Rivera *et al.*, “Compact and flexible raster scanning multiphoton endoscope capable of imaging unstained tissue.,” *Proc. Natl. Acad. Sci. U. S. A.*, vol. 108, no. 43, pp. 17598–603, Oct. 2011, doi: 10.1073/pnas.1114746108.
- [2.327] A. Lukic *et al.*, “Endoscopic fiber probe for nonlinear spectroscopic imaging,” *Optica*, vol. 4, no. 5, p. 496, May 2017, doi: 10.1364/OPTICA.4.000496.
- [2.328] R. F. Begley, A. B. Harvey, and R. L. Byer, “Coherent anti-Stokes Raman spectroscopy,” *Appl. Phys. Lett.*, vol. 25, no. 7, pp. 387–390, Oct. 1974, doi: 10.1063/1.1655519.
- [2.329] S. W. Chan *et al.*, “Second harmonic generation in zinc oxide nanorods,” *Appl. Phys. B*, vol. 84, no. 1–2, pp. 351–355, Jul. 2006, doi: 10.1007/s00340-006-2292-0.
- [2.330] K. Vyas, M. Hughes, B. G. Rosa, and G.-Z. Yang, “Fiber bundle shifting endomicroscopy for high-resolution imaging,” *Biomed. Opt. Express*, vol. 9, no. 10, pp. 4649–4664, Oct. 2018, doi: 10.1364/boe.9.004649.
- [2.331] A. Acemoglu, N. Deshpande, and L. S. Mattos, “Towards a Magnetically-Actuated Laser Scanner for Endoscopic Microsurgeries,” *J. Med. Robot. Res.*, vol. 3, no. 2, 2018, doi: 10.1142/S2424905X18400044.
- [2.332] A. Acemoglu, D. Pucci, and L. S. Mattos, “Design and Control of a Magnetic Laser Scanner for Endoscopic Microsurgeries,” *IEEE/ASME Trans. Mechatronics*, vol. 24, no. 2, pp. 527–537, Apr. 2019, doi: 10.1109/TMECH.2019.2896248.
- [2.333] M. Rubinstein and W. B. Armstrong, “Transoral laser microsurgery for laryngeal cancer: A primer and review of laser dosimetry,” *Lasers Med. Sci.*, vol. 26, no. 1, pp. 113–124, Jan. 2011, doi: 10.1007/s10103-010-0834-5.
- [2.334] S. Patel, M. Rajadhyaksha, S. Kirov, Y. Li, and R. Toledo-Crow, “Endoscopic laser scalpel for head and neck cancer surgery,” in *Photonic Therapeutics and Diagnostics VIII*, Feb. 2012, vol. 8207, p. 82071S. doi: 10.1117/12.909172.
- [2.335] A. Acemoglu and S. Leonardo Mattos, “Non-Contact Tissue Ablations with High-Speed Laser Scanning in Endoscopic Laser Microsurgery,” in *Proceedings of the Annual International Conference of the IEEE Engineering in Medicine and Biology Society, EMBS*, Oct. 2018, vol. 2018-July, pp. 3660–3663. doi: 10.1109/EMBC.2018.8513055.
- [2.336] M. Remacle, G. Lawson, M.-C. Nolleaux, and M. Delos, “Current State of Scanning Micromanipulator Applications with the Carbon Dioxide Laser,” *Ann. Otol. Rhinol. Laryngol.*, vol. 117, no. 4, pp. 239–244, Apr. 2008, doi: 10.1177/000348940811700401.
- [2.337] N. Deshpande *et al.*, “Design and Study of a Next-Generation Computer-Assisted System for Transoral Laser Microsurgery,” *OTO Open*, vol. 2, no. 2, p. 2473974X1877332, Apr. 2018, doi: 10.1177/2473974x18773327.
- [2.338] C. L. Hoy *et al.*, “Optical design and imaging performance testing of a 9.6-mm diameter femtosecond laser microsurgery probe,” *Opt. Express*, vol. 19, no. 11, p. 10536, May 2011, doi: 10.1364/oe.19.010536.
- [2.339] C. L. Hoy *et al.*, “Miniaturized probe for femtosecond laser microsurgery and two-photon imaging,” *Opt. Express*, vol. 16, no. 13, p. 9996, Jun. 2008, doi: 10.1364/oe.16.009996.
- [2.340] R. Renevier, B. Tamadazte, K. Rabenoroso, L. Tavernier, and N. Andreff, “Endoscopic Laser Surgery: Design, Modeling, and Control,” *IEEE/ASME Trans. Mechatronics*, vol. 22, no. 1, pp. 99–106, Feb. 2017, doi: 10.1109/TMECH.2016.2595625.
- [2.341] A. Aloy and M. Grasl, “Endoscopy of Larynx and Trachea with Rigid Laryngo- Tracheoscopes Under Superimposed High-Frequency Jet Ventilation (SHFJV),” in *Endoscopy*, 2013. doi: 10.5772/52996.
- [2.342] H. E. Eckel, S. Berendes, M. Damm, J. P. Klussmann, and K. Wassermann, “Suspension laryngoscopy for endotracheal stenting,” *Laryngoscope*, 2003, doi: 10.1097/00005537-200301000-00002.
- [2.343] K. Rabenoroso, B. Tasca, A. Zerbib, P. Rougeot, N. Andreff, and T. E. Pengwang, “Squipabot: A Mesoscale Parallel Robot for a Laser Phonosurgery,” *Int. J. Optomechatronics*, 2015, doi: 10.1080/15599612.2015.1059534.
- [2.344] J. A. Seon, B. Tamadazte, and N. Andreff, “Decoupling Path Following and Velocity Profile in

- Vision-Guided Laser Steering,” *IEEE Trans. Robot.*, 2015, doi: 10.1109/TRO.2015.2400660.
- [2.345] N. Andreff and B. Tamadazte, “Laser steering using virtual trifocal visual servoing,” *International Journal of Robotics Research*. 2016. doi: 10.1177/0278364915585585.
- [2.346] M. Barret, S. Leblanc, A. Rouquette, S. Chaussade, B. Terris, and F. Prat, “EUS-guided pancreatic radiofrequency ablation: preclinical comparison of two currently available devices in a pig model,” *Endosc. Int. Open*, vol. 07, no. 02, pp. E138–E143, Feb. 2019, doi: 10.1055/a-0668-5653.
- [2.347] M. Barthet *et al.*, “Endoscopic ultrasound-guided radiofrequency ablation for pancreatic neuroendocrine tumors and pancreatic cystic neoplasms: A prospective multicenter study,” *Endoscopy*, vol. 51, no. 9, pp. 836–842, 2019, doi: 10.1055/a-0824-7067.
- [2.348] T. J. Song *et al.*, “Initial experience of EUS-guided radiofrequency ablation of unresectable pancreatic cancer,” *Gastrointest. Endosc.*, vol. 83, no. 2, pp. 440–443, Feb. 2016, doi: 10.1016/j.gie.2015.08.048.
- [2.349] S. Lakhtakia *et al.*, “EUS-guided radiofrequency ablation for management of pancreatic insulinoma by using a novel needle electrode (with videos),” *Gastrointest. Endosc.*, vol. 83, no. 1, pp. 234–239, Jan. 2016, doi: 10.1016/j.gie.2015.08.085.
- [2.350] E. R. Jonica and M. S. Wagh, “Endoscopic treatment of symptomatic insulinoma with a new EUS-guided radiofrequency ablation device,” *VideoGIE*, 2020, doi: 10.1016/j.vgie.2020.05.028.
- [2.351] S. Lakhtakia and D. W. Seo, “Endoscopic ultrasonography-guided tumor ablation,” *Digestive Endoscopy*, vol. 29, no. 4. Blackwell Publishing, pp. 486–494, May 01, 2017. doi: 10.1111/den.12833.
- [2.352] J. Satiya, I. Schwartz, J. H. Tabibian, V. Kumar, and M. Girotra, “Ablative therapies for hepatic and biliary tumors: Endohepatology coming of age,” *Translational Gastroenterology and Hepatology*, vol. 5. AME Publishing Company, Jan. 05, 2020. doi: 10.21037/TGH.2019.10.17.

Chapter 3

Bessel-Gauss beam modelling and characterisation, experimental methodology and murine intestinal tissue ablation trials

3.1 Theoretical modelling of Bessel-Gauss beams

The axicons used within this thesis are produced from high-quality UV Fused-Silica (which is an ideal material for the high-powered laser applications that the underpinning surgical applications entail) by Thorlabs via a manufacturing process that entails dicing, grinding, bevelling and polishing [3.1]. These are coated with an anti-reflective hard refractory-oxide coating that is effective over the 650 – 1050 nm wavelength range, listed as a “-B coating” [3.2]. This is important as this improves the transmission efficiency for the CB1-05 Carbide laser system (from Light Conversion) used, which emits a central wavelength of 1028 ± 5 nm [3.3]. This is especially true for multiple lens systems. As an example, for setups consisting of three consecutive lenses (relevant to the work carried out within this thesis), these coatings reduce an otherwise 21.7% loss in transmitted power (a cumulative effect from the 4% lost at each surface) to 3.2%, even with this calculation taking the peak values for reflectance in the example datasets provided by Thorlabs [3.2].

To better understand their relative axial intensity distributions, some theoretical modelling of these axicons was carried out using the OpticStudio software from Zemax. This optical design software package is considered the gold standard among both researchers and a range of market leaders across the optics industry, courtesy of its comprehensive and versatile nature. Computer modelling of the beam properties was performed to save both time and money compared to experimental methods, as this would have otherwise entailed a range of axicons being purchased and characterised for various input beam widths. Additionally, for the small central core diameters exhibited by these Bessel-Gauss beams, alignment and axial scanning of a suitably high-resolution camera would again be both time consuming and expensive. However, an important practical limitation to consider prior to carrying out this theoretical modelling include the fact that the damage threshold of the optics to be implemented into the end of an endoscopic probe design could potentially be close to the ablation threshold of the biological tissue itself. With the end goal being integration into a fibre delivered solution, it becomes clear that simply increasing the power of the input beam indefinitely is not a viable solution.

3.1.1 Laser simulation methods within OpticStudio

There are numerous means of simulating lasers within the OpticStudio software. These include sequential and non-sequential ray tracing (*i.e.* the rays either propagate from one object to the next in a linear manner, or they are not traced in such a predefined manner but are instead traced through objects in a way determined by their own direction and the physical positions and properties of said objects, allowing for them to be reflected back to prior objects), paraxial Gaussian beams and Physical Optics Propagation (POP). While both ray tracing techniques are computationally fast and easy to setup, they are limited in their capacity to act as a complete model for Gaussian beams since they always travel in a straight line, meaning that

collimated beams modelled via this technique remain the same size and diverging beams simulated in this manner maintain the same degree of divergence throughout their propagation (as ray tracing does not allow for dynamic changes in divergence). This means that this only provides a good approximation while within the Rayleigh range (where the beam size changes relatively slowly, meaning it can be approximated as a collimated ray bundle) or far beyond the Rayleigh range (where changes in the beam size become linearly proportional to the propagation distance, thus it can be approximated as a point source). Consequently, ray tracing is also insufficient for modelling diffraction-limited spots, due to these fundamental differences between the constituent rays and Gaussian beam.

Paraxial Gaussian beams are also computationally fast and provide easy access to Gaussian beam traits, including the Rayleigh range and the size of the beam waist. They are also able to incorporate beam divergence. However, they assume an ideal Gaussian beam and are therefore unable to account for aberrations within the optical system, thus may provide overly optimistic results.

POP meanwhile allows for more detailed study of arbitrary, non-Gaussian optical beams, as it simulates the propagation of coherent wavefronts through the optical system via performing diffraction calculations across discretely sampled grids. This entails calculating the amplitude, phase and intensity of the optical beam at each point within the grids located at each of the user-defined surfaces (with key parameters including the dimensions and sampling rates of these surfaces) across the set range of propagation. This allows for both the aberrations present within the system of interest and the coherent interference that the beam undergoes to be comprehensively modelled. The latter is particularly important for the Bessel-Gauss beams of interest, as these are formed via interference mechanisms as discussed previously.

POP is normally used when geometrical ray tracing is not sufficient, such as when the beam comes to an intermediate focus. This is especially the case near optics that shorten the beam. For example, if there was a pinhole in the middle of a system, a ray-based calculation would show the beam coming to a perfect focus, which is impossible due to diffraction effects – the effect the pinhole will have on the beam cannot be simply ignored. Additionally, POP should be used when diffraction effects far from focus are of interest and/or when the propagation length is long and the beam is nearly collimated.

POP does suffer from being computationally intensive (particularly with regards to RAM requirements, as the entire beam must be stored in computer memory at once) and thus can also be time consuming due to the high sampling rates that are often required to accurately model the beam across the entire axial range of interest. Additionally, this modelling process must balance these high sampling rates to achieve an appropriately high beam resolution with a sufficiently wide grid width so that all the spatial frequencies are captured, meaning that the results from these simulations must be manually verified by the user every time. Yet, it is also the only method of simulating lasers within the OpticStudio software that can be used to determine the irradiance at each surface, as well as the phase profiles, while also allowing quantification of the beam quality via the implementation of a specific beam divergence parameter. Dr. McCarthy oversaw the initial use of this feature within the OpticStudio software.

3.1.2 Physical Optics Propagation (POP) modelling of axicons – time-averaged total power model

The appropriate surface positions for POP can be informed via ray tracing. To do so in a way that accurately represents the experimental laser setup used, the Gaussian Apodization Type is set to Gaussian, which imparts an amplitude variation across the illumination of the entrance pupil that takes the form of a Gaussian distribution. The Apodization Factor was then set to 1 – this alters the rate of decrease in beam amplitude as a function of the pupil coordinate in such a way as to place the $1/e^2$ values relative to the peak amplitude at the edges of the pupil.

The CB1-05 Carbide laser system was used for all the ablation experiments carried out within the scope of this work. This laser is suitable for surgical applications, as it is capable of producing ultrashort pulses (232 fs to 10 ps) of a high beam quality, meaning non-linear absorption can be achieved within the focal volume of various optical setups (courtesy of the laser providing pulse energies of up to around 85 μJ), although there remains a compromise between high peak powers and high ablation rates. Additionally, the 1028 ± 5 nm emission wavelength lies within the near-infrared regime, meaning it is able to penetrate deeply into biological tissues, as said tissues have higher scattering coefficients within the near-infrared regime compared to the more highly absorbed wavelengths within the mid and far-infrared regimes [3.4]. Furthermore, as the plasma-mediated ablation is a non-linear process, the absorption coefficient is of less importance (*i.e.* optimisation of the linear absorption regime is not significant for this application, with the lower absorption even potentially aiding the occurrence of the plasma formation process). However, it is also important to note that this higher scattering coefficient could inhibit the propagation of Bessel-Gauss beams through the tissue, as it may hinder the coherency of the constituent interfering rays that underpin the formation of such beams as they translate through the tissue, particularly as the depth increases.

The properties of the laser source are very important within the context of this work, as the minimally invasive modality intended for performing the ultrafast pulsed laser ablation processes within clinical environments necessitates fibre delivery. From this, both the peak energy of sustainable transmission (*i.e.* no damage being incurred by the fibre) and the transmission efficiency will inevitably form experimental constraints, with simply increasing the input laser power indefinitely not being a viable solution. Previous work by the group has shown that 6 ps is an ideal pulse duration to perform soft-tissue ablation studies with, as it offers adequate peak pulse energies for plasma generation at the laser focus while also reducing bend losses and avoiding nonlinear effects while propagating through hollow-core negative curvature fibres [3.5]. As a result of this finding the majority of the laser ablation trials carried out within this thesis were performed using this pulse duration setting.

This laser has a manufacturer quoted value of 1.53 mm for the FWHM beam diameter along the major elliptical axis of the laser beam spot whilst operating at the 5 W 60 kHz preset, with a corresponding M^2 value of 1.09 for this major axis, at 0.6 m from the output (Light Conversion, personal communication, April 26th 2020). This equates to a $1/e^2$ beam diameter value of 2.6 mm, hence this was used for the initial input beam definition for both the ray tracing and POP simulations. While the axial extent over which the Bessel profile is maintained can be tailored by modifying the width of the input beam (with a wider input beam leading to an extended Bessel zone, as illustrated in figures 3.1 and 3.2), to initially keep the setup as simple as possible the unmodified Carbide laser output beam was used within this POP modelling. It is

important to note that this meets the criteria for maximum transmission efficiency while considering a Gaussian beam transferring through a hard-aperture, as in this case the axicon is over 1.86 times the diameter of the input beam [3.6]. A wider input beam can cause diffraction from the axicon edges that leads to heightened modulation of the on-axis optical intensity (which can be avoided by using an input beam with a diameter of less than half of that of the axicon itself), and the extended focal region this offers comes at the expense of intensity by spreading out the finite pulse energy over an even longer axial range. Input beams that are too small are also undesirable as these lead to more compressed focal depths.

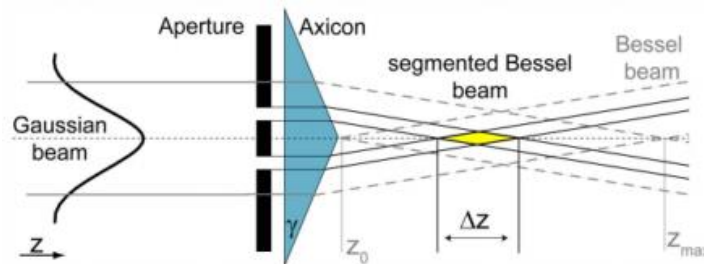


Figure 3.1 – Graphical depiction of the effect that varying the aperture/input beam size has on the Bessel zone length, with the dotted lines representing the Bessel beam that is produced when the illustrated aperture is removed [3.7].

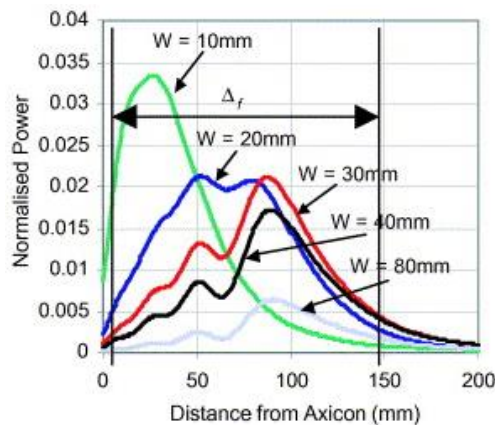


Figure 3.2 – The variation of the on-axis intensity of the central maximum of a Bessel-Gauss beam produced by an axicon with a physical angle of 20° and a radius of 30 mm for Gaussian beams of varying beam widths (W). The power of each incident Gaussian beam is normalised, thus as the Gaussian becomes relatively large compared to the radius of the axicon aperture, less power ends up being coupled into the Bessel-Gauss beam. Δ_f signifies the limited diffraction focal range, at which the central maxima of the Bessel-Gauss beam dissipates [3.8].

A preliminary distance of 0.4 metres was inserted between the surface simulating this laser output measurement plane (surface 1) and the various individual axicons based off the space available on the optical bench that the Carbide laser is mounted to, with an approximated total separation of 1 metre between the laser output facet and the various axicons proving suitable. The various axicons tested were imported from the “Lens Catalogs” available within the OpticStudio libraries.

A POP analysis can be performed once the Layout window indicates that the beam will be well captured along its propagation. The constituent rays of the input beam propagate down a cone, forming the rings that will be observed using the POP feature. Prior to doing so, on the Lens Data window it is important to change the output pilot radius within the Physical Optics settings from “Best Fit” (default) to “plane” at the conical lens surface. This is done as the pilot beam needs to be reset (which is done by effectively comparing the phase to that of a plane) at the conical surface as the default “Best Fit” Gaussian beam does not propagate

very well (Zemax, personal communication, March 28th 2018). This is due to the axicon destroying the chief-ray-referenced nature of the wavefront (unless compensated for by another axicon), which consequently results in it being hindered by a short phase radius, causing complications with the sampling along its propagation range that leads to it self-interfering.

The input beam was defined using the “Gaussian Size + Angle” beam type, which uses the beam size at some point along its propagation (as opposed to the beam waist) and the far-field divergence half-angle in degrees. The latter was quoted by Light Conversion to equal 0.25 mrad for the 5 W 60 kHz preset (Light Conversion, personal communication, December 14th 2017). The initial X- and Y-widths were set to 10 mm as these would provide suitable resolutions for accurately resolving the beam profile, in conjunction with the high 8192 x 8192 sampling rate, while also providing an adequate guard band of at least three times the size of the beam itself [3.9]. This prevents the beam from self-interfering along its propagation.

Due to the high sampling rates required, these simulations were performed on a computer equipped with 16 GB of RAM to address the computational demand, although even with this computer system the top sampling rate of 16384 x 16384 proved to be too demanding. Sampling rates of 2048x2048 and 4096x4096 proved to be too low for adequately resolving the central cores of the various simulated Bessel-Gauss beams while also allowing for appropriate X- and Y-widths throughout the simulation to prevent the aforementioned self-interference problem.

As the size of the beam changes rapidly as it is transmitted through each axicon, resampling was necessary at the surface immediately following the conical lens tip for each of these simulations, particularly as the resolution at a surface is inversely proportional to the grid width at the prior surface. It was of vital importance that the beam was well sampled at each surface (as is the case for the surface depicted in figure 3.3), as any pixilation is representative of fast changes in the intensity values, which causes artefacts further along the propagation axis [3.9]. However, there is a balance between achieving an adequate resolution and not using too small a frame for the surface, as this can lead to an “Inadequate guard band”, as touched upon previously.

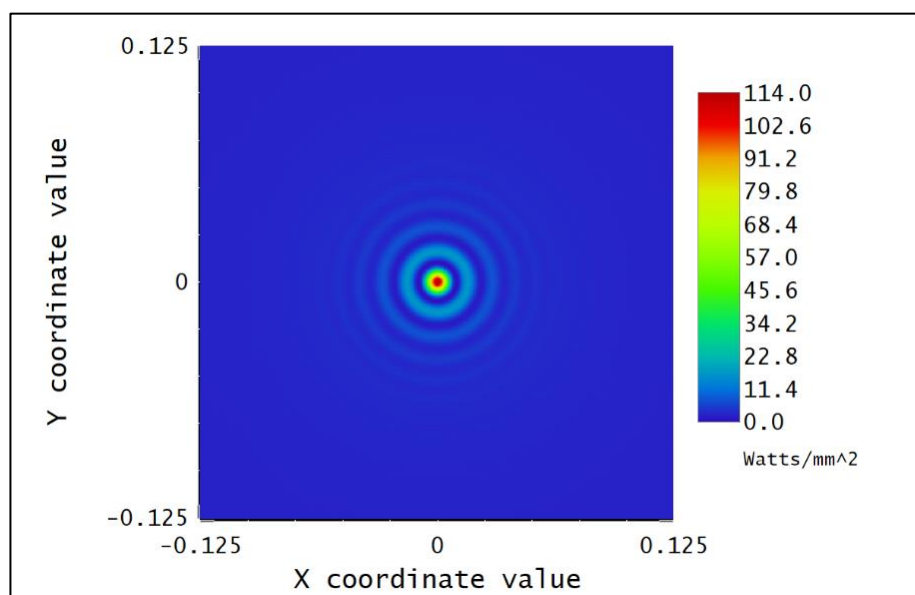


Figure 3.3 – Irradiance profile of the Bessel-Gauss beam produced by a 5° axicon (AX255-B) sampled at a plane 2mm away from the conical tip. The X and Y coordinate value axes are in millimetres.

The total width for the core of each Bessel-Gauss beam was extracted using a MATLAB script. These were compared to theoretical values, calculated using the following formula [3.10]:

$$R_B = \frac{2.4048}{k \sin \beta}; \quad (3.1)$$

where R_B is the central core radius of the Bessel-Gauss beam, k is a wavevector and β is the deflection angle of the axicon. Table 3.1 below shows good agreement between the values obtained using these two methods.

Axicons and their respective conical angles	Theoretical core diameter (μm)	OpticStudio POP core diameter (μm)
AX2505-B, 0.5°	196.0	200.7
AX251-B, 1°	97.8	100.3
AX252-B, 2°	48.9	50.3
AX255-B, 5°	19.5	20.3
AX2510-B, 10°	9.6	9.8
AX2520-B, 20°	4.5	4.6

Table 3.1 – Bessel-Gauss beam core diameter values from theoretical calculations and POP simulations.

After investigating these core diameters, the axial peak irradiance distributions were investigated for the time averaged input beam. As previously mentioned, variations in both the lateral and axial intensity distributions for these axicons can be attributed to both the shape/angle of the axicon used and the properties of the input beam profile. From the specific laser presets available, the input power was set to 5 W to simulate that which provides the highest possible pulse energy (5 W 60 kHz output). A plot of the axial distributions of the peak irradiance obtained from each axicon is shown in figure 3.4.

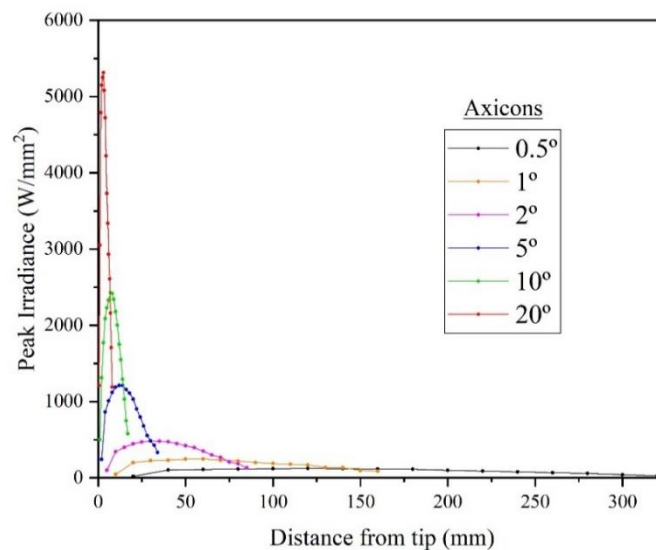


Figure 3.4 – Peak irradiance values plotted against distance from the respective tips for the range of tested axicons, modelled using POP analysis.

The 10° and 20° axicons were of particular interest, as these provided the highest peak irradiance values, courtesy of the smaller spot sizes and comparatively confined axial intensity profiles exhibited by the higher conical angles. A zoomed in view of the axial peak irradiance distributions obtained from these two axicons is shown in figure 3.5. These axicons possessed the highest physical angles available from Thorlabs at the time this modelling was performed, although they do now offer a 40° axicon as well. While this offers even higher intensities, the Bessel zone is further compressed, the standoff from the tip is reduced and the lateral spot size is even smaller (making characterisation measurements even more challenging), hence this was not deemed appropriate for the tissue ablation experiments that were carried out.

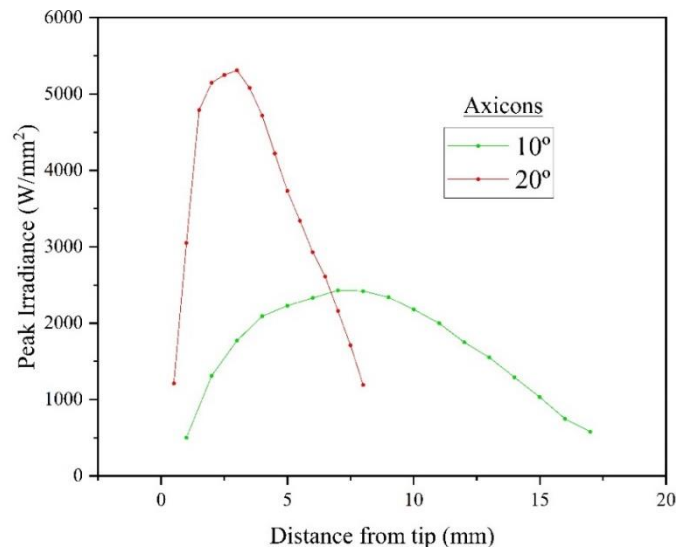


Figure 3.5 – Peak irradiance values obtained from POP analysis for the 10° and 20° axicons for a time-averaged input beam.

All of these peak irradiance plots were again in good agreement with the theory regarding the axial extents of the Bessel regions formed. The following equation was used to calculate the axial length of the Bessel zone (L_B) for comparison purposes [3.11]:

$$L_B = \frac{\omega}{\tan\beta}; \quad (3.2)$$

where ω is the radius of the incident beam upon the planar surface of the axicon. Comparisons between the Bessel zone lengths modelled in OpticStudio and those calculated with equation 3.2 are shown in table 3.2.

Axicons and their respective conical angles	Theoretical Bessel zone length, L_B (mm)	OpticStudio POP Bessel zone length (mm)
AX2505-B, 0.5°	323.8	320.0 ± 20.0
AX251-B, 1°	161.6	160.0 ± 10.0
AX252-B, 2°	80.8	80.0 ± 5.0
AX255-B, 5°	32.2	32.0 ± 2.0
AX2510-B, 10°	15.8	16.0 ± 1.0
AX2520-B, 20°	7.3	7.5 ± 0.5

Table 3.2 – Axial extent over which Bessel beam shape realisation from theoretical calculations and POP simulations.

These Bessel zone lengths were determined by examining the consistency of the beam profile across the propagation axis. This was done by manually going through the surfaces for each simulation and marking down the corresponding axial distance from the tip of the surface at which the Bessel distribution is lost. As the intensity envelope drops off at these points, capturing the beam beyond these points was negligible to the application of interest.

However, one of the limitations of this model is that it essentially assumes a CW laser source by using the time averaged parameter of “Total Power” to define the input beam. The ultrashort nature of the laser pulses to be used is paramount to achieving plasma formation on the tissue surface, through the high peak powers these can reach, courtesy of the temporal distribution of the pulse energy. By switching to the “peak irradiance” input beam definition, these temporal properties of the ultrafast laser source can be considered.

3.1.3 Physical Optics Propagation (POP) modelling of axicons – peak irradiance model

To take the temporal properties of the laser source into consideration, the peak fluence must first be calculated. The following formula for a Gaussian pulse was used [3.12]:

$$P_F = E_p \frac{2}{\pi w_0^2}; \quad (3.3)$$

where P_F is the peak fluence of the laser pulse, E_p is the pulse energy and w_0 is the half-width of the spatial profile of the pulse at an intensity level equal to $1/e^2$ of the peak (1.3 mm). To obtain the peak irradiance of the pulse (P_I), this peak fluence must then be divided by the full width at half maximum duration of the pulse (τ_p) [3.13]:

$$P_I = 0.94 \frac{P_F}{\tau_p}; \quad (3.4)$$

with the 0.94 factor arises from the pulse having a Gaussian temporal profile. This gave a peak irradiance value of 5.01×10^6 W/mm² for an 85 μ J pulse with a FWHM duration of 6 ps. This pulse duration was measured by Dr. Mohan with an autocorrelator supplied by APE PulseCheck (figure 3.6) [3.5].

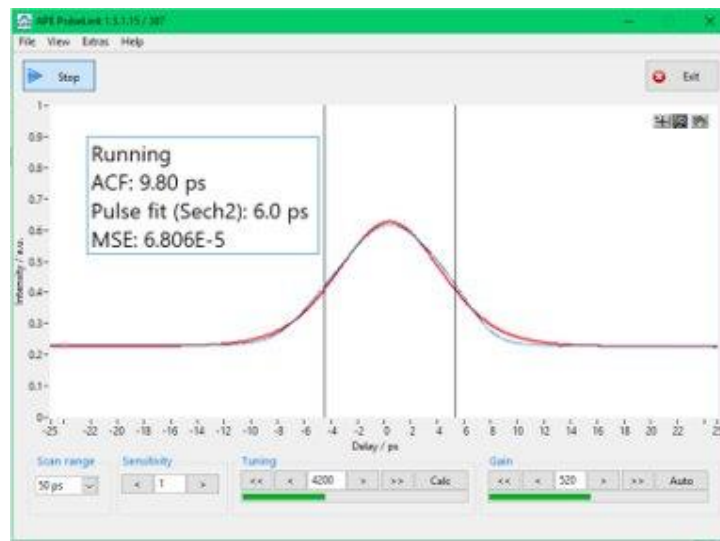


Figure 3.6 – Autocorrelator measurement for the pulse duration, verifying the 6 ps this was set to via the Carbide laser software [3.5].

Using this peak irradiance value to define the input beam as opposed to the time averaged power gives the axial intensity distribution plot for the various axicons presented in figure 3.7.

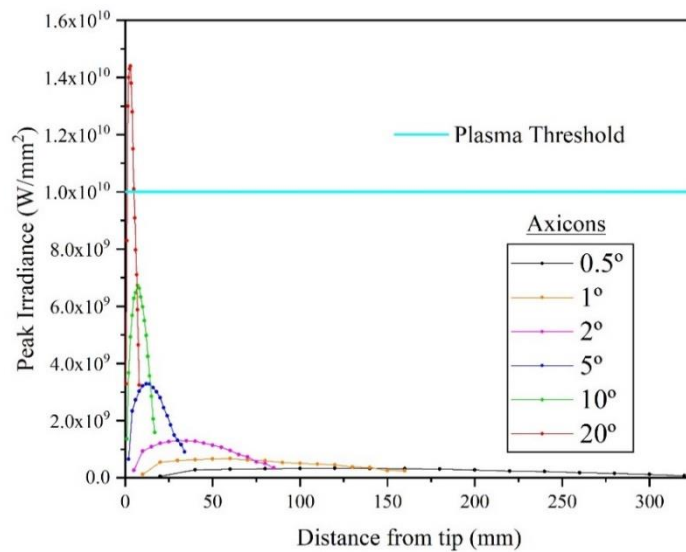


Figure 3.7 – Peak irradiance values obtained from POP analysis for the range of tested axicons for an input beam defined by its own peak irradiance, thus taking its ultrashort temporal distribution into account.

As can be observed from this plot, the 20° axicon is the only one among the range of tested axicons available from Thorlabs that is able to theoretically achieve intensity levels capable of exceeding the plasma formation threshold in biological tissue ($\approx 10^{10} \text{ W/mm}^2$ for picosecond pulses of near-infrared wavelength, similar to that observed for water) for the 85 μJ input pulse, which as previously mentioned is the maximum pulse energy that the Carbide laser can produce [3.14],[3.15]. A zoomed in view of this particular irradiance plot, along with that obtained for the 10° axicon, can be observed in figure 3.8. For the other axicons to also exceed this threshold, either a laser system capable of producing higher pulse energies or appropriate reimaging telescopes would be required, or even a combination of the two.

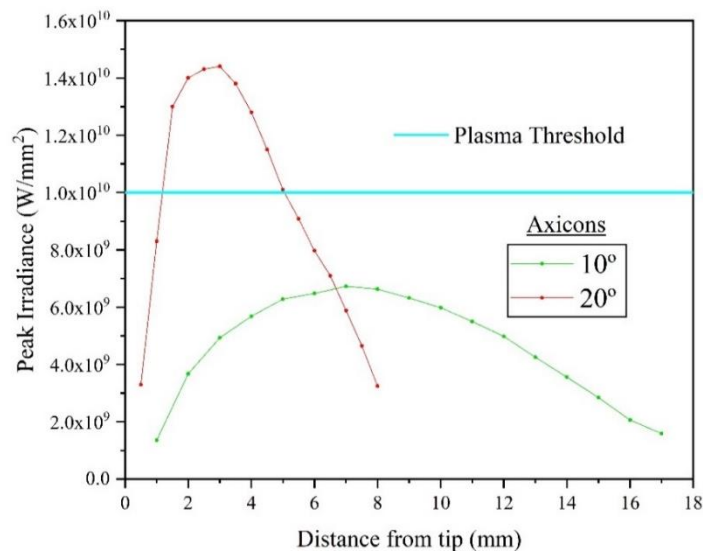


Figure 3.8 – Peak irradiance values obtained from POP analysis for the 10° and 20° axicons for an input beam defined by its own peak irradiance, thus taking its ultrashort temporal distribution into account.

Consequently, the 20° was chosen for the majority of the Bessel-Gauss beam ablation tests carried out within this thesis, courtesy of these higher peak intensities that it offers. Based on these results, while it is

capable of achieving plasma formation for the specified beam input, it does not exceed peak irradiances above the 10^{12} W/cm² regime, at which point reshaping of the Bessel beam can occur via self-focussing and nonlinear losses [3.10],[3.16],[3.17]. However, even if this threshold were to be exceeded, there would still be ample room for reducing the incident pulse energy. Additionally, it has been noted within the literature that higher conical angle axicons can sustain a more consistent propagation-invariant regime at ablation level-intensities, avoiding some the undesirable effects encountered by Gaussian beams at this threshold, such as plasma defocusing [3.18].

These higher intensities also offer a higher tolerance to losses within both a larger scale optical bench test setup and upon later potential integration into a fibre delivered solution (inevitably entailing some scattering and bend losses), which based on the endoscopically deployable modality of interest for achieving precise ultrafast beam delivery to the target pre-cancerous or cancerous tissue site is of paramount importance. It also still provides suitable working distances (with the desired focal depth being one that exceeds the level of tissue inhomogeneity), despite the high degree of compression exhibited by the modelled axial intensity profile relative to the other axicons, while potentially benefitting from the sharp drop-off in the intensity profile along its propagation axis. This stark drop-off in intensity could minimise the potential for thermal damage at the bottom of the ablated features compared to the more gradual tapers in the axial intensity distributions showcased by the axicons with smaller conical angles.

Additionally, within the literature the regime of axicons with smaller cone angles ($< 10^\circ$) has been characterised as having more distinct intensity fluctuations across its axis of propagation above a certain input beam power threshold, while the regime of larger cone angles ($\geq 10^\circ$) has been shown to exhibit comparatively uniform light channels across their Bessel zones at equivalent input powers, in turn leaving uniform plasma tracks from the central Bessel core, which intuitively is the primary site of absorption of the input laser energy [3.11]. This also leads to a more consistent ratio between the intensities of the central core and the nearest surrounding annular ring. This helps to ensure that this ring remains below the ablation threshold of the material being processed, across the whole axial extent of the Bessel zone, at incident powers for which the central core area itself exceeds said threshold. However, as the 20° axicon possesses a smaller core diameter, this unavoidably leads to complications regarding the characterisation of the beam, as does the fact that for higher conical angles the intensity is distributed more closely to the tip along the propagation axis of the beam.

Other limitations of this imported “Odd Asphere” surface type POP model include the fact that it assumes perfect centring and orthogonality of the incident beam upon the planar surface of the axicon and a perfectly sharp conical tip, hence why the characteristic intensity fluctuations witnessed from an oblate tip are not observed here [3.19]. Additionally, as previously discussed, these Bessel-Gauss beams are formed via interference, meaning that the conventional theoretical models for the interaction between focussed laser beams and material (in this context biological tissue) do not apply, thus the need for experimental validation on whether they do indeed show merit towards clinically relevant ablation trials. This will be evaluated through both live measurements (a thermal camera to image any potential heat accumulation on the samples and high-speed imaging) and post-processing measurement modalities, including both surface profiling and histopathology.

3.2 Bessel-Gauss beam characterisation

As previously discussed, the 20° axicon (AX2520-B, Thorlabs) was selected among those that were commercially available from Thorlabs, due to the peak intensity values it provides being theoretically validated as being sufficient for achieving plasma formation within biological tissue by combining peak pulse energy equations with Physical Optics Propagation (POP) modelling in OpticStudio. This axicon would require a reimaging telescope for experimental characterisation, as the CMOS camera chosen (DCC1645C, Thorlabs) had a pixel size of 3.6 μm , so to obtain measurements at a suitable resolution of the central Bessel-Gauss core (modelled in OpticStudio to have a diameter of approximately 4.6 μm) the output beam would have to be expanded. Additionally, the lack of standoff from the standalone axicon setup would inhibit direct measurements with the CMOS camera as the distance between the front of the camera mount and the active sensor was greater than the modelled axial range of the Bessel-Gauss beam produced from the 2.6 mm diameter $1/e^2$ Gaussian input beam.

Numerous considerations were factored into choosing appropriate lenses for creating the required beam expander. A Keplerian beam expander was used due to the relatively short working distance from the conical tip of the 20° axicon and the divergent nature of the annular waveform that the Bessel-Gauss beam produces in its far-field region. While a longer focal length for the first lens would reduce potential aberrations, the 25.4 mm diameter apertures of the lenses limited the extent to which the output beam could be expanded for imaging with the DCC1645C camera, as it was important that clipping of the beam was avoided (Appendix 1a). This is especially true between the axicon and the first telescope lens, as all the power ends up being distributed throughout the outer annular rings further along the propagation axis for the Bessel-Gauss profile. The previously described ray tracing feature within the OpticStudio software was used to optimise the magnification factor and the resulting total length of the telescope, while also preventing clipping of the beam.

25.4 mm and 250 mm focal length plano-convex lenses (LA1951-B and LA1461-B respectively, Thorlabs) were chosen as the first (objective) and second (imaging) lenses in this reimaging telescope as a magnification factor of around 10x was desired to provide an adequate resolution for the beam characterisation images, while simultaneously ensuring that the propagation-invariant extent (or Bessel zone) of the reimaged Bessel-Gauss beam would exist within a working range that was compatible with the available space on the optical bench (Appendix 1b). The optimal distance between the two telescope lenses was tested in OpticStudio by using the Local Optimisation feature within the Merit Function Editor, with the thickness of the intermediate surface between the two lenses being selected as the variable within the lens data window. The damped least squares algorithm was chosen as this is ideal for imaging systems. The REAY operand was applied as this checks the real ray height at the specified surface - in this instance a dummy surface placed after the second (250 mm focal length) lens. The RAED operand was also used as this optimises the real ray angle normal to the surface. The target for this was set to 0 at the same dummy surface used for the REAY operand, as the angle normal to the vertical dummy surface should be as small as possible to achieve optimal collimation. This gave a spacing of 269.439 mm between the lenses, which is slightly larger than simply the sum of the quoted back focal lengths (265 mm) [3.20]. This was in accordance with the experimentally measured spacing of 268 ± 1 mm.

These mounted reimaging lenses were placed in a 30 mm cage system (Thorlabs) along with the 20° axicon to provide robustness to the setup and aid the process of aligning the three elements along a common optical axis, making it easier to identify any misalignments of any individual elements (figure 3.9). Optical mirrors with suitable wavelength compatibility (NB1-K14, Thorlabs) were used to redirect the output beam to the cage system. Collimation of the telescope was verified by using an infrared detector card (VRC4, Thorlabs) along with an infrared viewing device (IRV2(1300)-02, Photonic Solutions). The magnification factor of the telescope was confirmed by reimaging a pinhole placed in the beam path and imaging this with the CMOS camera.

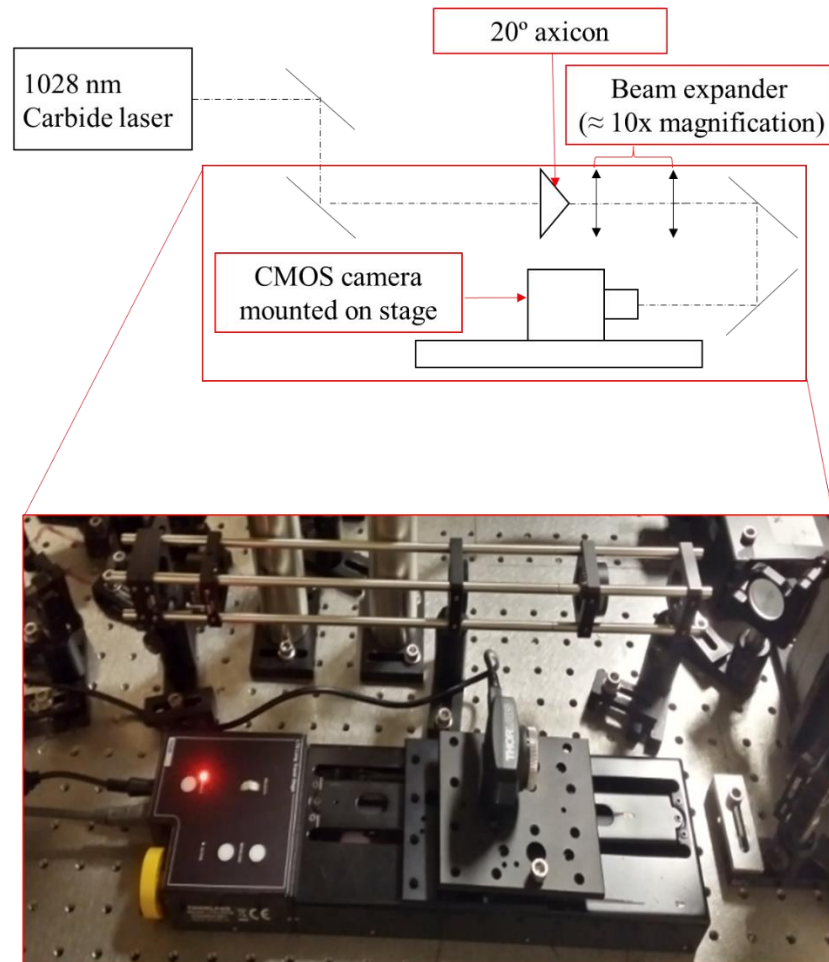


Figure 3.9 – Bessel-Gauss beam characterisation setup.

Optimisation of the standoff distance between the 20° axicon and the objective lens was informed via OpticStudio ray tracing. The objective lens was placed at a distance slightly greater than its front focal length away from the conical tip of the axicon (approximately 1 mm further away). This front portion of the Bessel zone was placed at the focus of the objective lens due to the requirement to be at least the focal length away from the imaging lens before the corresponding portion of the reimaged beam could be resolved using the CMOS camera. This avoided any clipping from occurring between the telescope lenses, while also providing adequate space along the propagation axis for the portion of the reimaged beam that is formed prior to the focus of the imaging lens. Additionally, the first approximately 0.5 cm axial extent of the reimaged beam (corresponding to the first 0.5 mm of the unmodified Bessel-Gauss beam) was unable to be imaged, as the space between the first mirror after the cage system and the imaging lens within said

cage system was obstructed by the end cage plate. As reported by Dudutis *et al.*, reimaging a Bessel-Gauss beam produced by an axicon widens the cross-sectional widths of the beam profile by the magnification factor of the telescope used, while extending the axial range over which the Bessel profile is maintained by an amount that is approximately equal to the squared product of the same magnification factor [3.10].

The DCC1645C camera was mounted on a translation stage (LTS150/M, Thorlabs) to enable precise positioning of the camera across the axial distance of the Bessel zone for the reimaged Bessel-Gauss beam. While the translation range of this stage was shorter than the axial extent of the reimaged Bessel-Gauss beam, the housing of the second telescope lens (*i.e.* the final lens in the reimaging setup) and the threaded flange of the CMOS camera were used as common reference points for measuring the varying distance between the camera and the reimaging telescope via a steel ruler. The quoted distance of 12.5 mm between the threaded flange and the active sensor of the camera and the calculated distance of 8.8 mm between the lens housing and the lens surface (taken as being approximately equal to the housing thickness of 11.4 mm minus 2.6 mm from the centre thickness of the lens) were both accounted for by adding these to the measured distances [3.21],[3.20].

Using this setup, the central core diameter of the reimaged Bessel-Gauss beam was found to consistently be 13 ± 1 pixels wide across the axial range over which the Bessel profile is maintained using the manual “Measure” tool within the ThorCam software. This corresponds to a central core diameter of 46.8 ± 3.6 μm , courtesy of the 3.6 μm pixel size, or an unmodified central core diameter of approximately 4.68 μm . This expanded Bessel-Gauss beam profile is shown in figure 3.10.

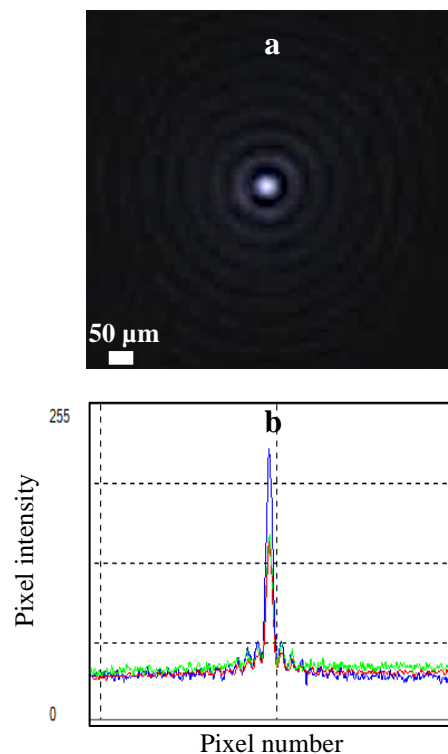


Figure 3.10 – Beam profile (a) image and (b) corresponding cross-sectional intensity profile of the 10x magnified reimaged Bessel-Gauss beam produced by the 20° axicon that is illuminated by the Carbide laser input beam (50% of the 2W 60 kHz preset, transmitted through a 3.0 OD ND filter to prevent damage to the active sensor area of the camera).

These profiles were captured 7 cm away from the reimaging telescope using the DCC1645C CMOS camera from Thorlabs.

A MATLAB script was written to compare the central core diameter values obtained via OpticStudio POP modelling (covered previously) and CMOS camera measurements of the Bessel-Gauss beam produced by the 20° axicon for the Carbide laser input beam (Gaussian beam with a 1/e² diameter of 2.6 mm at the 5W 60 kHz preset) along its propagation axis (figure 3.11). The CMOS camera measurements consisted of both the previously mentioned manual measurements performed within the ThorCam software and applying data fitting to the images using MATLAB. The distances measured experimentally were converted back to the corresponding millimetre scale distances from the conical tip by simply dividing these by the square of the magnification factor.

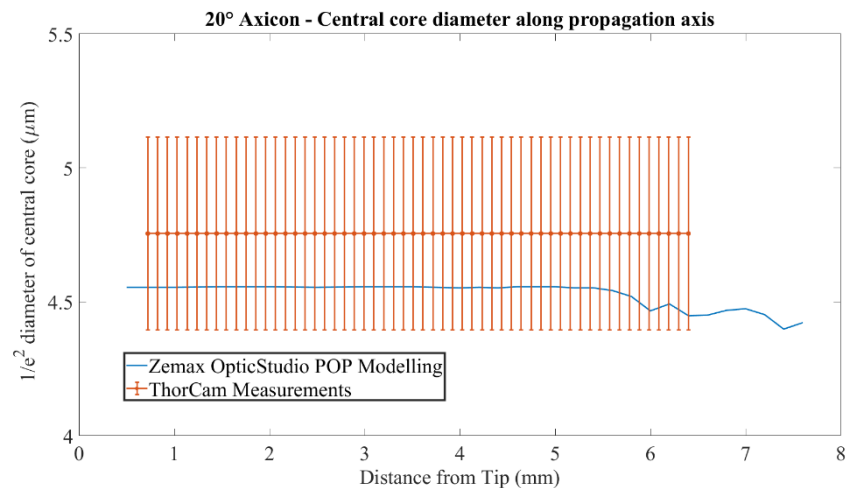


Figure 3.11 – Plot of the central core diameter of the Bessel-Gauss beam formed by a 20° axicon with its planar surface illuminated by a 2.6 mm 1/e² Gaussian beam across its respective axial range over which the Bessel profile is maintained. This data was plotted for the POP model described earlier in this chapter, as well as ThorCam measurements that had a 1/e² data fit applied to the central core of the observed Bessel-Gauss beam using MATLAB. The error bars indicate the limited pixel resolution of the ThorCam, even after magnification of the beam. The distances from the tip for the ThorCam measurements were calculated by dividing the measured distances between the telescope and the camera by the squared product of the magnification factor of the telescope.

As can be seen in figure 3.11, the manual measurements performed via the ThorCam “Measure” tool highlight the relatively limited pixel resolution, despite the expansion of the beam with the reimaging telescope. While the core diameters between the theoretical modelling and experimental measurements were found to be in good agreement, some truncation of the beam was observed across the axial range over which the Bessel profile is maintained experimentally. This discrepancy was attributed to a combination of the background subtraction used within the MATLAB script to fit the data, slight positional errors between the reimaging telescope lenses, the oblate (rounded) tip and the significantly lower power used to avoid damage to the CMOS camera sensor (50% attenuation of the 2W 60 kHz preset through a 3.0 OD ND filter, as opposed to the 5W specified for the POP modelling). Higher powers (*i.e.* reduced attenuation settings within the Carbide User App software) were paired with ND filters for these, as the laser is comparatively unstable at lower power settings.

To further investigate this discrepancy between the modelled and experimentally measured axial ranges of the Bessel zone, an experiment was setup using the standalone 20° axicon and the CMOS camera. To account for the short standoff from the conical tip the sensor within the camera was removed from its casing to effectively remove the flange spacing which would otherwise prohibit measurements of the axial

intensity distribution produced by the 20° axicon. The axicon was placed at the end of a 30 mm cage system (Thorlabs) to ensure that the beam was incident normal to the planar surface of the lens.

Care was taken to avoid saturation of the camera, as obtaining a robust reference point for measuring the axial ranges of the beam propagation involved bringing the conical tip of the axicon and the sensor into physical contact with each other. This meant that removing the in-built protective filter within the camera was necessary (due to its rubber housing protruding approximately 4 mm from the sensor surface). Consequently, three ND filters (OD 1.0, 2.0 + 3.0) were placed within the laser beam path (prior to the 20° axicon) to avoid damage to the camera. Additionally, avoiding this saturation across the measured range of the Bessel zone allowed for normalising of the intensity scale.

The relative intensity levels measured across the three colour filters (red, green and blue) were averaged for each reading. The use of a ball bearing stage allowed for a resolution of 0.1 mm along the translation (z) axis through the micrometre scale found on the actuator (figure 3.12).

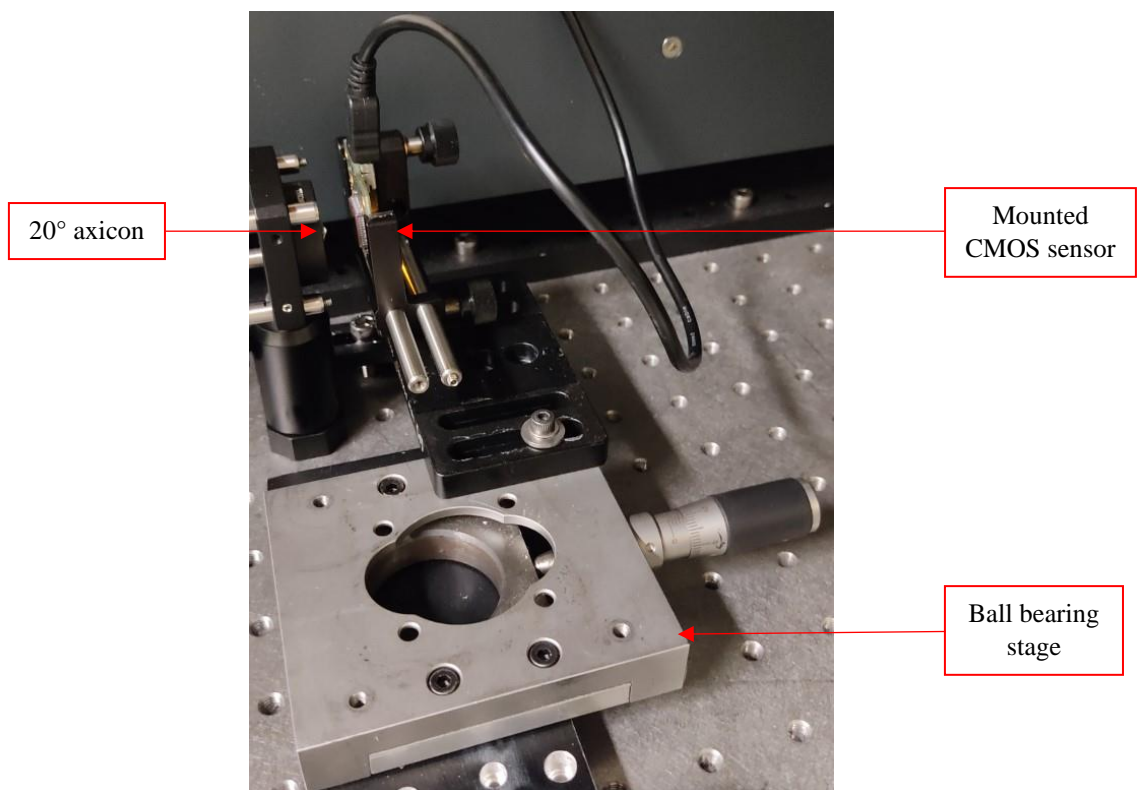


Figure 3.12 – DCC1645C CMOS camera sensor mounted on a on a ball bearing stage (253537, Micro-Controle).

A rounded tip axicon model was also created within the OpticStudio software by using the “Standard” surface type within the Lens Data window in order to represent a non-ideal axicon. A conic term of -8.54 was calculated for this imperfect conical surface using the following formula, as stated within the OpticStudio help function:

$$z = r \tan \alpha = \frac{r}{\sqrt{-(1+k)}}; \quad (3.5)$$

where α is the physical angle of the axicon, r is the estimated radius of curvature of the rounded tip and k is the conic constant. The radius of curvature was approximated to be equal to 50 μm based on a manual measurement made with the Leica microscope, but as stated within the OpticStudio help function the

precise value of this is insignificant as long as it is at least three orders of magnitude smaller than the radial aperture of the axicon.

High axial sampling/small surface spacing of 0.05 mm was required along the simulated propagation range to resolve the comparatively small intensity oscillations, as this model still closely resembles an almost perfect tip geometry. This, combined with the high sampling rate of 8192 x 8192, meant that this simulation was particularly computationally intensive.

As can be observed from figure 3.13, the rounded tip led to oscillations along the axial intensity profile as expected (based on observations from previous studies)[3.10],[3.22],[3.23]. The larger oscillations observed experimentally compared to the OpticStudio rounded tip model were attributed to the increased sensitivity caused by the need to highly attenuate the beam in conjunction with the rounded tip model in OpticStudio being closer to the ideal case. To explore the cause of the intensity oscillations in more depth, a physical characterisation of the axicon surface itself was performed.

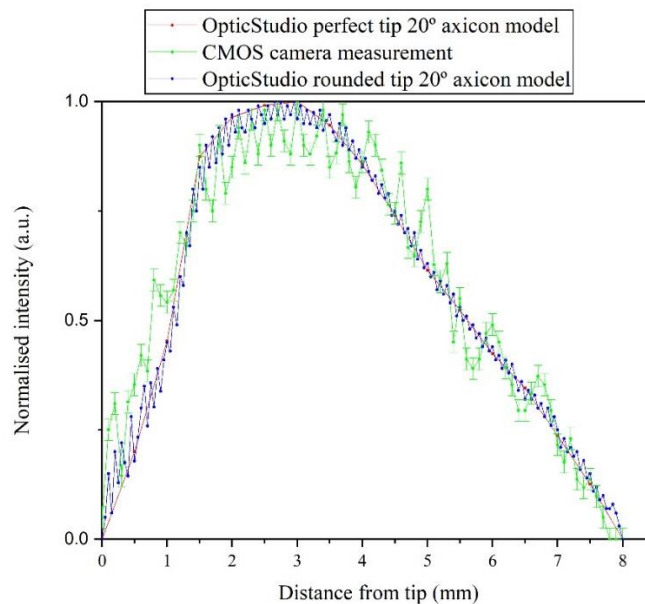


Figure 3.13 – Normalised intensity plots obtained for the 20° axicon via OpticStudio POP modelling and CMOS camera measurements. The OpticStudio models consisted of an imported “Odd Asphere” surface type axicon model with an ideal (perfectly sharp) tip and an imperfect (rounded) tip model simulated by using a “Standard” surface type with a calculated conic term.

3.3 Physical axicon characterisation

While Thorlabs quote a minimum apex rounding diameter of 0.70 mm, there is unfortunately no information provided regarding the curvature of the conical tip [3.24]. Consequently, the tip curvature of the 20° axicon was examined using a stylus profiler system (Tencor P-7, KLA instruments), as shown in figure 3.14. These measurements were carried out within the onsite nanofabrication laboratory suite.

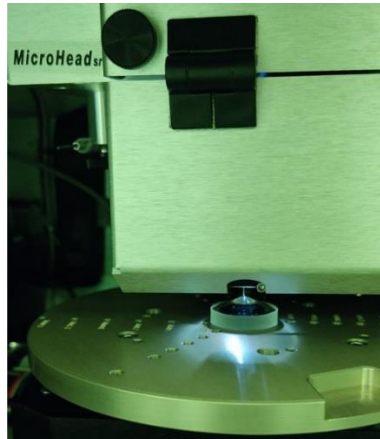


Figure 3.14 – 20° axicon placed within the Tencor P-7 stylus profiler system.

A sampling area of 1 x 1 mm was initially tested, but this caused the profiler to diverge outwith its operational height range due to the relatively steep angle around the conical tip. Consequently, a sampling area of 500 x 500 μm was used alongside the “Up-Edge” feature detection setting and Y spacings of 1 μm .

The maximum vertical range setting of 327 μm was used in conjunction with the positive amplitude profile type to accommodate the aforementioned relatively steep angle around the conical tip. From the surface map obtained, line profiles that intersected the highest point (*i.e.* the peak of the rounded tip) could be generated through the Apex Advanced Analysis software.

The underlying raw data from the surface was extracted into MATLAB for increased flexibility with regards to data handling and visualisation (figure 3.15). Using this method, rigorous data fitting could be applied to measure the discrepancy between the actual tip geometry (*i.e.* rounded) and the ideal case (*i.e.* perfectly sharp tip).

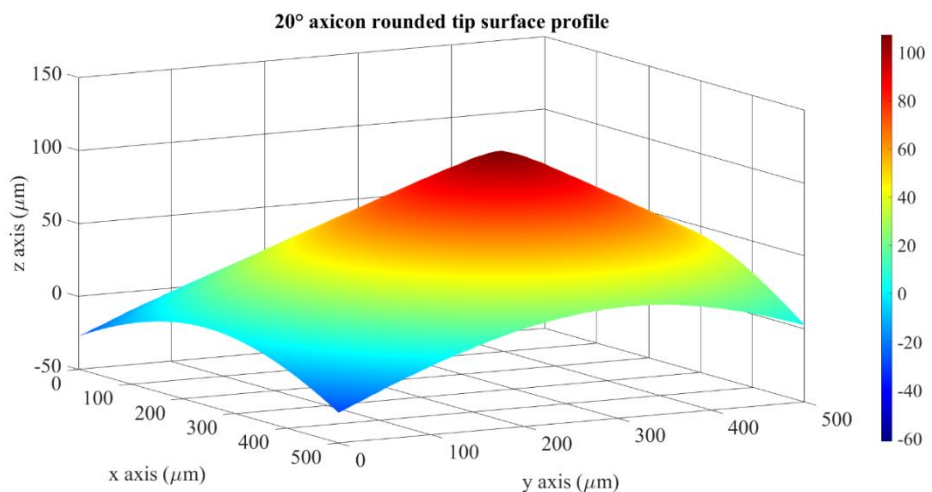


Figure 3.15 – Surface plot of the oblate tip of the 20° axicon generated in MATLAB.

MATLAB was used to fit line profiles along both the x- and y-axes that intersected the peak of the conical tip, similar to the line profiles that were fitted within the Apex Advanced Analysis software. 20° lines were then fitted to the outermost points of these line profiles to best simulate the perfectly sharp point that is indicative of the ideal axicon case (figures 3.16 and 3.17). The difference between the intersection point of these 20° lines and the peak of the rounded tip in the z-axis was then taken as the perfect tip deviation parameter.

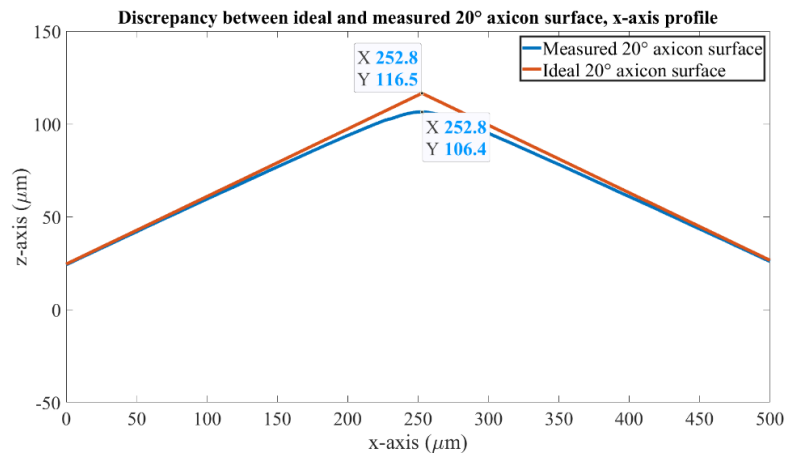


Figure 3.16 – Plot showing the discrepancy between the measured and ideal 20° axicon conical surface profile peaks along the x-axis.

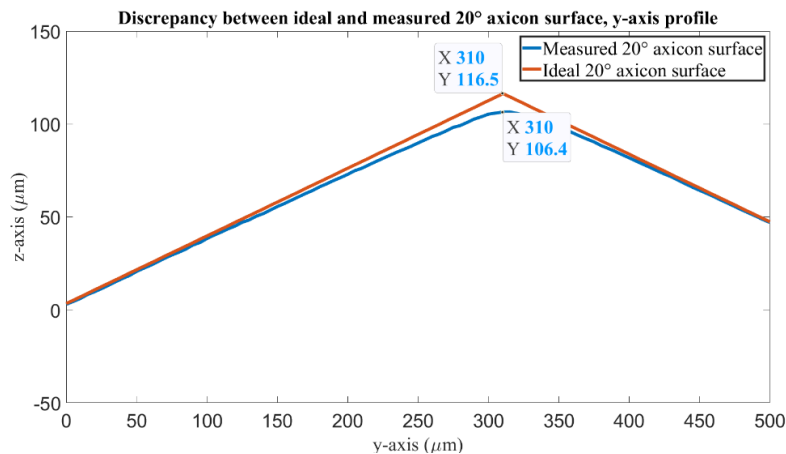


Figure 3.17 – Plot showing the discrepancy between the measured and ideal 20° axicon conical surface profile peaks along the y-axis.

The deviation parameter was found to be equal to $10.1 \pm 1.0 \mu\text{m}$. The deviation measurements along both the x- and y-axis profiles were found to match. The correlation between this deviation measurement and the oscillations observed along the axial intensity distribution (figure 3.13) agreed reasonably well with findings cited in the literature (with calculations by Brzobohatý *et al.* showing a 10 μm discrepancy leading a to maximum intensity oscillation of approximately 10% within the low intensity region at the front of the Bessel zone generated by a 5° axicon, with the oscillations along the high intensity region being insignificant) [3.22]. The intensity oscillations observed for the 20° examined here are more significant due to the greater magnitude and higher axial confinement of the intensity profile, although these were still deemed acceptable for the tissue processing applications under consideration [3.23]. This was concluded

as the uneven morphology of the tissue surfaces would have a significantly greater impact upon the final shape of the ablated features due to the relatively finite nature of the oscillations observed.

3.4 Experimental methodology

3.4.1 Tissue ablation parameters

There are a multitude of parameters which determine the efficacy of laser ablation of tissue [3.25].

These include:

Beam shape: The primary aim of this thesis was to investigate the differences in ablation characteristics obtained from using more conventional Gaussian shaped ultrashort laser pulses compared to those with a Bessel-Gauss beam geometry. The shape of the beam determines the axial range over which plasma formation can occur for a given set of (suitably intense) laser parameters. This range is typically described as the focal depth for conventionally focussed Gaussian beams (which is double the Rayleigh range). For Bessel-Gauss beams, this is perhaps most easily described as some portion of the Bessel zone length.

Wavelength: For thermal (*i.e.* linear absorption) based laser ablation processes of tissue, the wavelength is a significant parameter as this determines the absorption and scattering characteristics of the incident light within the tissue [3.26]. This holds true when either a continuous-wave or a long-pulsed laser source is used. As mentioned previously, the 1028 ± 5 nm wavelength produced by the Carbide CB1-05 laser system was used for all the experimental ablation trials carried out within the scope of this thesis. However, as the pulses produced by this laser system are ultrashort in nature (with the pulse duration varying from 232 fs to 10 ps), the wavelength is of less importance, as the intensities that the laser pulses are focussed down to lead to the occurrence of non-linear absorption processes. This means the ablation process is significantly less sensitive to linear absorption [3.27].

Pulse duration: The pulse duration is of paramount importance with regards to achieving plasma formation within tissue while performing laser ablation. It is the high temporal confinement of the laser pulses that enable the intensity levels required for plasma-mediated ablation to occur as this, in combination with the pulse energy, determines the peak power of each laser pulse. This peak power in turn provides the required intensity profiles (*i.e.* exceeds the plasma formation threshold for biological tissues) for suitably well focussed/small laser spots.

Pulse energy: As discussed above, the pulse energy, in conjunction with the pulse duration, determines the peak power contained within each laser pulse. This parameter is determined by the average output power of the pulsed laser source divided by the pulse repetition rate.

Pulse repetition rate: The pulse repetition rate defines the number of laser pulses emitted per second by the laser source. While higher pulse repetition rates can potentially allow for faster ablation processes, the reduced temporal separation of the applied laser pulses has the potential to lead to an onset of undesirable effects. These include increased shockwave generation from both the generated plasma itself and the amplified interactions between the collapsing cavitation bubbles, as well as the inhibition of energy transferral from subsequent laser pulses into the tissue due to these pulses colliding with the aforementioned cavitation bubbles, particularly when these pulses have higher spatial overlaps [3.15],[3.28],[3.29],[3.30].

Spatial pulse overlap: The spatial pulse overlap is defined as the percentage area over which the subsequent pulse intersects with the area covered by the previous one. Within the scope of the work carried out within this thesis, the spatial pulse overlap is defined by the pulse repetition rate, scanning speed of the translation stages and the spot size of the focussed laser pulses.

Scanning pattern: Simple line and raster scans were used for all the ablation trials undertaken within this thesis. This allowed for increased simplicity of the synchronisation between the laser system and the translation stages used. While spiral scans have been shown to allow for effective tissue removal via their optimisation of applied laser energy (from not dwelling at the edges or requiring the laser to be switched off to avoid this dwelling effect, as is the case for raster scans), these required high acceleration of the scanned beam which was provided via the actuated mirrors within a galvanometer scanhead [3.30]. Unfortunately, the axicon was not compatible with this scanhead due to the finite aperture of this system and the divergent nature of the annular beam produced in the far-field region of the Bessel-Gauss beams propagation. Also, Lissajous and spiral scans can both suffer from significant non-uniformities between the inner and outer regions of the scanning area. This is particularly noticeable for larger spiral scans, making it potentially difficult to maintain a consistent spatial pulse overlap. The comparative simplicity of implementing line and raster scan patterns allowed for a more straight-forward comparison between the ablation properties observed for the Gaussian and Bessel-Gauss beams.

Number of passes: The number of passes was simply the number of times the laser spot was translated over the same area for the various line and raster scans performed. A higher number of passes intuitively led to greater ablated depths.

The above parameters, with the exception of the pulse duration and wavelength, were varied to study the respective differences between the two beam shapes. Optimal conditions were sought for both lower (1, 2 and 3 kHz) and higher (5, 10 and 20 kHz) pulse repetition rates as the maximum scanning speed (and consequently the minimum achievable spatial pulse overlap for a given pulse repetition rate) is likely to be one of the potential limiting factors in an endoscopic device. This would enable comparison between the two beam shapes for both low and high temporal overlapping of the laser pulses in addition to a comprehensive range of spatial overlap values for each pulse repetition rate. While testing more intermediate pulse repetition rates would have been of interest with regards to further potential optimisation, limited sample availability of clinically relevant tissue hindered this from being implemented. This was further exacerbated by each set of laser parameters being tested across at least two tissue samples - one for histological analysis and one for surface profilometry.

3.4.2 Tissue handling process for ablation trials

All of the experimental processes regarding clinically relevant animal tissues were carried out within the scope of the regulations set out by the NHS Health Research Authority and with ethics approval established by the Ethics Committee on biological tissue handling based at Heriot-Watt University. To maximise the relevance of the model provided by the various laser ablation trials on *ex vivo* tissue samples to operational procedures performed in human patients, it is of paramount importance that the cellular properties within the tissue samples are maintained as much as possible from the point of harvesting.

The porcine intestinal and skin tissue samples were obtained from both mature pigs and piglets that were euthanised via a schedule 1 kill across the numerous ablation trials performed throughout the work detailed in this thesis. These tissue samples were harvested within a 1-hour window of the pigs being euthanised in each instance, with the laser processing trials themselves being performed within a 48-hour window of this harvesting process, as this is the period within which the tissue has been verified for not degrading too severely (*i.e.* degrading to the point where the relevance of the model to *in vivo* human tissue is potentially compromised) [3.30].

The cellular and morphological quality of the harvested tissue samples was preserved between the point of harvest and the laser ablation trials by being submerged in phosphate buffer solution within sealed containers that were subsequently placed on ice. The tissue samples were placed on DispoCut (CellPath Inc.) board upon being taken out of this chilled solution, which provides a stable surface for dissecting the samples down to more appropriate dimensions using a conventional scalpel. This DispoCut board was then placed within a petri dish, ensuring any bacteria from the *ex vivo* tissue samples were contained. This was important in ensuring compliance with the health and safety procedures that were in place as part of the University's biohazardous experimental protocols.

After the laser ablation trials were completed, half of the tissue samples were placed in 10% neutral buffered formalin solution (CellPath Inc.) for a period of 48 – 72 hours, after which they were transferred into a 70% ethanol solution. These samples were placed back into phosphate buffer solution for mailing to histological research project partners based at the University of Leeds, with them being replaced into 70% ethanol upon being received. This histological analysis allowed for any undesirable thermal or cavitation effects to be detected, via the presence of necrotic tissue and cavitation bubbles respectively, for the various laser processing parameters tested.

The other half of the samples were copies of those placed into the formalin solution with regards to the laser processing parameters used for the various ablated features, but these were instead submerged in 3% glutaraldehyde solution (25% solution, Sigma-Aldrich, diluted with deionised water) post-ablation. This rigidly fixed the tissue, allowing the ablated features to be measured via three-dimensional surface profilometry.

3.4.3 Histological and three-dimensional surface profilometry post-ablation analysis of tissue samples

The histological analysis procedure carried out within the pathology laboratories at the University of Leeds entailed the fixated tissues being processed via a tissue processor (ASP200, Leica) as part of a standard overnight protocol. After being embedded in Cellwax Plus (CellPath Inc.), thin sections of 4 µm width were cut into the sample using a manual rotary microtome (RM2235, Leica). These sections were then placed on glass microscope slides for haematoxylin and eosin staining. The haematoxylin and eosin (H&E) staining on the tissue enabled clear observation of the ablated depths and any collateral thermal damage around the surgical zone for each laser resected area.

Thermal damage margins were measured on a worst-case basis for each set of tested laser parameters by taking the maximum thickness of damaged/disrupted tissue surrounding the ablated site. Tissue damage/disruption was evaluated based on denaturing of the tissue, which is observed as a loss of cellular detail and therefore homogenisation of the tissue surrounding the ablated areas, as well as cavitation bubble

formation which is also clearly visible in the histology images as typically large (relative to the crypt and cellular structures) irregular white areas around the ablated regions. Reference scans are performed at high pulse repetition rates, high powers and slow stage scanning speeds (thus high spatial pulse overlaps) to induce such cavitation bubble formation, thermal buildup and/or carbonisation. These are implemented at both a known distance away from the rest of the ablated regions to correlate the ablated features in the tissue samples to the correct laser parameters and in an asymmetric manner to also act as a guide regarding the samples orientation in the histology images. An example of one of these reference features, as well as examples of the previously mentioned tissue denaturing and cavitation bubble formation are highlighted in figure 3.18.

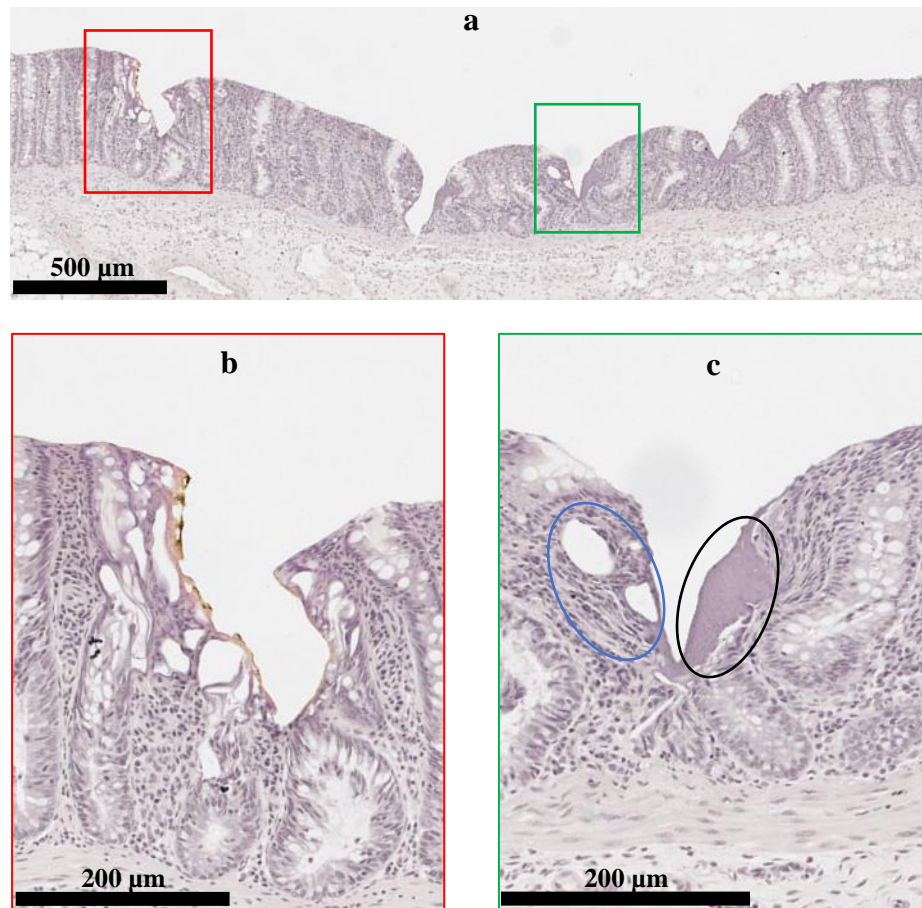


Figure 3.18 – Example H&E stained histology images of ultrafast laser ablated porcine intestinal tissue where a) showcases how the reference marks work with regards to knowing the sample orientation through asymmetrical design. Here a reference feature has been scanned to one side of the other three ablated features but not along the other. A zoomed in view of the reference feature is shown in b) with carbonisation and cavitation bubble formation being distinctly visible on the left edge and c) shows an example of an ablated feature with cavitation bubble formation to the left (circled in blue) and tissue denaturing/homogenisation to the right (circled in black).

For the three-dimensional profilometric measurements, a surface profilometer (InfiniteFocus G4, Alicona) was used (figure 3.19). This allowed for high resolution measurements of the laser ablated features created on the tissue surface. 5x, 10x, 20x and 50x magnification lenses were all tested, with the 10x and 20x usually being found to provide the best balance between appropriate resolutions and overall field-of-view for the ablated features that were examined throughout the work carried out within this thesis. The InfiniteFocus profilometer combines the small depth of focus from the various mounted microscope objective lenses with vertical scanning to form high resolution three-dimensional topographical profiles via

focus variation technology. This method stitches together a series of two-dimensional images that fall between the user defined top and bottom imaging planes (corresponding to focusing levels positioned just above and below the highest and lowest points of the ablated features respectively). This leads to the accurate reconstruction of three-dimensional surface profiles for the various laser ablated tissue samples.

The resolution of these three-dimensional measurements depends on the objective lens used, as this determines both the sampling rate of the reflected rays at each focus plane and the extent of averaging required by the algorithm that stitches these images together. The vertical resolution settings employed in this work were 3 μm , 1 μm and 0.3 μm for the 5x, 10x and 20x magnification objective lenses respectively unless otherwise stated. The fidelity of the measurements taken was assured by verifying the repeatability threshold information available within the IF-MeasureSuite software. The InfiniteFocus line of profilometers have previously been shown to benefit from a high level of repeatability in their measurements [3.31]. Line profile measurements taken from the captured surfaces were averaged over 50 lines.

The profilometer measurements taken in this work were used as a means of testing the repeatability of the laser parameters by cross-referencing the surface profiles and histology images obtained. While the measurement of biological tissues is unconventional with this type of device, the fixation processes (formalin or glutaraldehyde) provided the tissue samples with surface finishes that were compatible with the non-contact optical measurement modality.



Figure 3.19 – Alicona InfiniteFocus G4 surface profilometer.

Additionally, the Alicona enabled the fitting of reference planes to the captured surface profiles of the various tissue samples. This is helpful as it greatly improves the consistency of the line and surface profile measurements, with the zeroing of the sample coordinate system around the edges of the ablated features allowing for the inconsistent surface morphology between samples to be accounted for.

3.5 Initial Bessel-Gauss beam material processing trials

Initial ablation/material modification tests were performed on thermal paper and acrylic sheets (figure 3.20). This testing of the general ablation characteristics was carried out to gain familiarity with the comparatively unconventional beam propagation and beam properties. A translation stage (LTS150/M, Thorlabs) was setup to allow for fixed pulse overlaps in the x (horizontal) axis via tailoring the stage speed in accordance with the corresponding spot size. A MicroBlock XYZ flexure stage (17AMB003/MD, Melles Griot) was mounted on this translation stage to allow for positioning of samples with micron scale accuracy across all 3 axes. Ablation of the thermal paper was observed over the axial range of around 6 mm as expected for the standalone 20° axicon setup with the 5W 60 kHz laser preset being predominantly used to provide the highest possible pulse energy, although it is worthwhile noting that ablation was also possible using the 2W 60 kHz preset.

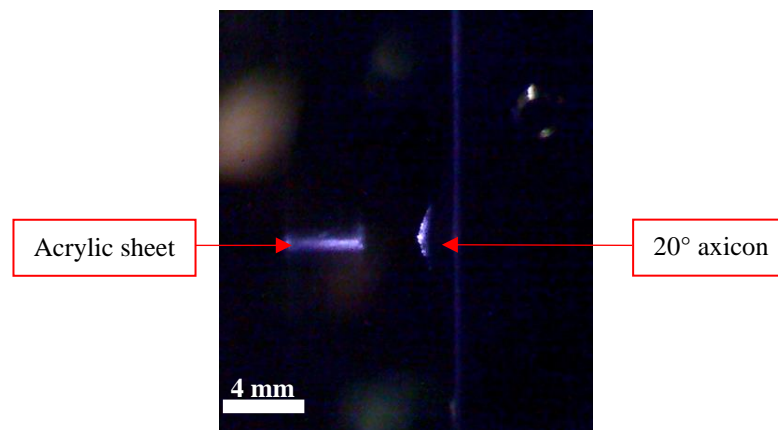


Figure 3.20 – Side profile image of material modification of acrylic sheet with the Bessel-Gauss beam produced by the 20° axicon. This was captured using an RS PRO USB digital microscope with an OD 1.0 ND filter to reduce saturation of the captured image.

The use of acrylic sheets was particularly insightful for this as transparent material processing is the most well-established application of Bessel beams within the existing scientific literature [3.32],[3.33]. It was observed that material modification occurred throughout the entire depth (approximately 4 mm) of the acrylic sheets with a single pass of the Bessel-Gauss beam, showcasing the increased focal depths that these beams can provide.

3.6 Preserved porcine tissue ablation trials

Following on from the initial ablation experiments with acrylic and thermal paper, trials were carried out on preserved porcine tissue (*i.e.* supermarket bought cooked ham). This provided a convenient way to study the ablation characteristics of various laser parameters on a soft tissue model that was inexpensive, readily available, easy to handle and non-biohazardous. The latter is of particular significance as this meant that the laboratory did not have to be locked down to exclude other users who were not authorised in the handling of freshly harvested, clinically relevant biological tissues prior to receiving the results from swab testing performed by the University's biological safety officer. These swab tests were required as part of the University's biohazardous experimental protocols to confirm the absence of any residual bacteria on the surfaces upon which these harvested tissues made contact. Additionally, the preserved porcine tissue samples possessed low surface waviness (highlighted in figure 3.21), with a measured S_a value of 8.6 ± 1.0

μm . This made them ideal for testing the focal ranges over which ablation was achievable for the various setups tested.

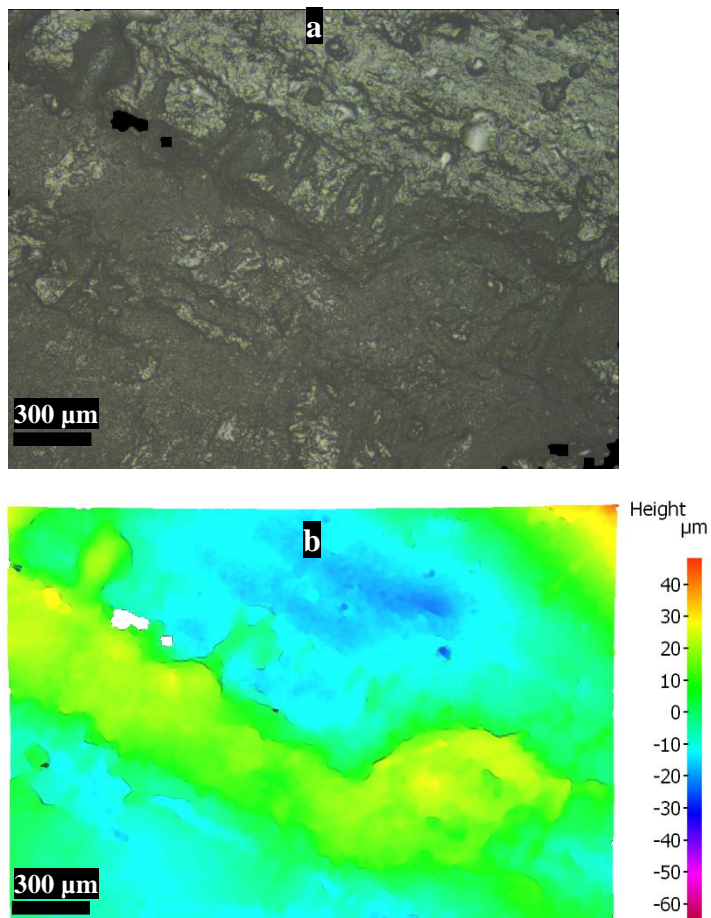


Figure 3.21 – Surface profile image in a) real colour and b) pseudo colour of non-ablated preserved porcine tissue obtained from the surface profilometer using the 5x magnification objective lens to extend the field-of-view over which the measurement was taken.

This profile was captured with a lateral resolution of $5\ \mu\text{m}$ and a vertical resolution of $1\ \mu\text{m}$.

With the standalone 20° axicon setup a white plasma plume could be observed on the surface of the preserved porcine tissue over an approximate range of around 3 mm. However, single passes of the Bessel-Gauss laser spot over this range produced only superficial features of less than $20\ \mu\text{m}$ depth at higher pulse energies, implying an impractically slow rate of ablation (figure 3.22). Ideally these depths would be in the sub-millimetre range to provide a balance between precise depth control and sufficient removal rates. Only two features were ablated on this sample due to these insufficient depths.

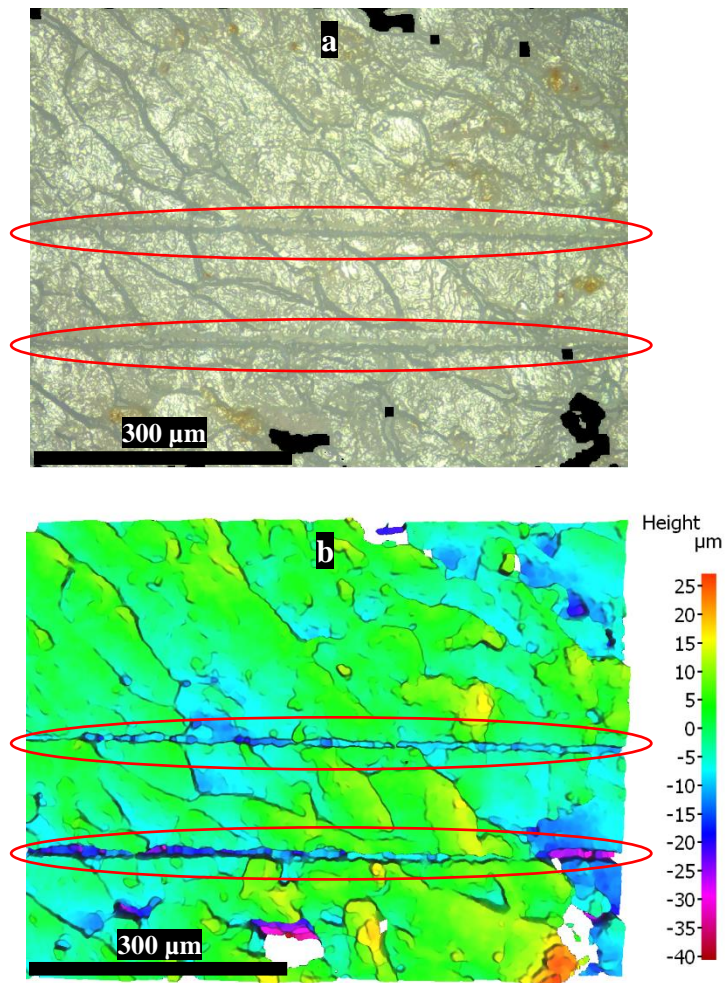


Figure 3.22 – 20x magnification surface profilometer image in a) real colour and b) pseudo colour of preserved porcine tissue (cooked ham) surface ablated with single passes of the Bessel-Gauss beam produced by the 20° axicon at 1 kHz and a 90% spatial pulse overlap. The ablated lines are circled in red. This profile was captured with a lateral resolution of 1 μm and a vertical resolution of 300 nm.

The white areas on the surface profile images are from missing data points. These arise from regions on the surface where the device is unable to receive the reflected light, typically due to said regions possessing high incline angles or sharp height transitions [3.34]. As a result, these typically show up in deeper/more distinct ablated cavities, although the inhomogeneous surfaces of the various tissues tested throughout the work carried out in this thesis presented some difficulties in optimising the lateral and vertical resolution settings for the range of objective lenses fitted to the InfiniteFocus G4 surface profilometer.

3.7 Murine intestinal tissue ablation trials

The first clinically relevant tissue trials were performed on murine intestinal tissue samples. These were harvested from a mouse colony developed at a project partner's site based at the University of Leeds. This model was formed with the intent to realise colorectal polyps within the harvested samples, with Apc (Min/+) mouse models acting as a popular animal model for abnormal cell growth within the human colon [3.35]. This complimented the porcine model previously used within the research group, as while the porcine model provides a more accurate analogue to human intestine with regards to both morphology and mechanical properties as covered previously in chapter 1, the onset and subsequent development of colorectal cancer is not observed within this species. The murine samples would therefore be able to provide

an opportunity to study the effects that the different mechanical properties between cancerous and healthy tissues have upon the ablation process, while also showcasing the potential for precise targeting of cancerous tumour sites using ultrashort pulsed lasers, which would not be possible using the porcine model alone.

The experimental setup consisted of a MicroBlock (17AMB003/MD, Melles-Griot) mounted to a translation stage (LTS150/M, Thorlabs) as shown in figure 3.23. The MicroBlock allowed for high resolution manual translation of the sample in the y- and z-axes, while the stage allowed for the sample to be moved relative to the incident Bessel-Gauss beam in the x-axis. This x-axis movement was automated via LabVIEW code. The murine intestine samples were pinned to DispoCut board. This DispoCut board was pinned to cork, which was glued to a petri dish. The petri dishes were stuck to a 90° angled bracket (which would allow for coarse adjustment along the z-axis to accommodate the intrinsic variation in thickness across the various tissue samples) via double sided adhesive tape, with this plate being mounted on a tilt platform (APY002/M, Thorlabs) for additional degrees of freedom with regards to the orientation of the tissue sample. This tilt platform was fitted to the top of the MicroBlock. An empty 30 mm cage plate (CP33/M, Thorlabs) was placed at the end of the cage system to prevent the conical tip of the 20° axicon that was protruding beyond the edge of the prior cage plate from colliding with the tissue samples. The tissue samples were vertically mounted to test the robustness of the ultrafast laser ablation process under a more operationally valid context (*i.e.* in an orientation where the lens is not directly above the tissue).

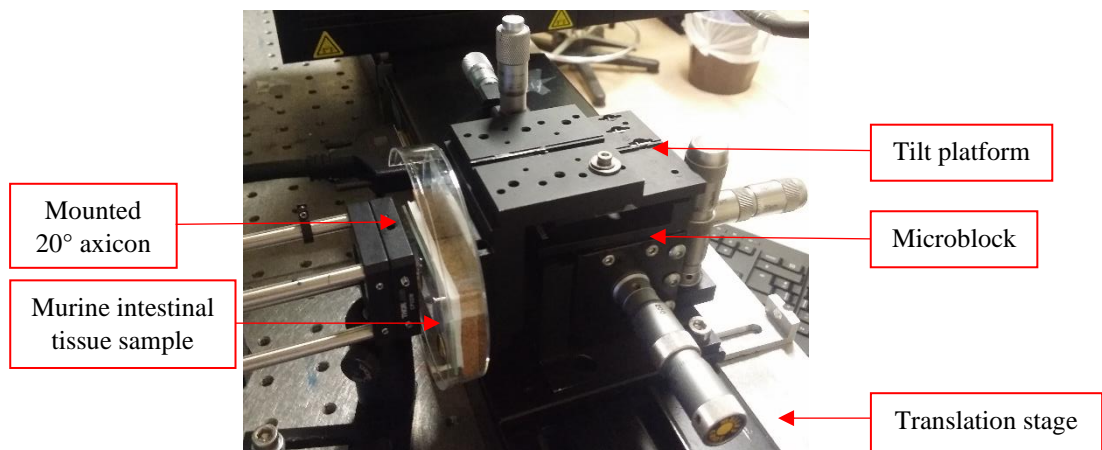


Figure 3.23 – Experimental setup used for the murine intestinal tissue ablation trials.

For these ablation trials, the standalone 20° axicon setup was tested with laser pulse repetition rates of 1, 3 and 5 kHz being primarily used, although some features were also scanned at 10 and 20 kHz. These higher repetition rates were implemented in an attempt to induce thermal damage/carbonisation from using the small spot size produced by the 20° axicon with high spatial and temporal overlaps of the applied laser pulses, allowing them to act as reference markers for the other ablated features. The number of passes was varied between 2 and 10 for the various lines scanned with the Bessel-Gauss beam across the 8 murine tissue samples that were tested. The spatial overlap of the laser pulses was mainly varied between 50% and 90%. The 5 W 60 kHz laser preset was used, providing a pulse energy of approximately 85 μ J.

The surfaces of the samples were viewed using an RS Pro USB microscope camera to determine if there were any ablation lines to be examined more closely using the Alicona InfiniteFocus G4 surface profilometer (figure 3.24). Those deemed suitable for further examination (either from visual feedback

during the ablation process itself or from this microscopic imaging process) were placed in a 3% glutaraldehyde fixative solution to preserve their surface properties.

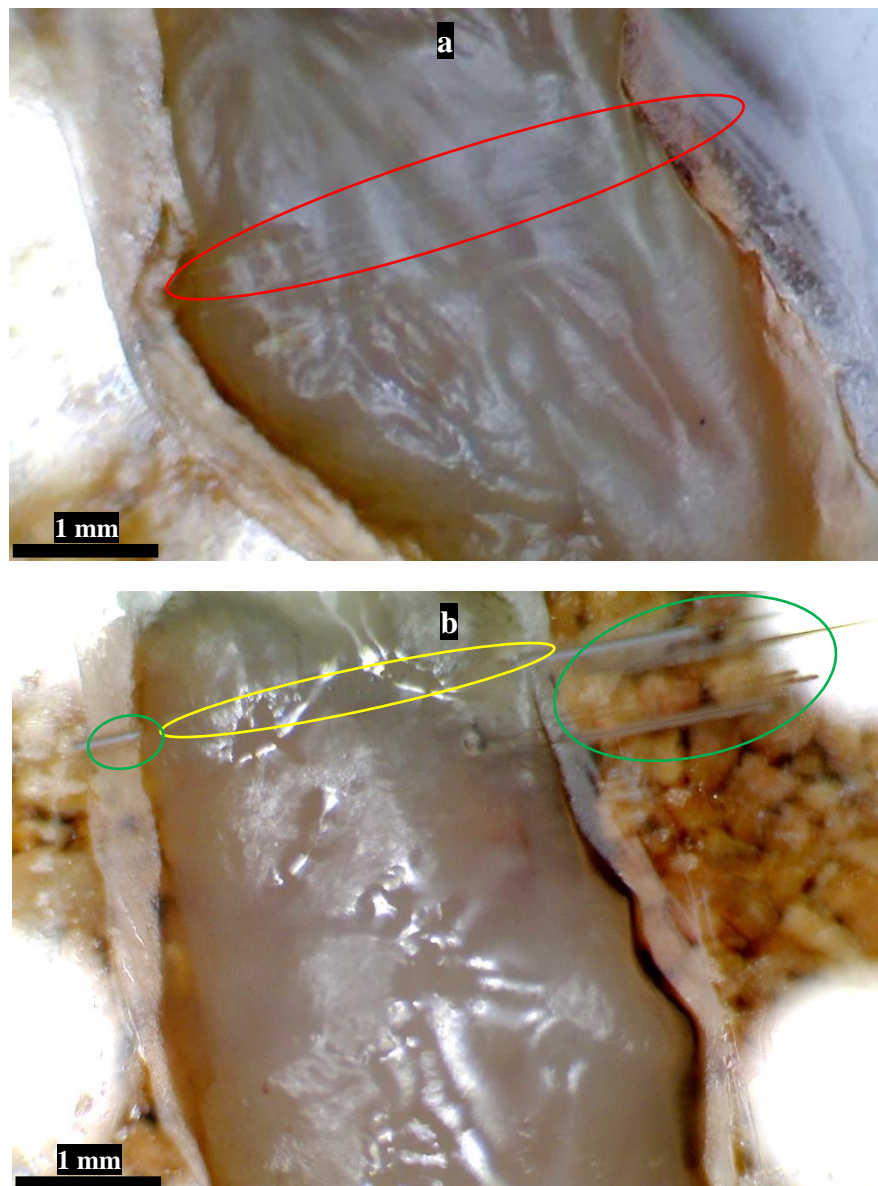


Figure 3.24 – Murine intestinal tissue samples mounted on glass slides with underlying cork board. In a) the region circled in red shows the ablation lines that appear to be on the murine tissue, but these were actually on the underlying glass. These features were thus transmitted through translucent sections of the tissue. In b) the region circled in yellow shows the reference line carried out at 10 kHz with 2 passes, showcasing some superficial thermal damage upon the surface of the tissue. The lines circled in green showcase surface ablation of the adjacent glass.

While some material modification was observed upon the glass underlying the transparent tissue, no ablation was observed upon the tissue surface itself except for some of the reference lines, despite the relatively high pulse energy applied (figures 3.25 and 3.26). In these instances, the marking upon the tissue surface can be attributed to the accumulation of thermal effects from the combination of the high pulse repetition rate, high spatial overlap and high number of passes, as opposed to the desired plasma-mediated ablation mechanisms.

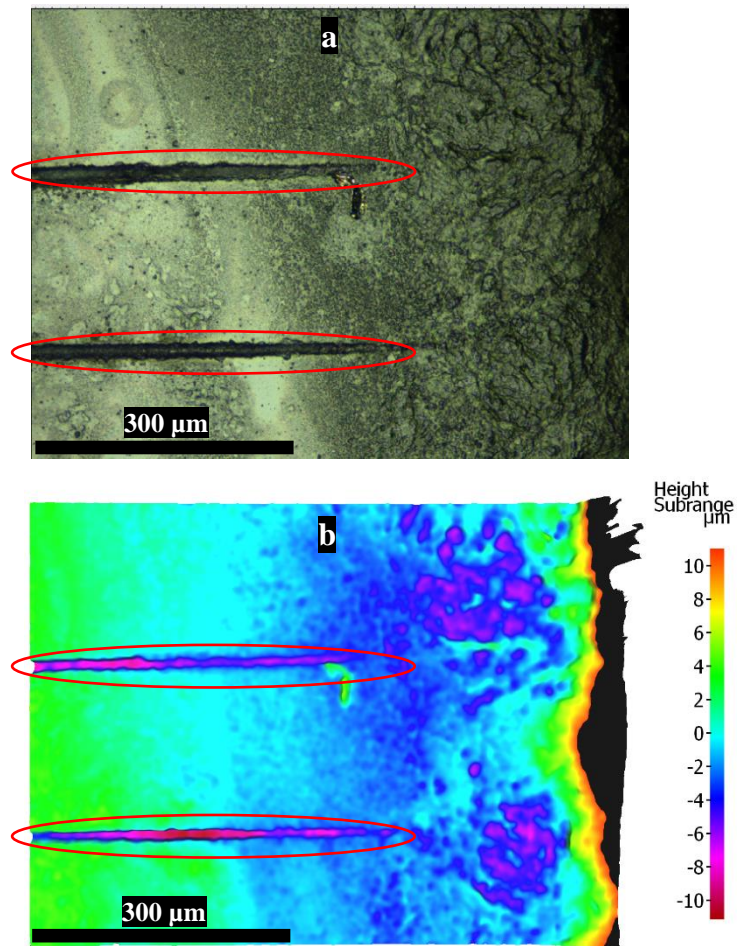


Figure 3.25 – 20x magnification surface profilometer image in a) real colour and b) pseudo colour of the edge transition between the glass microscope slide and the murine tissue. While surface ablation is observed upon the glass surface in the areas circled in red, this is not transferred across to the tissue surface. The features here were ablated with single passes of the Bessel-Gauss beam produced by the 20° axicon at 1 kHz and an approximately 90% spatial pulse overlap. The black area to the right of the pseudo colour image is the edge of the murine tissue which has been cut off via the colour scaling to allow clearer observation of the ablated areas. This profile was captured with a lateral resolution of 1 μm and a vertical resolution of 300 nm.

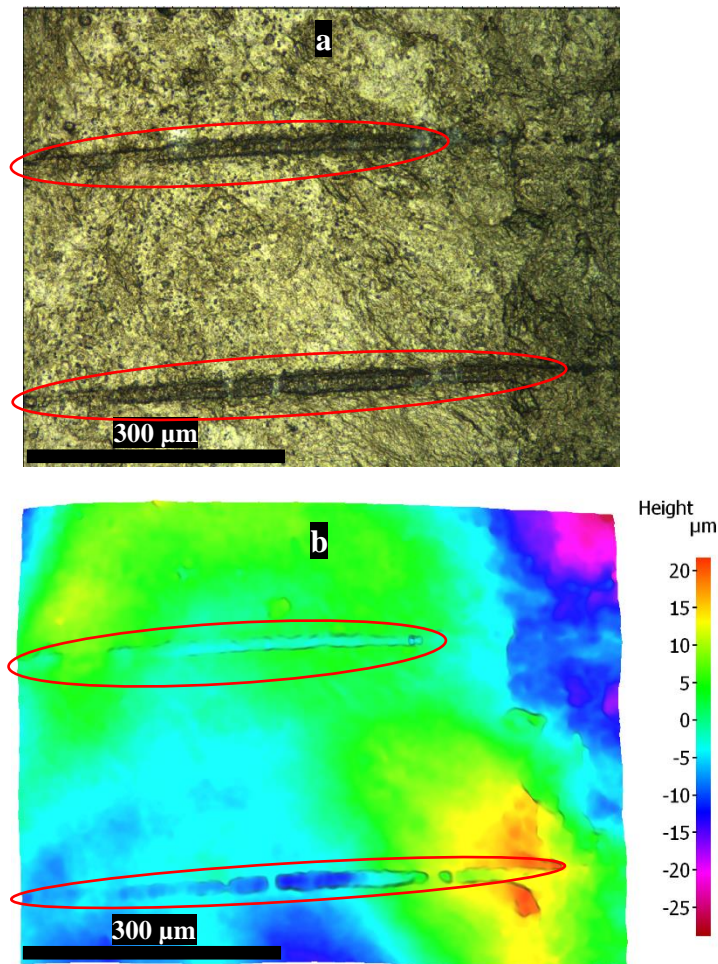


Figure 3.26 – 20x magnification surface profilometer image in a) real colour and b) pseudo colour of the murine tissue sample surface. While surface ablation is observed here in the areas circled in red, it is superficial in nature and can be attributed to thermal accumulation as opposed to originating from plasma-mediated mechanisms. The features here were ablated with six passes of the Bessel-Gauss beam produced by the 20° axicon at 20 kHz and an approximately 85% spatial pulse overlap. This profile was captured with a lateral resolution of 1 μm and a vertical resolution of 300 nm.

A prominent issue throughout these ablation trials was the relatively short working distance between the conical tip of the 20° axicon and the tissue. While this had not been an issue during the previous preserved porcine tissue trials, the significantly higher level of water retention within the murine intestinal tissue samples (which was maintained by being kept within the preservative phosphate buffer solution) led to a substantial degree of condensation building up on the axicon surface. This appeared to obstruct the laser pulses incident upon the tissue, despite the well-documented diffraction resistant nature of Bessel-Gauss beams. This also meant that the lens had to be cleaned numerous times between scanning lines, likely affecting the optical surface quality of the lens and further disrupting the time-sensitive trials. Again, while a 40° axicon (AX2540-B, Thorlabs) would offer higher intensities than the 20° axicon, this would come at the expense of further exacerbating this working distance issue.

To address this, a 10° axicon (AX2510-B, Thorlabs) was also tested. While this had a sufficient working distance from the conical tip to mitigate this condensation issue, it lacked the axial intensity required to realise plasma-mediated ablation upon the tissue surface. This also ruled out testing the rest of the axicons provided by Thorlabs in this standalone manner due to their lower physical angles leading to lower peak intensities, as illustrated by the POP modelling covered previously.

The murine intestine samples that were stored in the neutral buffered 10% formalin solution were over-fixated from being left for too long (over the University holiday period). This caused severe deformation of the morphology of the delicate murine tissue samples, with the surfaces becoming heavily wrinkled. This degradation effect on the histomorphology has been recorded in murine tissue samples previously, with 70% ethanol solutions stated as being preferable with regards to preserving both the quantity and quality of biomolecules within such tissue samples over longer periods [3.36]. Combining this development with the superficial nature of the ablated features, it was concluded that it was not worthwhile to send these samples for histological analysis.

With only superficial surface damage being obtained across the various murine intestinal tissue samples for the various tested axicons, an increase in the applied laser fluence was deemed necessary, due to the lack of nonlinear absorption processes (*i.e.* plasma formation) observed despite using the highest pulse energy the Carbide laser system was capable of producing (85 μJ). Combining this with the relatively limited murine intestinal tissue sample availability, it was determined that redesigning of the optical setup would be required prior to further laser ablation trials on clinically relevant tissue samples.

While there are numerous means of altering the Bessel-Gauss beams produced by axicons, including the intentional interference of multiple zero order beams with different radial and longitudinal wave vectors to reduce the central core diameter, these often come at the expense of actually causing a loss of intensity within the beam [3.37]. In this cited example this loss of intensity (despite the reduction of the central core diameter) occurs from the presence of destructive interference regions. A demagnifying telescope would simultaneously increase both the working distance and the fluence, while being comparatively simpler to experimentally implement and allowing for a greater degree of tailoring both in the lateral and axial dimensions [3.10]. This would address the two primary limitations of the various axicon setups that were tested for these ablation trials. The increase in intensity would be particularly significant, with 10 J cm^{-2} being recommended repeatedly within the existing literature for performing ablation of the mucosal layer within the gastrointestinal tract, albeit within the scope of radiofrequency ablation devices as opposed to laser systems [3.38]. Consequently, chapter 4 covers the design of this new experimental setup and the ablation results obtained from it.

3.8 References

- [3.1] “Custom Optics Manufacturing and OEM Ordering.” https://www.thorlabs.com/newgrouppage9.cfm?objectgroup_id=6843 (accessed Jun. 09, 2020).
- [3.2] “Optical Coatings.” https://www.thorlabs.com/newgrouppage9.cfm?objectgroup_id=5840 (accessed Jun. 10, 2020).
- [3.3] “Light Conversion Carbide Femtosecond Lasers for Industry and Science.” <https://www.lastek.com.au/ultrafast/compact-fsps/1821-light-conversion-carbide> (accessed Jun. 10, 2020).
- [3.4] B. Guo *et al.*, “Laser-based mid-infrared reflectance imaging of biological tissues,” *Opt. Express*, vol. 12, no. 1, p. 208, Jan. 2004, doi: 10.1364/opex.12.000208.
- [3.5] S. M. P. C. Mohanan *et al.*, “Preclinical evaluation of porcine colon resection using hollow core negative curvature fibre delivered ultrafast laser pulses,” *J. Biophotonics*, vol. 12, no. 11, Nov. 2019, doi: 10.1002/jbio.201900055.
- [3.6] H. T. Yura and T. S. Rose, “Gaussian beam transfer through hard-aperture optics,” *Appl. Opt.*, vol. 34, no. 30, p. 6826, Oct. 1995, doi: 10.1364/ao.34.006826.
- [3.7] A. Müller, M. C. Wapler, and U. Wallrabe, “Depth-controlled Bessel beams,” *Int. Conf. Opt. MEMS Nanophotonics*, vol. 2016-September, Jul. 2016, doi: 10.1109/OMN.2016.7565918.
- [3.8] N. Trappe, R. Mahon, W. Lanigan, J. A. Murphy, and S. Withington, “The quasi-optical analysis of Bessel beams in the far infrared,” *Infrared Phys. Technol.*, vol. 46, no. 3, pp. 233–247, Jan. 2005, doi: 10.1016/j.infrared.2004.04.002.
- [3.9] E. Elliot, “Using Physical Optics Propagation (POP), Part 2: Inspecting the beam intensities · MyZemax,” 2016. <https://my.zemax.com/en-US/Knowledge-Base/kb-article/?ka=KA-01602> (accessed May 04, 2021).
- [3.10] J. Dudutis, P. GeČys, and G. RaČiukaitis, “Non-ideal axicon-generated Bessel beam application for intra-volume glass modification,” *Opt. Express*, vol. 24, no. 25, pp. 28433–28443, Dec. 2016, doi: 10.1364/oe.24.028433.
- [3.11] M. Lamperti *et al.*, “Invited Article: Filamentary deposition of laser energy in glasses with Bessel beams,” *APL Photonics*, vol. 3, no. 12, p. 120805, Dec. 2018, doi: 10.1063/1.5053085.
- [3.12] C. W. Cheng, “Ablation of copper by a scanning Gaussian beam of a femtosecond laser pulse,” *Int. J. Adv. Manuf. Technol.*, vol. 92, no. 1–4, pp. 151–156, Sep. 2017, doi: 10.1007/s00170-017-0101-z.
- [3.13] S. I. Mitryukovskiy, Y. Liu, A. Houard, and A. Mysyrowicz, “Re-evaluation of the peak intensity inside a femtosecond laser filament in air,” *J. Phys. B At. Mol. Opt. Phys.*, vol. 48, no. 9, p. 094003, May 2015, doi: 10.1088/0953-4075/48/9/094003.
- [3.14] P. S. Tsai *et al.*, “Plasma-mediated ablation: an optical tool for submicrometer surgery on neuronal and vascular systems,” *Curr. Opin. Biotechnol.*, vol. 20, no. 1, pp. 90–9, Feb. 2009, doi: 10.1016/j.copbio.2009.02.003.
- [3.15] A. Vogel and V. Venugopalan, “Mechanisms of pulsed laser ablation of biological tissues,” *Chem. Rev.*, vol. 103, no. 2, pp. 577–644, Feb. 2003, doi: 10.1021/cr010379n.
- [3.16] P. Polesana *et al.*, “Near-field dynamics of ultrashort pulsed Bessel beams in media with Kerr nonlinearity,” *Phys. Rev. E - Stat. Nonlinear, Soft Matter Phys.*, vol. 73, no. 5, 2006, doi: 10.1103/PhysRevE.73.056612.
- [3.17] K. Jamshidi-Ghaleh and N. Mansour, “Nonlinear absorption and optical limiting in Duran glass induced by 800 nm femtosecond laser pulses,” *J. Phys. D. Appl. Phys.*, vol. 40, no. 2, pp. 366–369, Jan. 2007, doi: 10.1088/0022-3727/40/2/012.
- [3.18] R. Stoian, M. K. Bhuyan, G. Zhang, G. Cheng, R. Meyer, and F. Courvoisier, “Ultrafast Bessel beams: Advanced tools for laser materials processing,” *Advanced Optical Technologies*, vol. 7, no. 3, pp. 165–174, 2018. doi: 10.1515/aot-2018-0009.
- [3.19] O. Brzobohatý, T. Čižmár, and P. Zemánek, “Quasi-Bessel beam generated by oblate-tip axicon,” in *16th Polish-Slovak-Czech Optical Conference on Wave and Quantum Aspects of Contemporary Optics*, Dec. 2008, vol. 7141, p. 714126. doi: 10.1117/12.822425.
- [3.20] “Mounted N-BK7 Plano-Convex Lenses (AR Coating: 650 - 1050 nm).” https://www.thorlabs.com/newgrouppage9.cfm?objectgroup_id=6278 (accessed Aug. 10, 2020).
- [3.21] “Thorlabs - DCC1645C USB 2.0 CMOS Camera, 1280 x 1024, Color Sensor.” <https://www.thorlabs.com/thorProduct.cfm?partNumber=DCC1645C> (accessed Mar. 17, 2021).
- [3.22] O. Brzobohatý, P. Zemánek, and T. Čižmár, “High quality quasi-Bessel beam generated by round-tip axicon,” *Opt. Express*, Vol. 16, Issue 17, pp. 12688-12700, vol. 16, no. 17, pp. 12688–12700, Aug. 2008, doi: 10.1364/OE.16.012688.
- [3.23] P. Wu, C. Sui, and W. Huang, “Theoretical analysis of a quasi-Bessel beam for laser ablation,” *Photonics Res.*, vol. 2, no. 3, pp. 82–86, 2014, doi: 10.1364/prj.2.000082.
- [3.24] “Axicons, UV Fused Silica.”

- https://www.thorlabs.com/newgrouppage9.cfm?objectgroup_id=4277&pn=AX2520-B#4282 (accessed Mar. 10, 2021).
- [3.25] S. M. P. C. Mohanan, "Picosecond laser procedures to enhance the efficacy of tissue resection," Heriot-Watt University, Edinburgh, 2019. Accessed: Sep. 07, 2021. [Online]. Available: <https://www.ros.hw.ac.uk/handle/10399/4246>
- [3.26] P. Wongchadukul and P. Rattanadecho, "Mathematical modeling of multilayered skin with embedded tumor through combining laser ablation and nanoparticles: Effects of laser beam area, wavelength, intensity, tumor absorption coefficient and its position," *Int. J. Heat Technol.*, vol. 39, no. 1, pp. 89–100, Feb. 2021, doi: 10.18280/IJHT.390109.
- [3.27] A. A. Oraevsky *et al.*, "Plasma mediated ablation of biological tissues with nanosecond-to-femtosecond laser pulses: Relative role of linear and nonlinear absorption," *IEEE J. Sel. Top. Quantum Electron.*, vol. 2, no. 4, pp. 801–809, 1996, doi: 10.1109/2944.577302.
- [3.28] N. Tinne, E. Lübking, H. Lubatschowski, A. Krüger, and T. Ripken, "The influence of a spatial and temporal pulse-overlap on the laser-tissue-interaction of modern ophthalmic laser systems," *Biomed. Eng. / Biomed. Tech.*, vol. 57, no. SI-1-Track-P, pp. 302–305, Sep. 2012, doi: 10.1515/BMT-2012-4115.
- [3.29] N. Tinne, B. Kaune, A. Krüger, and T. Ripken, "Interaction Mechanisms of Cavitation Bubbles Induced by Spatially and Temporally Separated fs-Laser Pulses," *PLoS One*, vol. 9, no. 12, p. e114437, Dec. 2014, doi: 10.1371/JOURNAL.PONE.0114437.
- [3.30] R. J. Beck *et al.*, "Dynamics of picosecond laser ablation for surgical treatment of colorectal cancer," *Sci. Rep.*, vol. 10, no. 1, Dec. 2020, doi: 10.1038/S41598-020-73349-W.
- [3.31] R. Danzl, F. Helml, and S. Scherer, "Automatic Measurement of Calibration Standards with Arrays of Hemi-Spherical Calottes," *Proc. 11th Int. Conf. Metrol. Prop. Eng. Surfaces*, pp. 44–46, 2007.
- [3.32] G. Zhang, R. Stoian, W. Zhao, and G. Cheng, "Femtosecond laser Bessel beam welding of transparent to non-transparent materials with large focal-position tolerant zone," *Opt. Express*, vol. 26, no. 2, p. 917, Jan. 2018, doi: 10.1364/oe.26.000917.
- [3.33] G. Cheng, A. Rudenko, C. D'Amico, T. E. Itina, J. P. Colombier, and R. Stoian, "Embedded nanogratings in bulk fused silica under non-diffractive Bessel ultrafast laser irradiation," *Appl. Phys. Lett.*, vol. 110, no. 26, p. 261901, Jun. 2017, doi: 10.1063/1.4987139.
- [3.34] W. Kaplonek, K. Nadolny, and G. M. Królczyk, "The use of focus-variation microscopy for the assessment of active surfaces of a new generation of coated abrasive tools," *Measurement Science Review*, vol. 16, no. 2. Slovak Academy of Sciences - Inst. Measurement Science, pp. 42–53, Apr. 01, 2016. doi: 10.1515/msr-2016-0007.
- [3.35] K. Washington and A. E. D. Zemper, "Apc-related models of intestinal neoplasia: a brief review for pathologists," *Surg. Exp. Pathol. 2019 21*, vol. 2, no. 1, pp. 1–9, Apr. 2019, doi: 10.1186/S42047-019-0036-9.
- [3.36] J.-Y. Chung *et al.*, "Histomorphological and Molecular Assessments of the Fixation Times Comparing Formalin and Ethanol-Based Fixatives:," <https://doi.org/10.1369/0022155417741467>, vol. 66, no. 2, pp. 121–135, Nov. 2017, doi: 10.1369/0022155417741467.
- [3.37] A. Kolodziejczyk, A. Kujawski, C. Gomez-Reino, and Z. Jaroszewicz, "Diffractive patterns of small cores generated by interference of Bessel beams," *Opt. Lett. Vol. 21, Issue 12, pp. 839-841*, vol. 21, no. 12, pp. 839–841, Jun. 1996, doi: 10.1364/OL.21.000839.
- [3.38] A. T. Committee *et al.*, "Radiofrequency ablation devices," *VideoGIE*, vol. 2, no. 10, p. 252, Oct. 2017, doi: 10.1016/J.VGIE.2017.06.002.

Chapter 4

Optical redesign for lower pulse repetition rate porcine intestinal tissue ablation trials

4.1 Optical redesign

4.1.1 Design of reimaged Bessel-Gauss beam setup

As discussed at the end of the previous chapter, the need to redesign the optical setup was identified from performing the murine intestinal tissue ablation trials. A demagnifying telescope was implemented, as this would simultaneously address the two primary issues of the standalone 20° axicon setup, which were:

- the excessively short standoff from the conical tip
- the lack of sufficient fluence to achieve significant and repeatable plasma-mediated ablation of the murine intestinal tissue across the Bessel zone of the generated Bessel-Gauss beam.

Although it remained uncertain whether these would also be issues for porcine intestinal tissue trials (*i.e.* if the porcine intestinal tissue would similarly lead to excessive condensation building up on the conical surface of the axicon despite its significantly different morphological properties compared to those of the murine intestinal tissue, and if the different absorptive properties of the more solid, opaque porcine tissue would lend itself to more easily attainable plasma-mediated ablation processes), it was decided that an appropriate optical setup should ultimately remain fairly robust to both of these issues regardless, particularly for the endoscopic applications under consideration for the work carried out within this thesis. The merit of such reimaged Bessel-Gauss beams has been showcased in ultrashort laser welding studies, where the large non-diffractive focal depth eased the focal plane positioning requirements over fivefold, although it is important to note that this required increasing the pulse energy from 2 μJ to 8 μJ to achieve similar welding performance as the Gaussian beam across this extended focal depth [4.1].

Alternatively, shorter pulse durations would have significantly increased the peak intensity of the generated Bessel-Gauss beam, potentially allowing for plasma-mediated ablation with this standalone 20° axicon setup. However, as previously discussed in chapters 2 and 3, these would not be well suited for delivery through optical fibres due to the nonlinear effects that are encountered for shorter laser pulses [4.2]. It has also been suggested that picosecond pulses are likely more efficient than femtosecond pulses with regards to laser energy deposition, albeit with the stipulation that this was in fused silica and borosilicate glass and that a sufficient fluence level was reached with the longer pulses [4.3].

Efficient transmission of the input pulse energy was one of the primary concerns due to the endoscopically deployable solution sought after. As effective plasma-mediated ablation of porcine intestinal tissue has already been showcased at lower pulse energies with the same laser system using different optical setups, a more efficient system design was deemed to be the most appropriate course of action towards the investigation of the impact that different beam shapes and smaller spot sizes have upon this process [4.4],[4.5].

Consequently, the required reimaging telescope was designed within the OpticStudio software suite. This reimaging telescope would inevitably compress the axial extent of the Bessel zone as well, thus it was

important to carefully consider the degree to which this demagnification occurred. This concept is showcased in figure 4.1. Here w_0 is the input beam radius, $Z_{\text{Bessel Zone}}$ indicates the axial extent of the unmodified Bessel-Gauss beam generated by the axicon from the Gaussian input beam and L_1 and L_2 are lenses 1 and 2 of respective focal lengths f_1 and f_2 . As the axial range of the Bessel zone is compressed (or extended if a magnifying telescope is used) by a factor approximately equal to the squared product of the magnification factor, if too high a demagnification factor was used then the prospective advantages of the Bessel-Gauss beam (*i.e.* increased tolerance against defocusing and higher achievable aspect ratio of the ablated features) would potentially be lost [4.6]. However, a more subtle extent of demagnification would allow for a notable increase of the on-axis intensity throughout the reimaged Bessel zone, as the Bessel-Gauss beam would be both laterally and axially compressed. Also, while a reimaging telescope provides the opportunity for spatial filtration of the Bessel-Gauss beam to remove the modulation of the axial intensity, this would further reduce the transmission efficiency of the beam, thus this was not implemented within the scope of this work [4.7].

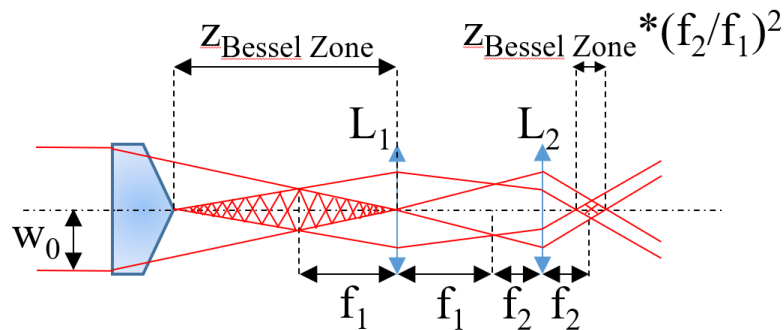


Figure 4.1 – Ray trace schematic of demagnified axicon setup using a 4F optical system. Figure adapted from reference 4.6.

A 50 mm plano-convex lens (LA1131-B, Thorlabs) was used as the objective lens in this setup (L_1 in figure 4.1), as this prevented clipping of the beam while also providing some flexibility regarding the extent to which the Bessel-Gauss beam would be demagnified. A 35 mm plano-convex lens (LA1027-B, Thorlabs) was used for the imaging lens (L_2 in figure 4.1), as this gave a modest demagnification factor of approximately 1.4x, while also providing the increased standoff that was desired courtesy of the larger working distance. This telescope was collimated using the REAY and RAED operands within the Merit Function Editor, as done previously for the 10x magnification beam expander designed in chapter 3. This optical setup is shown in Appendix 2a. The POPD operand was also used to set the M^2 value of this beam to 1.3, as measured previously using a scanning slit beam profiler by Dr. Mohan (BeamMap 2, Dataray), and the $1/e^2$ diameter of the input beam to 2.6 mm [4.8]. This demagnification factor provides a theoretical core diameter of approximately $3.2 \mu\text{m}$, based on both the experimentally measured and theoretically calculated values (obtained using POP simulations and equations cited within the scientific literature).

While this small spot size would present numerous challenges, including characterisation of the beam, more computationally intensive theoretical modelling through increased sampling demands, lower ablation depths and slower ablation processes (due to both slower scanning speeds being required for equivalent spatial pulse overlaps and the spot itself being smaller), it would also be an important step towards the realisation of an endoscopically deployable device. The minimally invasive nature of such procedures necessitates shorter focal lengths, which in turn produce smaller laser spots. The previously published work

within the group on this subject has predominantly involved the use of a galvo-scanhead setup with a 100 mm focal length f-theta lens that has a focal depth of approximately 470 μm , but the clinical (endoscopic) equivalent would likely be on the order of 10s of microns based on the shorter focal lengths required [4.4],[4.5],[4.8]. The significance of the lateral accuracy (*i.e.* the degree of thermal damage confinement) of the plasma-mediated ablation processes for the surgical applications under consideration also lends itself well to the testing of smaller laser spot sizes. Additionally, the maximum scanning speed is typically one of the limiting factors in endoscopic device designs, and a smaller spot size would potentially allow for ablation processes to be performed at higher laser pulse repetition rates due to the reduced spatial overlap for a given scanning speed compared to larger laser spots [4.9].

The smaller spot sizes would also be potentially beneficial in observing plasma formation at lower input pulse energies due to the associated increase in intensity that more tightly focused spots provide. Additionally, the use of smaller spots can further help in the avoidance of self-focusing as this undesirable nonlinear effect depends only on the peak power of the pulse, although it is noted that the reduced power requirements for achieving plasma-mediated ablation come at the expense of increased spherical aberrations, particularly when focusing into the tissue without the use of refraction index matching immersion fluid [4.10],[4.11]. This in turn increases the focal volume, which can reduce the precision of ablation.

While the imperfect axicon tip model would have been interesting to test within the OpticStudio software for the reimaged Bessel-Gauss beam setup, the high axial and lateral sampling required to observe the intensity oscillations, combined with the comparatively long simulated propagation distance (particularly for a high conical angle axicon where the central cores a smaller, thus requiring greater sampling), prohibited this from being implemented. Therefore, for an appropriate comparison, an optical setup that would produce a Gaussian spot of roughly the same size as the central core of the reimaged Bessel-Gauss beam at its focus was designed.

4.1.2 Design of Gaussian beam setup

For the surgical applications under consideration, precision (both lateral and axial) is of paramount importance. As a result, equating the spot sizes of the different beam shapes was found to be the most appropriate way to facilitate comparison of the two different beam shapes within this work. This is a consequence of there being no standardised way of comparing these two different beam shapes in material processing contexts (due to the intrinsic way the Bessel-Gauss beam is formed, with there being no classical “focus”). While Matsuoka *et al.* used “micron sized” spots and the axial ranges over which the Gaussian and Bessel-Gauss beams maintained at least 80% of their respective peak fluences to compare the two different beam shapes for performing micro drilling of austenitic stainless steel, this led to the use of a Bessel-Gauss beam of 6 μm $1/e^2$ diameter and a Gaussian spots of 26 μm and 11 μm $1/e^2$ diameters [4.12]. As spatial pulse overlap is one of the key variables examined within the scope of this thesis, this would lead to noticeably different scanning speeds for equivalent spatial overlaps and pulse repetition rates. Consequently, this was concluded to be an inappropriate way to equate the two beams for the surgical contexts in mind.

While increased spherical aberration would be an inevitable consequence of going to such small spot sizes with a conventional Gaussian beam shape, this trend towards smaller spot sizes is necessary for progressing

towards an endoscopically deployable device as previously discussed. This is due to the short focal lengths that will be required because of the constraints placed on the working distances from the probe head to be compatible with the intended minimally invasive operational modality. While longer focal lengths could potentially be implemented for the focusing lens at the end of the probe head, this would require the length of the probe head to be increased to give the beam output by the fibre bundle a longer axial range over which to diverge (effectively increasing the input beam size to the focusing lens, producing smaller spots for set focal lengths). This is clearly undesirable as this further inhibits the achievable degree of miniaturisation for the probe head design. Additionally, this spot size was above the diffraction limit.

To design the optical setup that would produce a focused Gaussian spot of around 3.2 μm , the following equation was used:

$$2w_o = \frac{4\lambda f M^2}{\pi D}; \quad (4.1)$$

where w_o is the beam waist radius, λ is the wavelength of the laser source, f is the focal length of the focusing lens, M^2 is the laser beam quality factor and D is the diameter of the input beam. From this equation, the required diameter of the input beam to produce the desired Gaussian spot of approximately 3.2 μm diameter using a 25.4 mm focal length convex focusing lens (LA1951-B, Thorlabs) was determined to be equal to 13 mm. The 1028 nm wavelength input beam produced by the Carbide laser had a previously measured M^2 value of 1.3 [4.8]. As the 5W 60 kHz preset of the Carbide had been previously measured to output a beam of 2.6 mm $1/e^2$ diameter, it was determined that a beam expander with a magnification factor of around 5 would need to be placed prior to the 25.4 mm focal length convex focusing lens.

To achieve this desired level of beam magnification, a Galilean beam expander consisting of a -50mm plano-concave lens (LC1715-B, Thorlabs) and 250 mm plano-convex lens (LA1461-B-ML, Thorlabs) was implemented prior to the 25.4 mm plano-convex focusing lens. This beam expander is shown in Appendix 2b. While lens-based beam expanders can introduce chromatic aberrations, the use of longer pulses in this work helps to account for propagation time delay and defocus dispersion is mitigated through the relatively narrow emission bandwidth of the Carbide CB1-05 laser system [4.13]. This telescope was again collimated using the REAY and RAED operands within the Merit Function Editor, with the calculated optimal distance between the lenses equaling 198.75 mm. This was congruent with the distance obtained by subtracting the focal length of the plano-concave lens from the back focal length of the plano-convex lens (197.4 mm) [4.14]. The peak irradiance, divergence (from the RAED operand, which gave a divergence value that was reduced by the magnification factor of the telescope as expected) and $1/e^2$ diameter of the beam output by this simulated telescope were recorded and used as the input beam definition for the 25.4 mm plano-convex focusing lens, as this would allow higher resolution sampling of the beam around the focus region without it being hindered by the frame widths imposed by the prior surfaces of the optical setup. This expanded beam being input to the focusing lens is shown in Appendix 2c. The curved surface of the lens is placed facing the incident collimated beam to reduce the spherical aberration [4.15].

To examine the extent of aberration present in the system a Seidel plot was produced, as shown in Appendix 2d. The Seidel plot is useful for analysing systems where third order aberrations are dominant, as is the

case here. The Seidel coefficients are calculated using the vertex power of the optics along with the chief (outermost) and marginal (innermost) rays, thus taking the whole field of view of the system into account. Appendix 2d shows that the spherical aberration is the dominant source of aberration in this system. Another concern would be the limited focal depth that such a tightly focused spot provides, with this being an inherent limitation of the Gaussian beam shape. This arises from the following relationship for the Rayleigh range:

$$z_r = \frac{\pi w_o^2}{M^2 \lambda}; \quad (4.2)$$

where z_r is the Rayleigh range and w_o is the beam waist radius. The depth of focus is often quoted as being equal to double this range for Gaussian beams. For the tightly focused $\approx 3 \mu\text{m}$ diameter Gaussian beam considered here, this gives a theoretical Rayleigh range of $24 \mu\text{m}$ (or a depth of focus of $48 \mu\text{m}$).

However, even with the beam being highly divergent from this tight focusing, it would still be able to achieve plasma-mediated ablation of tissue across a range of several $100 \mu\text{m}$ as a result of it maintaining a spot size on the order of 10 's of microns over said range from the equation:

$$w(z) = w_o \sqrt{1 + \left(\frac{M^2 \lambda z}{\pi w_o^2}\right)^2}; \quad (4.3)$$

where $w(z)$ is the radius of the laser spot at position z along the beam propagation axis. The spot size at focus was tested via the POP feature within the OpticStudio software, using the REAY operand to find the focus position and the same input beam parameters as those previously used for the axicon modelling carried out in chapter 3 to simulate the 1028 nm Carbide laser input source that was used experimentally. The simulated focused spot is shown in figure 4.2.

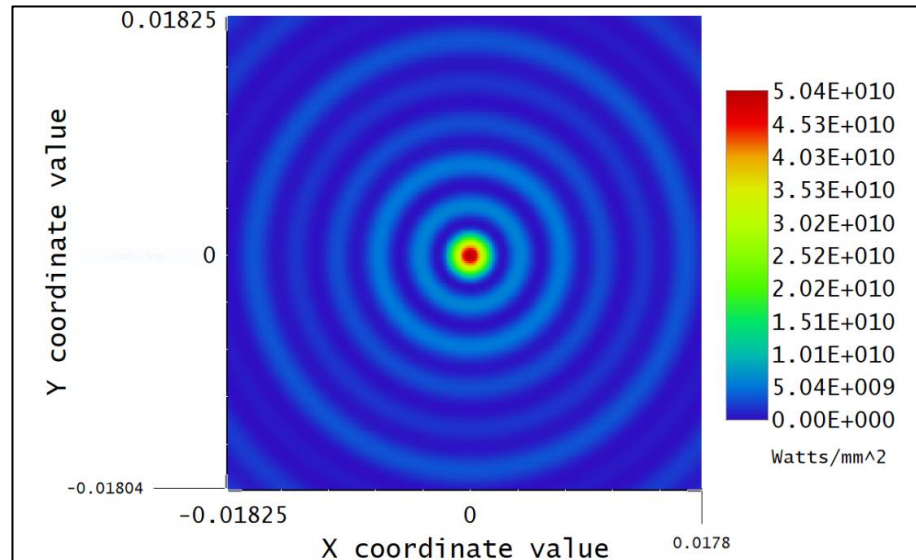


Figure 4.2 – Irradiance profile of the Gaussian beam at focus. The X and Y coordinate value axes are in units of mm.

By examining the cross-sectional data of the irradiance profile at focus, the $1/e^2$ central spot diameter was confirmed to be equal to $3.2 \mu\text{m}$ as expected. The surrounding rings are a consequence of some spherical aberration but were of considerably lower intensity than the central core. While this would avoid plasma formation across these rings, they may still contribute to some residual thermal damage.

4.2 Spot size measurements

4.2.1 BP209-VIS/M profiler measurements

The BP209-VIS/M profiler from Thorlabs was specified as being compatible with beam diameters as small as $2.5\ \mu\text{m}$ [4.16]. Additionally, the profiler can be used to measure pulsed laser beams with repetition rates greater than 10 Hz and wavelengths between 200 and 1100 nm, making it compatible with the Carbide laser system. The Thorlabs “Beam” analysis software that this profiler uses was also specified as being able to perform both Gaussian and Bessel fits to the measured beam profiles.

The $25\ \mu\text{m}$ slits were used in conjunction with the knife-edge mode, as this was necessary to resolve beams with diameters under $20\ \mu\text{m}$. The photodiode bias was turned on as this shortens the rise/fall time which is important for measuring small beam diameters. The scan rate was reduced to 2.1 Hz and the bandwidths were switched to the maximum of 1000 kHz as these settings provide the maximum spatial resolution of $0.13\ \mu\text{m}$. The measurements for both the Bessel-Gauss and Gaussian beams are shown in figure 4.3.

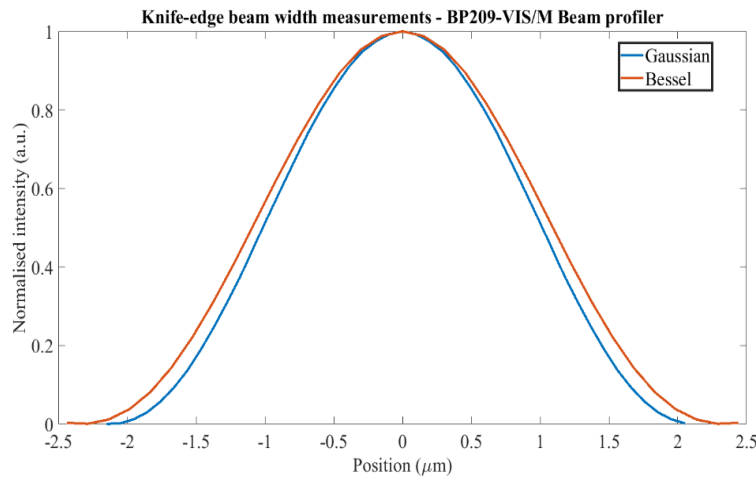


Figure 4.3 – Knife-edge profile measurement of the Gaussian beam from the BP209-VIS/M scanning slit profiler.

While stable $1/e^2$ diameter measurements within the expected range of $3 - 4\ \mu\text{m}$ were obtained from the knife-edge profiles ($3.5 \pm 0.3\ \mu\text{m}$ for Bessel, $3.3 \pm 0.3\ \mu\text{m}$ for Gaussian), there were several limitations encountered with these measurements. The first was regarding the mismatch between the “Measured Data” and “Reconstructed Knife-Edge Data”. This is due to the reliance on scanning slits that are larger than the beam diameter, leading to there being no direct display of the knife-edge measurement, with it instead acting as an overlay.

Additionally, despite the high resolution used, the knife-edge measurements were hindered by slight positional instability of the edges of the measured beam. This arises from both the relatively low pulse repetition rate of the respective measured beams and long pulse duration, as the photodiode has to average a series of input pulses to approximate a continuous wave (CW) signal. This allows for the current amplifier to accurately approximate pulsed laser sources with high repetition rates ($\approx 100\ \text{MHz}$) and short pulse durations ($< 100\ \text{fs}$) as CW sources, as the limited bandwidth of the current amplifier within the photodiode is unable to resolve individual pulses for these laser parameters. Consequently, the “Hold Maximum” function had to be applied in combination with scan rates that were not a direct integer multiple of the pulse repetition rate (hence the 2.1 Hz scan rate applied, as opposed to the minimum of 2 Hz), as this ensures that

each scan measures a different portion of the beam profile, which was important for trying to approximate the lower repetition rate, longer pulse duration beam profiles as CW sources as accurately as possible.

Finally, due to the scanning slit nature of the profiler, the “Measured Data” for both the Gaussian and Bessel-Gauss beams was stretched as a result of the scanning slit profile relying on summed row or column plots, meaning that the minimums (spaces of destructive interference between spherical aberration rings and annular rings respectively) do not go to zero as seen in figure 4.4. This, in combination with the need to again apply the “Maximum Hold” function due to the laser source being pulsed, causes some stretching of the “Measured Data” profiles from slight positional instabilities of the beam profile.

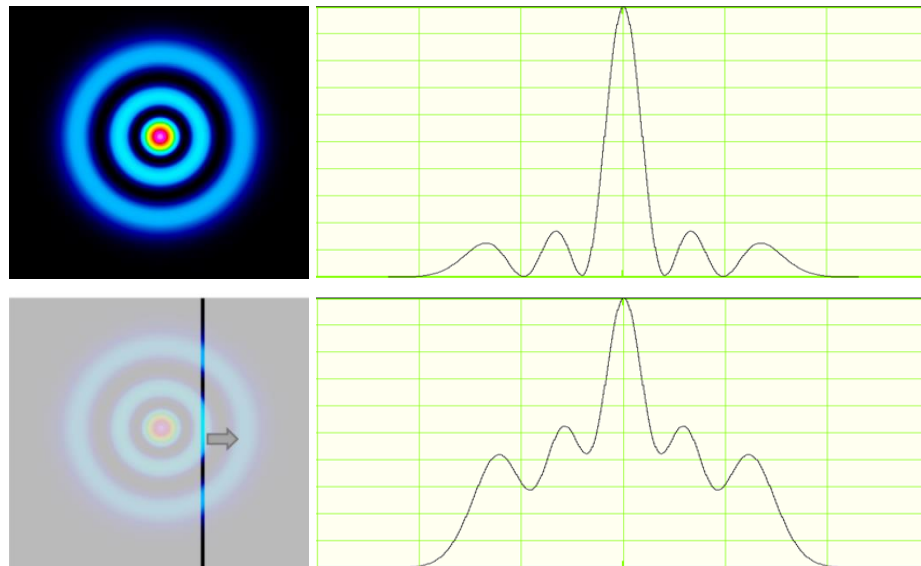


Figure 4.4 – Comparison of profile measurements of a Laguerre Gaussian beam from camera and scanning slit profilers (Dataray, personal communication, 2nd June 2019). The camera provides a profile across a line through the image, while the scanning slit profile acts as a summed row or column plot.

4.2.2 Stainless steel damage threshold test measurements

From the limitations described above regarding the profiler measurements, further verification of the spot sizes for the respective setups was sought. A damage threshold test was devised by taking sheets of stainless steel (mild steel was initially used but the surface roughness proved too high to accurately discern the spot sizes of the respective setups), mounting these at an angle of 45° relative to the incident beams and marking these with the lowest pulse energies at which distinct features could be observed with the Alicona InfiniteFocus G4 surface profilometer [4.17]. The measurements were made using the 100x objective lens to maximise the resolution of these measurements and are shown in figures 4.5 and 4.6 for the Bessel-Gauss and Gaussian beams respectively. The smallest widths along the burn marks were around $3.4 \pm 0.3 \mu\text{m}$ for the Bessel-Gauss beam and $3.5 \pm 0.3 \mu\text{m}$ for the Gaussian beam, with these measurements corresponding to the distances between the green and red crosses in the below images.

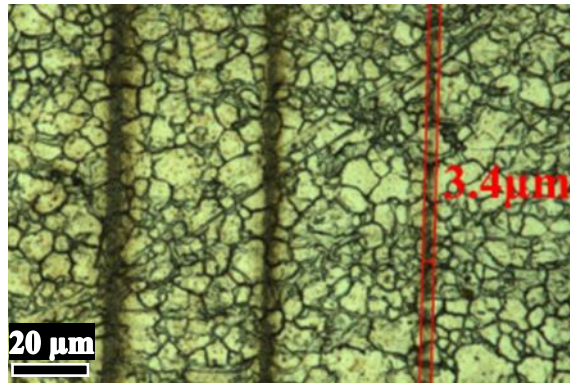


Figure 4.5 – Surface profiler measurement of features machined into stainless steel with the Bessel-Gauss beam. The image was taken using the 100x objective lens. The width of the smallest discernible feature was measured as $3.4 \pm 0.3 \mu\text{m}$. The image here showcases the other lines marked upon the stainless steel with progressively lower powers. Note here the consistency of the thickness of the machined features from the consistent spot size.

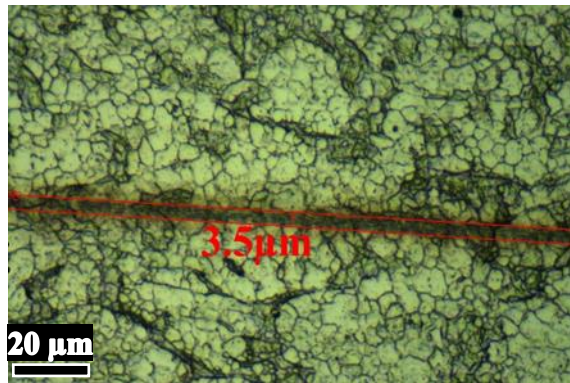


Figure 4.6 – Surface profiler measurement of feature machined into stainless steel with the Gaussian beam. The image was taken using the 100x objective lens. The width of the smallest features was measured as $3.5 \pm 0.3 \mu\text{m}$.

Despite measuring the damage threshold as opposed to the spot size directly, these measurements were able to reinforce the knife-edge measurements detailed above.

4.3 Initial ablation trials with redesigned setups

4.3.1 Ablation tests on preserved porcine tissue samples

Prior to undertaking ablation trials on clinically relevant harvested tissue samples, experiments were again performed on preserved porcine tissue samples. As part of these, thermal camera (FLIR i7, FLIR Systems) measurements were performed to experimentally validate the extent of thermal accumulation on the samples for various laser parameters. These images (figures 4.7 and 4.8) were captured immediately post ablation, as the timescale for thermal diffusion is short for the relatively small heated volumes. Lines were scanned with the laser spot between the two brass pins used to mount the preserved porcine tissue to the underlying dispoct board. These areas are indicated on figures 4.7 and 4.8 by the yellow circled regions. The heads of these pins (at either side of the yellow circled areas) were covered with black tape to reduce the saturation observed from their reflective surfaces.

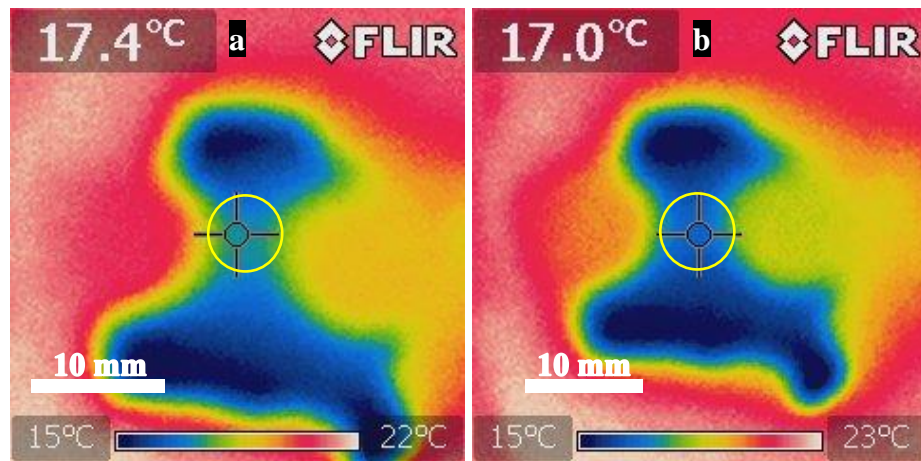


Figure 4.7 – Thermal camera measurements of preserved porcine tissue a) prior and b) post ablation using the reimaged Bessel-Gauss beam at 2 kHz with a 70% spatial overlap. Here it is evident that there is no appreciable thermal build up occurring. No significant thermal accumulation was observed at lower repetition rates for the Bessel-Gauss beam. This is significant as even a temperature change of only a few degrees Celsius is enough to cause destruction of DNA.

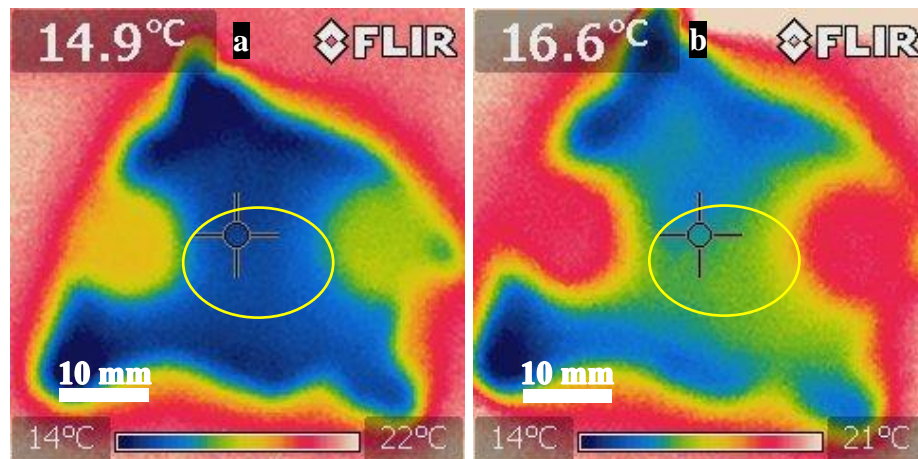


Figure 4.8 – Thermal camera measurements of preserved porcine tissue a) prior and b) post ablation using the reimaged Bessel-Gauss beam at 20 kHz with a 90% spatial overlap. Here it is evident that there is some significant thermal build up occurring from the combination of the high repetition rate and high spatial overlap of the pulses, indicated by the yellow area on the tissue surface between the two pins.

Thermal accumulation was observed however at higher repetition rates (20 kHz) with high spatial overlap of the pulses (90 %), as would be expected. This is indicated by the yellow area on the tissue surface in figure 4.8b.

These measurements served as an early indicator of any thermal build-up occurring for certain sets of laser scanning parameters prior to receiving histological data from the ablation trials performed on clinically relevant tissue. This held particularly true for the sets of laser scanning parameters shown here, with both more conservative and liberal approaches to laser pulse delivery (using a low pulse repetition rate alongside only a moderate spatial pulse overlap and a high pulse repetition rate combined with a high spatial pulse overlap respectively) being highlighted.

However, while this method enables immediate post-ablation measurement, it inherently lacks the insight provided by histological analysis when evaluating thermal accumulation as it does not allow direct

observation of the tissue neighbouring the ablated volumes down to the cellular level. This made it significantly less useful for intermediate laser scanning parameter regimes where this thermal accumulation is still present to varying degrees but is not always detectable. It is important to note though that with the histological analysis that there is the potential for some small extent of the damage to be cleared up from the necessary handling and submersion into various solutions.

Focus tolerance tests for both the Bessel-Gauss and Gaussian beam setups were also performed on preserved porcine tissue samples. These tests were performed by translating the preserved porcine tissue samples through the focus/Bessel zone regions of both beams in set increments. These were able to showcase working (ablation) ranges of over 1 mm for the Bessel-Gauss beam and around 400 μm for the Gaussian beam, shown in figure 4.9.

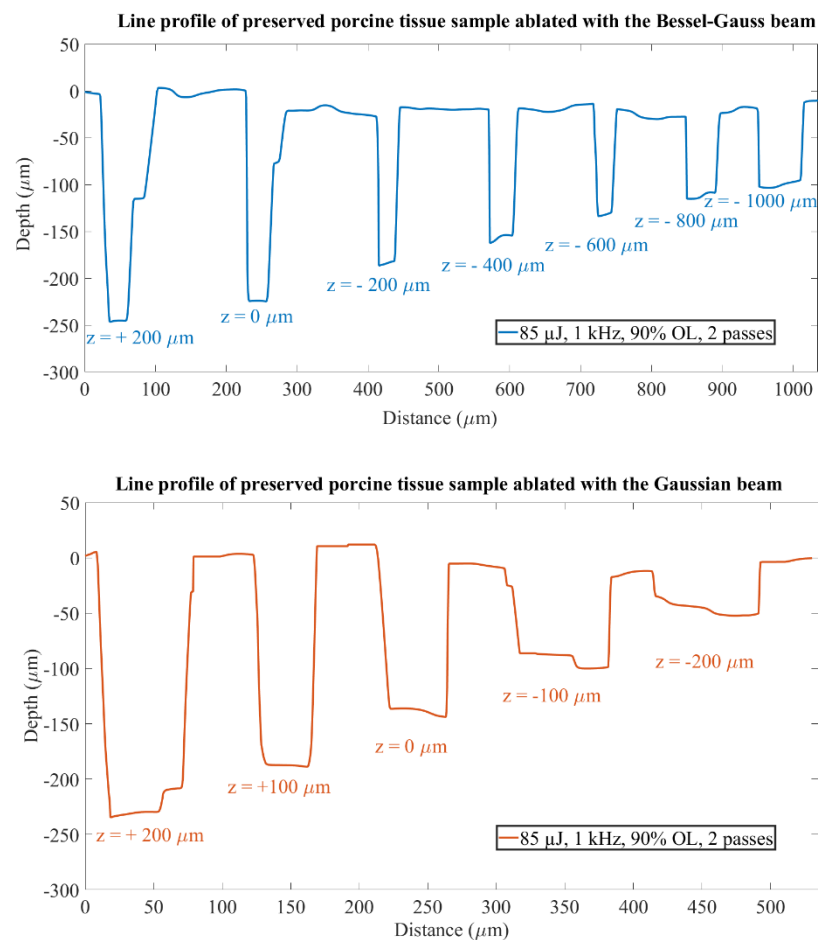


Figure 4.9 – Line profiles of preserved porcine tissue ablated using a) the Bessel-Gauss beam with axial translation intervals of 200 μm and b) the Gaussian beam with axial translation intervals of 100 μm . These line profiles are taken from surface profiles captured using the 10x objective lens on the Alicona surface profilometer. The notation used here for the z-axis is positive for when the preserved porcine tissue surface is above the focus (measured as the point of peak intensity along the beam propagation axis for both setups) and negative for when the preserved porcine tissue surface is below the focus. Here the lines were ablated with 2 passes each using the maximum input pulse energy of 85 μJ . These were applied at a repetition rate of 1 kHz with a 90% spatial overlap (stage speed of 0.35 mm/s).

For both beam shapes, peak ablation depths were achieved as the focus (or comparable axial position of peak intensity in the case of the Bessel-Gauss beam) was translated into the sample, although these also seemed to be the point beyond which only comparatively superficial features were observed. This was attributed to the respective drops in the intensity at the surface.

4.3.2 Successive ablation trials on murine intestinal tissue samples

Following the initial tests of the reimaged Bessel-Gauss setup on the preserved porcine tissue, the opportunity of performing some ablation experiments on more clinically relevant murine intestinal tissue with the redesigned optical setup arose. Unfortunately, the murine peritoneal tumour model (discussed in chapter 3) did not develop well, which limited the subsequent sample availability. Consequently, while some histology data was obtained from this set of tissue samples, no accompanying surface profile measurements were taken.

This set of experiments was able to confirm that the reimaged Bessel-Gauss beam provided sufficient levels for nonlinear absorption to occur, as plasma was consistently observed upon the tissue surface. However, the histology images showed that some of the parameters tested were suboptimal, with considerable cavitation being observed across these respective sections. This cavitation effect results from bubbles being formed in the tissue during the laser induced optical breakdown process that follows the non-linear absorption of the applied high intensity ultrashort laser pulses (as covered in the secondary effects of plasma-mediated ablation of tissue section in chapter 2). It was particularly noticeable for the reference features scanned at a repetition rate of 20 kHz, as would be expected from the combination of high spatial and temporal overlap [4.5],[4.18]. This is highlighted by red circles in figure 4.10, with the blue circles highlighting the ablated (removed) regions of tissue. The homogeneous regions of tissue highlighted by the red dimension bars (*i.e.* where tissue detail has been lost) around the ablated feature is indicative of thermal damage/necrosis.

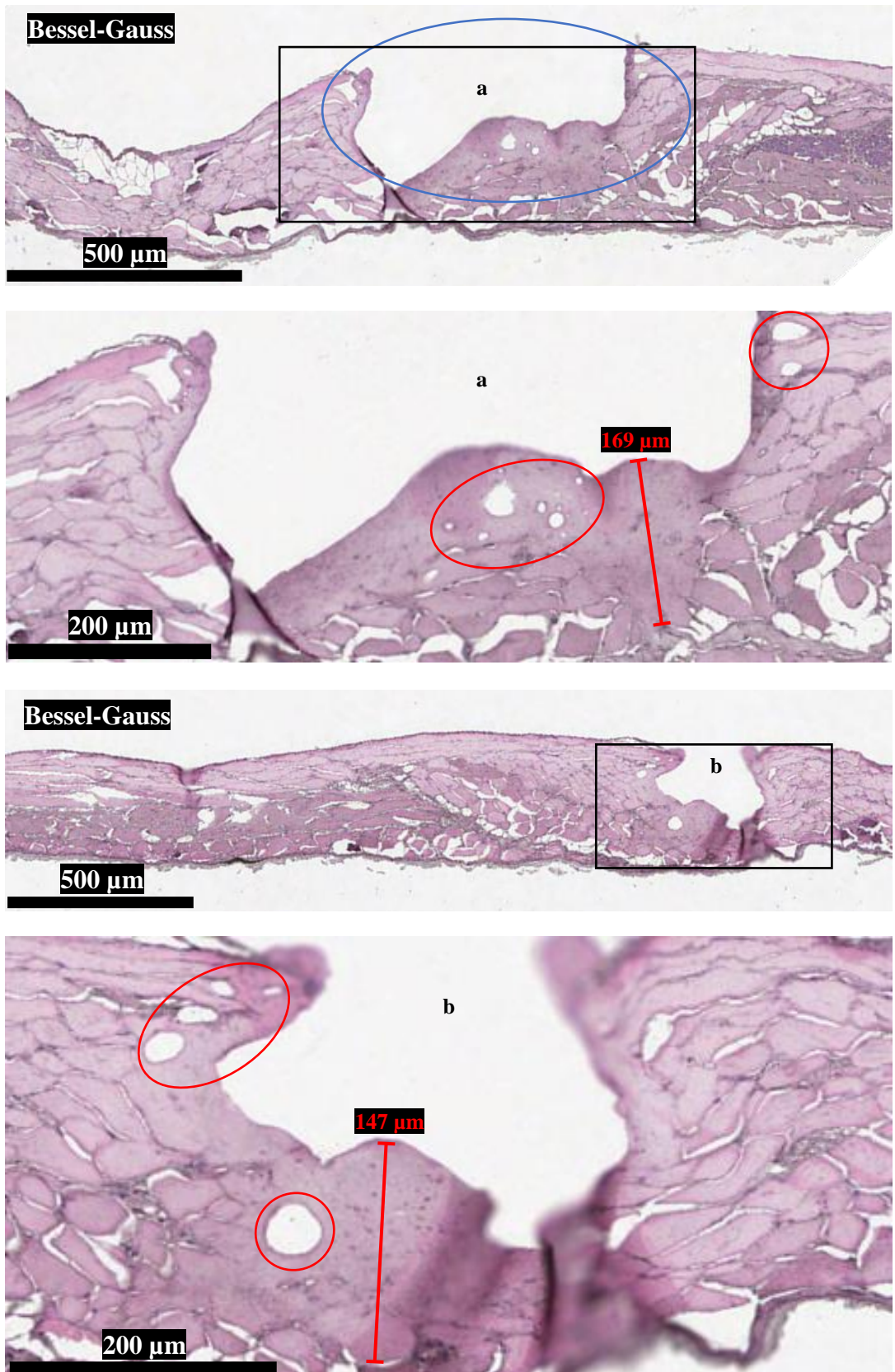


Figure 4.10 – Histology H&E images (with zoomed-in views) of murine intestinal tissue sections. Both features a) and b) were scanned with the Bessel-Gauss beam using 85 μJ pulses applied at a repetition rate of 20 kHz with a > 99% spatial overlap (stage speed of 0.35 mm/s). Both features consisted of 10 lines of single passes each, with the scanned lines spaced out by 10 μm. There is significant cavitation and thermal accumulation observed here, indicated by white circular sections where bubbles have formed (highlighted by the red circles) and sections of homogenised tissue (*i.e.* loss of tissue structure/detail, highlighted by the red dimension bars) accordingly. The black boxes indicate the frames of the zoomed-in images.

Features were also scanned using a repetition rate of 10 kHz. While these looked better with regards to collateral damage to the surrounding healthy tissue than the reference lines scanned at 20 kHz ($< 20 \mu\text{m}$ as opposed to $> 150 \mu\text{m}$), some undesirable cavitation and thermal accumulation effects were still observed (shown in figure 4.11).

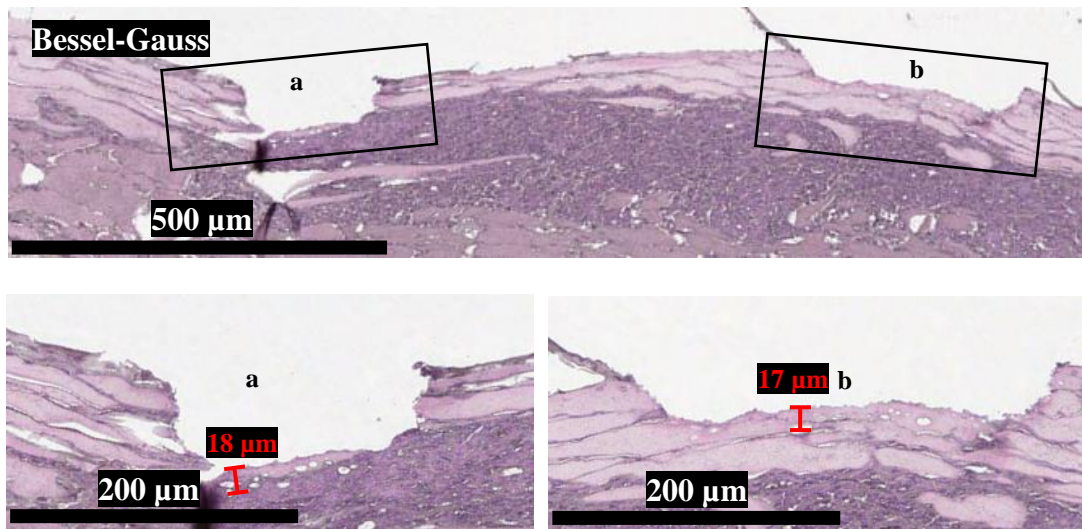


Figure 4.11 – Histology H&E image (with zoomed-in views) of murine intestinal tissue section. These features were scanned with the Bessel-Gauss beam using 85 μJ pulses applied at a repetition rate of 10 kHz with a 55% spatial overlap (15 mm/s stage speed).

There is still some degree of cavitation and thermal accumulation observed here, although considerably less than at the higher repetition rate of 20 kHz with a higher spatial overlap of the pulses.

These cavitation effects were avoided at 1 kHz, even at high spatial overlaps, although some thermal accumulation was still present, as shown by figure 4.12. Reducing the pulse energy showed that the depth of ablation can be tailored accordingly for a given number of passes, in accordance with previously published work [4.5]. Wider features were scanned by manually translating the sample via the y-axis micrometre on the MicroBlock to combine scan lines.

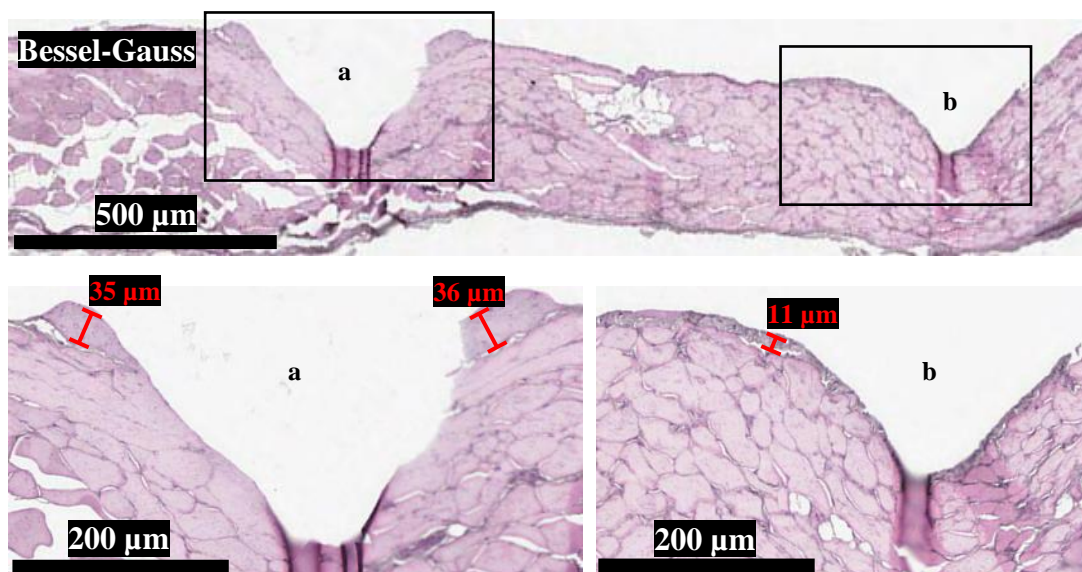


Figure 4.12 – Histology H&E image (with zoomed-in views) of murine intestinal tissue section. Here the features were scanned with the Bessel-Gauss beam using a) 85 μJ and b) 50 μJ pulses applied at a repetition rate of 1 kHz with a 90% spatial overlap (0.35 mm/s stage speed). The scans consisted of 10 lines of 2 passes each, with raster line spacings of 20 μm . There is still some thermal accumulation here, although there are no cavitation bubbles around the ablated sites. This lack of cavitation was attributed to the lower temporal overlap of the pulses than at the higher repetition rates of 10 and 20 kHz.

Reductions in the thermal accumulation observed at 1 kHz were possible either by reducing the pulse energy or the spatial overlap of the pulses, although these both come at the expense of total ablation depth (as shown in figure 4.13).

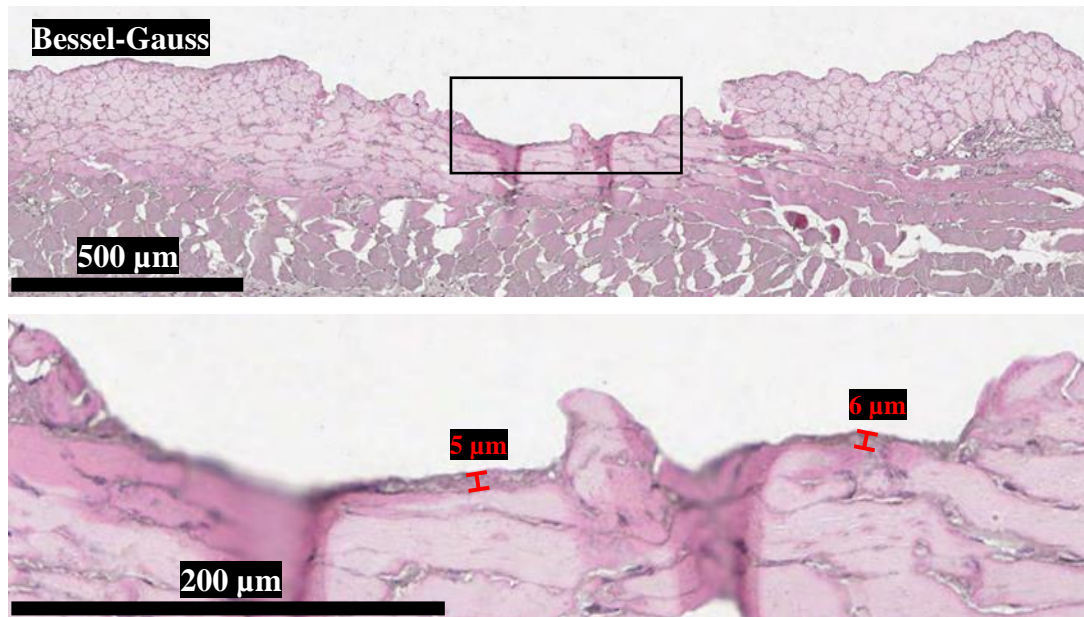


Figure 4.13 – Histology H&E image (with zoomed-in view) of murine intestinal tissue section. These features were scanned with the Bessel-Gauss beam using 85 μJ pulses applied at a repetition rate of 1 kHz with an approximately 70% spatial overlap (1.05 mm/s stage speed). The features consisted of 10 lines of single passes each, with the scanned lines spaced out by 20 μm . The thermal damage present here is highly localised, extending just over 5 μm away from the ablated region.

Some cavitation was observed around the edges of the ablated site at higher spatial overlaps for 2 kHz at this high pulse energy (figure 4.14).

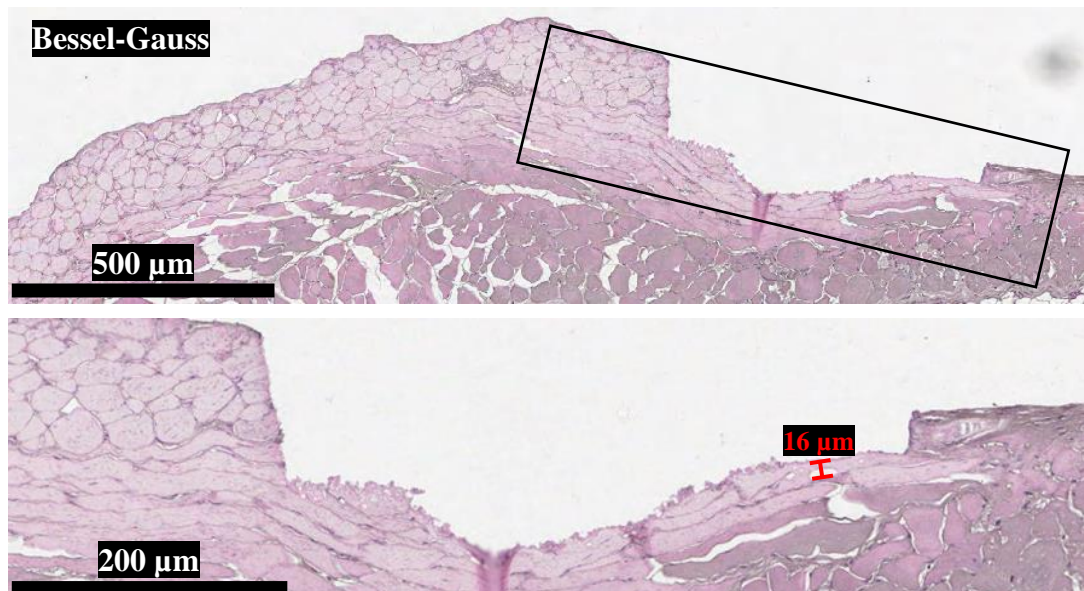


Figure 4.14 – Histology H&E image (with zoomed-in view) of murine intestinal tissue section. This feature consisted of 30 lines of 1 pass each, spaced out by 20 μm . This feature was scanned with the Bessel-Gauss beam using 85 μJ pulses applied at a repetition rate of 2 kHz with a 90% spatial overlap (0.7 mm/s stage speed). Again, the thermally damaged tissue present here is highly localised, extending just over 15 μm away from the ablated region. However, some minor cavitation is also observed around the ablated site.

This undesirable cavitation effect was reduced by reducing the spatial overlap of the pulses (figure 4.15), as suggested by references 4.4, 4.5, 4.8, 4.18 and 4.19.

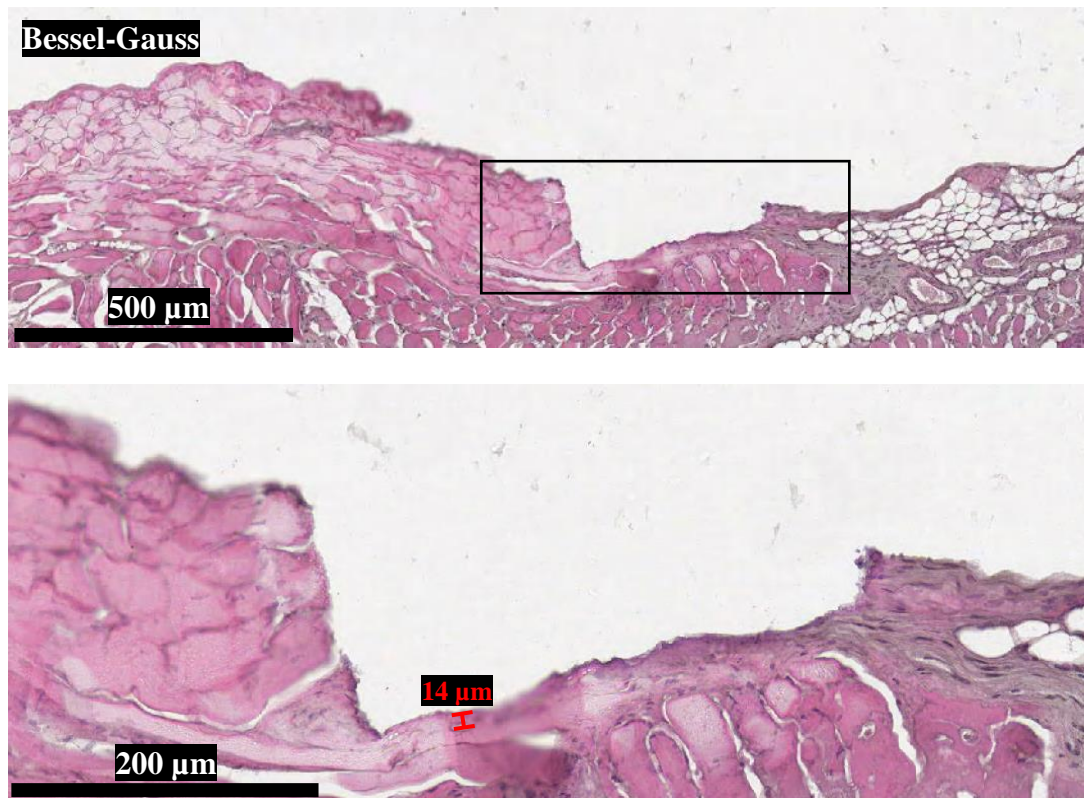


Figure 4.15 – Histology H&E image (with zoomed-in view) of murine intestinal tissue section. Here the feature was scanned with the Bessel-Gauss beam using 85 μJ pulses applied at a repetition rate of 2 kHz with a 70% spatial overlap (2.1 mm/s stage speed). This feature consisted of 30 lines of 1 pass each spaced out by 10 μm. The thermal accumulation observed here is once again highly localised, extending just under 15 μm away from the ablated region. No cavitation bubbles were observed for this feature.

Increasing the repetition rate to 3 kHz, the cavitation effect observed at higher spatial overlaps (90 %) becomes more prominent, although it is still reasonably localised around the ablated region (figure 4.16).

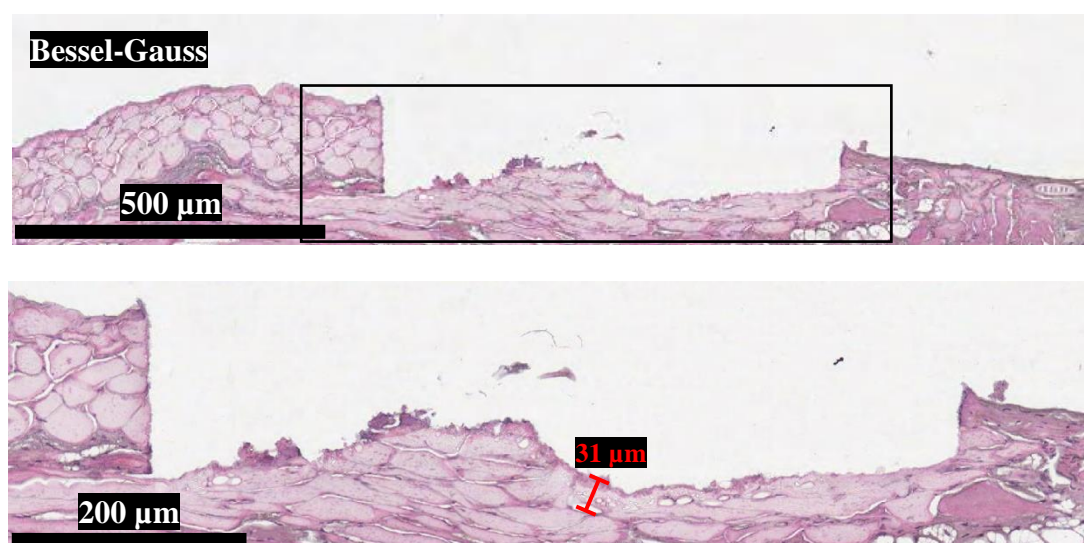


Figure 4.16 – Histology H&E image (with zoomed-in view) of murine intestinal tissue section. The feature here was scanned with the Bessel-Gauss beams using 85 μJ pulses applied at a repetition rate of 3 kHz with a 90% spatial overlap (1.05 mm/s stage speed). This feature consisted of 30 lines of 1 pass each, spaced out by 20 μm. While some cavitation bubbles and thermal accumulation is observed, these are both still fairly localised, extending just over 30 μm from the ablated region.

As the hyperplasia step in the colorectal cancer development process has a comparatively flat structure, the relatively thin/flat removal volume showcased here is potentially ideal, whereas conventional (electrocautery) tools would struggle. Consequently, it can be concluded that these follow-up murine intestinal tissue ablation trials showed some initial promise regarding the reimaged Bessel-Gauss beam setup, both in terms of achievable ablation depths and lateral confinement of thermal damage. A summary of these trials can be seen in table 4.1.

Pulse Repetition Rate (kHz)	Pulse energy (μJ)	Spatial pulse overlap (%)	Number of passes per line	Raster line spacing (μm)	Approximate mean depth (μm)	Peak thermal damage (μm)	Secondary effects of plasma generation
1	50	70	1	20	50	6	No
	85	90	2	20	100	36	No
2	85	70	1	10	90	14	No
		90	1	20	80	16	Cavitation bubbles
3	85	90	1	20	100	31	Cavitation bubbles
10	85	55	1	10	50	18	Cavitation bubbles
20	85	> 99	1	10	120	169	Cavitation bubbles and heat accumulation

Table 4.1 – Murine intestinal tissue ablation trials using the Bessel-Gauss beam.

Wavelength = 1030 nm, Pulse duration = 6 ps.

4.3.3 Initial low pulse repetition rate ablation trials on porcine intestinal tissue samples

Further clinically relevant tissue ablation trials were performed on porcine intestinal tissue. Sample availability allowed for both the Bessel-Gauss and Gaussian beams to be tested. Single pass lines around the centre of the respective focal regions were compared for both beam shapes. While the Bessel-Gauss beam showed slightly greater depths and improved repeatability, the differences in ablated depths were marginal and both beams showed high levels of lateral confinement regarding thermal damage ($< 5 \mu\text{m}$). The lines ablated with the Bessel-Gauss and Gaussian beams are shown in figures 4.17 and 4.18 respectively.

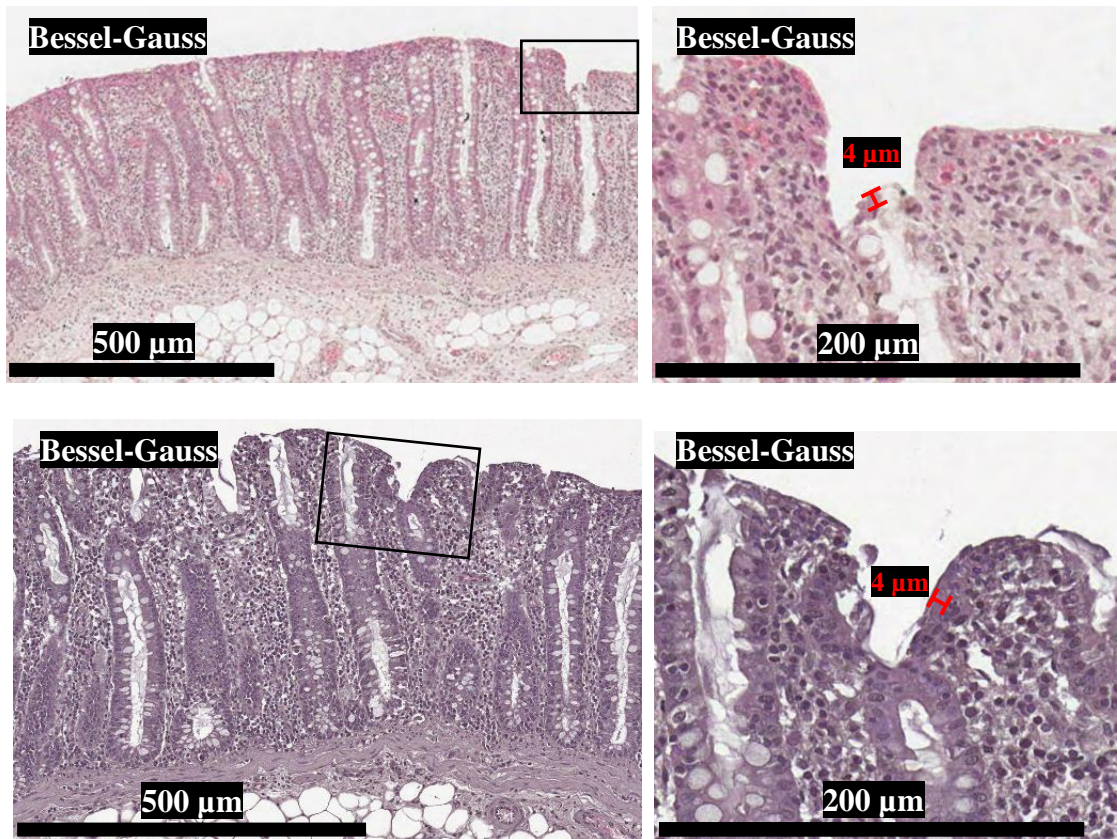


Figure 4.17 – Histology H&E images (with zoomed-in views) of porcine intestinal tissue sections. The features here were scanned via single passes around the centre of the Bessel zone region of the Bessel-Gauss beam using 85 μJ pulses applied at a repetition rate of 1 kHz with a 70% spatial overlap (1.05 mm/s stage speed). While some thermal accumulation is present, both are very localised, spanning just under 5 μm from the ablated region.

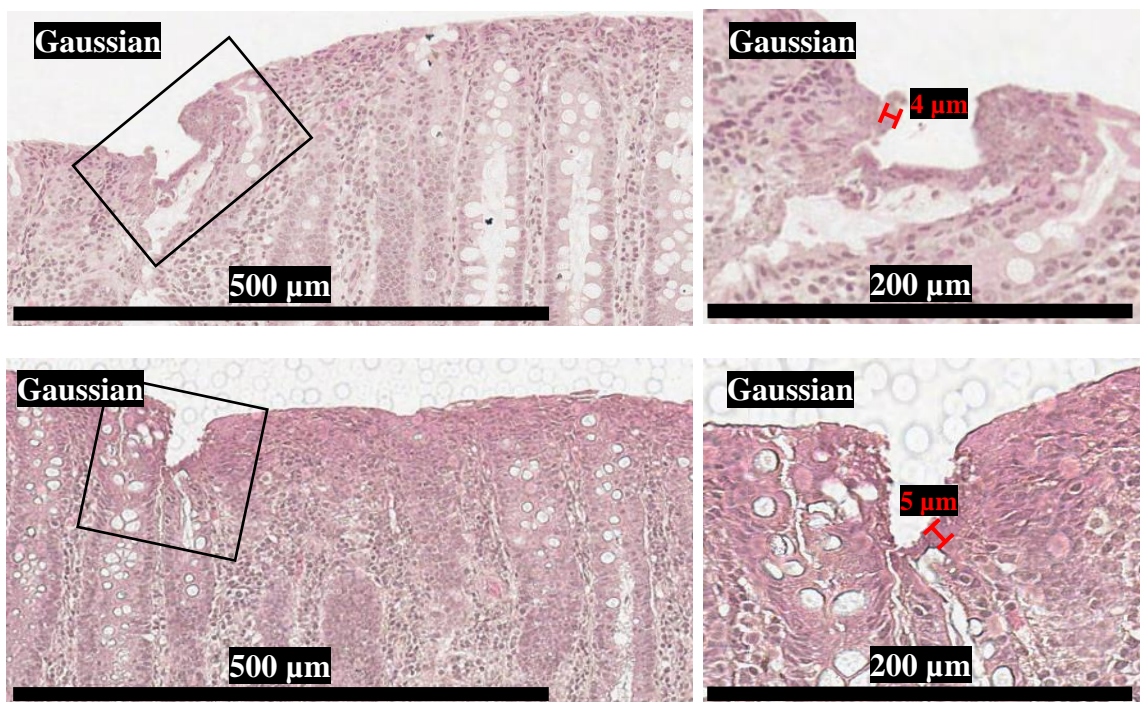


Figure 4.18 – Histology H&E images (with zoomed-in views) of porcine intestinal tissue sections. The features here were scanned with the Gaussian beam using 85 μJ pulses applied at a repetition rate of 1 kHz with a 70% spatial overlap (1.05 mm/s stage speed). These features were created via single passes around the focus region. While some thermal accumulation is observed, it is highly localised, extending just 5 μm or less from the ablated region.

Larger scan patterns were also tested to observe how the ablation characteristics offered by both beam shapes scaled up while simulating more applicable tumour resection modalities (figures 4.19 and 4.20). The Bessel-Gauss beam exhibited a trend for increased ablation depths for equivalent scanning parameters, courtesy of its greater depth of focus. Additionally, while both beams were able to showcase limited thermal damage margins, the Gaussian was less consistent in this regard, with it occasionally exhibiting noticeably higher levels of thermal accumulation (up to nearly 25 μm versus $< 15 \mu\text{m}$). This was attributed to its more divergent spot leading to higher spatial overlaps, causing the beam to dwell on finite areas of the tissue surface for longer than anticipated.

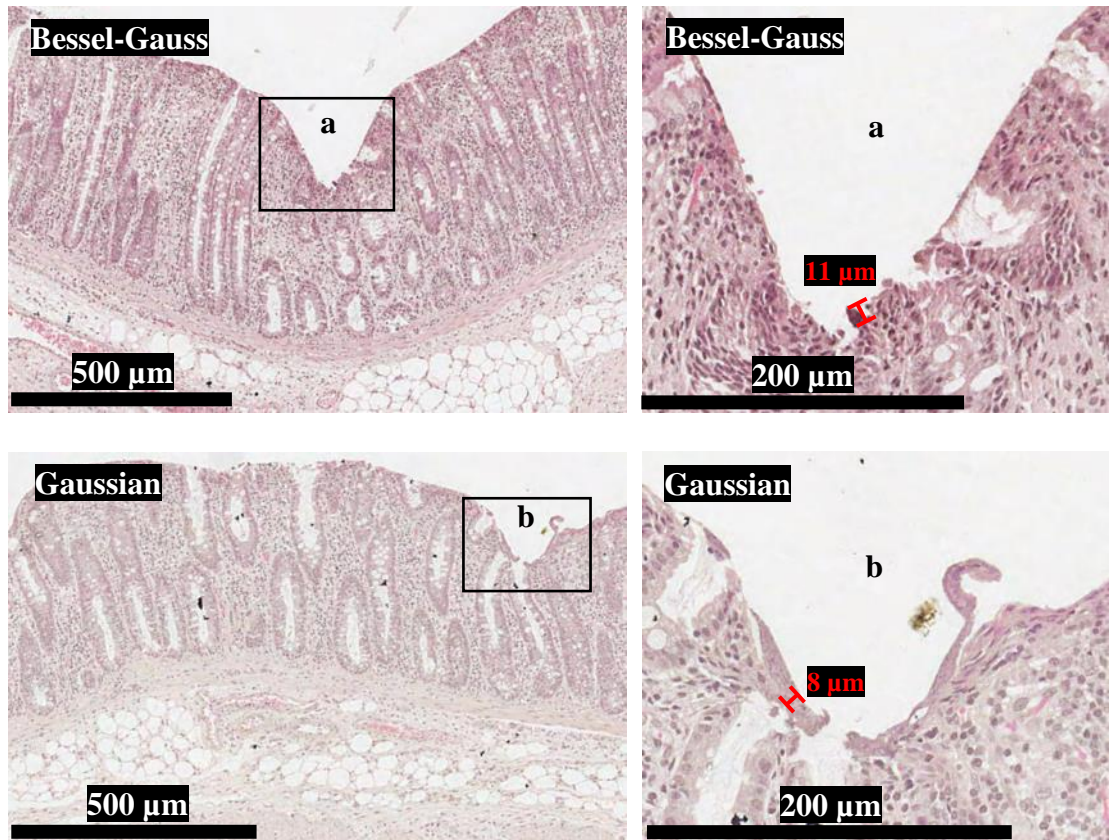


Figure 4.19 – Histology H&E images (with zoomed-in views) of porcine intestinal tissue sections. The features here were scanned with the a) Bessel-Gauss beam and b) Gaussian beam using 85 μJ pulses applied at a repetition rate of 1 kHz with a 70% spatial overlap (1.05 mm/s stage speed). The scans consisted of 5 lines of 2 passes each, spaced out by 20 μm . While some thermal accumulation is observed, it is highly localised, extending around 10 μm from the ablated region.

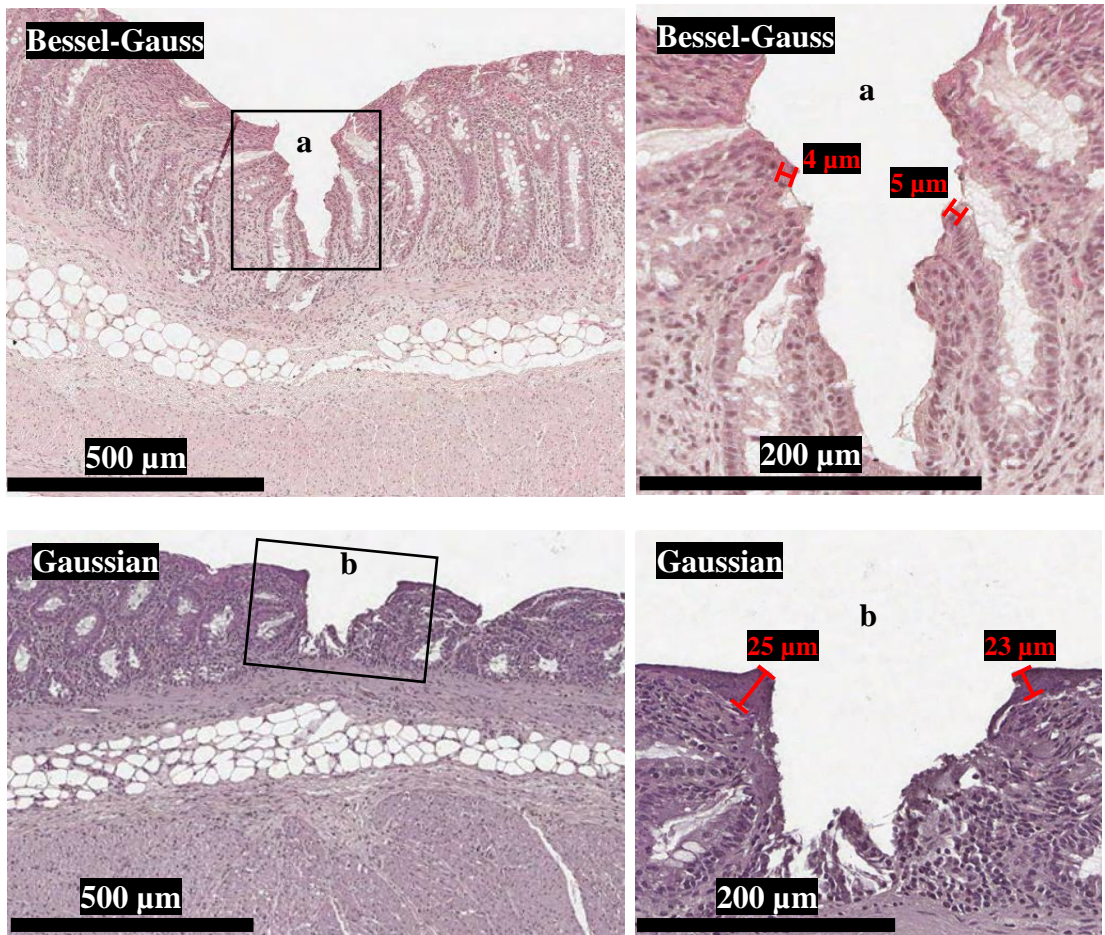


Figure 4.20 – Histology H&E images (with zoomed-in views) of porcine intestinal tissue sections. The features here were scanned with the a) Bessel-Gauss beam and b) Gaussian beam using 85 μJ pulses applied at a repetition rate of 1 kHz with a 70% spatial overlap (1.05 mm/s stage speed). The scans consisted of 5 lines of 4 passes each, separated by 20 μm . More thermal accumulation is observed for the Gaussian beam, which was reasoned to be from the comparatively rapid changes in the spot size across the inhomogeneous tissue surface leading to higher-than-expected spatial overlap of the pulses.

Wider features at increased pulse repetition rates were also tested (figure 4.21). The Bessel-Gauss beam again showed greater depths, but both beams showed the potential for high confinement of thermal damage.

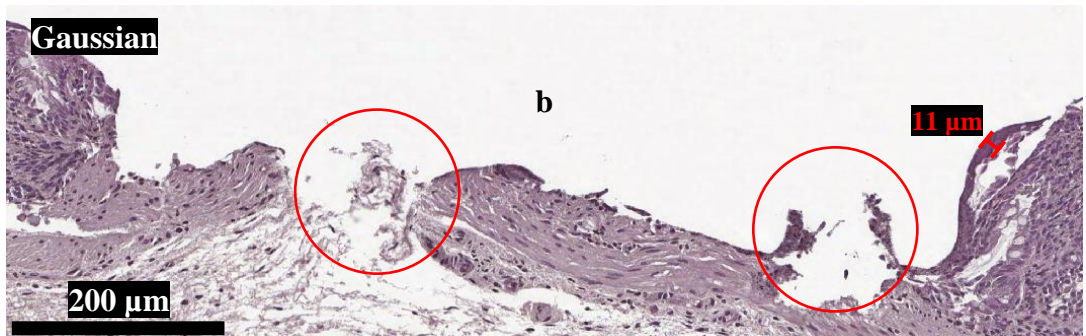
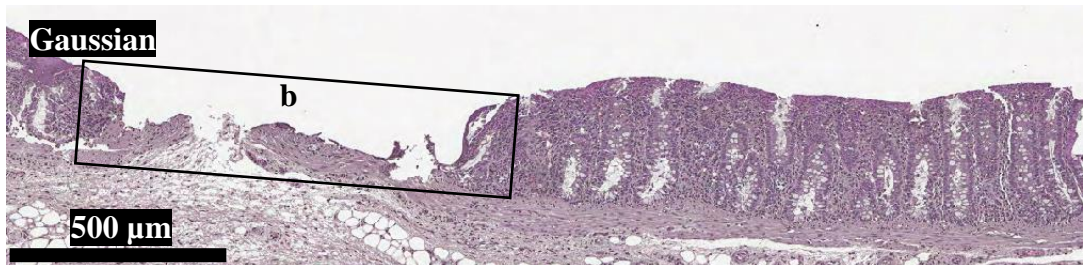
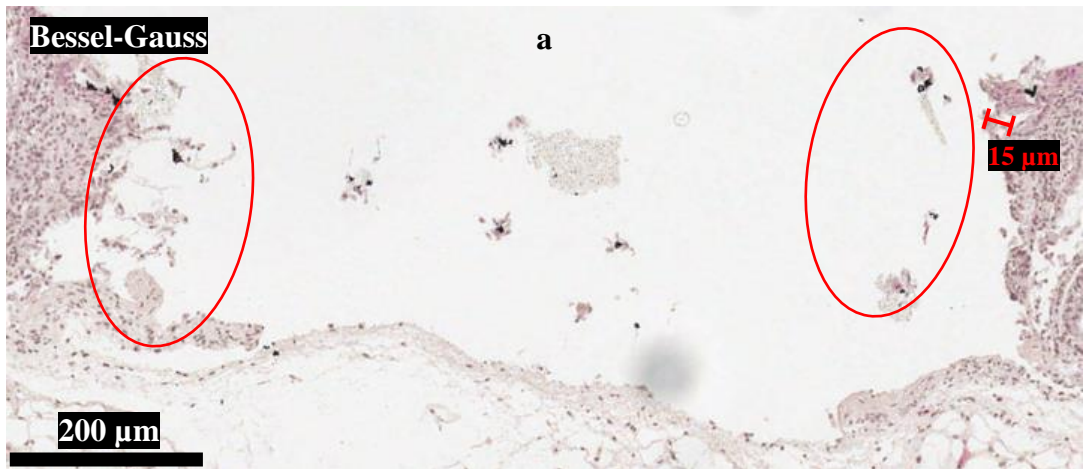
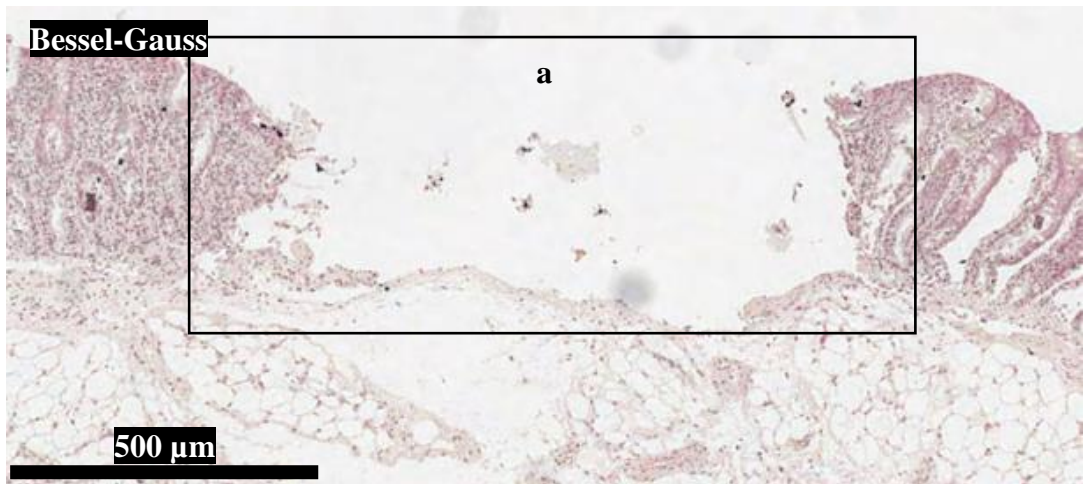


Figure 4.21 – Histology H&E images (with zoomed-in views) of porcine intestinal tissue sections. The features here were scanned with the a) Bessel-Gauss beam and b) Gaussian beam using 85 μJ pulses applied at a repetition rate of 2 kHz with a 70% spatial overlap (2.1 mm/s stage speed). The scans consisted of 40 lines of 4 passes each, spaced out by 20 μm . While some thermal accumulation is observed, it is highly localised, extending just over 10 μm from the ablated region in both cases. Unfortunately, splitting of the tissue (highlighted by the red circles) that occurred from the microtome sectioning process affected the potential reliability of these measurements.

Higher numbers of passes were also tested to examine the capacity of both beams for precise drilling of the tissue (figure 4.22). Both beams again exhibited good confinement of thermal damage, but the Bessel-Gauss beam showed more consistency regarding the depth of ablation along the scanned feature.

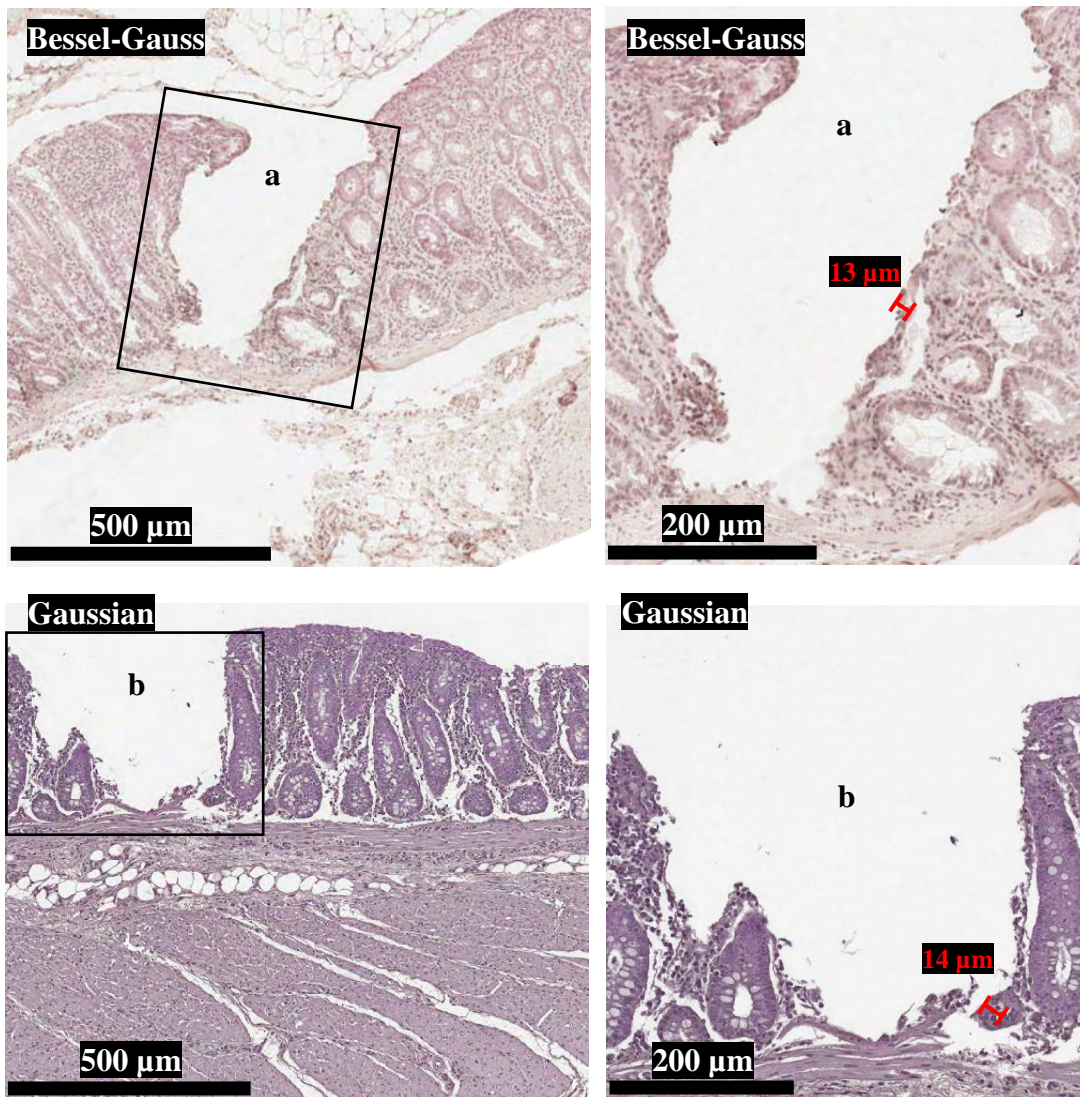


Figure 4.22 – Histology H&E images (with zoomed-in views) of porcine intestinal tissue sections. The features here were scanned with the a) Bessel-Gauss beam and b) Gaussian beam using 85 μJ pulses applied at a repetition rate of 2 kHz with a 70% spatial overlap (2.1 mm/s stage speed) right image. The scans consisted of 10 lines of 6 passes each, spaced out by 20 μm . Thermal damage in both features is highly localised, extending just under 15 μm for both features.

Wider features were also tested for both beams at further increased pulse repetition rates (figure 4.23). This led to increased thermal damage margins for both beams, but this was particularly noticeable with the Gaussian, with the combination of the higher pulse repetition rate and less consistent spot size even leading to some cavitation bubbles being observed (circled in red in figure 4.23b).

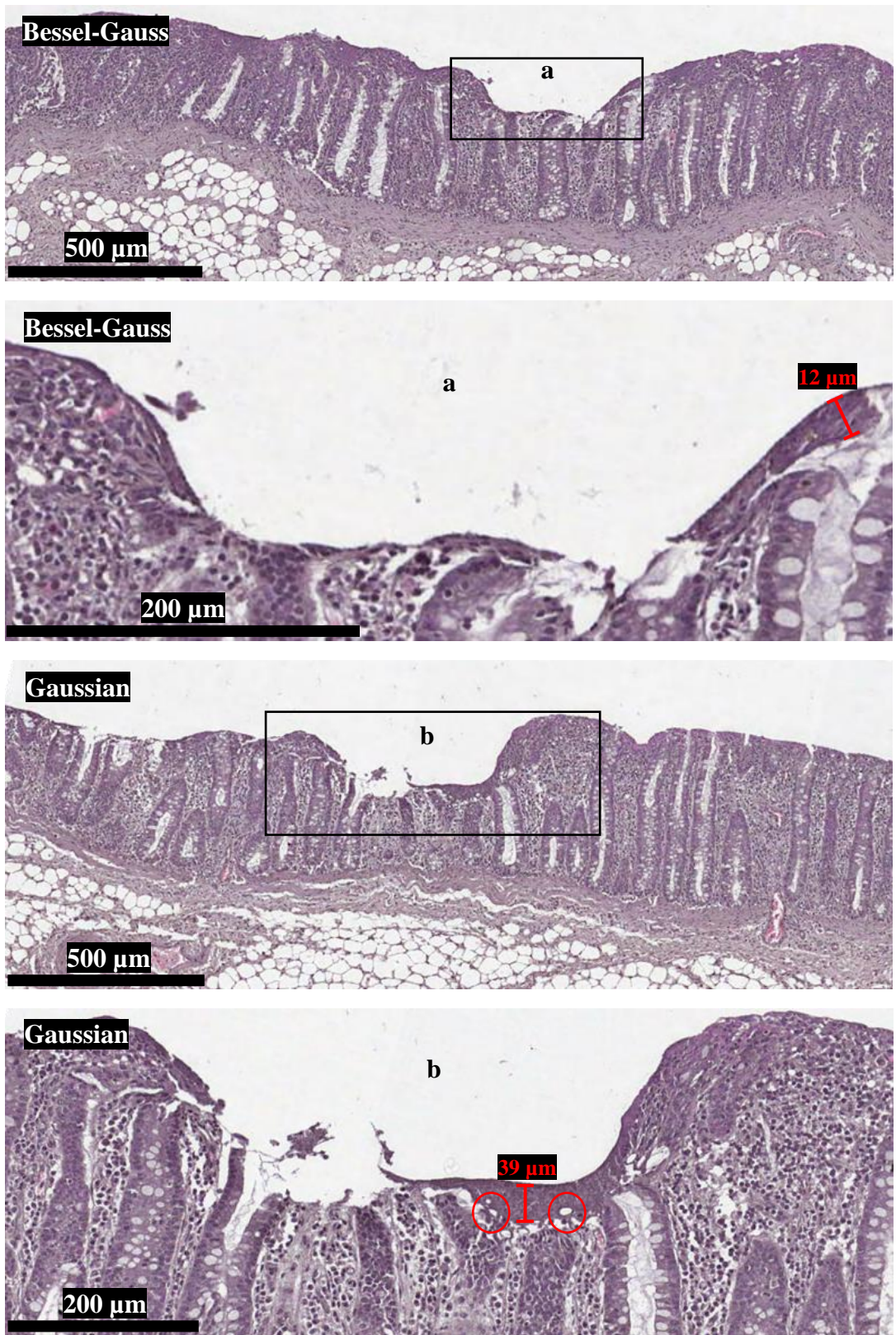


Figure 4.23 – Histology H&E images (with zoomed-in views) of porcine intestinal tissue sections. The features here were scanned with the a) Bessel-Gauss and b) Gaussian beam using 85 μJ pulses applied at a repetition rate of 3 kHz with a 70% spatial overlap (3.15 mm/s stage speed). The scans consisted of 15 lines of 2 passes each, spaced out by 20 μm . More significant thermal accumulation is observed alongside some cavitation bubbles for the Gaussian beam (highlighted in red), extending over more than 30 μm from the ablated region. This was attributed to the combination of the higher pulse repetition rate and shorter depth of focus compared to the Bessel-Gauss beam.

A summary of these initial porcine intestinal tissue ablation trials can be seen in tables 4.2 and 4.3 for the Bessel-Gauss and Gaussian beams respectively. While thermal damage margins for both beams are similar (with the exception of the 3 kHz feature where cavitation effects and thermal accumulation become pronounced for the Gaussian beam), the Bessel-Gauss beam shows a general trend of improved ablation depths courtesy of its extended depth of focus.

Pulse Repetition Rate (kHz)	Number of passes per line	Raster line spacing (μm)	Approximate mean depth (μm)	Peak thermal damage (μm)	Secondary effects of plasma generation
1	1	N/A	40	4	No
	2	20	100	11	No
	4	20	200	5	No
2	4	20	330	15	No
	6	20	430	13	No
3	2	20	50	12	No

Table 4.2 – Initial porcine intestinal tissue ablation trials using the Bessel-Gauss beam.

Wavelength = 1030 nm, Pulse duration = 6 ps, Pulse energy = 85 μJ , Spatial pulse overlap = 70%.

Pulse Repetition Rate (kHz)	Number of passes per line	Raster line spacing (μm)	Approximate mean depth (μm)	Peak thermal damage (μm)	Secondary effects of plasma generation
1	1	N/A	40	5	No
	2	20	70	8	No
	4	20	100	25	No
2	4	20	120	11	No
	6	20	180	14	No
3	2	20	270	39	Cavitation bubbles and heat accumulation

Table 4.3 – Initial porcine intestinal tissue ablation trials using the Gaussian beam.

Wavelength = 1030 nm, Pulse duration = 6 ps, Pulse energy = 85 μJ , Spatial pulse overlap = 70%.

4.3.4 Optical cage system orientation redesign

Due to the time sensitive nature of the clinically relevant tissue ablation trials that were carried out, increases in the throughput of these experiments was desirable. Consequently, a second linear motorised translation stage (LTS150/M, Thorlabs) was incorporated into the experimental setup to allow for automation of raster scanning via LabVIEW code with micron scale precision. Vertical mounting of the respective 30 mm cage systems for the Gaussian and Bessel-Gauss beam setups allowed for more precise variation of the tissue samples along the beam propagation axis across a greater range through the inclusion

of a dial gauge and lab jack. The lab jack had an observed backlash error of approximately $\pm 10 \mu\text{m}$, which was deemed acceptable upon consideration of the inherent waviness of the tissue surfaces to be ablated. This greater range of variability along the propagation axis of both beams would also help to account for the variability in thickness across the various tissue samples. This redesign of the optical setup is illustrated in figure 4.24.

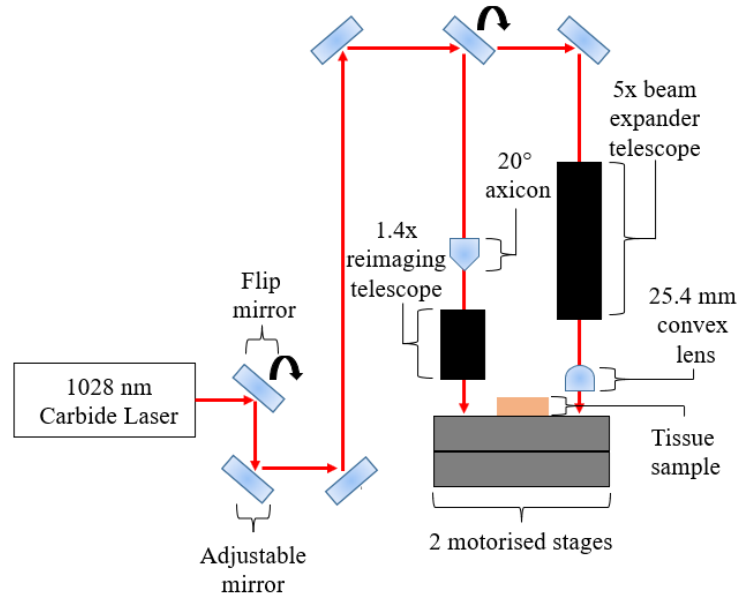


Figure 4.24 – Schematic of the experimental setup with vertical orientation of the 30 mm cage systems relative to the tissue samples. The first 2 mirrors direct the beam to the periscope formed by the third and fourth mirrors.

Additionally, automating the stage scanning along a second axis enabled a common reference point for all the ablated lines/scans. While it would be of interest to test how tolerant the axicon was to scanning of the beam relative to the sample, it was decided that moving the sample relative to the incident beam would be simpler for the early stage investigations of how the shape of the beam influences the plasma-mediated ablation process for soft biological tissues.

This vertical mounting of the cage systems also allowed for a diode laser (LCM-T-111, Laser-export) to be incorporated as a means of finding the focus levels of both optical setups much more quickly upon the tissue surfaces. This was done by finding the critical energy density level (*i.e.* the *z*-axis plane at which plasma could still be observed for minimal input power) upon the surface of an aluminium sheet for the Bessel-Gauss beam. While the $1/e$ points of the axial intensity plot would ideally be used to model the depth of focus for both setups, this is much more difficult to account for experimentally. While the fluctuations observed along the intensity profile of the Bessel-Gauss beam from the rounded tip may inhibit the use of the peak intensity as a reference point, this would still be a potential issue for using the $1/e$ points. An aluminium sheet is used for this surface finder due to its low surface roughness of approximately $3.7 \pm 0.4 \mu\text{m}$, providing an even reference plane.

Once this critical energy density level was found for the Bessel-Gauss beam, the sample was translated across to the imaging setup that would act as the reference measurement for setting the surface of each tissue sample at this peak energy density focal plane. This technique was developed by Dr. Gora [4.19]. This imaging setup consisted of a 10x objective lens (LINOS) connected to a CMOS camera (DCC1645C, Thorlabs) via a lens tube. The diode laser was positioned at an angle where the light reflected from the

aluminium sheet was collected by the CMOS camera at this peak intensity focal plane. This reference plane was found to be accurate to $\pm 10 \mu\text{m}$, which again was deemed acceptable since this would be outweighed by the inherent inhomogeneity of the tissue samples. ND filters (NE10A-A and NE05A-A, Thorlabs) were mounted together and placed in front of the green laser diode to prevent saturation of the CMOS sensor.

The same aluminium sheet was finally translated to underneath the Gaussian beam setup. The position of the 25.4 mm focal length convex focusing lens in the cage system for the Gaussian setup was adjusted using the z-axis translation mount (SM1ZA, Thorlabs) it was fitted in so that the critical energy density level of both setups matched. The position of this focusing lens could be adjusted along the cage system as it had a well collimated (expanded) beam being input to it. The experimental setup is shown in figure 4.25.

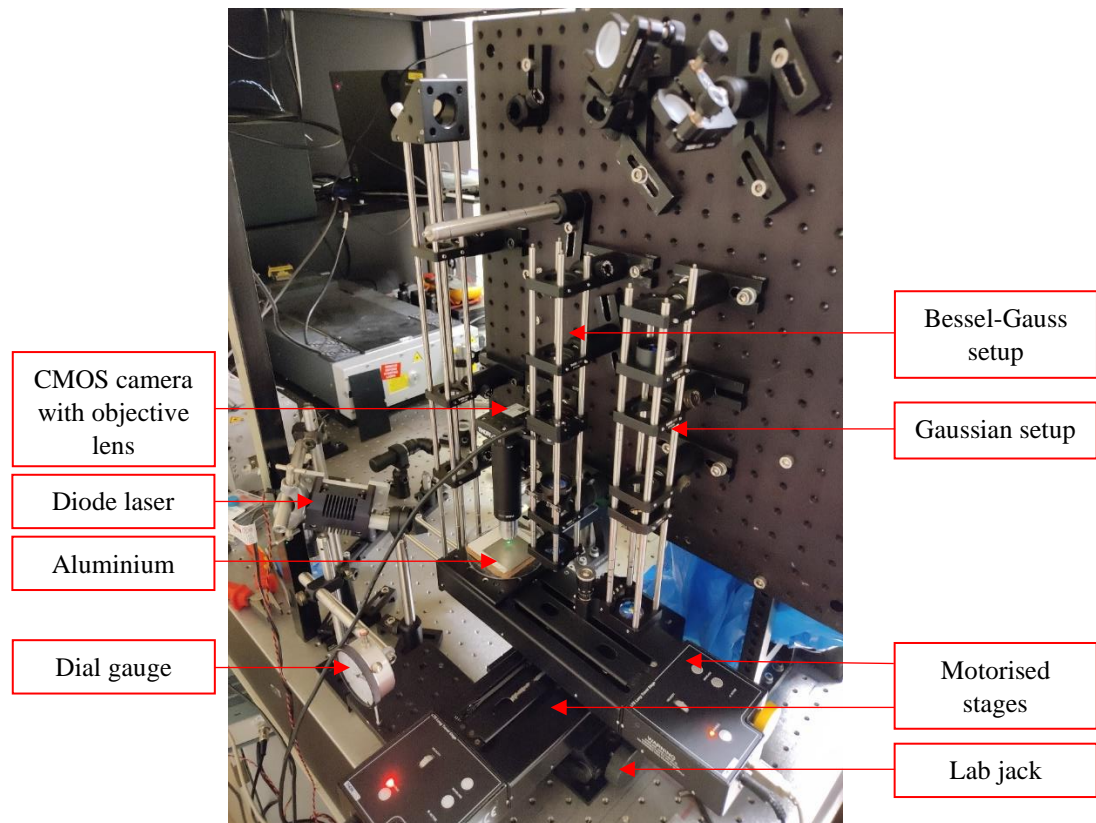


Figure 4.25 – Experimental setup with vertical orientation of the 30 mm cage systems relative to the tissue samples.

4.3.5 Successive low pulse repetition rate ablation trials on porcine intestinal tissue samples

Further clinically relevant pig intestinal tissue laser ablation trials were performed using both the Bessel-Gauss and Gaussian beams to allow for more comparisons between the ablation characteristics. Low pulse repetition rates were again used initially to try and avoid any cavitation effects, as these allow for low temporal overlap of the pulses, meaning they do not interact with each other as the collapse of the cavitation bubble induced by the plasma formation occurs prior to the next pulse interaction taking place [4.5],[4.18]. This provides the ablated tissue region adequate time for heat to disperse prior to the arrival of the subsequent laser pulse, although these lower repetition rate trials suffer from the drawback of reduced scanning speeds for equivalent spatial pulse overlap values, leading to lower removal rates and therefore lower ablation efficiency. Raster scans of 5 mm width were used, as this was the upper limit allowed by the histology wax embedding process while also coinciding with clinical requirements.

As there was a trend for greater depths of material removal in the preserved porcine tissue ablation trials for increasing spatial overlaps, two of the tissue samples were ablated with the reimaged Bessel-Gauss beam using the peak pulse energy of around 85 μJ at repetition rates of 1, 2 and 3 kHz at high spatial overlaps (approximately 97%). This corresponded to 0.1, 0.2 and 0.3 mm/s stage translation speeds accordingly. While the sample fixed in glutaraldehyde for surface profilometry showcased depths that initially looked promising, and increased approximately linearly with the number of laser passes (with the raster scans consisting of 5 lines, each spaced 10 μm apart, with 1, 2 and 4 passes at each line for the 1, 2 and 3 kHz repetition rates respectively), the paired sample (*i.e.* the sample that was ablated using the same parameters) that was sent for histology analysis showcased considerable thermal damage relative to the ablated depths in each case (figure 4.26). This was attributed to the slow translation speeds and high pulse energy leading to thermal accumulation and even observable cavitation bubble formation for the craters ablated using 2 and 3 kHz repetition rates, potentially from the high spatial overlap causing the subsequent pulses to interact with the mechanical ruptured area left by prior ones despite their temporal separation [4.20]. This cavitation effect has been reported for reimaged Bessel-Gauss beams in bulk silica when single pulses were applied to produce uniform voids, albeit in the femtosecond regime [4.21]. It is important to note however that the degree of thermal damaged observed here is still significantly less than that for electrocautery techniques, which can be on the millimetre scale [4.22].

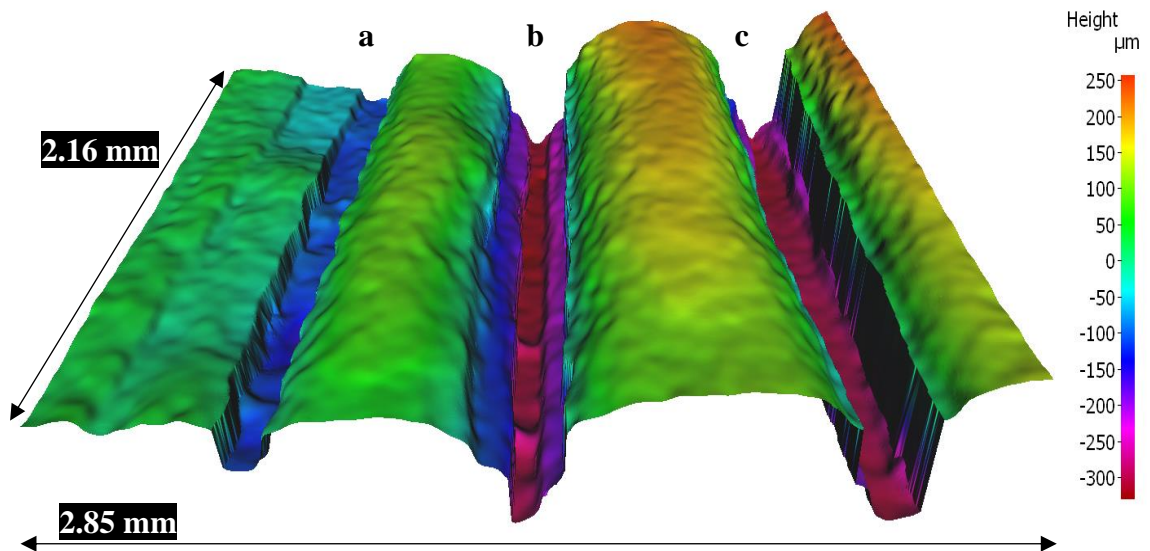
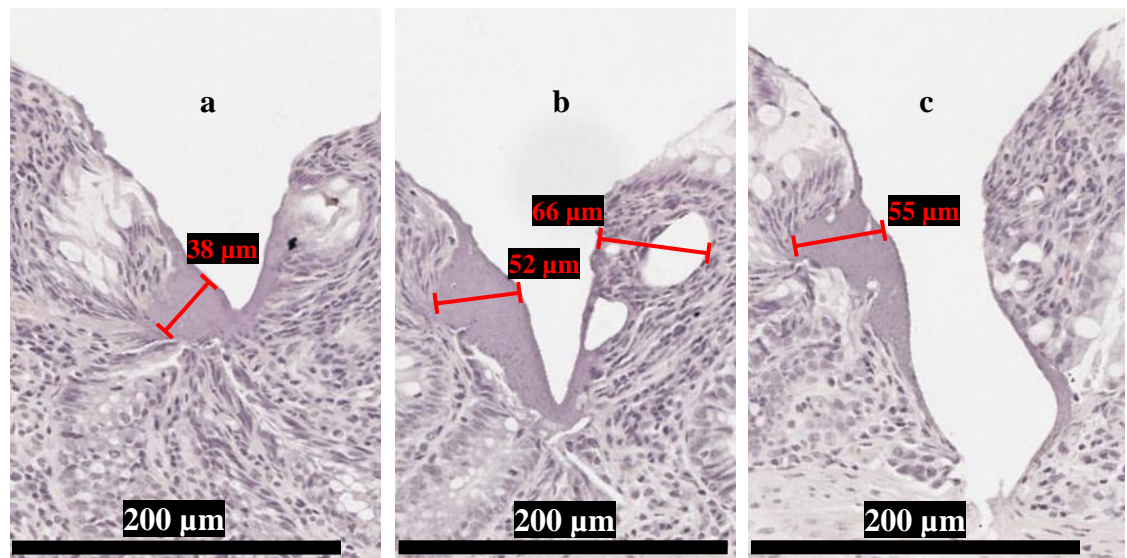
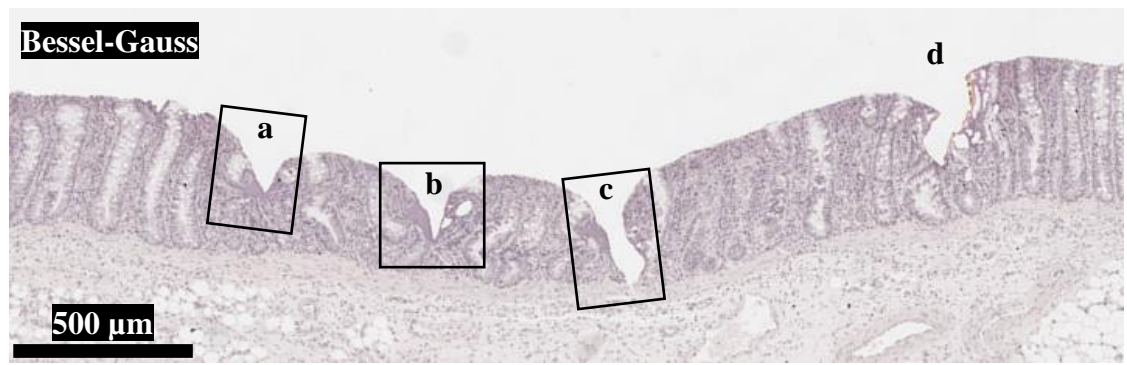


Figure 4.26 – Histological H&E stained images (with zoomed-in views) and surface profile (captured at 5x magnification) of pig intestine samples ablated with the Bessel-Gauss beam using 85 μJ pulses with spatial overlaps of 97%. The scanning patterns consisted of a) 1 kHz, 0.1 mm/s, 5 lines of 1 pass, b) 2 kHz, 0.2 mm/s, 5 lines of 2 passes and c) 3 kHz, 0.3 mm/s, 5 lines of 4 passes. The scan lines were spaced out by 10 μm . Some significant thermal accumulation (represented by the regions of homogeneous tissue, highlighted by the red dimension bars) is observed alongside some cavitation bubbles (large irregular white areas neighbouring the ablated zones), both of which extend over more than 50 μm from the ablated region for the 2 and 3 kHz features. This was attributed to the combination of the higher pulse repetition rates and higher spatial overlap of the pulses. The increased smoothing of the surface profile was from using a lower vertical resolution of 4 μm initially. A reference feature indicated by d) scanned at 20 kHz with a high spatial pulse overlap is also shown which is used to ensure correct orientation of the sample when correlating laser parameters to ablated features.

These parameters were repeated for the Gaussian beam setup (figure 4.27). Here the ablated depths were not as high, which was attributed to the shorter focal depth of the Gaussian beam. Additionally, the high spatial overlap again led to thermal accumulation despite the relatively low pulse repetition rates applied.

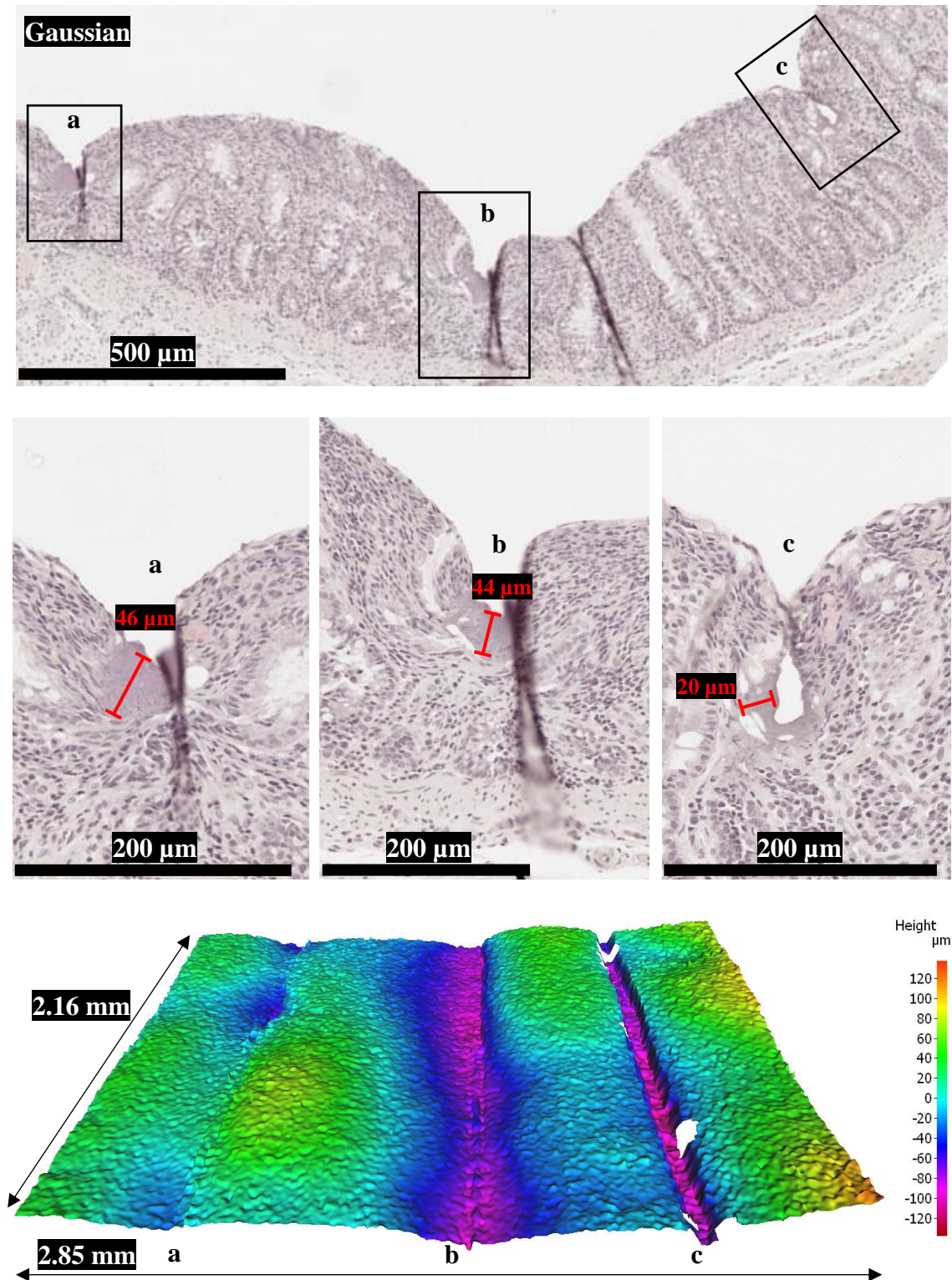


Figure 4.27 – Histological H&E stained images (with zoomed-in views) and surface profile (captured at 5x magnification) of pig intestine samples ablated with the Gaussian beam using 85 μJ pulses with spatial overlaps of 97%. The scanning patterns consisted of a) 1 kHz, 0.1 mm/s, 5 lines of 1 pass, b) 2 kHz, 0.2 mm/s, 5 lines of 2 passes and c) 3 kHz, 0.3 mm/s, 5 lines of 4 passes. The scan lines were spaced out by 10 μm . Unfortunately the feature ablated at 3 kHz closed up during the histology sectioning process, as shown in histology image c) above. The surface profile captured here has less smoothing applied from using a higher vertical resolution of 1.5 μm .

As the features ablated for the Gaussian looked comparatively superficial on the tissue surface, this set of parameters was repeated to test the level of repeatability offered by the tightly focused Gaussian spot (figure 4.28). Unfortunately, the same trend of low ablated depths and considerable thermal accumulation was observed again. This again was attributed to the short focal depth, as previous publications from the group have shown well-defined ablation at 1 kHz with Gaussian beams using larger spot sizes of around 20 and 30 μm and (and therefore greater depths of focus) [4.4],[4.5].

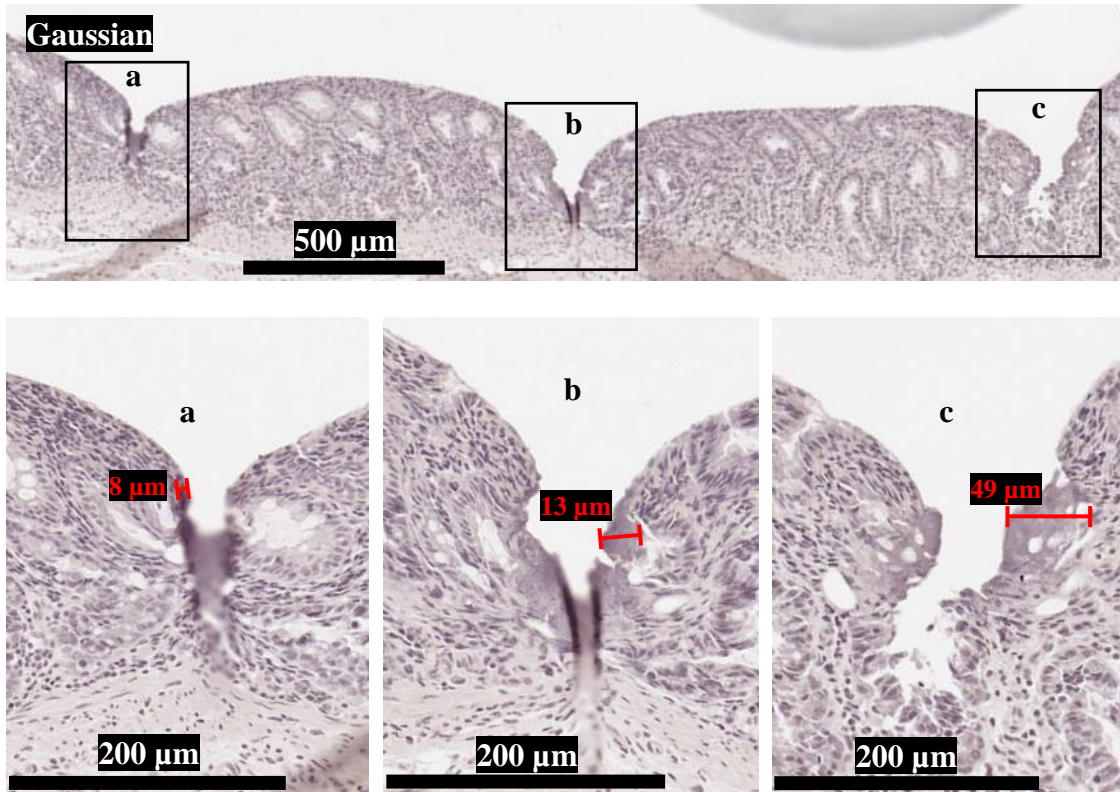


Figure 4.28 – Histological H&E stained images (with zoomed-in views) of a pig intestine sample ablated with the Gaussian beam using 85 μJ pulses with spatial overlaps of 97%. The scanning patterns consisted of a) 1 kHz, 0.1 mm/s, 5 lines of 1 pass, b) 2 kHz, 0.2mm/s, 5 lines of 2 passes and c) 3 kHz, 0.3 mm/s, 5 lines of 4 passes. The scan lines were spaced out by 10 μm .

Another pair of samples were ablated using slightly more conservative spatial overlaps of around 85% for the Bessel-Gauss beam setup (figure 4.29). These were again performed at 1, 2 and 3 kHz, at stage speeds of 0.5, 1 and 1.5 mm/s respectively. The 1 kHz feature was ablated using a raster scan consisting of 30 lines of 4 passes each to see how the process scaled up laterally across the tissue surface. The 2 kHz feature consisted of 5 lines at 2 passes each. The 3 kHz feature again consisted of 5 lines of 2 passes each. The raster line spacing was 20 μm here. While these features were able to remove appreciable sections of the mucosal layer (or the entirety of the mucosal layer for the 1 and 3 kHz features), the 2 and 3 kHz features showcased significant cavitation and thermal accumulation around the crater edges. The 1 kHz feature however showcased very minimal thermal damage margins of 12.5 μm peak thickness, which was concluded to be from a combination of the more modest spatial overlap and the higher temporal spacing from the lower pulse repetition rate.

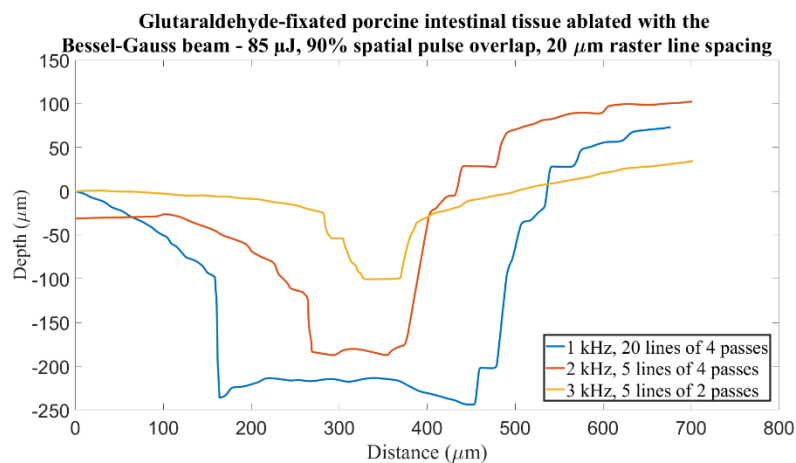
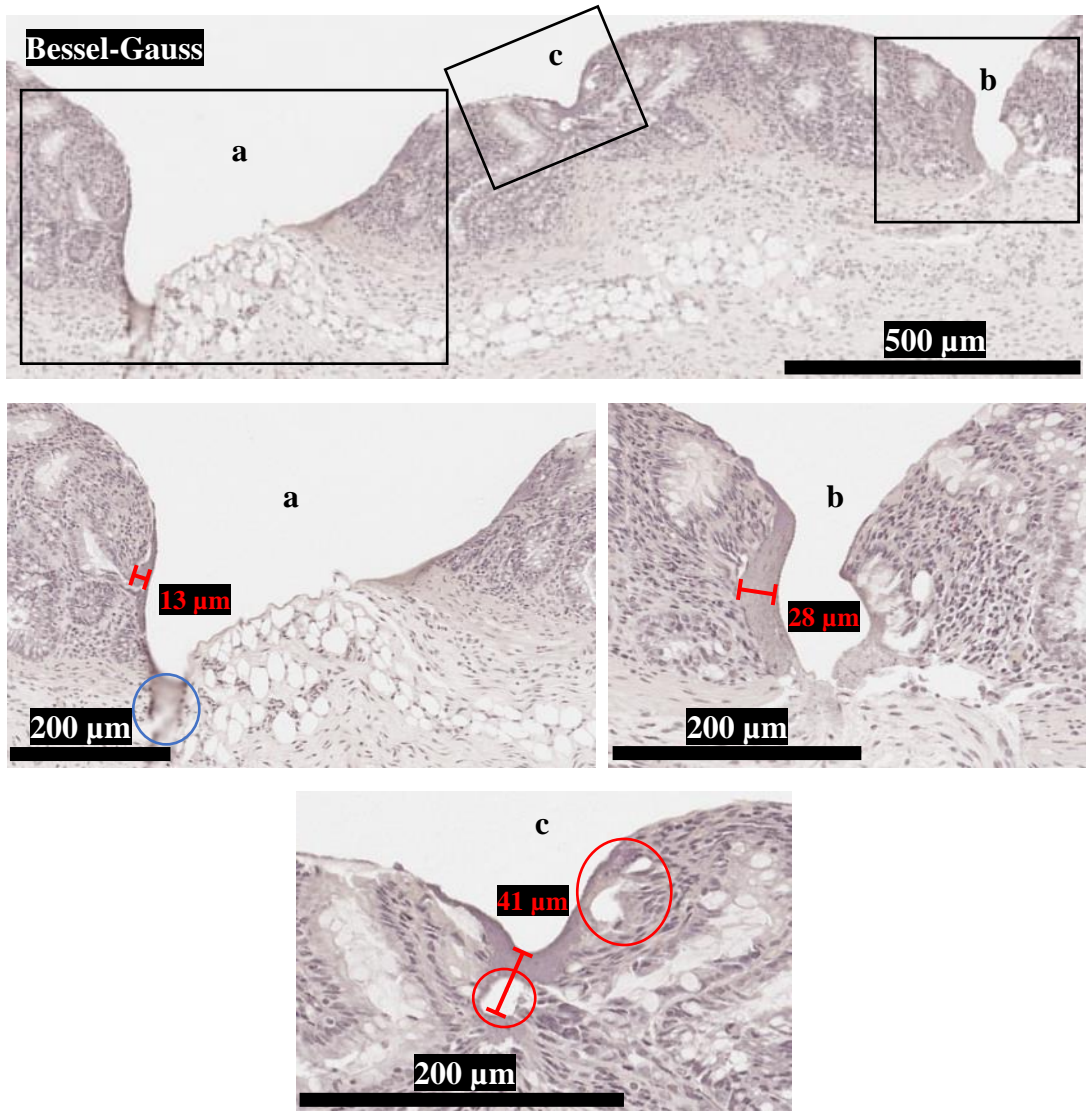


Figure 4.29 – Histological H&E stained images (with zoomed-in views) and line profiles taken from surface profilometer measurements of pig intestine samples ablated with the Bessel-Gauss beam using 85 μ J pulses and a 90% spatial pulse overlap. The scanning patterns consisted of a) 1 kHz, 0.5 mm/s, 20 lines of 4 passes, b) 2 kHz, 1 mm/s, 5 lines of 4 passes and c) 3 kHz, 1.5 mm/s, 5 lines of 2 passes. The scan lines were spaced out by 20 μ m. Some relatively significant thermal accumulation is observed, extending over more than 25 μ m from the ablated region for the 2 and 3 kHz features, with some cavitation bubbles (highlighted by red circles) being observed at 3 kHz. This was again attributed to the combination of the higher pulse repetition rates and higher spatial overlap of the pulses. The out of focus feature to the left of histology feature a) (highlighted by the blue circle) was confirmed to be an artefact of the histology sectioning process by Nicholas West, a histologist project partner. Some lateral shrinking of the 20 line scan was noted in the glutaraldehyde-fixed sample which was attributed to dehydration of the tissue.

Focal plane tolerance tests (*i.e.* translating through the focus/Bessel zone regions of the beam in set axial translation increments) were also performed by translating the pig intestine samples through the focus of both setups in 100 μm steps, with single lines being scanned with the laser at each axial position at 1 kHz with an approximate spatial overlap of 50%. Although plasma was observed on the surface of the tissue samples at multiple positions along the beam propagation for both setups, the small spot sizes used in conjunction with the scans consisting of only single lines led to comparatively superficial features being observed for both setups under both the surface profiler and histology images. This was attributed to the small volumes removed in both instances courtesy of the small cross-sectional areas of the generated plasma in conjunction with the lower spatial overlap, number of passes and repetition rate of the pulses, along with changes in the tissue morphology post-ablation from the samples being transferred across various solutions for both the glutaraldehyde and formalin fixative processes (for surface profilometry and histological analysis respectively). Despite this, it can be observed that the Bessel-Gauss beam (figure 4.30) produced more consistent features across a longer range than the Gaussian beam (figure 4.31), courtesy of its more consistent spot size and longer depth of focus. Some thermal accumulation is observed in the histology image for the Gaussian setup, which was concluded to be from the increase in the spatial overlap value of the laser pulses as the beam diverges either side of its focus.

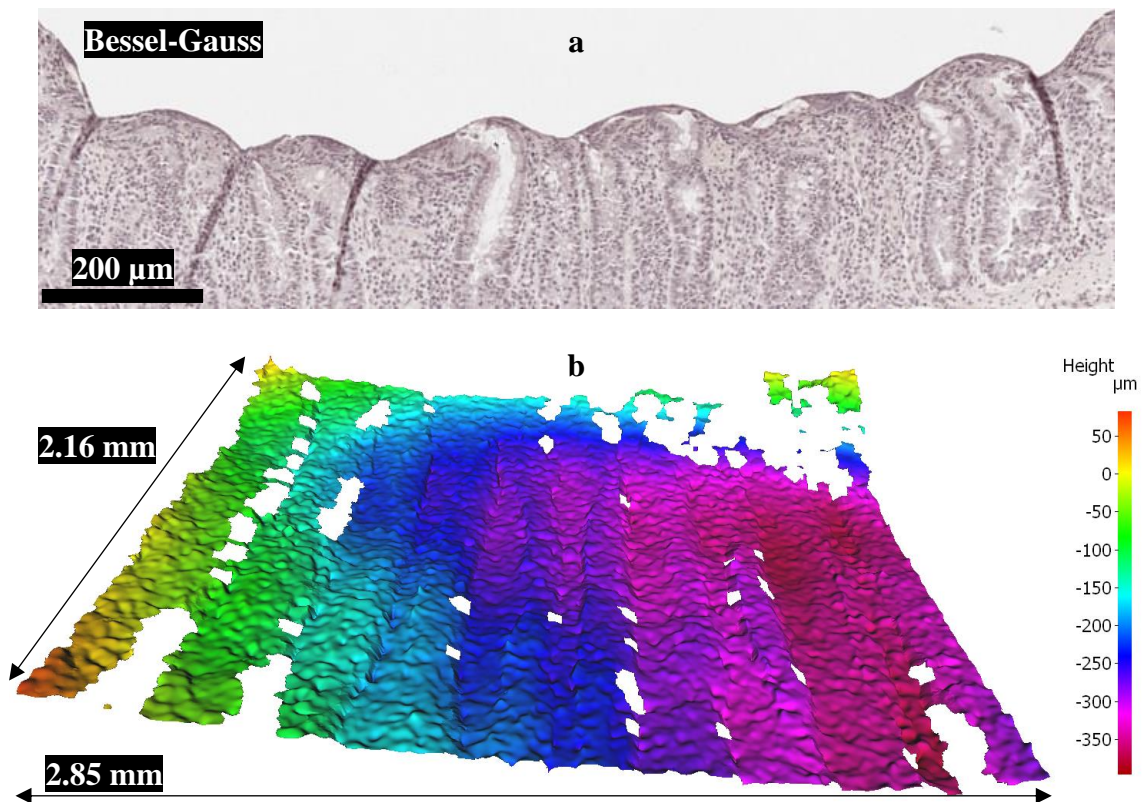


Figure 4.30 – a) Histological H&E stained image and b) 5x magnification surface profile of pig intestine samples ablated with single passes of the Bessel-Gauss beam at 100 μm axial translation intervals of the sample through the beam. The applied pulse rate was 1 kHz with a 50% spatial overlap.

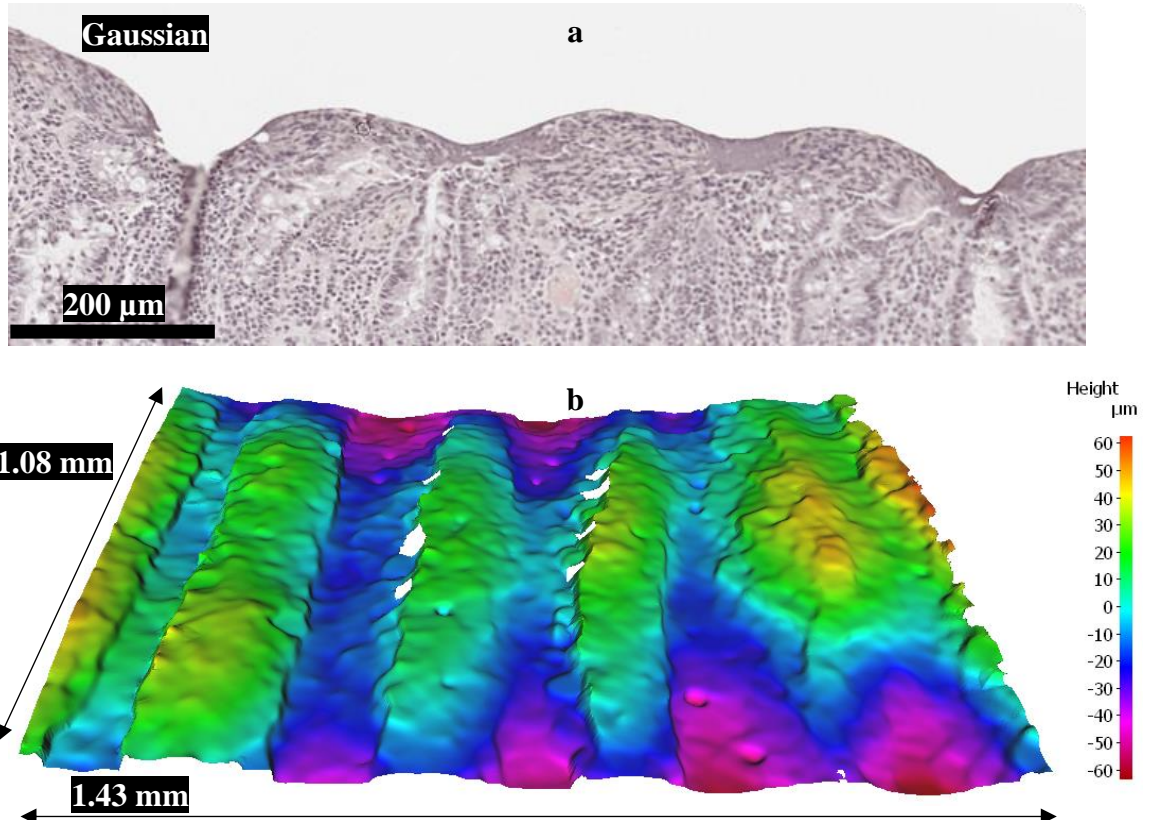
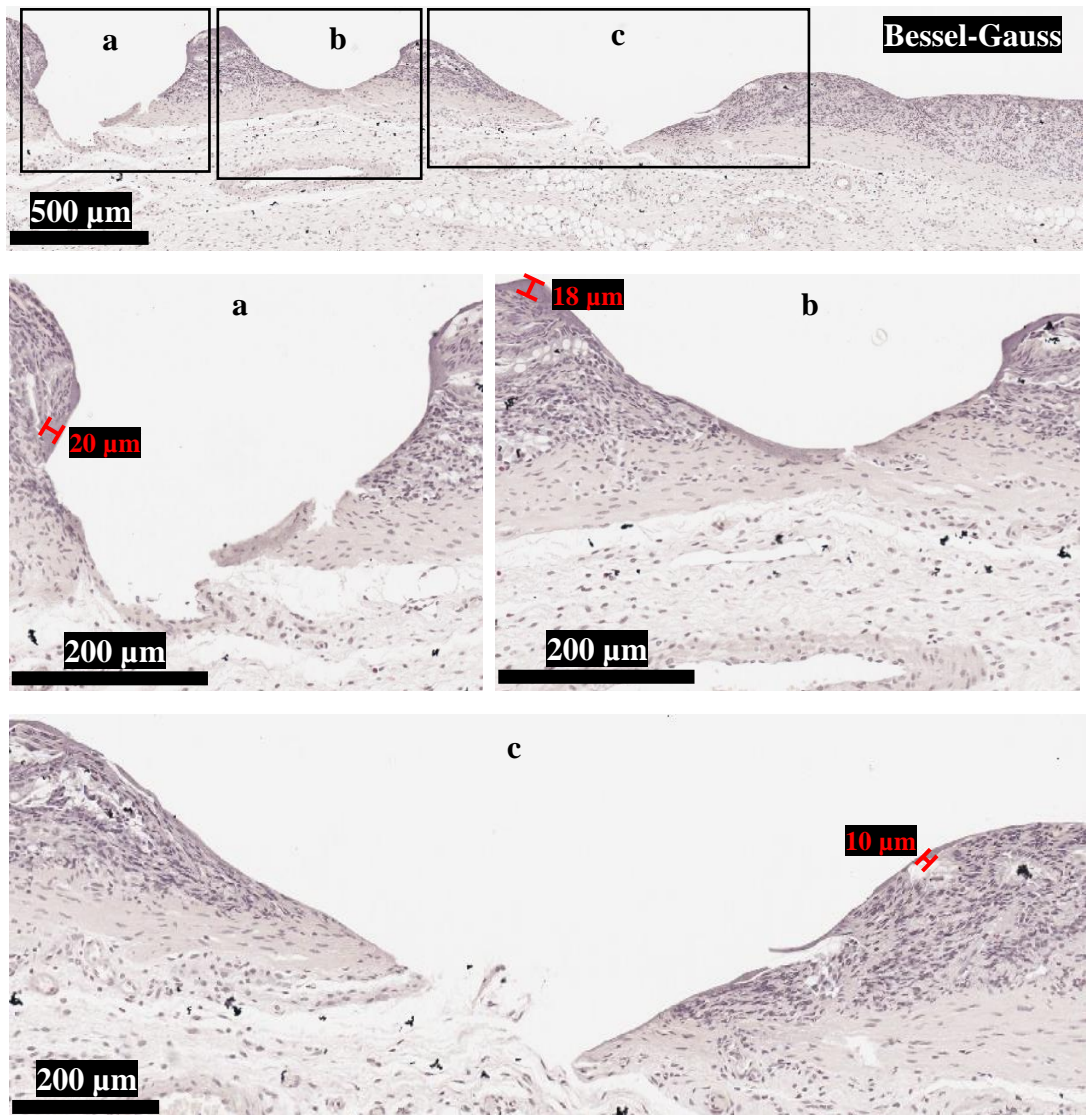


Figure 4.31 – a) Histological H&E stained image and b) 10x magnification surface profile of pig intestine samples ablated with single passes of the Gaussian beam at 100 μm axial translation intervals of the sample through the beam. The applied pulse rate was 1 kHz with a 50% spatial overlap.

Following these focal depth tests, the scalability of the Bessel-Gauss beam was again tested via wider spacing between the raster scan lines (30 μm) and the testing of higher pulse repetition rates (going up to 5 kHz for the raster scans in this case). This is shown in figure 4.32. A spatial overlap of around 70% was used for ablating these samples. While the larger raster spacing led to more gradual tapers in the ablated features, the thermal damage margins were again promising in this case. However, it was observed that for the feature ablated using 5 kHz there was a greater extent of tapering across both tested samples, potentially alluding to a greater difficulty in maintaining lateral control at higher repetition rates with these larger raster spacings despite the apparent low degree of thermal damage.



Glutaraldehyde-fixed porcine intestinal tissue ablated with the Bessel-Gauss beam - 85 μJ , 70% spatial pulse overlap, 30 μm raster line spacing, 10 lines of 6 passes

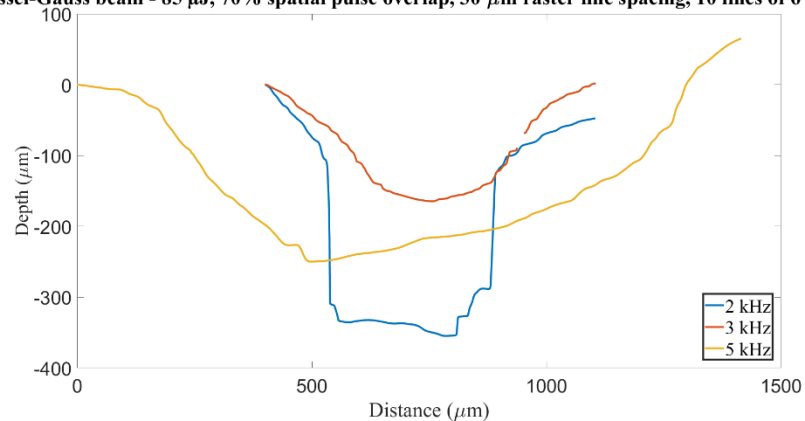


Figure 4.32 – Histological H&E stained images (with zoomed-in views) and line profiles of pig intestine sample ablated with the Bessel-Gauss beam using 85 μJ pulses. The scanning patterns consisted of a) 2 kHz with a spatial overlap of 70% (3 mm/s), 10 lines of 6 passes, b) 3 kHz with a spatial overlap of 70% (4.5 mm/s), 10 lines of 6 passes and c) 5 kHz with a spatial overlap of 70% (7.5 mm/s), 10 lines of 6 passes. The scan line spacing was increased to 30 μm for these features.

Wider scans via larger raster scan line spacing were also tested using the Gaussian beam, but unfortunately these features were lost during the histological sectioning process, as some tearing of the tissue caused the features to merge (figure 4.33). Despite this, cavitation (highlighted by the red circle) was still observed around the remnants of some of the ablated features via histology. Again, this was concluded to have likely

been a consequence of the spatial overlap value changing (increasing) either side of the focus for the divergent Gaussian beam.

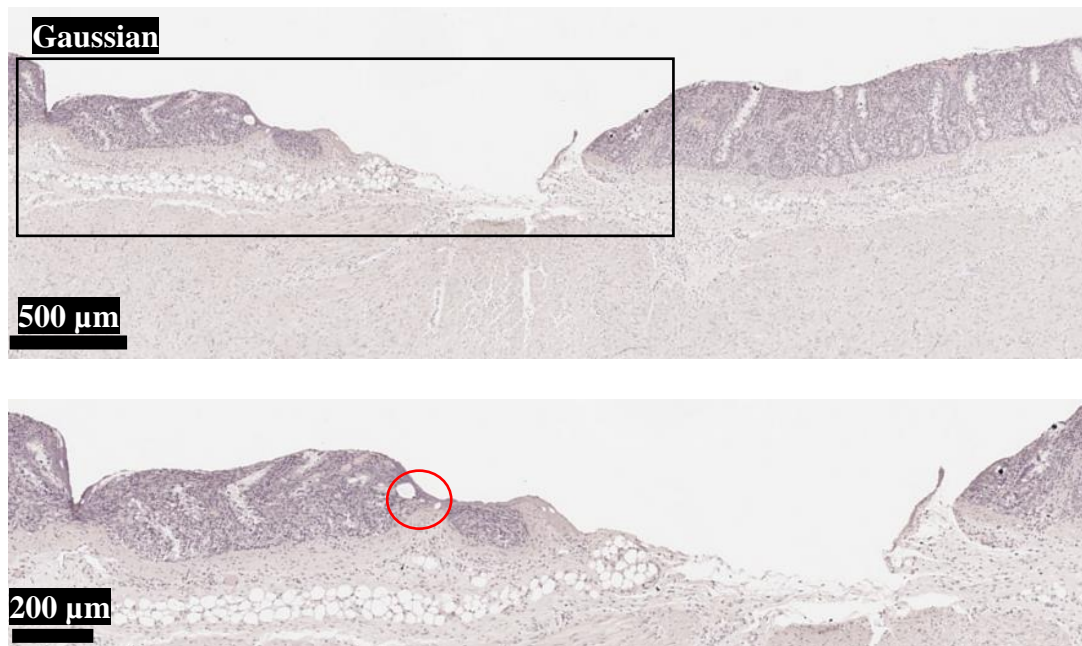


Figure 4.33 –Histological H&E stained image (with zoomed-in view) of pig intestine sample ablated with Gaussian beam using 85 μJ pulses at various repetition rates with wider raster line spacing. Unfortunately, the features blended into one as the tissue tore during histological sectioning. Despite this however, some cavitation was still observed (highlighted by the red circle). The feature to the left is a reference line.

The capacity for both beams to drill to even greater depths within the tissue was further tested by increasing the number of passes per scan line. To decrease the duration of these scans the stage speeds were increased, decreasing the spatial overlap to 70% accordingly. The Bessel-Gauss beam showed great promise here (figure 4.34), with peak depths of over a millimetre being achieved whilst still showcasing minimal thermal damage ($< 25 \mu\text{m}$). Increasing the number of passes to 10 per line allowed for this precise ablation at greater depths using a 70% spatial overlap at repetition rates of 1, 2 and 3 kHz. Additionally, despite the number of passes with the laser, penetration of the muscularis (the muscular tissue that lies beneath the fatty tissue layer) appeared to be hindered by the inherent mechanical strength of this tissue layer. This apparent resistance to laser ablation is highly advantageous, as damage to this layer is dangerous due to it being directly linked to perforation risk [4.23].

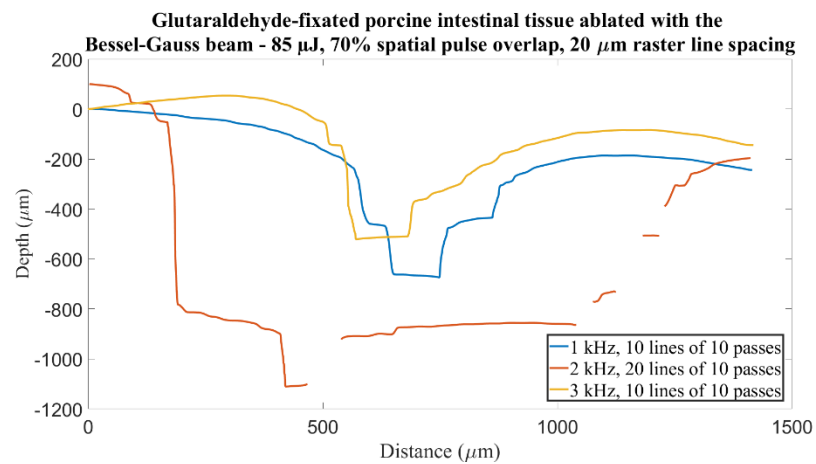
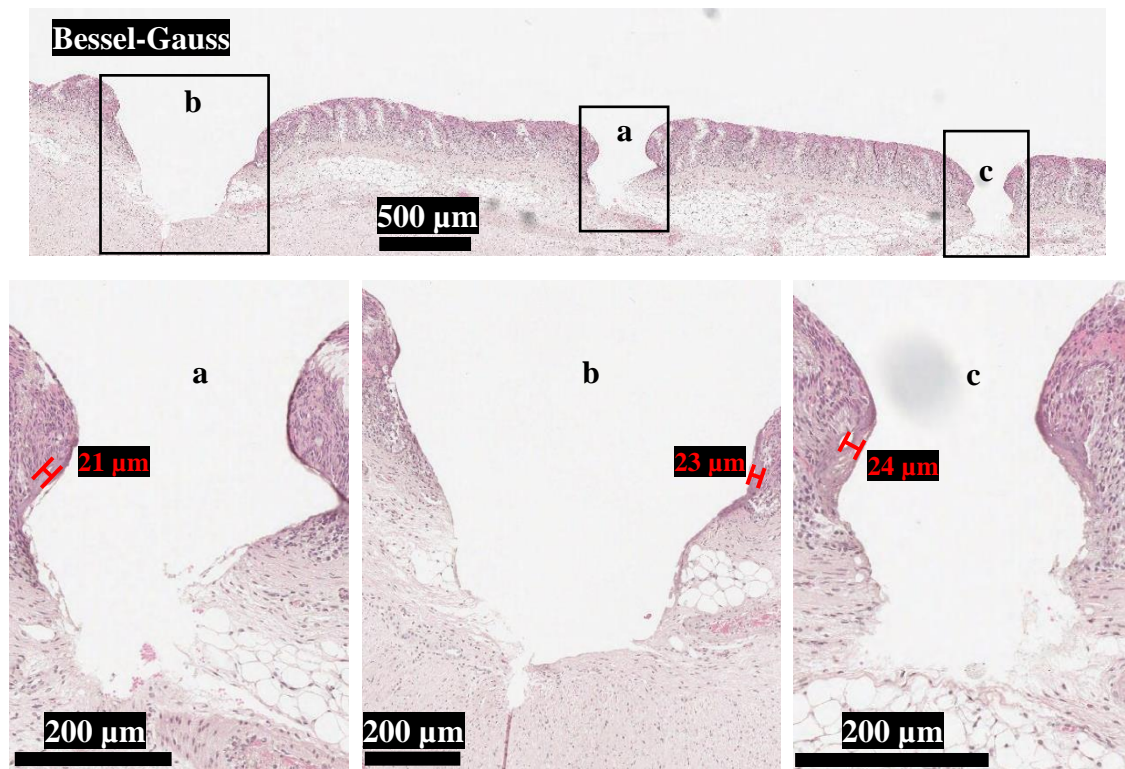


Figure 4.34 – Histological H&E stained images (with zoomed-in views) and line profiles of pig intestine sample ablated with the Bessel-Gauss beam using 85 μ J pulses. Here the features were ablated using scanning patterns consisting of a) 10 lines of 10 passes each at 1 kHz with a spatial overlap of 70% (1.5 mm/s stage speed) b) 20 lines of 10 passes each at 2 kHz with a spatial overlap of 70% (3 mm/s stage speed) and c) 10 lines of 10 passes each at 3 kHz with a spatial overlap of 70% (4.5 mm/s stage speed). The scan lines were spaced out by 20 μ m.

The same parameters were then tested for the Gaussian (figure 4.35). While some of these features looked promising regarding thermal damage margins, it lacked both the consistency and depths achieved with the Bessel-Gauss beam. Cavitation bubble formation was observed for both the 2 and 3 kHz scans.

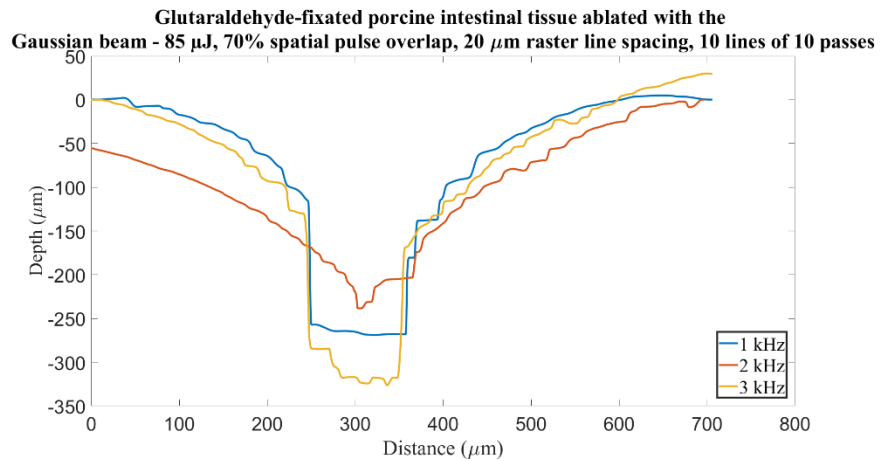
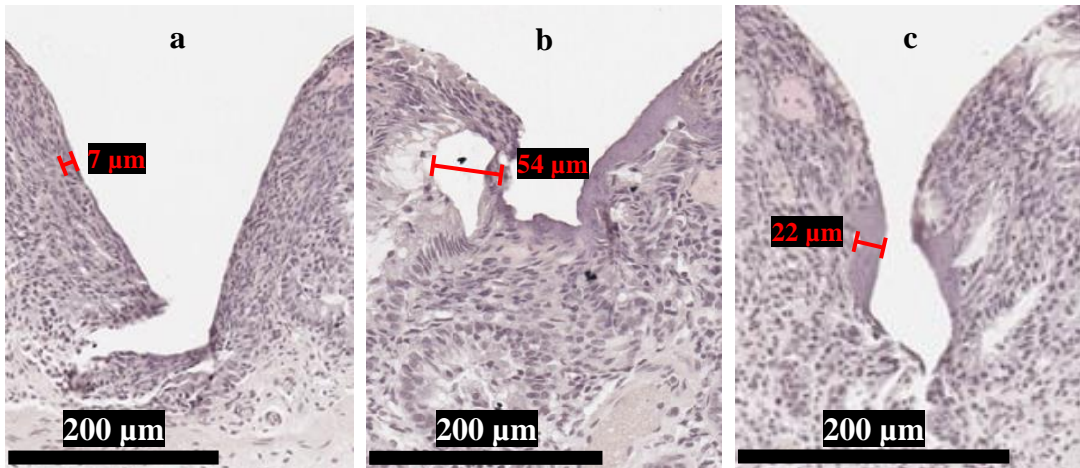
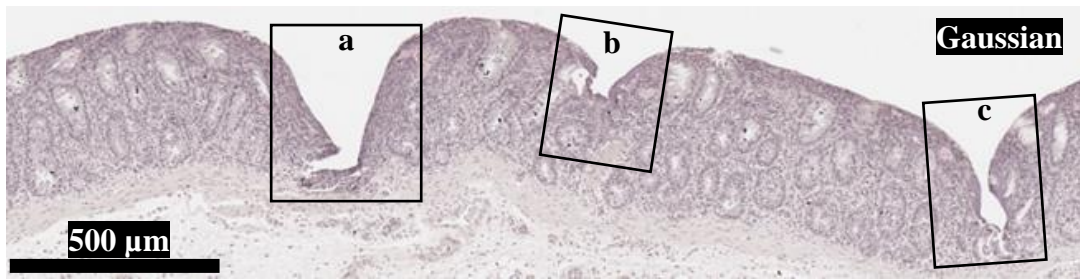


Figure 4.35 – Histological H&E stained images (with zoomed-in views) and line profiles of pig intestine sample ablated with the Gaussian beam using 85 μ J pulses. The feature shown here were ablated using scanning patterns consisting of a) 10 lines of 10 passes each at 1 kHz with a spatial overlap of 70% (1.5 mm/s stage speed) b) 10 lines of 10 passes each at 2 kHz with a spatial overlap of 70% (3 mm/s stage speed) and c) 10 lines of 10 passes each at 3 kHz with a spatial overlap of 70% (4.5 mm/s stage speed). The scan lines were spaced out by 20 μ m.

A summary of these subsequent porcine intestinal ablation trials can be observed in tables 4.4 and 4.5 for the Bessel-Gauss and Gaussian beams respectively.

Pulse Repetition Rate (kHz)	Spatial pulse overlap (%)	Number of passes per line	Raster line spacing (μm)	Approximate mean depth (μm)	Peak thermal damage (μm)	Secondary effects of plasma generation
1	70	10	20	500	21	No
	90	4	20	200	13	No
	97	1	10	70	38	No
2	70	6	30	500	20	No
		10	20	700	23	
	90	4	20	140	28	Cavitation bubbles and heat accumulation
	97	2	10	90	66	
3	70	6	30	130	18	No
		10	20	300	24	Cavitation bubbles
	90	2	20	70	41	Cavitation bubbles and heat accumulation
	97	4	10	200	55	
5	70	6	30	170	10	Mechanical damage (splitting of tissue)

Table 4.4 – Subsequent porcine intestinal tissue ablation trials using the Bessel-Gauss beam.

Wavelength = 1030 nm, Pulse duration = 6 ps, Pulse energy = 85 μJ .

Pulse Repetition Rate (kHz)	Spatial pulse overlap (%)	Number of passes per line	Raster line spacing (μm)	Approximate mean depth (μm)	Peak thermal damage (μm)	Secondary effects of plasma generation
1	70	10	20	200	7	No
	97	1	10	50	46	No
2	70	10	20	60	54	Cavitation bubbles and heat accumulation
	97	2	10	70	44	
3	70	10	20	200	22	
	97	4	10	90	49	

Table 4.5 – Subsequent porcine intestinal tissue ablation trials using the Gaussian beam.

Wavelength = 1030 nm, Pulse duration = 6 ps, Pulse energy = 85 μJ .

From these results there are clear early indications that the Bessel-Gauss beam can help to mitigate the requirement for precise control of the working distance between the respective optical setup and the tissue samples through its ability to decouple the spot size from the depth of focus, providing enhanced reproducibility of results through its greater tolerance to focal range. This also leads to the potential for greater depth control, which is important for the surgical applications under consideration. The consistency of the features ablated using the Gaussian beam was hindered by its comparatively short depth of focus paired with the inhomogeneity of the tissue surface leading to poorer depth discrimination. These factors both exacerbate the need to further increase the pulse energy to reach the plasma formation threshold as the focus is moved deeper into the scattering tissue structure, with attenuation occurring in accordance with the Beer-Lambert law [4.24].

The Bessel-Gauss beam results here show the potential for increased depths and reduced thermal damage margins compared to previously published work by the group which focused on showing the potential for fibre delivery of picosecond pulses of the same duration (6 ps), albeit using lower pulse energies and less passes of the laser than those used here [4.4]. This fibre delivery focused work used 33 and 46 μJ pulse energies, scanned in spiral patterns via the incorporation of a galvanometer scanhead, as well as 29 and 42 μJ pulses delivered via hollow core negative curvature fibre. These fibre delivered pulses were again scanned in spiral patterns using a movable arm from a multi-axis robotic device (AxiDraw V3), as opposed to the raster scanning of the tissue samples themselves used here. The thermal damage margins were up to 84 μm in this case.

Another recent laser ablation trial by Quero *et al.* on gastrointestinal tissue samples used Nd:YAG continuous wave laser sources and mouse models [4.25]. While these trials showed no full-thickness perforations across 210 samples, the laser spot dwelled on one area in each case as opposed to being scanned and the collateral thermal damage margins to either side of the ablated features were not considered, with only the ablated depth being used as a damage metric despite histological sections being obtained for further analysis. An older study on laser ablation of porcine intestinal tissue by Higbee *et al.* was able to showcase efficient and precise removal of the mucosal layer using a Ti:Sapphire laser, but this required femtosecond pulses which as previously discussed are not currently suited for fibre delivery [4.26]. A study by Choi and Yun again used a Ti:Sapphire laser, but instead examined the application of 110 fs laser pulses to mouse intestinal tissue and was able to showcase real-time intraoperative imaging via the implementation of multiphoton imaging through an endoscopic probe [4.27]. However, pulse energies of up to only 2.5 nJ were used, as the regeneration of the epithelium after injury was the interest of this work. As a result, only superficial damage to the blood vessels in the mucosal layer was observed as opposed to distinct tissue ablation.

More recent femtosecond laser ablation studies by Li *et al.* on soft tissue samples have examined the ablation of mouse tongues [4.28]. Again, these pulses are ill-suited to fibre delivery (which was not a concern for the transoral surgery applications that were the primary consideration of this work) and air-cooling was used in this instance to reduce carbonisation. This study also highlighted both an ideal average power range between 3 and 8 W (with the slightly > 5 W used in this work fitting nicely in the middle of this optimal range) and issues with the focal position sensitivity, which the implementation of a Bessel-Gauss beam here seeks to address. The laser light on the mouse tongue tissue surfaces changed from white

to green once the optimal distance of 4.7 mm between the laser aperture and soft tissue surface was exceeded, which came with a significant reduction in the ablation efficiency. This indicates that a marked drop in the on-axis intensity of the pulses led to a change from a plasma-mediated process to a linear photothermally driven one.

A recent study by Pyo *et al.* used a pulsed Ho:YAG laser to ablate *ex vivo* porcine stomach tissue [4.29]. These pulses were around 350 μ s in duration, had a pulse energy of approximately 1 J and were applied at a rate of 10 Hz. This laser system was coupled to a silica optical fibre with a core diameter of 375 μ m. While a peak ablation depth of 2.1 ± 0.3 mm was achieved for 3 passes of the laser at a stage speed of 0.5 mm/s (with the sample being injected with saline and the laser being scanned in single line patterns), this also showcased thermal damage margins of up to 1.1 mm. Similar damage margins of around 1 mm were also observed with these same scanning parameters when no saline was injected into the tissue samples, although in this case the ablation depth increased to 2.5 mm which ended up removing some of the muscular propria layer. This study also showed that increasing the number of laser passes led to increased thermal damage margins in this pulse duration regime. Consequently, the authors state that decreasing the pulse energy and increasing the repetition rate (albeit still in the scope of the microsecond pulse regime, with corresponding suggested ranges of 0.3 to 0.5 J and 30 – 50 Hz) would likely be beneficial in reducing potential rupturing of the surrounding tissue for improving the drilling capability of these laser ablation methods. This has been effectively showcased in this work but with the suggested parameter alterations being made more severely.

The Bessel-Gauss beam was able to achieve plasma formation on the tissue surface across an axial range of over 1 mm at the maximum pulse energy of 85 μ J, while the Gaussian beam of an equivalent focussed spot size was only capable of plasma formation on the tissue surface across an axial range of around 400 μ m for this same applied pulse energy (although this was still significant given that it has a theoretical depth of focus of only 48 μ m as mentioned previously). This larger axial range also resulted in noticeably increased ablation depths for equivalent scanning parameters, as the beam does not suffer as severely from reductions in intensity with increasing ablation depths as the more divergent Gaussian beam does, meaning the Bessel-Gauss beam is able to maintain intensities above the plasma formation threshold of the tissue over greater axial ranges [4.30]. While this concept has been showcased before by Ashforth *et al.* in the ablation of bovine and ovine bone tissue, with the Bessel-Gauss beam achieving approximately 3 times the ablation depth of the Gaussian beam for a given number of applied pulses, the presence of the heat affected zone was only evaluated through optical and single electron microscopy, which is not as insightful as the histology results presented here. This reliance on microscopy methods for evaluation of thermal damage limited the indicators of any heat affected zones to discoloration, cracking and/or signs of charring, all of which lack the fidelity provided by histological analysis. Additionally, this study used 110 fs pulses and a spatial light modulator (SLM) as opposed to an axicon.

The larger ablation depths for equivalent scanning parameters observed in the work showcased here can also be theoretically explained by the self-healing properties of the Bessel-Gauss beam allowing it to mitigate some of the pulse energy losses that occur from absorption into and reflection from the plasma formed during the ablation process [4.31]. The use of a large cone angle and picosecond pulses also allows for comparatively uniform energy deposition, as indicated by the more linear relationship between the

number of laser passes applied and the achieved ablation depth, whereas with the Gaussian beam there appears to be a more noticeable drop-off [4.3].

Factors potentially limiting the total ablation depths obtained with the reimaged Bessel-Gauss beam setup include the intensity oscillations from the oblate tip which have been showcased with previous reimaged Bessel-Gauss beam setups [4.32],[4.33]. While this can be accounted for via spatial filtering, this would also introduce another potential source of loss into the system. The comparatively limited ablation depths obtained with the Gaussian beam could potentially be mitigated by using longer focal lengths to provide a greater Rayleigh range, but the resulting increase in the spot size could potentially inhibit lateral precision. Additionally, implementing longer focal lengths may not be practical for an endoscopic probe design due to the limited working distances available and the increased demands this could place on the imaging modality used.

All the potential advantages provided by the Bessel-Gauss beam are not carried over to the highly scattering biological tissue however, with multiple passes being required to fully realise ablation depth potential due to the reliance on interference mechanisms between the divergent rays, leading to limited penetration depths for single passes [4.12],[4.34]. The significantly improved efficacy of the ablation process for subsequent passes can also likely be attributed to pulse-to-pulse incubation effects, allowing for optical breakdown of the tissue to occur more effectively despite the consistent pulse energy applied [4.30]. The Bessel-Gauss beam setup also required a reimaging telescope for sufficient fluence and stand-off, which would necessitate more space if implemented into an endoscopic probe head design. Convex lenses also benefit from being easier to manufacture, which could be significant for simplifying the microfabrication process. Furthermore, it is not as easy to upscale the spot size while maintaining suitable fluences with the Bessel-Gauss beam, as this requires either a smaller physical axicon angle or a magnifying telescope, both of which significantly affect the fluence contained within the central core. It is important to note though that the Gaussian beam would possibly require an additional lens (or telescope) for collimation of the beam output from the fibre and/or adequate space for the beam to diverge from the output facet of the fibre. This would allow the beam to adequately fill the back aperture of the convex microlens, avoiding potential issues with regards to damage thresholds of distal end optical components and maximising efficiency of the delivery of the incident pulse energy.

The interaction of the axially stretched out fluence and the resultant increase in the ablated volume for a given number of passes observed with the Bessel-Gauss beam clearly showcases some promise in these ablation trials. However, it was concluded that it would be of interest to see how the ablation process using both beams would scale up at higher pulse repetition rates, which if translated successfully would decrease laser processing times, thus be more operationally valid. It was surmised that the consistent spot size and more stretched out fluence profile of the Bessel-Gauss beam may produce favourable results regarding the inhibition of undesirable thermal cavitation and effects. This is due to both the maximum bubble diameter and lifetime increasing with increasing laser fluence, and that this effect would potentially become more significant at higher pulse repetition rates [4.18],[4.35]. If this were to be observed, this could help to mitigate the time constraints on ablation trials (*i.e.* how fast they can be performed while avoiding undesirable cavitation effects) being effectively determined by the maximum scanning speed of the laser spot, as this determines the minimum obtainable spatial overlap of the pulses at a given pulse repetition rate.

4.4 References

- [4.1] G. Cheng, G. Zhang, R. Stoian, and W. Zhao, "Femtosecond laser Bessel beam welding of transparent to non-transparent materials with large focal-position tolerant zone," *Opt. Express*, Vol. 26, Issue 2, pp. 917-926, vol. 26, no. 2, pp. 917–926, Jan. 2018, doi: 10.1364/OE.26.000917.
- [4.2] S. Wu, B. Siwicki, R. M. Carter, F. Biancalana, J. D. Shephard, and D. P. Hand, "Impact of nonlinear effects on transmission losses of hollow-core antiresonant negative curvature optical fiber," *Appl. Opt.*, vol. 59, no. 16, p. 4988, Jun. 2020, doi: 10.1364/ao.382350.
- [4.3] M. Lamperti *et al.*, "Invited Article: Filamentary deposition of laser energy in glasses with Bessel beams," *APL Photonics*, vol. 3, no. 12, p. 120805, Dec. 2018, doi: 10.1063/1.5053085.
- [4.4] S. M. P. C. Mohanan *et al.*, "Preclinical evaluation of porcine colon resection using hollow core negative curvature fibre delivered ultrafast laser pulses," *J. Biophotonics*, vol. 12, no. 11, Nov. 2019, doi: 10.1002/jbio.201900055.
- [4.5] R. J. Beck *et al.*, "Dynamics of picosecond laser ablation for surgical treatment of colorectal cancer," *Sci. Rep.*, vol. 10, no. 1, Dec. 2020, doi: 10.1038/S41598-020-73349-W.
- [4.6] J. Dudutis, P. Gečys, and G. Račiukaitis, "Non-ideal axicon-generated Bessel beam application for intra-volume glass modification," *Opt. Express*, vol. 24, no. 25, pp. 28433–28443, Dec. 2016, doi: 10.1364/oe.24.028433.
- [4.7] O. Brzobohatý, T. Cižmár, and P. Zemánek, "Quasi-Bessel beam generated by oblate-tip axicon," in *16th Polish-Slovak-Czech Optical Conference on Wave and Quantum Aspects of Contemporary Optics*, Dec. 2008, vol. 7141, p. 714126. doi: 10.1117/12.822425.
- [4.8] S. M. P. C. Mohanan, "Picosecond laser procedures to enhance the efficacy of tissue resection," Heriot-Watt University, Edinburgh, 2019. Accessed: Sep. 07, 2021. [Online]. Available: <https://www.ros.hw.ac.uk/handle/10399/4246>
- [4.9] H. Wang and S. Zuo, "Laparoscopic surgical device with modular end tools for real-time endomicroscopy and therapy," *Med. Biol. Eng. Comput.*, vol. 59, no. 4, pp. 787–797, Mar. 2021, doi: 10.1007/s11517-021-02341-x.
- [4.10] C. L. Hoy, "Development of Femtosecond Laser Endoscopic Microsurgery," pp. 26–28, May 2011, Accessed: Sep. 18, 2021. [Online]. Available: <https://repositories.lib.utexas.edu/handle/2152/ETD-UT-2011-05-2659>
- [4.11] V. Nuzzo, M. Savoldelli, J.-M. Legeais, and K. Plamann, "Self-focusing and spherical aberrations in corneal tissue during photodisruption by femtosecond laser," *J. Biomed. Opt.*, vol. 15, no. 3, p. 038003, 2010, doi: 10.1117/1.3455507.
- [4.12] Y. Matsuoka, Y. Kizuka, and T. Inoue, "The characteristics of laser micro drilling using a Bessel beam," *Appl. Phys. A Mater. Sci. Process.*, vol. 84, no. 4, pp. 423–430, Sep. 2006, doi: 10.1007/s00339-006-3629-6.
- [4.13] Z. Cui *et al.*, "Dynamic chromatic aberration pre-compensation scheme for ultrashort petawatt laser systems," *Opt. Express*, vol. 27, no. 12, pp. 16812–16822, Jun. 2019, doi: 10.1364/oe.27.016812.
- [4.14] "Mounted N-BK7 Plano-Convex Lenses (AR Coating: 650 - 1050 nm)." https://www.thorlabs.com/newgrouppage9.cfm?objectgroup_id=6278 (accessed Aug. 10, 2020).
- [4.15] E. Hecht, *Optics*. Pearson, 2016.
- [4.16] "Scanning-Slit Optical Beam Profilers." https://www.thorlabs.com/newgrouppage9.cfm?objectgroup_id=804 (accessed Mar. 24, 2021).
- [4.17] W. R. Harp, A. G. Paleocrassas, and J. F. Tu, "A Practical method for determining the beam profile near the focal spot," *Int. J. Adv. Manuf. Technol.*, vol. 37, no. 11–12, pp. 1113–1119, Jul. 2008, doi: 10.1007/s00170-007-1067-z.
- [4.18] A. Vogel and V. Venugopalan, "Mechanisms of pulsed laser ablation of biological tissues," *Chem. Rev.*, vol. 103, no. 2, pp. 577–644, Feb. 2003, doi: 10.1021/cr010379n.
- [4.19] W. S. Góra, R. M. Carter, B. Dhillon, D. P. Hand, and J. D. Shephard, "Ultrafast laser machining

- of porcine sclera,” in *Optics InfoBase Conference Papers*, Jul. 2014, vol. 9542, pp. 144–148. doi: 10.1117/12.2183627.
- [4.20] N. Tinne, B. Kaune, A. Krüger, and T. Ripken, “Interaction mechanisms of cavitation bubbles induced by spatially and temporally separated fs-laser pulses,” *PLoS One*, vol. 9, no. 12, Dec. 2014, doi: 10.1371/journal.pone.0114437.
- [4.21] A. Mermillod-Blondin, F. Bourquard, J. P. Colombier, M. Somayaji, M. K. Bhuyan, and R. Stoian, “Ultrafast laser nanostructuring in bulk silica, a ‘slow’ microexplosion,” *Opt. Vol. 4, Issue 8*, pp. 951–958, vol. 4, no. 8, pp. 951–958, Aug. 2017, doi: 10.1364/OPTICA.4.000951.
- [4.22] T. V. Nechay *et al.*, “Thermal effects of monopolar electrosurgery detected by real-time infrared thermography: An experimental appendectomy study,” *BMC Surg.*, vol. 20, no. 1, pp. 1–12, May 2020, doi: 10.1186/s12893-020-00735-6.
- [4.23] S. MP, B. MJ, M. A, W. SJ, H. A, and M. A, “The target sign: an endoscopic marker for the resection of the muscularis propria and potential perforation during colonic endoscopic mucosal resection,” *Gastrointest. Endosc.*, vol. 73, no. 1, pp. 79–85, Jan. 2011, doi: 10.1016/J.GIE.2010.07.003.
- [4.24] C. L. Hoy, “Development of femtosecond laser endoscopic microsurgery,” pp. 9–10, May 2011, Accessed: Aug. 23, 2021. [Online]. Available: <https://repositories.lib.utexas.edu/handle/2152/ETD-UT-2011-05-2659>
- [4.25] G. Quero *et al.*, “Modular laser-based endoluminal ablation of the gastrointestinal tract: in vivo dose–effect evaluation and predictive numerical model,” *Surg. Endosc. 2018 3310*, vol. 33, no. 10, pp. 3200–3208, Nov. 2018, doi: 10.1007/S00464-018-6603-4.
- [4.26] R. G. Higbee, B. S. Irwin, M. N. Nguyen, Y. Zhang, and W. L. Warren, “Femtosecond laser ablation of porcine intestinal mucosa: potential autologous transplant for segmental cystectomy,” in *Photonic Therapeutics and Diagnostics*, Apr. 2005, vol. 5686, pp. 631–641. doi: 10.1117/12.591262.
- [4.27] M. Choi *et al.*, “In vivo femtosecond endosurgery: an intestinal epithelial regeneration-after-injury model,” *Opt. Express, Vol. 21, Issue 25*, pp. 30842–30848, vol. 21, no. 25, pp. 30842–30848, Dec. 2013, doi: 10.1364/OE.21.030842.
- [4.28] W. Li, J. Zheng, Y. Zhang, F. Yuan, and P. Lyu, “Temperature and depth evaluation of the in vitro effects of femtosecond laser on oral soft tissue, with or without air-cooling,” *Lasers Med. Sci.*, vol. 34, no. 4, pp. 649–658, Jun. 2019, doi: 10.1007/S10103-018-2634-2/FIGURES/5.
- [4.29] H. Pyo, H. Kim, and H. W. Kang, “Evaluations on laser ablation of ex vivo porcine stomach tissue for development of Ho:YAG-assisted endoscopic submucosal dissection (ESD),” *Lasers Med. Sci. 2020 367*, vol. 36, no. 7, pp. 1437–1444, Nov. 2020, doi:10.1007/S10103-020-03182-0.
- [4.30] S. A. Ashforth, R. N. Oosterbeek, and M. C. Simpson, “Ultrafast pulsed Bessel beams for enhanced laser ablation of bone tissue for applications in LASSOS,” *Proc. SPIE*, vol. 10094. pp. 100941O–100941O–9, 2017. doi: 10.1117/12.2250068.
- [4.31] R. N. Oosterbeek, S. Ashforth, O. Bodley, and M. C. Simpson, “Measuring the ablation threshold fluence in femtosecond laser micromachining with vortex and Bessel pulses,” *Opt. Express*, vol. 26, no. 26, pp. 34558–34568, Dec. 2018, doi: 10.1364/oe.26.034558.
- [4.32] O. Brzobohatý, T. Cizmar, and P. Zemánek, “High quality quasi-Bessel beam generated by round-tip axicon,” *Opt. Express*, vol. 16, no. 17, pp. 12688–12700, Aug. 2008, doi: 10.1364/oe.16.012688.
- [4.33] P. Wu, C. Sui, and W. Huang, “Theoretical analysis of a quasi-Bessel beam for laser ablation,” *Photonics Res.*, vol. 2, no. 3, pp. 82–86, 2014, doi: 10.1364/prj.2.000082.
- [4.34] M. Duocastella and C. B. Arnold, “Bessel and annular beams for materials processing,” *Laser Photon. Rev.*, vol. 6, no. 5, pp. 607–621, Sep. 2012, doi: 10.1002/LPOR.201100031.
- [4.35] N. Tinne, E. Lübking, H. Lubatschowski, A. Krüger, and T. Ripken, “The influence of a spatial and temporal pulse-overlap on the laser-tissue-interaction of modern ophthalmic laser systems,” *Biomed. Eng. / Biomed. Tech.*, vol. 57, no. SI-1-Track-P, pp. 302–305, Sep. 2012, doi: 10.1515/BMT-2012-4115.

Chapter 5

Ablation of porcine intestinal tissue at higher pulse repetition rates

5.1 Characterisation of Carbide laser

Following on from the previous porcine ablation trials, a firmware update was installed for the Carbide laser software. Subsequently, a slight increase in the output power was observed for the 5W 60 kHz output setting (from 5.3 W to 5.6 W on the 5W 60 kHz preset). Characterisation of the beam was performed to ensure the spatial properties of the beam had remained similar to prior measurements. The DataRay BeamMap 2 beam profiler was used to do this (figure 5.1).

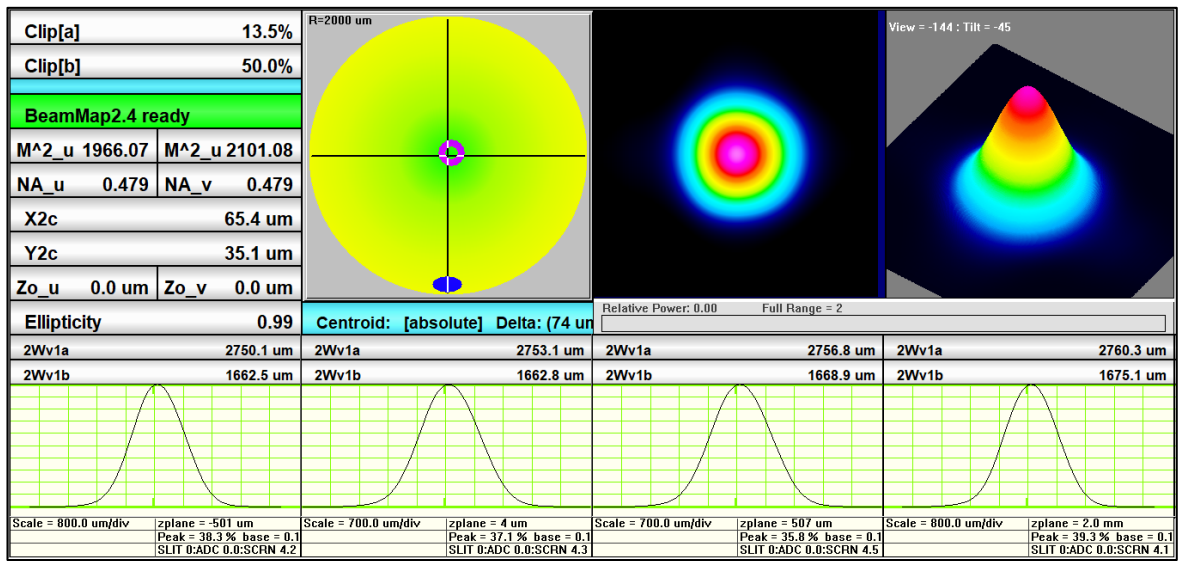


Figure 5.1 – BeamMap 2 beam profiler measurement of beam output produced by Carbide laser.

The gain was set to 0 dB to maximise the signal-to-noise ratio. The “Delta” (*i.e.* the XY displacement from the centre of the scanning slit at the 4 μm axial position reference plane) was kept under 100 μm, as recommended in the guide of measuring pulsed laser sources [5.1]. The M² values were ignored as the profiler is unable to measure this parameter if the beam does not come to a focus across the 4 scanning slits. The measured 1/e² beam width of 2.75 mm was found to be of minimal difference with regards to the previously quoted beam width of 2.6 mm. This is particularly true when considering that this measurement was taken approximately 1 metre away from the laser output (with this being as close as the profiler could be placed prior to the vertically mounted optical cage setups), as opposed to the 0.6 m distance quoted for the 2.6 mm measurement (Light Conversion, personal communication, April 26th 2020). The beam was attenuated using two mirrors positioned at 45° relative to the input beam (figure 5.2).

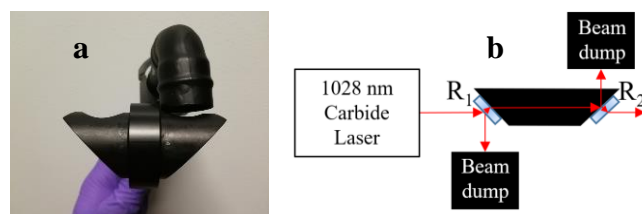


Figure 5.2 – a) Photograph and b) diagram of dual mirror beam attenuator, with R₁ and R₂ representing mirrors 1 and 2 respectively.

Additionally, the M^2 of the beam was measured using this same beam profiler with a 25.4 mm plano-convex focusing lens (LA1951-B, Thorlabs) to generate an appropriately sized beam waist (around $20 \mu\text{m}$ $1/e^2$ diameter). The M^2 value remained around 1.3 (figure 5.3).

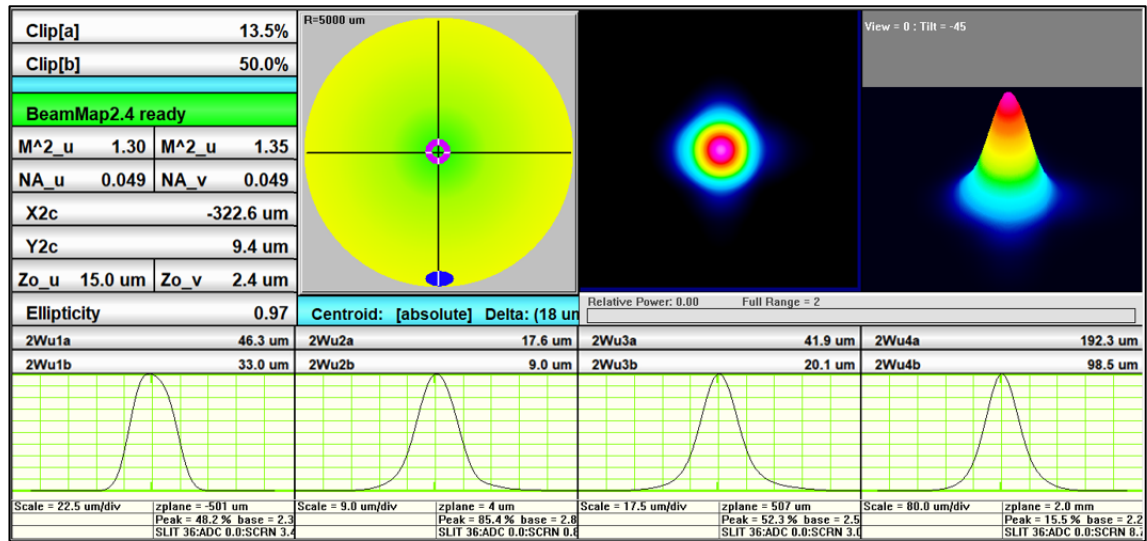


Figure 5.3 – BeamMap 2 beam profiler measurement of beam output produced by 25.4 mm plano-convex lens focusing the input beam from the Carbide laser.

5.2 Surface characterisation of porcine intestinal tissue samples

The final set of tissue ablation trials performed within this thesis focussed on increasing the pulse repetition rates used during the ablation procedures for both beams with the aim of reducing the durations of these to make them more economically viable from a clinical perspective. These higher pulse repetition rates are crucial for speeding up the ablation process as they enable faster scanning speeds of the laser spot for obtaining equivalent spatial pulse overlap values when compared to lower pulse repetition rates, which in turn can provide higher removal rates. Histology evaluation would allow for any difference between the cavitation dynamics imposed by the different beam shapes to be observed. The more consistent spot size and self-healing properties of the Bessel-Gauss beam were hypothesised to make it less prone to undesirable cavitation effects (as discussed in in the secondary effects of plasma-mediated ablation of tissue section in chapter 2).

While the focal tolerance tests carried out previously would have been interesting to repeat at these higher pulse repetition rates (especially given that this would allow for more passes of the laser spots within a set period), this was deemed comparatively wasteful given the tendency for producing superficial ablation as shown in the earlier ablation trials covered in chapter 4. This was particularly true given the limited sample availability and histology sections available. As a result, these trials were performed predominantly at the peak critical energy density plane for both setups, with the inherent inhomogeneity of the tissue surfaces determining the characteristics of the ablated features based on the respective axial intensity distributions of the Gaussian and Bessel-Gauss beams.

Surface scans of non-ablated porcine intestine samples were captured using the Alicona InfiniteFocus G4 surface profilometer to quantify this surface inhomogeneity (figures 5.4 - 5.6). Additionally, this was only done for fixated porcine intestinal tissue samples as these surface scans were time consuming (taking up to a couple of hours to process), meaning that non-fixated tissue would be at risk of drying out during the scanning process. The S_a parameter, which represents the absolute value of the difference in height of each

point compared to the arithmetical mean of the surface, was used to do this [5.2]. The selected areas for these measurements coincided with where the tissue surface looked suitable for laser processing (*i.e.* avoiding edges).

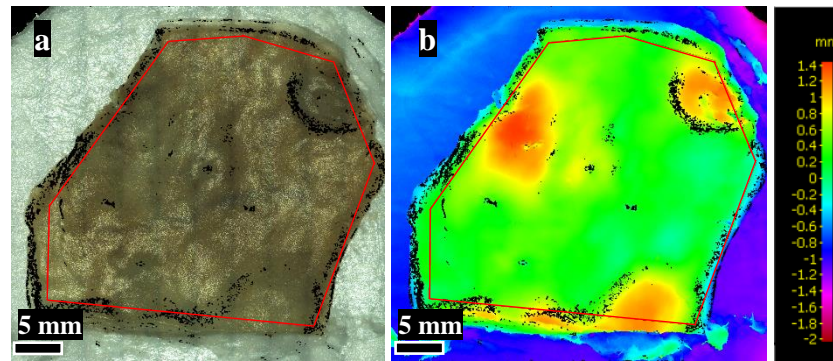


Figure 5.4 – a) Normal and b) surface profile images of formalin fixated porcine intestine tissue sample with underlying DispoCut board, captured using the 5x objective lens on the Alicona surface profilometer. The red outline represents the selected measurement area, with black areas representing missing data points.

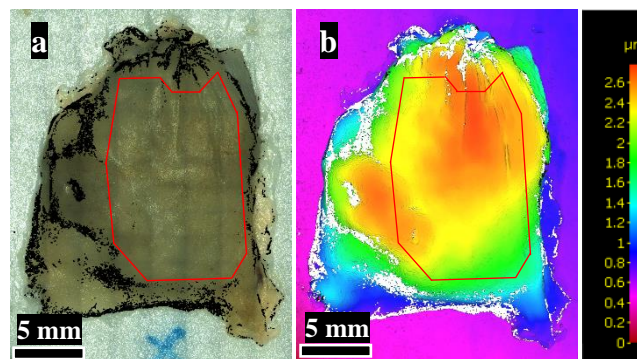


Figure 5.5 – a) Normal and b) surface profile images of formalin fixated porcine intestine tissue sample with underlying DispoCut board, captured using the 5x objective lens on the Alicona surface profilometer. The red outline represents the selected measurement area, with white areas representing missing data points.

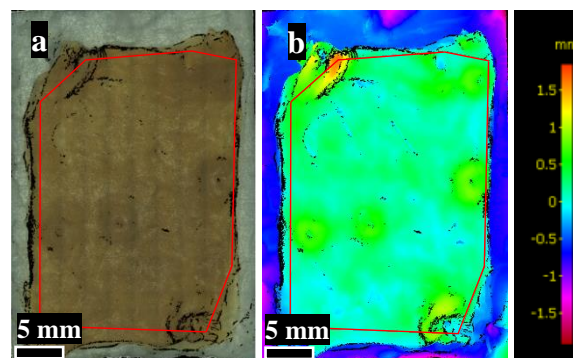


Figure 5.6 – a) Normal and b) surface profile images of glutaraldehyde fixated porcine intestine tissue sample with underlying DispoCut board, captured using the 5x objective lens on the Alicona surface profilometer. The red outline represents the selected measurement area, with black areas representing missing data points.

The obtained S_a measurements from these measurements were around $261 \pm 3 \mu\text{m}$, $356 \pm 3 \mu\text{m}$ and $150 \pm 3 \mu\text{m}$ respectively. The lower S_a measured for the sample fixed in 3% glutaraldehyde solution can be attributed to the increased shrinkage of tissue samples that has been reported for fixation in higher concentration glutaraldehyde solutions [5.3]. Meanwhile, in porcine ocular tissues, 24 hour fixation periods in 10% formalin solution gave average percentage differences across a range of parameters that represent

sample shape and size as small as 1% when compared to fresh samples [5.4]. Regardless, these measurements help to explain the higher inconsistency of the ablation observed previously with the Gaussian beam compared to the Bessel-Gauss beam, courtesy of its significantly lower focal depth (calculated to be approximately 50 μm).

5.3 5 kHz ablation of porcine intestinal tissue samples with Bessel-Gauss beam

Ablation trials were performed on porcine intestinal tissue using both beams at 5, 10 and 20 kHz. The Bessel-Gauss beam showed promising damage margins ($< 30 \mu\text{m}$) across all of the stage translation speeds/spatial pulse overlaps at 5 kHz (figures 5.7 and 5.8). A general trend of higher ablated depths was observed for increased spatial pulse overlaps, as would be intuitively expected. However, at this higher pulse repetition rate it was noted that it became increasingly difficult to control the general structure of the resected volume of tissue when higher spatial overlaps were applied, with lateral splitting of the tissue being an issue despite the high thermal confinement. This is particularly noticeable at 70% spatial pulse overlaps, shown in figure 5.8d. This was attributed to the increased density of energy applied to the tissue at the edges of the raster scans as the stage decelerates. The missing sections on the line profile plots are from missing data points on the surface scans performed using the surface profilometer (InfiniteFocus G4, Alicona). These arise from regions on the surface of the tissue sample where the device is unable to collect the reflected light. This is typically attributed to said regions having high incline angles and/or sharp height transitions [5.5].

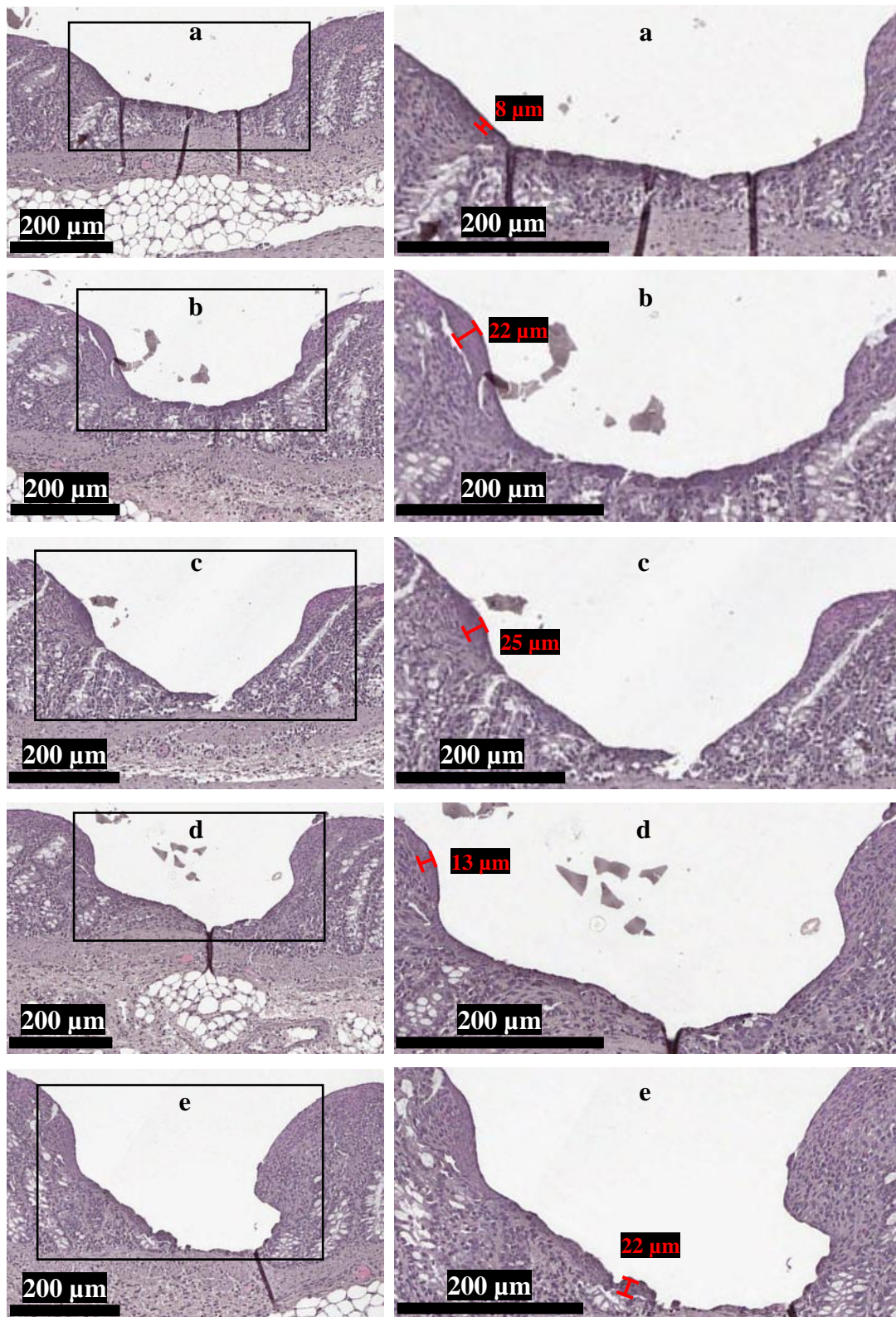


Figure 5.7 – Histological H&E stained images (with zoomed-in views) of porcine intestinal tissue samples, scanned with the Bessel-Gauss beam using 85 μJ pulses (measured after the optical setups for the trials detailed in this chapter) applied at a repetition rate of 5 kHz with spatial overlaps of a) 0% (285% spot separation, 50 mm/s) b) 0% (230% spot separation, 40 mm/s) c) 0% (200% spot separation, 35 mm/s) d) 0% (170% spot separation, 30 mm/s) e) 0% (145% spot separation, 25 mm/s). The scans consisted of 20 lines of 4 passes each, spaced out by 20 μm . The observed thermal damage margins are highly localised, extending slightly more than 20 μm from the ablated region in the worst case. The black boxes again represent the frames for the zoomed-in images.

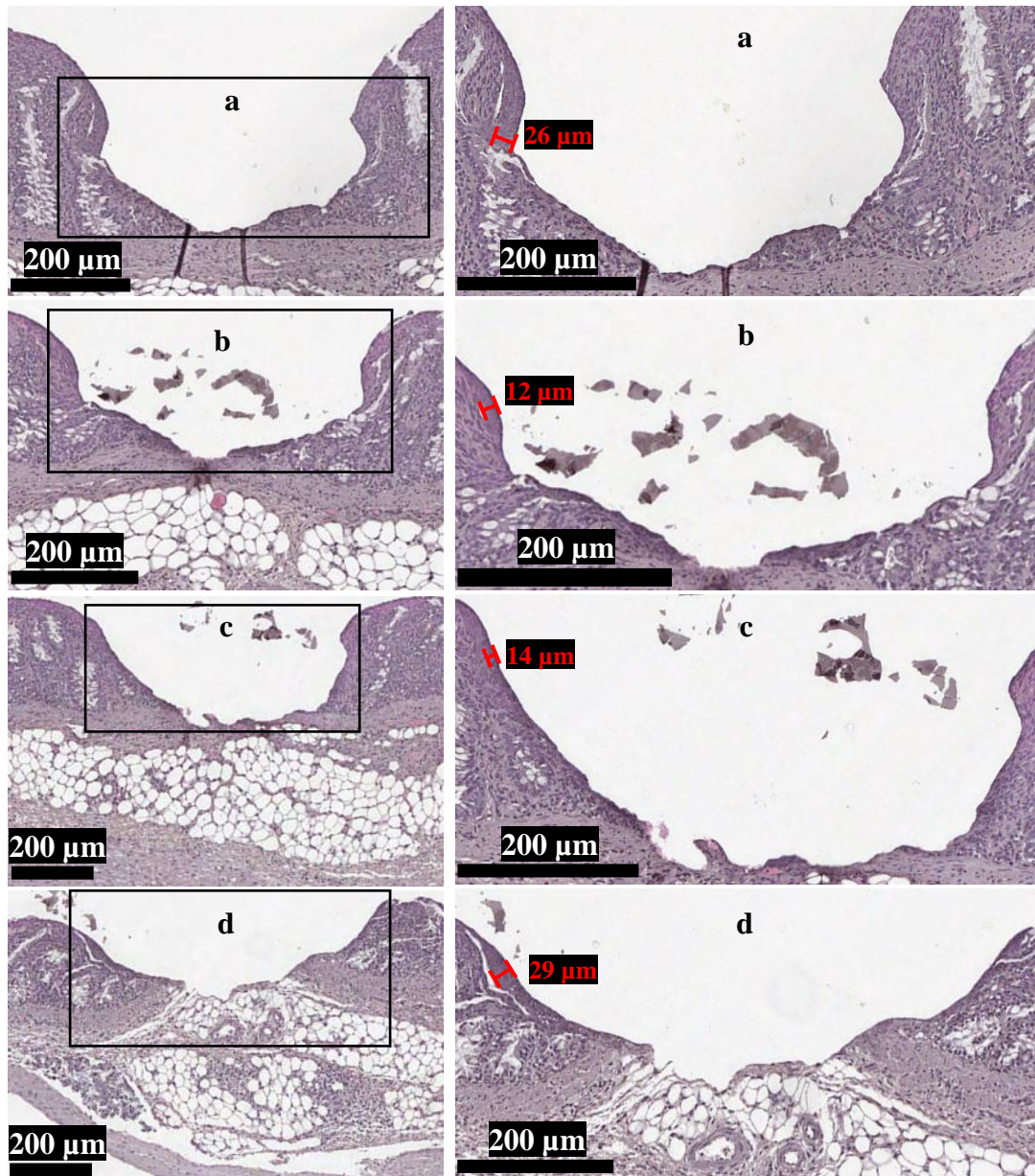


Figure 5.8 – Histological H&E stained images (with zoomed-in views) of porcine intestinal tissue samples. The features here were scanned with the Bessel-Gauss beam using 85 μJ pulses applied at a repetition rate of 5 kHz with spatial overlaps of a) 0% (115% spot separation, 20 mm/s) b) 15% (15 mm/s) c) 45% (10 mm/s) d) 70% (5 mm/s). The scans consisted of 20 lines of 4 passes each, spaced out by 20 μm . The observed thermal damage margins are highly localised, extending just under 30 μm from the ablated region in the worst case. However, the shape of the ablated feature is harder to control as the spatial overlap of the pulses is increased at this higher pulse repetition rate.

A plot of line profiles measured from the surface maps captured using the surface profilometer of the corresponding glutaraldehyde-fixated samples is shown in figure 5.9.

Glutaraldehyde-fixated porcine intestinal tissue ablated with the Bessel-Gauss beam - 85 μ J, 5 kHz, 20 μ m raster line spacing, 20 lines of 4 passes

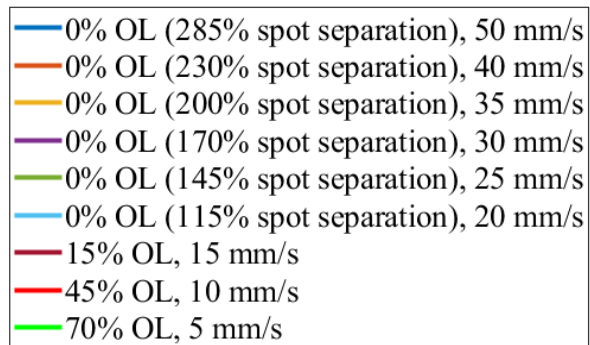
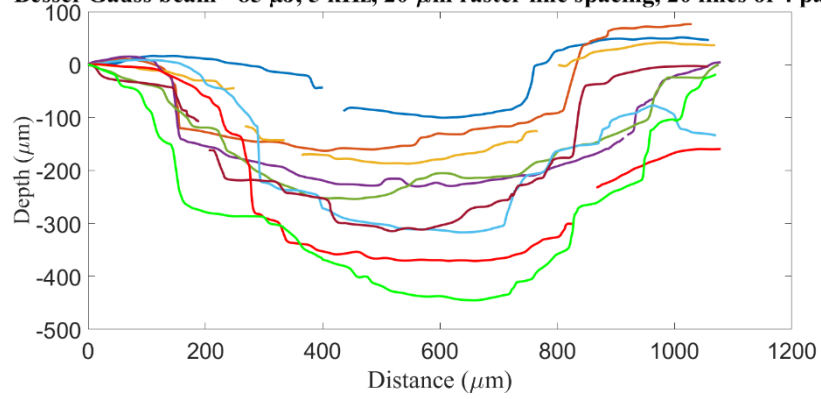


Figure 5.9 – Line profiles taken from the surface maps captured using the surface profilometer of the corresponding glutaraldehyde-fixated porcine intestinal tissue samples ablated using the same parameters for the Bessel-Gauss beam as those shown in the previous histology images. The overall shape of the ablated feature becomes harder to control as the spatial overlap of the pulses is increased at this higher pulse repetition rate. OL = spatial pulse overlap.

5.4 5 kHz ablation of porcine intestinal tissue samples with Gaussian beam

The Gaussian beam exhibited promising thermal damage margins across faster stage translation speeds/lower spatial pulse overlaps (figure 5.10). However, the lower depth of focus led to issues regarding the consistency of ablation along the raster scans and at higher pulse overlaps excessive cavitation bubble formation was observed, which led to further difficulties in controlling the ablation process, with this leading to comparatively extensive damage margins of up to more than 120 μm (figure 5.11c).

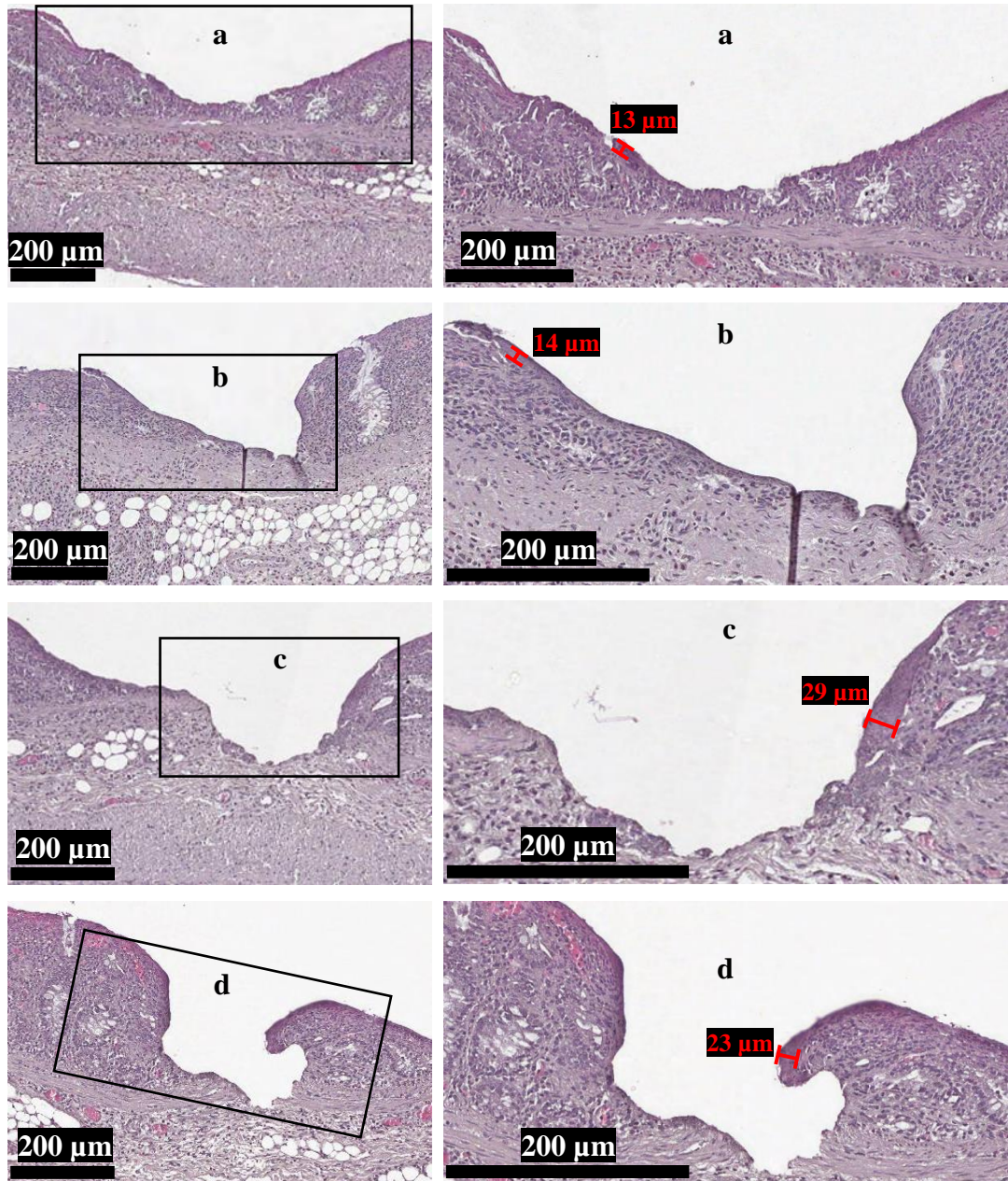


Figure 5.10 – Histological H&E stained images (with zoomed-in views) of porcine intestinal tissue samples. The features here were scanned with the Gaussian beam using 85 μJ pulses applied at a repetition rate of 5 kHz with spatial overlaps of a) 0% (285% spot separation, 50 mm/s) b) 0% (230% spot separation, 40 mm/s) c) 0% (200% spot separation, 35 mm/s) d) 0% (145% spot separation, 25 mm/s). The scans consisted of 20 lines of 4 passes each, spaced out by 30 μm . The observed thermal damage margins are highly localised, extending just under 20 μm from the ablated region in the worst case. The individual scan lines observed in surface profile a) are a result of the low spatial overlap, low pulse frequency and short focal depth.

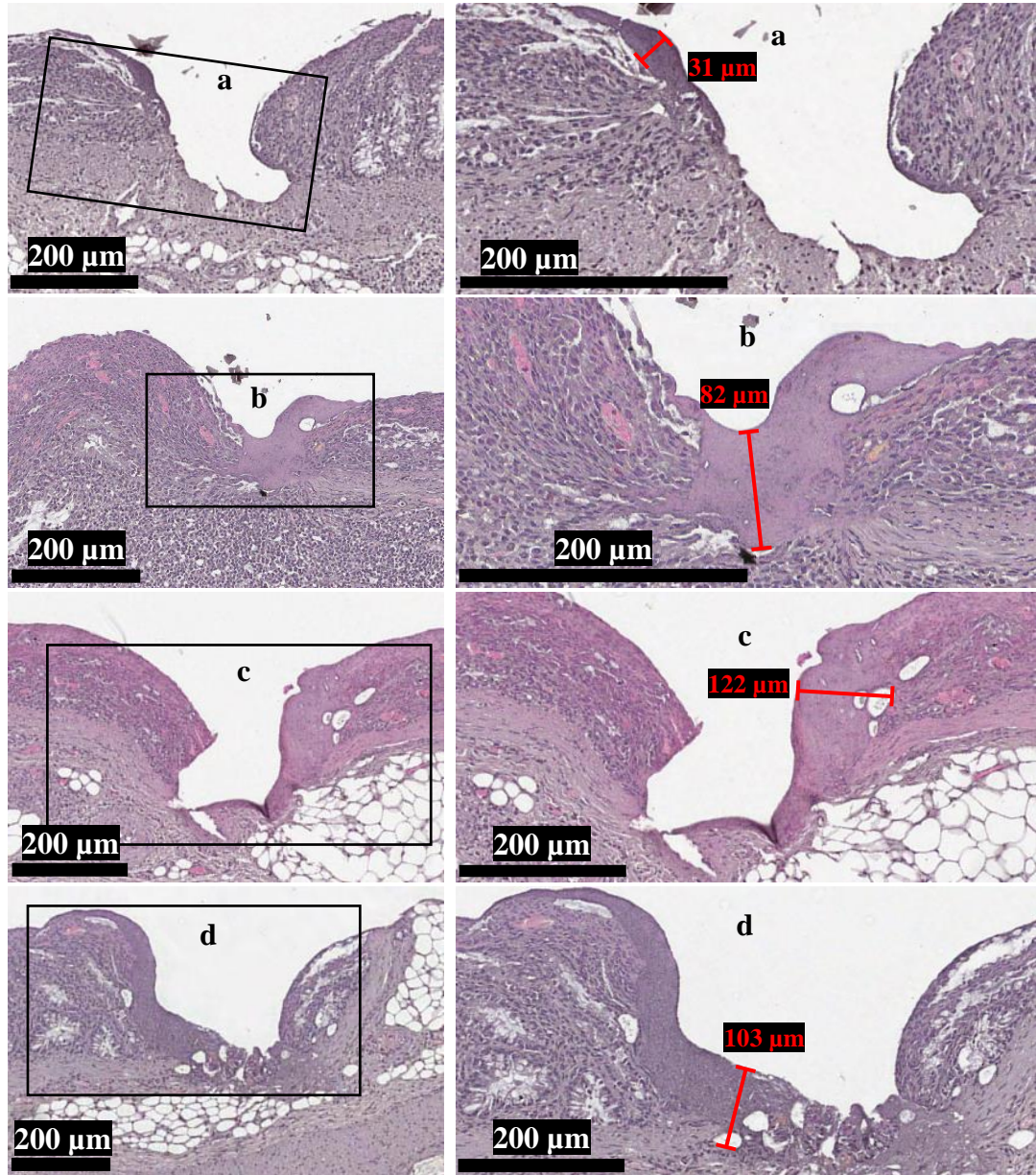


Figure 5.11 – Histological H&E stained images (with zoomed-in views) of porcine intestinal tissue samples. The features here were scanned with the Gaussian beam using 85 μJ pulses applied at a repetition rate of 5 kHz with spatial overlaps of a) 0% (115% spot separation, 20 mm/s) b) 15% (15 mm/s) c) 45% (10 mm/s) d) 70% (5 mm/s). The scans consisted of 20 lines of 4 passes each, spaced out by 20 μm . The observed thermal damage margins are again more extensive here, stretching over more than 120 μm from the ablated region in the worst case. This occurs due to the cavitation effects that arise from the combination of the high fluence with the high pulse repetition rate and spatial overlap of the pulses.

A plot of line profiles measured from the surface maps captured using the surface profilometer of the corresponding glutaraldehyde-fixed samples is shown in figure 5.12.

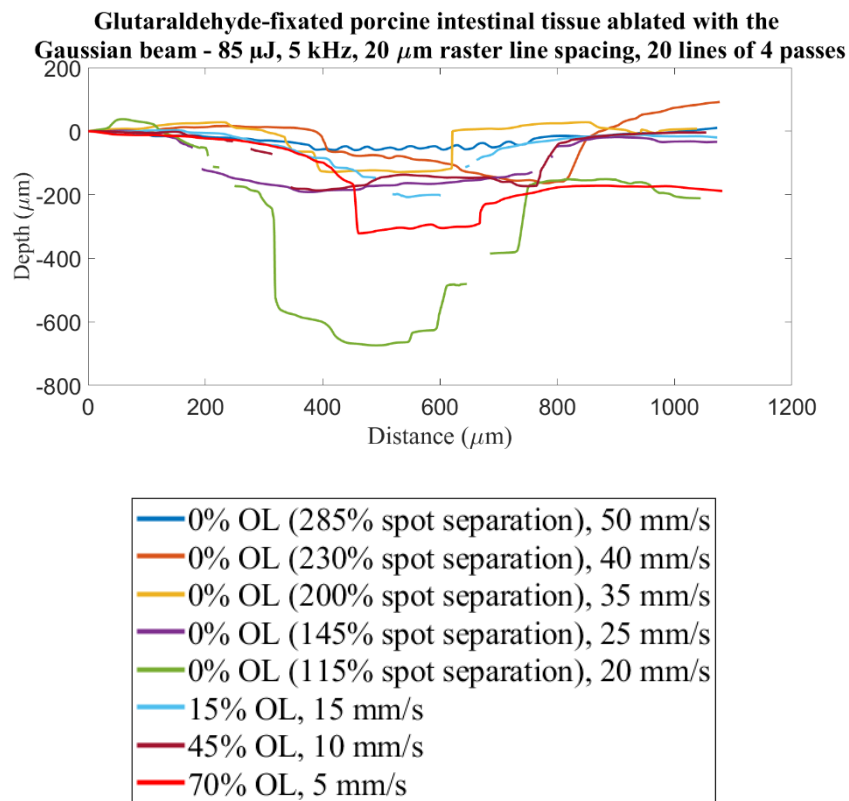


Figure 5.12 – Line profiles taken from the surface maps captured using the surface profilometer of the corresponding glutaraldehyde-fixated porcine intestinal tissue samples ablated using the same parameters for the Gaussian beam as those shown in the previous histology images. The lack of consistency in the overall shape of the ablated features while varying the spatial overlap of the pulses is attributed to a combination of the high fluence, the lower temporal separation of the pulses at this increased pulse repetition rate and the combination of the short depth of focus with the inherent inhomogeneity of the sample surfaces.

5.5 10 kHz ablation of porcine intestinal tissue samples with Bessel-Gauss beam

The Bessel-Gauss beam again showed promising damage margins across all the stage translation speeds/spatial pulse overlaps tested (figures 5.13 and 5.14). However, at this further increased pulse repetition rate it was noted that the structure of the resected volume of tissue started to become more difficult to control at higher spatial overlaps than for the 5 kHz, with lateral splitting of the tissue being an issue despite the high thermal confinement. This would perhaps be intuitively expected from the decreased temporal separation of the applied laser pulses. Additionally, some considerable cavitation was observed at the slowest stage translation speed of 5 mm/s (the histology image shown in figure 5.14d).

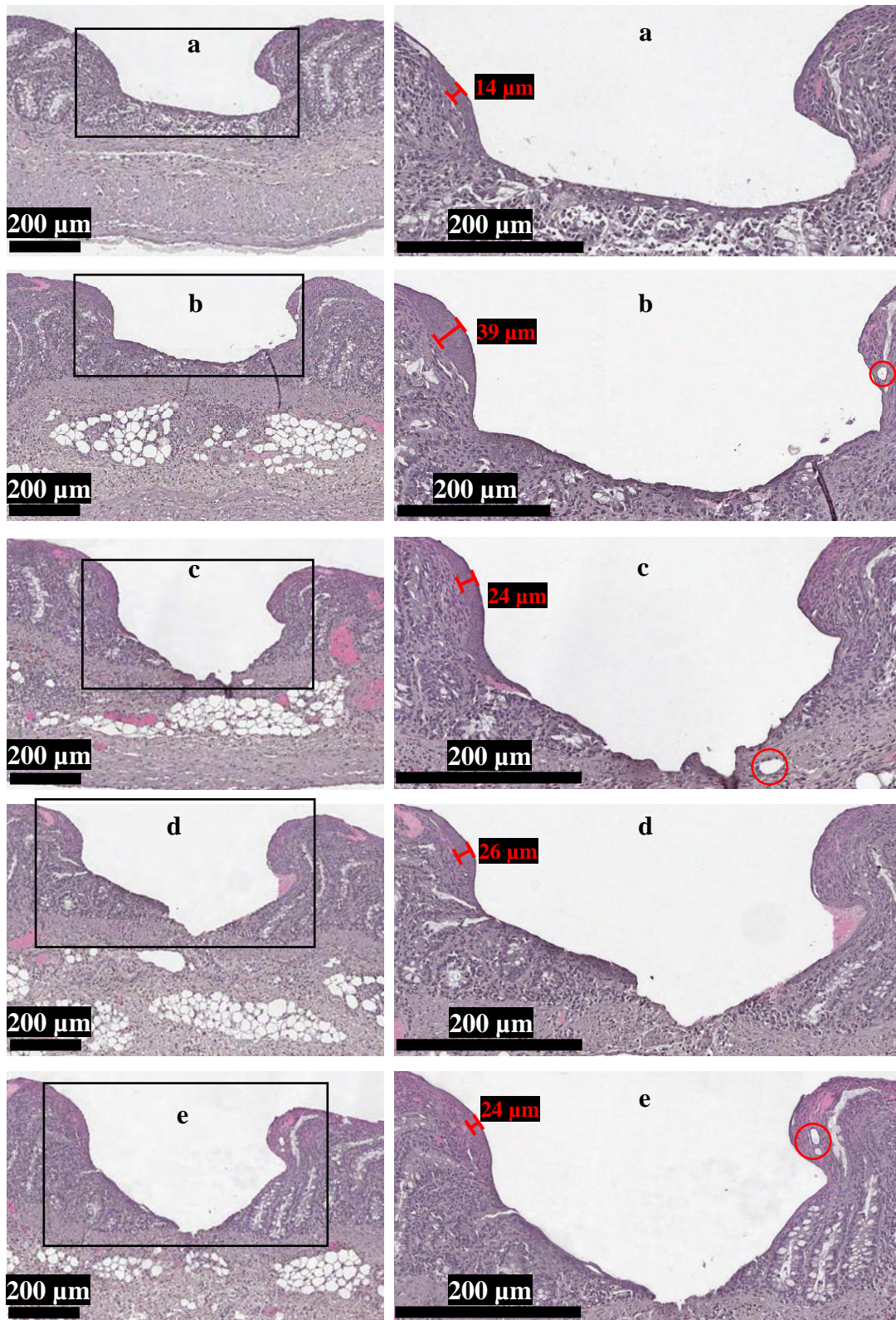


Figure 5.13 – Histological H&E stained images (with zoomed-in views) of porcine intestinal tissue samples. The features here were scanned with the Bessel-Gauss beam using 85 μ J pulses applied at a repetition rate of 10 kHz with spatial overlaps of a) 0% (145% spot separation, 50 mm/s) b) 0% (115% spot separation, 40 mm/s) c) 0% (35 mm/s) d) 15% (30 mm/s) e) 30% (25 mm/s). The scans consisted of 20 lines of 4 passes each, spaced out by 20 μ m. The observed thermal damage margins are highly localised, extending just under 40 μ m from the ablated region in the worst case. What were first surmised to be cavitation bubbles in b), c) and e) (highlighted by red circles) were confirmed to likely be goblet cells in b) and e) and a lymphatic vessel in c) (all from having surrounding cell linings intact) by Nicholas West, a histologist project partner.

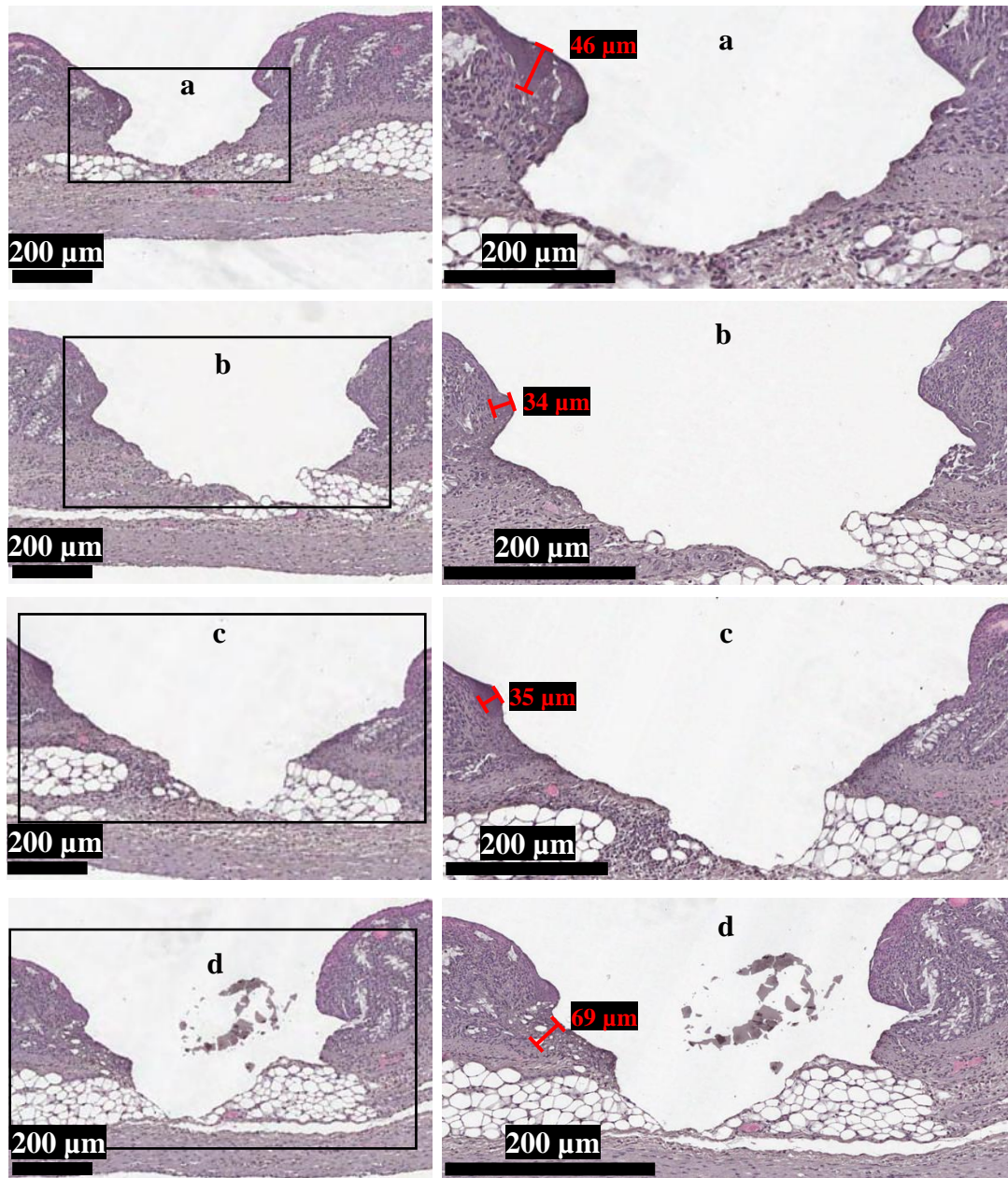


Figure 5.14 – Histological H&E stained images (with zoomed-in views) of porcine intestinal tissue samples. The features here were scanned with the Bessel-Gauss beam using 85 μJ pulses applied at a repetition rate of 10 kHz with spatial overlaps of a) 45% (20 mm/s) b) 55% (15 mm/s) c) 70% (10 mm/s) d) 85% (5 mm/s). The scans consisted of 20 lines of 4 passes each, spaced out by 20 μm . The observed thermal damage margins are highly localised, spanning under 50 μm with the exception of d), where noticeable cavitation (*i.e.* bubble formation) is observed. However, the overall shape of the ablated feature is again harder to control as the spatial overlap of the pulses is increased at this higher pulse repetition rate.

A plot of line profiles measured from the surface maps captured using the surface profilometer of the corresponding glutaraldehyde-fixed samples is shown in figure 5.15.

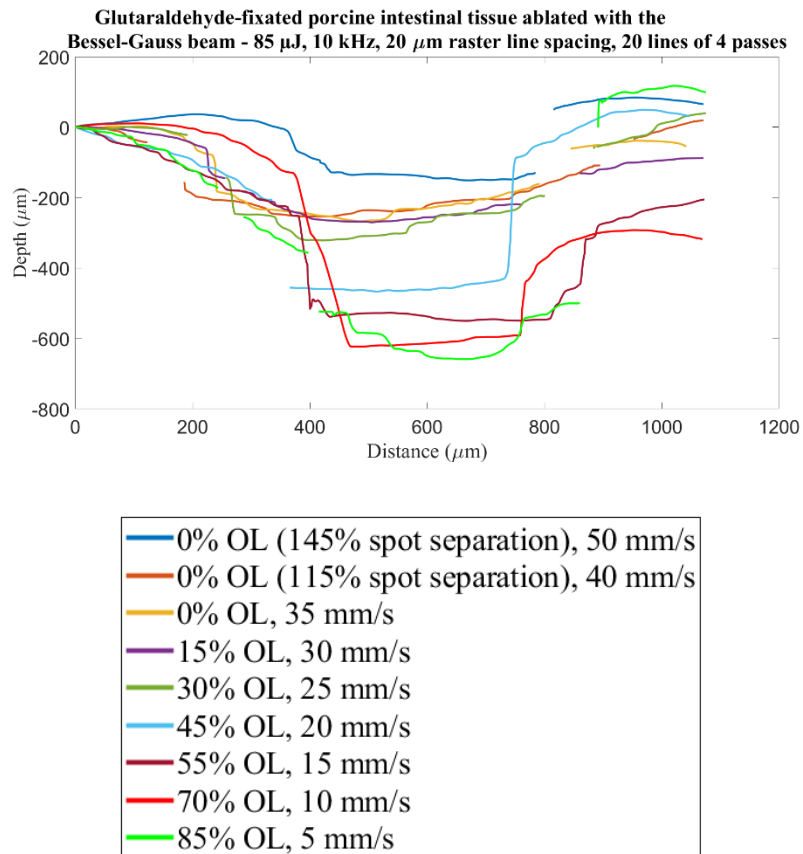


Figure 5.15 – Line profiles taken from the surface maps captured using the surface profilometer of the corresponding glutaraldehyde-fixated porcine intestinal tissue samples ablated using the same parameters for the Bessel-Gauss beam as those shown in the previous histology images. Again, the overall shape of the ablated feature becomes harder to control as the spatial overlap of the pulses is increased at this higher pulse repetition rate.

5.6 10 kHz ablation of porcine intestinal tissue samples with Gaussian beam

The Gaussian beam exhibited promising damage margins across faster stage translation speeds/lower spatial pulse overlaps (figure 5.16). At this further increased repetition rate the lack of consistency in the ablation due to the lower depth of focus was less prominent but cavitation bubble formation and thermal accumulation were more significant, with this leading to even greater damage margins than at 5 kHz due to the decreased temporal separation of the pulses (figure 5.17). Some cavitation bubbles can be observed at spatial pulse overlaps as low as 30% (shown in the histology image in figure 5.16e). This becomes more severe as the pulse overlap is increased, as shown across the histology images in figure 5.17.

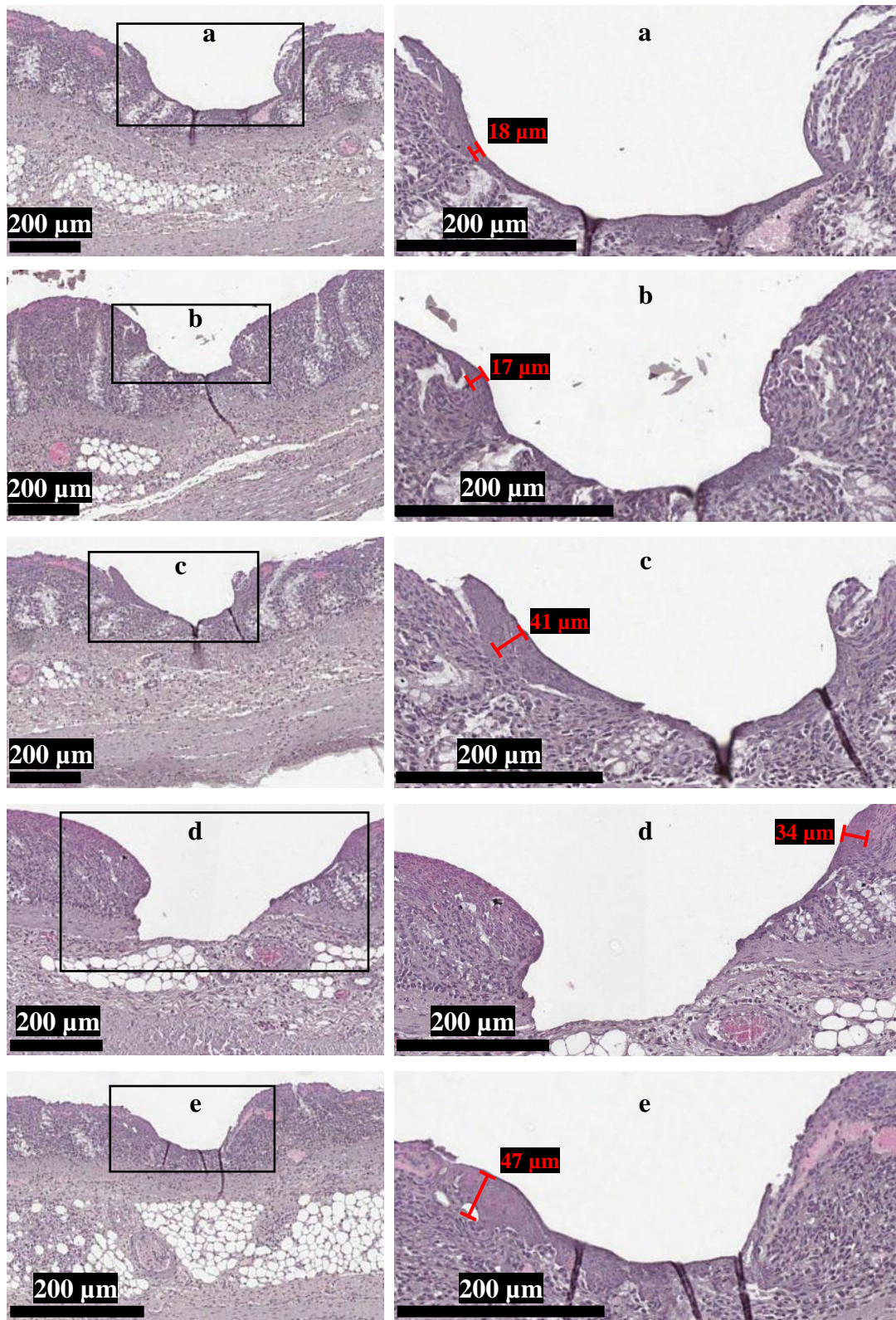


Figure 5.16 – Histological H&E stained images (with zoomed-in views) of porcine intestinal tissue samples. The features here were scanned with the Gaussian beam using 85 μJ pulses applied at a repetition rate of 10 kHz with spatial overlaps of a) 0% (145% spot separation, 50 mm/s) b) 0% (115% spot separation, 40 mm/s) c) 0% (35 mm/s) d) 15% (30 mm/s) e) 30% (25 mm/s). The scans consisted of 20 lines of 4 passes each, spaced out by 20 μm . The observed thermal damage margins are highly localised, extending just under 50 μm from the ablated region in the worst case. However, some cavitation is observed for e).

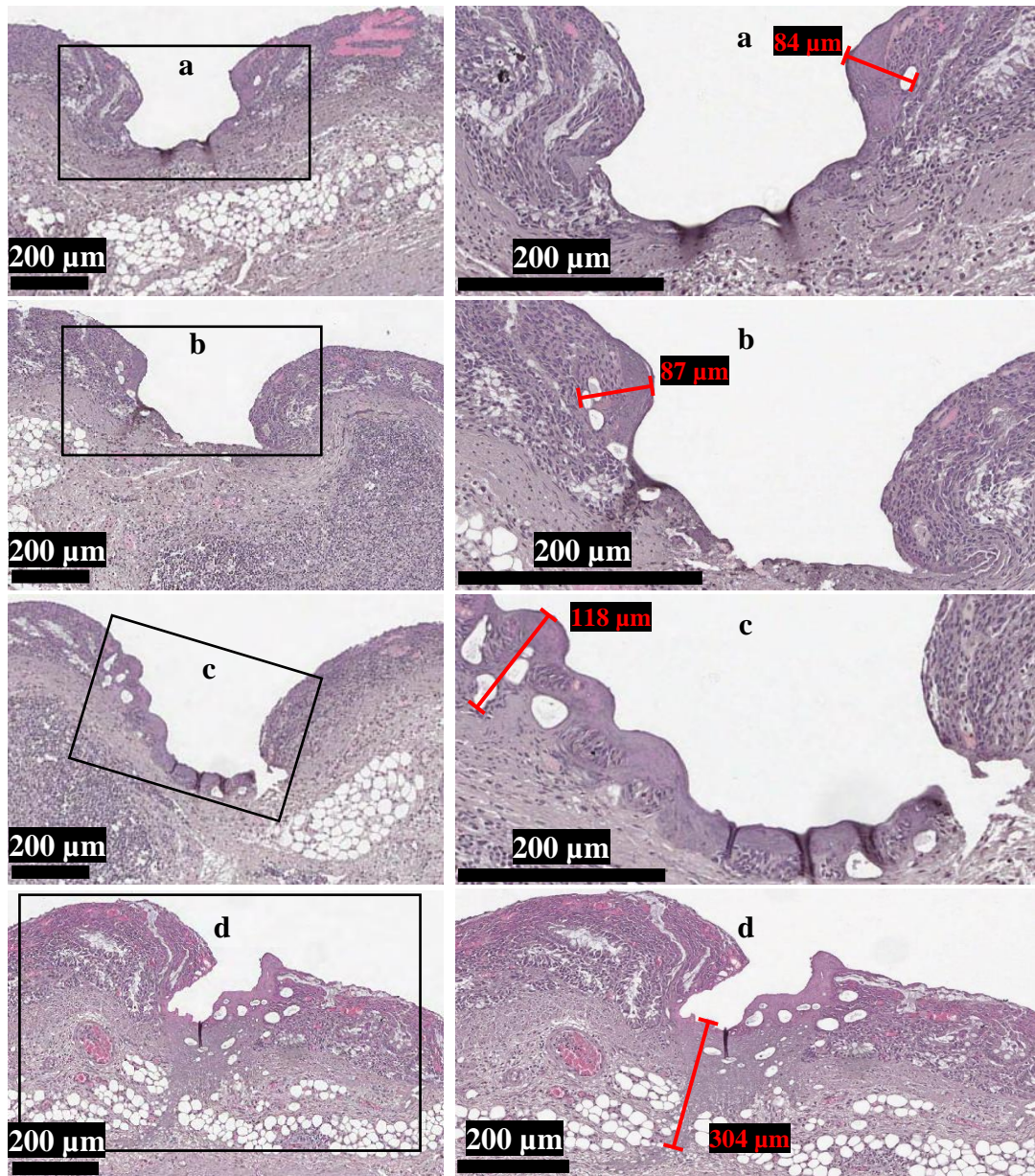


Figure 5.17 – Histological H&E stained images (with zoomed-in views) of porcine intestinal tissue samples. The features here were scanned with the Gaussian beam using 85 μJ pulses applied at a repetition rate of 10 kHz with spatial overlaps of a) 45% (20 mm/s) b) 55% (15 mm/s) c) 70% (10 mm/s) d) 85% (5 mm/s). The scans consisted of 20 lines of 4 passes each, spaced out by 20 μm . The observed thermal damage margins are more extensive here, extending over more than 200 μm from the ablated region in the worst case. This is attributed again to the cavitation effects that arise from the combination of the high fluence with the high repetition rate and spatial overlap of the pulses.

A plot of line profiles measured from the surface maps captured using the surface profilometer of the corresponding glutaraldehyde-fixed samples is shown in figure 5.18.

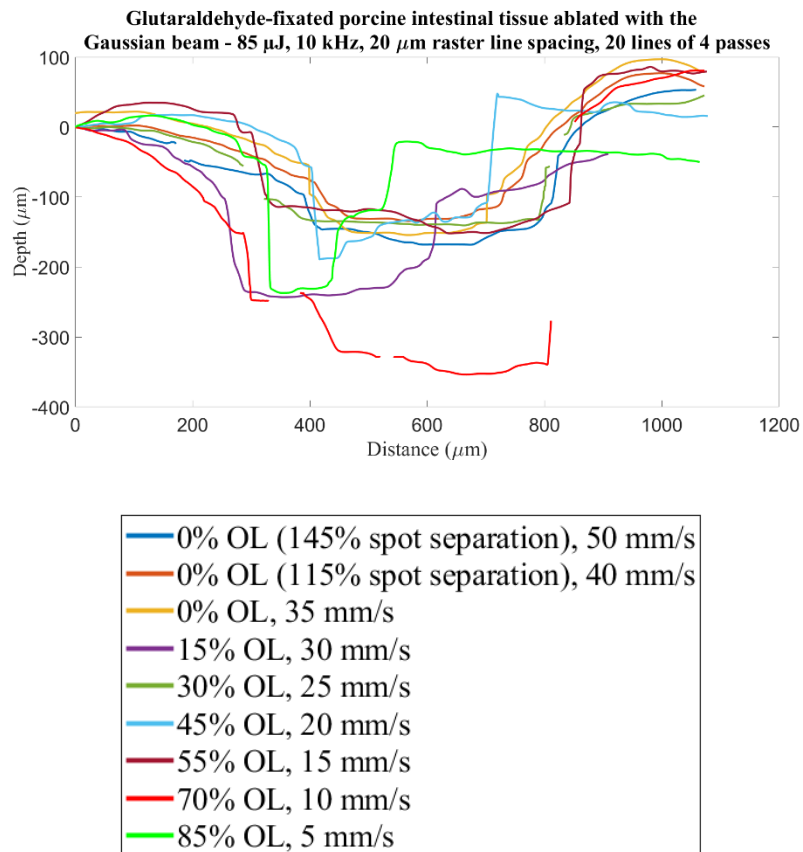


Figure 5.18 – Line profiles taken from the surface maps captured using the surface profilometer of the corresponding glutaraldehyde-fixed porcine intestinal tissue samples ablated using the same parameters for the Gaussian beam as those shown in the previous histology images. The lack of consistency in the overall shape of the ablated features while varying the spatial overlap of the pulses is again attributed to a combination of the high fluence, the lower temporal separation of the pulses at this increased pulse repetition rate and the combination of the short depth of focus with the inherent inhomogeneity of the sample surfaces.

5.7 20 kHz ablation of porcine intestinal tissue samples with Bessel-Gauss beam

The Bessel-Gauss beam once again showed impressive thermal damage margins across all the stage translation speeds/spatial pulse overlaps tested (figure 5.19). However, while undesirable cavitation effects such as bubble formation were minimal when compared to those observed at 20 kHz using the Gaussian beam, the shape of the ablated features is still increasingly difficult to control as the spatial overlap of the applied pulses increases. At this maximum tested pulse repetition rate of 20 kHz it was noted that the structure of the resected volume of tissue was even more difficult to control at the higher spatial pulse overlap values than for either the 5 or 10 kHz ablation trials, with lateral splitting of the tissue continuing to be a prominent issue at these slower stage translation/sample scanning speeds despite the high thermal confinement. This again would be intuitively expected from the decreased temporal separation of the applied laser pulses.

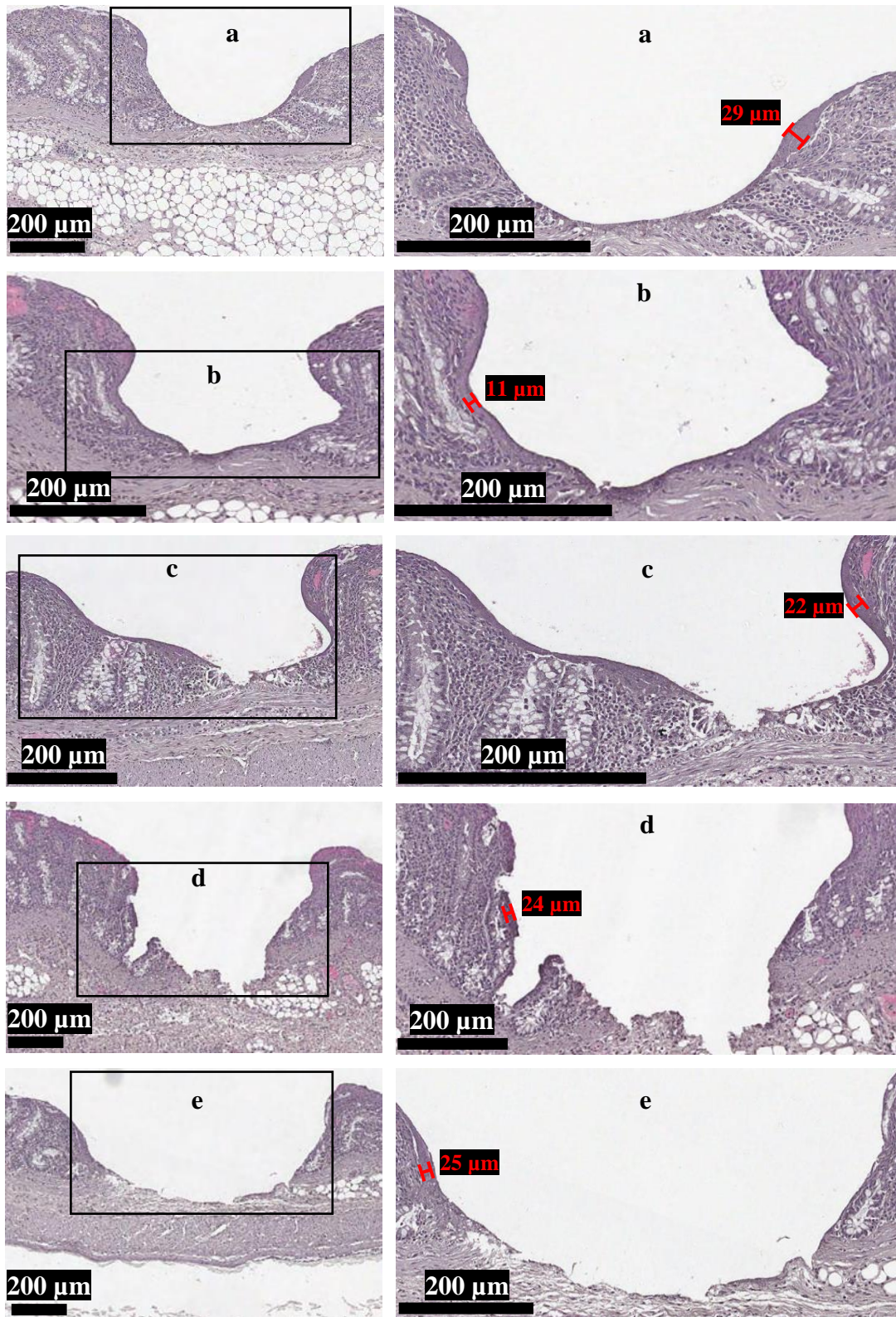


Figure 5.19 – Histological H&E stained images (with zoomed-in views) of porcine intestinal tissue samples. The features here were scanned with the Bessel-Gauss beam using 85 μJ pulses applied at a repetition rate of 20 kHz with spatial overlaps of a) 30% (50 mm/s) b) 45% (40 mm/s) c) 55% (30 mm/s) d) 70% (20 mm/s) e) 85% (10 mm/s). The scans consisted of 20 lines of 4 passes each, spaced out by 20 μm . The observed thermal damage margins are highly localised, extending just under 30 μm from the ablated region in the worst case. However, the overall shape of the ablated feature is harder to control as the spatial overlap of the pulses is increased at this higher pulse repetition rate yet again.

A plot of line profiles measured from the surface maps captured using the surface profilometer of the corresponding glutaraldehyde-fixed samples is shown in figure 5.20.

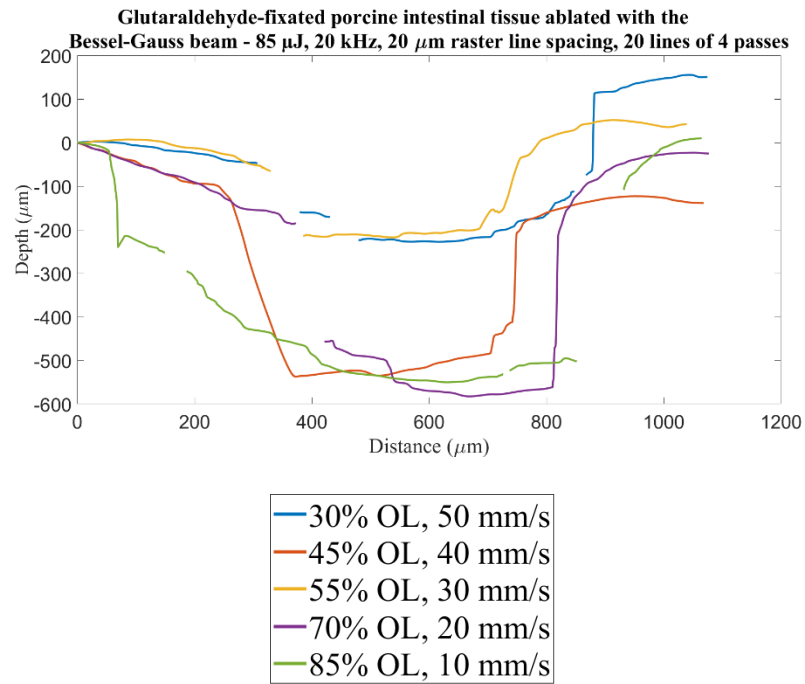


Figure 5.20 – Line profiles taken from the surface maps captured using the surface profilometer of the corresponding glutaraldehyde-fixated porcine intestinal tissue samples ablated using the same parameters for the Bessel-Gauss beam as those shown in the previous histology images. Again, the overall shape of the ablated feature becomes harder to control as the spatial overlap of the pulses is increased at this higher pulse repetition rate.

5.8 20 kHz ablation of porcine intestinal tissue samples with Gaussian beam

The Gaussian beam exhibited extensive cavitation bubble formation and thermal accumulation across all of the tested stage speeds for the maximum pulse repetition rate of 20 kHz used within the scope of this work (figure 5.21). The consistency of the ablated features across both the histology images and the surface profile measurements is again significantly impaired by this thermal accumulation and cavitation bubble formation due to the decreased temporal separation of the pulses.

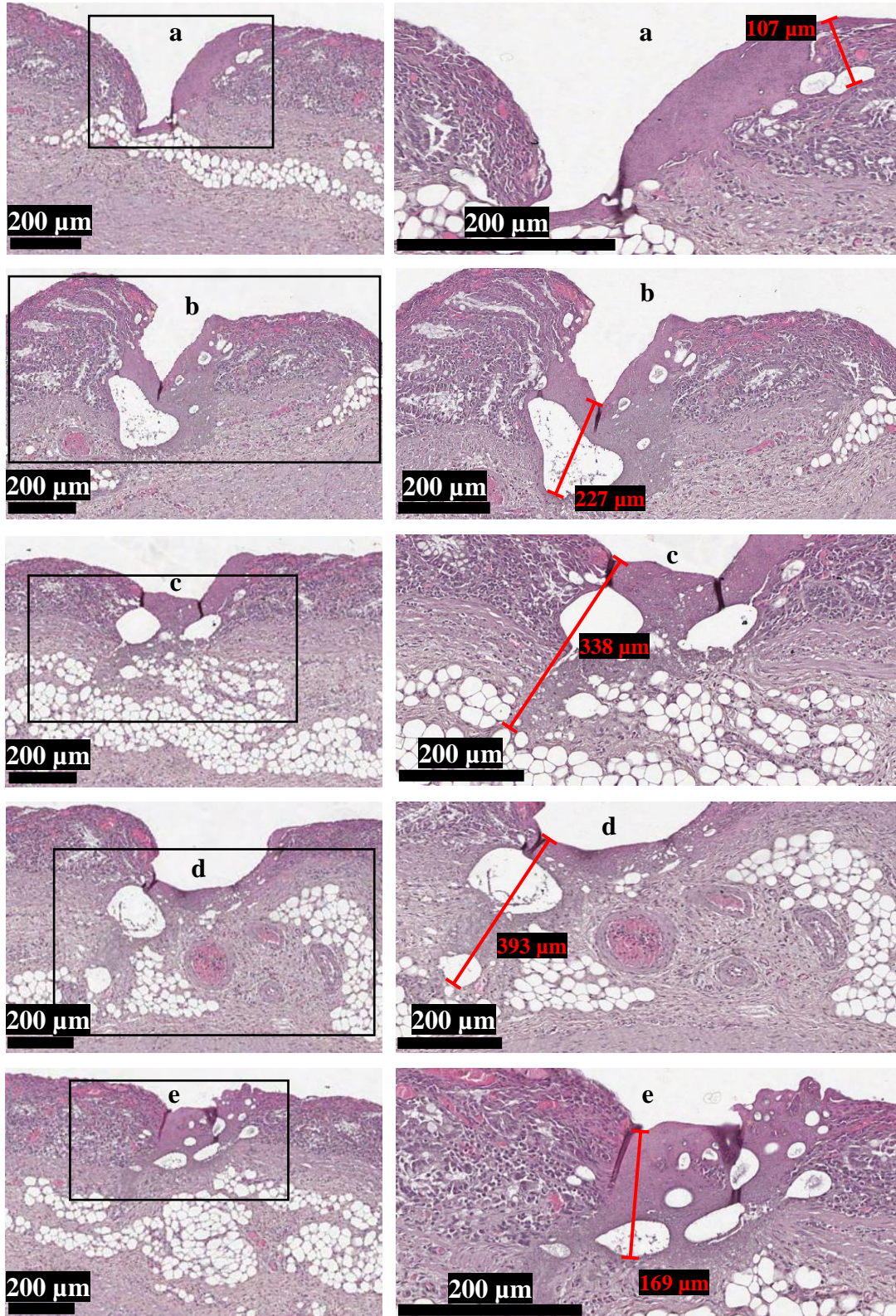


Figure 5.21 – Histological H&E stained images (with zoomed-in views) of porcine intestinal tissue samples scanned with the Bessel-Gauss beam using 85 μJ pulses applied at a repetition rate of 20 kHz with spatial overlaps of a) 30% (50 mm/s) b) 45% (40 mm/s) c) 55% (30 mm/s) d) 70% (20 mm/s) e) 85% (10 mm/s). The scans consisted of 20 lines of 4 passes each, spaced out by 20 μm . The observed thermal damage margins are highest here, extending almost as much as 400 μm away from the ablated region in the worst case. The cavitation effects leads to the least consistent ablation across all of the trials, with the shape of the ablated features being very difficult to control across all of the tested spatial pulse overlap values.

A plot of line profiles measured from the surface maps captured using the surface profilometer of the corresponding glutaraldehyde-fixated samples is shown in figure 5.22.

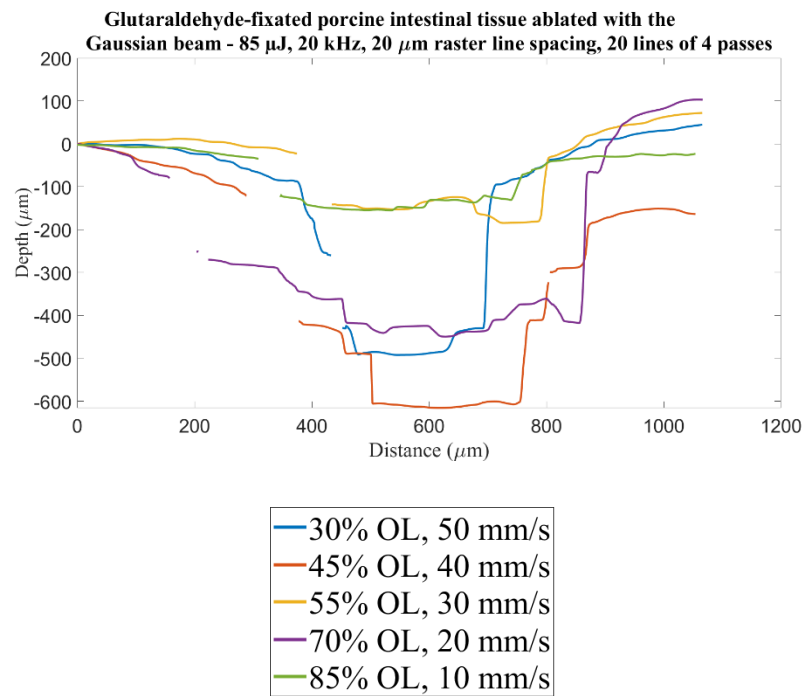


Figure 5.22 - Line profiles taken from the surface maps captured using the surface profilometer of the corresponding glutaraldehyde-fixated porcine intestinal tissue samples ablated using the same parameters for the Gaussian beam as those shown in the previous histology images. The lack of consistency in the overall shape of the ablated features while varying the spatial overlap of the pulses is once again attributed to a combination of the high fluence, the lower temporal separation of the pulses at this increased pulse repetition rate and the combination of the short depth of focus with the inherent inhomogeneity of the sample surfaces.

5.9 Summary of higher pulse repetition rate ablation trials

All of the ablation trials at these higher pulse repetition rates again exhibited plasma formation on the surfaces of the various tissue samples across axial ranges of over 1 mm for the Bessel-Gauss beam and around 400 μ m for the Gaussian beam at the maximum input pulse energy of 85 μ J. For the majority of the trials the ablated depths resulted in the partial or complete removal of the mucosal layer despite the small spot sizes used, which is significant as this layer is where the majority of early-stage cancerous tumours begin to develop within the intestinal tract [5.6]. Additionally, despite the multiple passes applied, the inherent characteristics of the muscularis layer (*i.e.* elasticity/rigidity) prevented any damage to it, as discussed previously in chapter 4. For both beams no spatial overlapping of the pulses (0%) provided optimal results to preserve lateral control of the resected volumes at these higher repetition rates, avoiding both mechanical splitting of the tissue (likely from the increased energy density applied to the tissue as the stage decelerates near the raster scan edges) or undesirable thermal build-up and/or cavitation bubble formation, although these lower spatial overlaps often come at the expense of the total ablated depth for a given number of passes (and therefore the maximum achievable ablation rate). Consequently, these higher pulse repetition rates are less precise (particularly for equivalent spatial pulse overlaps) but significantly faster than the lower pulse repetition rates tested in chapter 4. Operation at these higher repetition rates

therefore allows for the lower scanning speeds required for smaller spot sizes to provide a given spatial pulse overlap value to be capitalised upon.

From these higher pulse repetition rate trials, the Bessel-Gauss beam highlighted a trend of being less prone to cavitation effects (*i.e.* bubble formation build-up) inhibiting the ablation process for a given set of ablation parameters (including spatial overlap of the pulses, number of passes and input pulse energy) than the Gaussian beam. This was attributed to a combination of the more stretched out nature of the intensity profile of the pulses, the self-healing properties of the beam and the more consistent spot size, which consequently leads to a more consistent spatial overlap of the applied pulses. The axially stretched out intensity profile provided by the large non-diffractive focal depth is of particular note, as higher intensity ultrashort pulses have been linked to larger cavitation bubbles with longer lifetimes [5.7],[5.8]. This becomes prominent as the pulse repetition rate increases due to the subsequent decrease in the temporal separation of the applied pulses, with heat dissipation outwith the focal volume being hindered by the arrival of the subsequent pulses. It is worthwhile to note that some cavitation was still observed towards the higher end of the tested spatial pulse overlaps with the Bessel-Gauss beam, due to the combination of high spatial and temporal overlapping of the pulses [5.9].

These laser ablation trials are summarised for both beam shapes shown in tables 5.1 and 5.2.

Pulse Repetition Rate (kHz)	Spatial pulse separation (%)	Spatial pulse overlap (%)	Approximate mean depth (μm)	Peak thermal damage (μm)	Secondary effects of plasma generation
5	285	0	90	8	No
	230	0	120	22	No
	200	0	150	25	No
	170	0	170	13	No
	145	0	190	22	No
	115	0	180	26	No
	85	15	250	12	No
	55	45	290	14	Mechanical damage (splitting of tissue)
	30	70	350	29	
10	145	0	100	14	No
	115	0	110	39	No
	100	0	140	24	No
	85	15	210	26	No
	70	30	270	24	No
	55	45	300	46	No
	45	55	290	34	No
	30	70	310	35	Mechanical damage (splitting of tissue)
	15	85	360	69	Mechanical damage (splitting of tissue) + cavitation bubble formation
20	70	30	210	29	No
	55	45	190	11	No
	45	55	480	22	Mechanical damage (splitting of tissue)
	30	70	540	24	
	15	85	490	25	

Table 5.1 – Higher pulse repetition rate porcine intestinal tissue ablation trials using the Bessel-Gauss beam.

Wavelength = 1030 nm, Pulse duration = 6 ps, Pulse energy = 85 μJ , 20 μm raster line spacing, 4 passes per line.

Pulse Repetition Rate (kHz)	Spatial pulse separation (%)	Spatial pulse overlap (%)	Approximate mean depth (μm)	Peak thermal damage (μm)	Secondary effects of plasma generation
5	285	0	40	13	No
	230	0	110	14	No
	200	0	120	29	No
	145	0	160	23	No
	115	0	520	31	No
	85	15	140	82	Considerable cavitation bubble formation and heat accumulation
	55	45	160	122	
	30	70	210	103	
10	145	0	170	18	No
	115	0	170	17	No
	100	0	180	41	No
	85	15	190	34	No
	70	30	140	47	Cavitation bubble formation and heat accumulation
	55	45	160	84	Considerable cavitation bubble formation and heat accumulation
	45	55	90	87	
	30	70	340	118	
	15	85	160	304	
20	70	30	380	107	Considerable cavitation bubble formation and heat accumulation
	55	45	470	227	
	45	55	150	338	
	30	70	370	393	
	15	85	140	169	

Table 5.2 – Higher pulse repetition rate porcine intestinal tissue ablation trials using the Gaussian beam.

Wavelength = 1030 nm, Pulse duration = 6 ps, Pulse energy = 85 μJ , 20 μm raster line spacing, 4 passes per line.

These results show that using a Bessel-Gauss beam for performing ultrafast laser ablation of soft biological tissues is potentially advantageous with regards to the consistency of the ablation across the inhomogeneous surfaces. The general trend of lower ablation depths observed with the Gaussian beam for equivalent scanning parameters could be accounted for by performing axial translation of the sample and/or endoscopic probe, although this would be difficult to realise within a clinical context. These results also highlight some potential for operating at higher repetition rates at a set maximum scanning speed if using a Bessel-Gauss beam as opposed to a more conventional Gaussian beam. This could be significant as this may enable higher ablation rates while alleviating undesirable effects from the plasma formation such as the aforementioned cavitation bubble build-up. Additionally, one of the inevitable design constraints for endoscopic probe devices is the maximum speed at which scanning at the distal end can be performed [5.10]. The ablation features produced using these higher repetition rates will require further pre-clinical trials however to evaluate the extent of potential cell apoptosis induced by the shockwave generation from the plasma formation. This has been reported as being a potential issue in the literature with some existing laser systems [5.11],[5.12],[5.13]. While obvious mechanical and/or thermal damage was observed with both beam shapes when combining higher pulse repetition rates with higher spatial pulse overlaps, cell apoptosis caused by the shockwaves may not be immediately evident, particularly in these trials where the samples were fixed in formalin shortly after ablation. This could be examined by varying the duration between ablation and fixation as well as transferring this work to both cell cultures and *in vivo* animal models. These experiments could prove to be particularly insightful for evaluating the clinical viability of implementing the spatial pulse overlap ranges that do not show immediate damage (thermal necrosis, cavitation bubble formation and/or mechanical splitting of the tissue) at these higher pulse repetition rates.

However, the Bessel-Gauss beam also shows some noticeable limitations. Foremost among these is the fact that the 20° axicon required a reimaging (demagnifying) telescope to achieve sufficient standoff from the optical components and enough fluence for achieving consistent plasma formation. This is a consequence of the higher input pulse energy required for the Bessel-Gauss beam to reach the plasma formation threshold of the biological tissue from the more axially stretched out intensity profile with the same input pulse energy [5.14]. This increased demand on the input pulse energy is significant as transmission efficiency remains one of the primary concerns when considering a fibre delivered solution, especially for ultrashort pulses.

Additionally, the Gaussian still works well at lower spatial overlap values for the pulses and offers more flexibility regarding the tailoring of the spot size, with this being determined by both the focal length of the lens and the input beam width, compared to the Bessel-Gauss beam, where the diameter of the central core along the Bessel zone is determined by the conical angle of the axicon. Further modification of the spot size for the Bessel-Gauss beam requires a reimaging telescope, as used here. Finally, it is more technically demanding to fabricate an axicon than a convex lens (as covered in previous chapters when discussing the manufacturing errors that are prominent for these conical surfaces).

5.10 High-speed imaging of ablation process on cryogenically preserved porcine skin tissue samples

To enable direct observation of the plasma-mediated ablation dynamics for the two different beam shapes, a high-speed imaging camera (Fastcam Mini AX200, Photron) setup, designed by Dr. Bitharas for live capturing of ultrafast processes, was used alongside a MATLAB script he developed for post-capture video editing (figure 5.23) [5.15]. This capturing of the picosecond laser ablation process has been covered in a publication by Dr. Beck *et al.* in more detail [5.16].

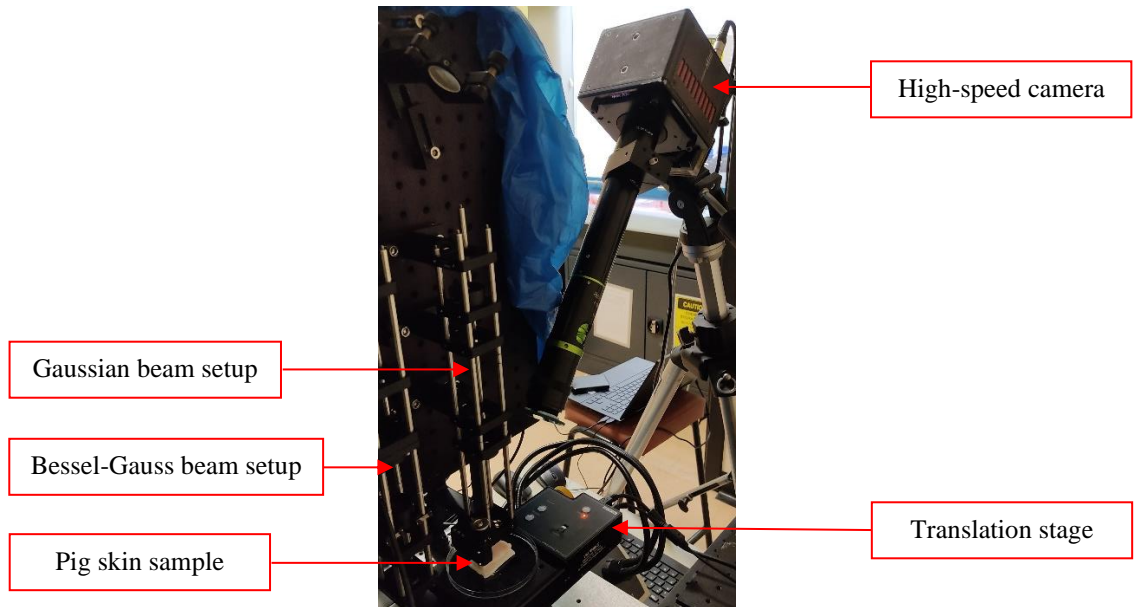


Figure 5.23 – High-speed imaging setup for capturing ablation process of porcine skin tissue.

Cryogenically preserved porcine skin tissue was used for these tests due to a lack of sample availability for fresh porcine intestinal tissue (figure 5.24).



Figure 5.24 – Frozen porcine skin tissue samples.

This porcine skin tissue, generously supplied by Sara Medina-Lombardero (a PhD student based at Heriot-Watt University), provided a good tissue model to highlight the increased tolerance offered by the Bessel-Gauss beam due to the high surface roughness (figure 5.25).

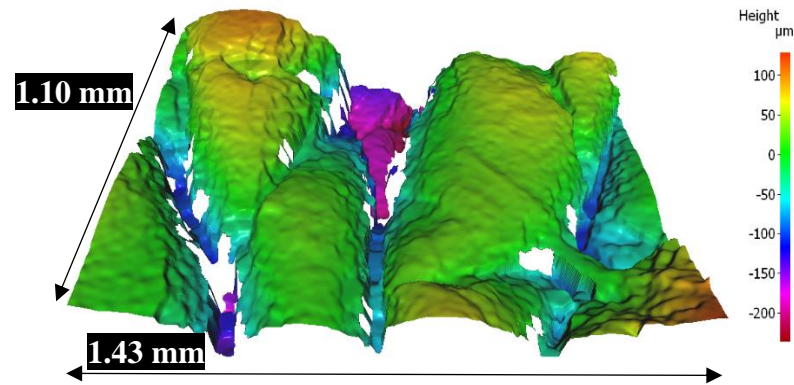


Figure 5.25 – Porcine skin surface profile captured using the 10x objective lens on the Alicona surface profilometer. While the Sa measurement of $40 \pm 1 \mu\text{m}$ appears smaller than the porcine intestine scans shown previously, this was performed over a much smaller surface area to correspond with the field of view offered by the high-speed imaging camera.

A routine protocol developed by Sara was used to prepare the cryogenically preserved porcine skin. This protocol is implemented to prevent excessive crystallisation of the tissue from the freezing process, as this is typically the primary source of damage during cryopreservation tissues [5.17].

While the Photron Fastcam Mini AX200 offered capturing framerates up to 10000 fps, the 6000 fps option was used as this allowed for adequate exposure from the high intensity light source required to illuminate the sample surface. Higher framerates allow for clearer observation of the ablation dynamics, but come at the expense of reduced exposure times thus worse illumination, which is itself limited by the high intensity light source drying out the tissue samples due to the heat produced. This illumination issue was further exacerbated by the relatively short working distances from both of the optical setups. Figure 5.26 shows a porcine skin sample being translated underneath the Bessel-Gauss beam.

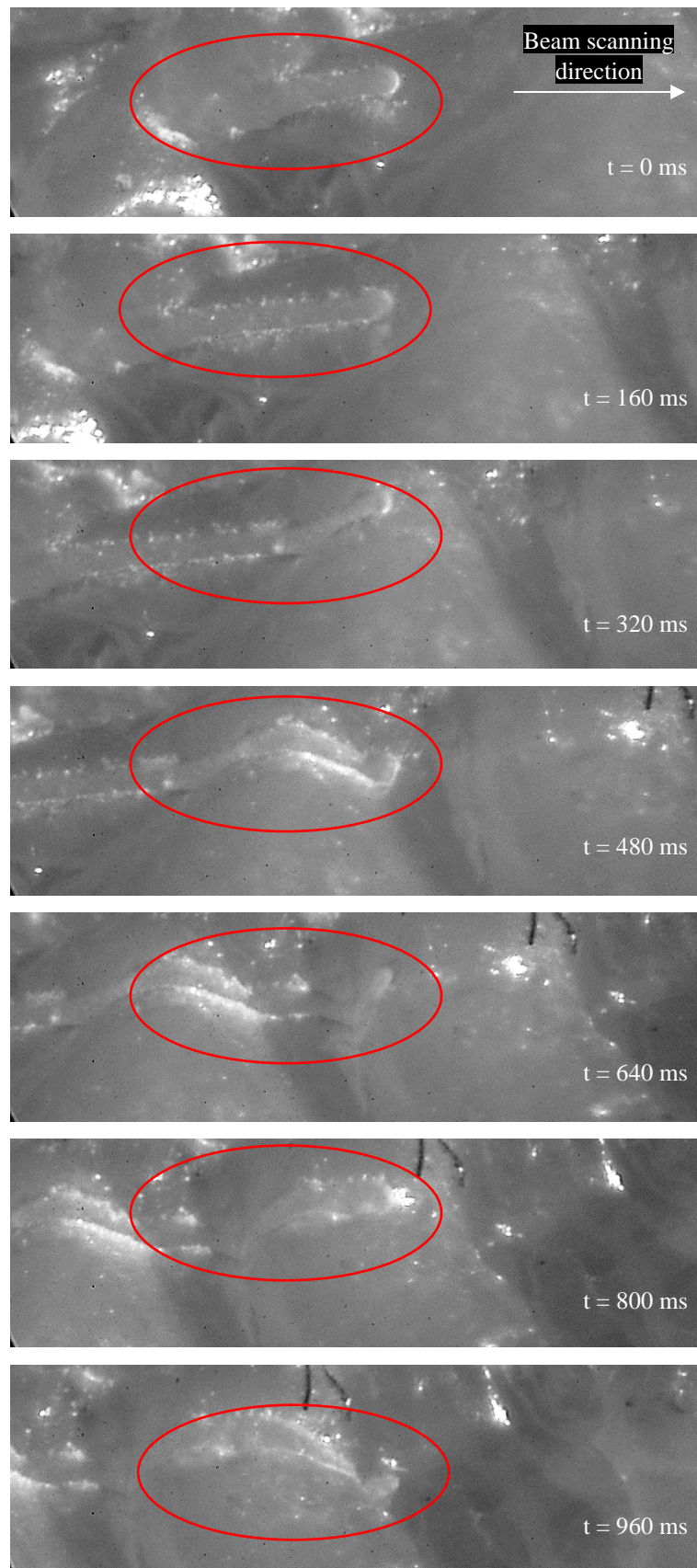


Figure 5.26 – High-speed video showcasing the focal tolerance of the reimaged Bessel-Gauss beam across porcine skin using $85 \mu\text{J}$ pulses applied at a repetition rate of 5 kHz and a spot separation of 100%. The scanned line is approximately $20 - 30 \mu\text{m}$ in width.

The areas circled in red highlight the ablated feature left by the laser spot as the sample is scanned relative to it.

Figure 5.27 shows another porcine skin sample being scanned underneath the Gaussian beam.

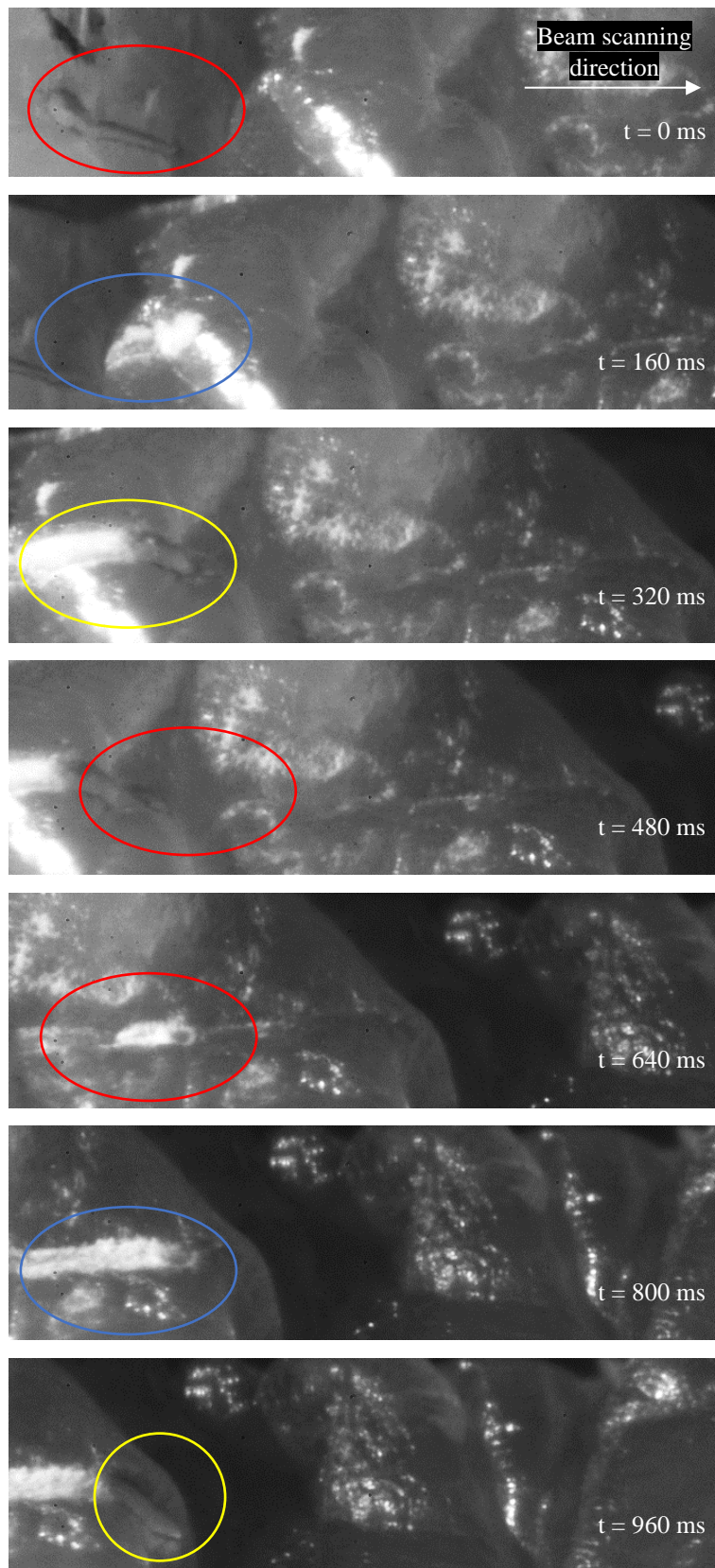


Figure 5.27 – High-speed video showcasing the less consistent ablation produced by the Gaussian beam across porcine skin, again using 85 μJ pulses applied at a repetition rate of 5 kHz and a spot separation of 100%. The scanned line on average is approximately 20 – 30 μm in width. Some particularly distinct ablation is observed at the 320 and 960 ms timestamps (circled in yellow), but more superficial thermal charring of the tissue surface is observed at the 160 and 800 ms timestamps (circled in blue). The areas circled in red again highlight the ablated feature left by the laser spot as the sample is scanned relative to it.

While the Gaussian beam was able to produce distinct ablation with satisfactory thermal confinement at 5 and 10 kHz when the applied pulses were sufficiently spaced apart on the porcine intestinal tissue, across the porcine skin surface the shorter focal depth led to issues regarding the consistency of the ablated features. Consequently, these high-frame-rate videos were able to showcase the advantage of the increased tolerance to the focus position offered by the reimaged Bessel-Gauss beam, courtesy of the inherent surface roughness of the porcine skin, as these samples are translated relative to the incoming beams. These samples were sent for histological analysis but unfortunately the results were not returned in time for inclusion within this thesis.

These increased focal tolerances provided by Bessel-Gauss beams have been capitalised upon elsewhere in recent research by Wang *et al.*, where 1, 1.5, 2 and 2.5° axicons were used to drill microholes in polymethyl methacrylate [5.18]. Aspect ratios as high as 348:1 were achieved courtesy of both the long focal depths and non-diffracting nature of the produced Bessel-Gauss beams, although this did require numerous applied pulses, as well as both reimaging of the beams and 216 fs pulse durations to reach sufficient intensities. Additionally, this was in a transparent material, as opposed to highly scattering tissue. Past research efforts looking at using Bessel-Gauss beams for materials processing are primarily focused around transparent material drilling (as highlighted previously in chapters 1, 2 and 3), as these materials allow for the sidelobes to penetrate through and form a long focus, while the scattering tissue ablated in this work required multiple passes to fully realise the potential depths offered by these extended focal depths [5.19],[5.20],[5.21]. Recent research efforts by Tekpınar *et al.* have hinted at the potential of addressing this by implementing Bessel-like beams, formed by off-axis coupling of light into a multimode fibre, to image multiple planes in a single lateral scan (which the authors state could possibly also be applied to ablative processes), albeit at the expense of requiring increased optical powers to do so [5.22].

In conclusion, the scattering nature of the tissue structures inhibited high aspect ratio ablation with single passes, as discussed in chapter 4. However, the increased tolerance to the focal position could be of great significance towards endoscopic applications, as the working distances from the distal end optics to the target regions within the gastrointestinal tract are of paramount importance. Easing the confinements around this parameter could aid not only the endoscopic device design process, but also the surgeons using these developed probes, while also increasing the lifetime of the endoscopic probes themselves. Coupling this with the exciting potential for performing tissue ablation procedures at higher repetition rates (and, importantly, therefore faster) may well result in greatly reducing the time taken for minimally invasive surgical procedures. This may even offer the potential for “ablation-cooled” material removal via ultrafast bursts of pulses in the future [5.23]. In addition, the increased depth of focus offered by the reimaged Bessel-Gauss beam favourably transferring across various types of tissue shows promise regarding its potential translation to surgical procedures elsewhere in the body, particularly after consideration of the various distinctive mechanical properties exhibited by cancerous tissues [5.24]. These include, but are not limited to, the heart, the neck and the mouth, all of which could be highly beneficial to both surgeons and patients alike [5.25],[5.26],[5.27].

5.11 References

- [5.1] “BeamMap2 - XYZ $\Theta\Phi$ Scanning Slit Beam Profiler | DataRay Inc.” <https://dataray.com/products/beammap2-xyztheta-phi-scanning-slit-beam-profiler-system> (accessed Nov. 06, 2021).
- [5.2] A. Townsend, “Characterisation of the Surface Topography of Additively Manufactured Parts,” University of Huddersfield, Huddersfield, 2018.
- [5.3] C. Lee, H. G. Lim, C. H. Lee, and Y. J. Kim, “Effects of glutaraldehyde concentration and fixation time on material characteristics and calcification of bovine pericardium: implications for the optimal method of fixation of autologous pericardium used for cardiovascular surgery,” *Interact. Cardiovasc. Thorac. Surg.*, vol. 24, no. 3, pp. 402–406, Mar. 2017, doi: 10.1093/ICVTS/IVW356.
- [5.4] H. Tran *et al.*, “Formalin Fixation and Cryosectioning Cause Only Minimal Changes in Shape or Size of Ocular Tissues,” *Sci. Reports 2017 71*, vol. 7, no. 1, pp. 1–11, Sep. 2017, doi: 10.1038/s41598-017-12006-1.
- [5.5] W. Kaplonek, K. Nadolny, and G. M. Królczyk, “The use of focus-variation microscopy for the assessment of active surfaces of a new generation of coated abrasive tools,” *Measurement Science Review*, vol. 16, no. 2. Slovak Academy of Sciences - Inst. Measurement Science, pp. 42–53, Apr. 01, 2016. doi: 10.1515/msr-2016-0007.
- [5.6] P. H. M. Leung *et al.*, “Characterization of mucosa-associated microbiota in matched cancer and non-neoplastic mucosa from patients with colorectal cancer,” *Front. Microbiol.*, vol. 10, no. JUN, p. 1317, 2019, doi: 10.3389/FMICB.2019.01317/BIBTEX.
- [5.7] A. Vogel and V. Venugopalan, “Mechanisms of pulsed laser ablation of biological tissues,” *Chem. Rev.*, vol. 103, no. 2, pp. 577–644, Feb. 2003, doi: 10.1021/cr010379n.
- [5.8] N. Tinne, E. Lübking, H. Lubatschowski, A. Krüger, and T. Ripken, “The influence of a spatial and temporal pulse-overlap on the laser-tissue-interaction of modern ophthalmic laser systems,” *Biomed. Eng. / Biomed. Tech.*, vol. 57, no. SI-1-Track-P, pp. 302–305, Sep. 2012, doi: 10.1515/BMT-2012-4115.
- [5.9] N. Tinne, B. Kaune, A. Krüger, and T. Ripken, “Interaction mechanisms of cavitation bubbles induced by spatially and temporally separated fs-laser pulses,” *PLoS One*, vol. 9, no. 12, Dec. 2014, doi: 10.1371/journal.pone.0114437.
- [5.10] S. M. H. Jayhooni, G. Hohert, B. Assadsangabi, P. M. Lane, H. Zeng, and K. Takahata, “A Side-Viewing Endoscopic Probe with Distal Micro Rotary Scanner for Multimodal Luminal Imaging and Analysis,” *J. Microelectromechanical Syst.*, vol. 30, no. 3, pp. 433–441, Jun. 2021, doi: 10.1109/JMEMS.2021.3072617.
- [5.11] R. I. Angunawela, R. Poh, S. S. Chaurasia, D. T. Tan, and J. S. Mehta, “A mouse model of lamellar intrastromal femtosecond laser keratotomy: Ultra-structural, inflammatory, and wound healing responses,” *Mol. Vis.*, vol. 17, pp. 3005–3012, 2011, Accessed: Sep. 16, 2022. [Online]. Available: /pmc/articles/PMC3236073/
- [5.12] Z. Qian *et al.*, “Pulsetrain-burst mode, ultrafast-laser interactions with 3D viable cell cultures as a model for soft biological tissues,” *Biomed. Opt. Express*, vol. 5, no. 1, p. 208, Jan. 2014, doi: 10.1364/boe.5.000208.
- [5.13] M. O. Steinhauser, “On the Destruction of Cancer Cells Using Laser-Induced Shock-Waves: A Review on Experiments and Multiscale Computer Simulations,” *Radiol. - Open J.*, vol. 1, no. 2, pp. 60–75, Sep. 2016, doi: 10.17140/roj-1-110.
- [5.14] G. Cheng, G. Zhang, R. Stoian, and W. Zhao, “Femtosecond laser Bessel beam welding of transparent to non-transparent materials with large focal-position tolerant zone,” *Opt. Express*, Vol. 26, Issue 2, pp. 917–926, vol. 26, no. 2, pp. 917–926, Jan. 2018, doi: 10.1364/OE.26.000917.
- [5.15] P. Bidare, I. Bitharas, R. M. Ward, M. M. Attallah, and A. J. Moore, “Fluid and particle dynamics in laser powder bed fusion,” *Acta Mater.*, vol. 142, pp. 107–120, Jan. 2018, doi: 10.1016/j.actamat.2017.09.051.
- [5.16] R. J. Beck *et al.*, “Dynamics of picosecond laser ablation for surgical treatment of colorectal cancer,” *Sci. Rep.*, vol. 10, no. 1, Dec. 2020, doi: 10.1038/S41598-020-73349-W.

- [5.17] O. Polivanova, O. Bobrova, O. Falko, O. Lipina, and V. Chyzhevskiy, "Preliminary Observations on the Effect of Fullerene and Cerium Oxide Nanoparticles on Phase Transitions of Aqueous DMSO Solutions," *IFMBE Proc.*, vol. 80, pp. 218–222, Nov. 2020, doi: 10.1007/978-3-030-64610-3_25.
- [5.18] H. Wang, F. Zhang, K. Ding, and J. Duan, "Non-diffraction-length Bessel-beam femtosecond laser drilling of high-aspect-ratio microholes in PMMA," *Optik (Stuttg.)*, vol. 229, p. 166295, Mar. 2021, doi: 10.1016/j.ijleo.2021.166295.
- [5.19] M. Wang, Z. Yu, N. Zhang, and W. Liu, "Drilling high aspect ratio holes by femtosecond laser filament with aberrations," *Front. Optoelectron.*, pp. 1–7, Jun. 2021, doi: 10.1007/s12200-021-1214-4.
- [5.20] B. K. Canfield, A. Terekhov, and L. Costa, "Responses of transparent dielectrics to Gaussian-focus and Bessel-beam laser machining with single, ultrashort pulses," *Front. Opt. / Laser Sci. (2020)*, *Pap. FTu2C.5*, p. FTu2C.5, Sep. 2020, doi: 10.1364/FIO.2020.FTu2C.5.
- [5.21] V. V. Belloni, M. Bollani, S. M. Eaton, P. Di Trapani, and O. Jedrkiewicz, "Micro-Hole Generation by High-Energy Pulsed Bessel Beams in Different Transparent Materials," *Micromachines 2021*, *Vol. 12*, *Page 455*, vol. 12, no. 4, p. 455, Apr. 2021, doi: 10.3390/M12040455.
- [5.22] M. Tekpinar and O. Ferhanoglu, "Synchronous imaging of multiple slices using higher-order bessel beams and a spherical lens," *IEEE Photonics Technol. Lett.*, vol. 32, no. 23, pp. 1477–1480, Dec. 2020, doi: 10.1109/LPT.2020.3036817.
- [5.23] C. Kerse *et al.*, "Ablation-cooled material removal with ultrafast bursts of pulses," *Nature*, vol. 537, no. 7618, pp. 84–88, 2016, doi: 10.1038/nature18619.
- [5.24] F. Sauer *et al.*, "Whole tissue and single cell mechanics are correlated in human brain tumors," *Soft Matter*, 2021, doi: 10.1039/d1sm01291f.
- [5.25] J. H. Mehaffey *et al.*, "Barriers to atrial fibrillation ablation during mitral valve surgery," *J. Thorac. Cardiovasc. Surg.*, Mar. 2021, doi: 10.1016/J.JTCVS.2021.03.039.
- [5.26] M. Zhang *et al.*, "Ultrasound-Guided Radiofrequency Ablation Versus Surgery for Low-Risk Papillary Thyroid Microcarcinoma: Results of over 5 Years' Follow-Up," *Thyroid*, vol. 30, no. 3, pp. 408–417, Mar. 2020, doi: 10.1089/THY.2019.0147/ASSET/IMAGES/LARGE/THY.2019.0147_FIGURE2.JPEG.
- [5.27] J. A. Lee, Y. J. Byun, S. A. Nguyen, E. J. Lentsch, and M. B. Gillespie, "Transoral Robotic Surgery versus Plasma Ablation for Tongue Base Reduction in Obstructive Sleep Apnea: Meta-analysis," *Otolaryngol. - Head Neck Surg. (United States)*, vol. 162, no. 6, pp. 839–852, Jun. 2020, doi: 10.1177/0194599820913533.

Chapter 6

Conclusions and Future Work

6.1 Conclusions

Bessel-Gauss and Gaussian beams of equivalent focal spot sizes have been compared within the context of performing ultrafast laser ablation of various biological tissues, with their respective merits and drawbacks being discussed in depth. A method for modelling the axial intensity profiles produced by various axicons (0.5°, 1°, 2°, 5°, 10° and 20° physical angles, Thorlabs) was established using the Physical Optics Propagation (POP) feature within OpticStudio to simulate the Carbide CB1-05 laser input beam. From this modelling, the 20° axicon (AX2520-B) was selected as the most appropriate option due to it being the only conical lens of the tested range to theoretically achieve peak intensity levels sufficient for obtaining plasma formation in soft biological tissues. The modelled axial intensity range was in good agreement with that observed experimentally via beam characterisation that was performed with a beam expanding telescope of approximately 10x magnification and a CMOS camera, as well as initial material processing trials using acrylic sheets. Characterisation of the curvature of the conical tip was also performed via a Tencor P-7 surface profiler and the deviation from the ideal surface (*i.e.* perfectly sharp tip) was found to only be $10.48 \pm 0.15 \mu\text{m}$. This was determined to be in line with the relatively small magnitude of the intensity fluctuations observed using the CMOS camera to measure the non-reimaged (but appropriately attenuated) Bessel-Gauss beam produced by the 20° axicon with the CB1-05 Carbide laser input beam.

While initial experimental trials on murine intestine samples using a standalone 20° axicon did not demonstrate the expected ablation upon the tissue surface (indicative of a lack of sufficient peak intensities to induce nonlinear absorption processes), a reimaged (1.4x demagnified) Bessel-Gauss beam allowed for consistent plasma-mediated ablation to be achieved. This optical setup was designed using OpticStudio to ensure no clipping occurred at any of the optical elements, while also not compressing the axial intensity profile to the point where the increased depth of focus was insignificant. A Gaussian beam of equivalent spot size was also designed to test alongside the reimaged Bessel-Gauss beam.

The spot sizes of both optical setups (diameters of approximately $3.5 \mu\text{m}$) were verified using a BP209-VIS/M scanning slit beam profiler, and also stainless steel damage threshold tests. Successive ablation trials on murine intestinal tissue were able to confirm sufficient intensities for performing plasma-mediated ablation with the reimaged Bessel-Gauss beam through histological analysis. Higher repetition rates of 10 and 20 kHz led to cavitation bubble formation in the murine intestinal tissue with high spatial overlapping (90% or greater) of the applied $85 \mu\text{J}$ pulses from the Bessel-Gauss beam. Spatial pulse overlapping of 70% at 1 and 2 kHz allowed for tissue removal with high thermal confinement ($< 15 \mu\text{m}$), while spatial pulse overlaps of 90% at 1, 2 and 3 kHz offered increased ablation depths at the same pulse energy, but at the expense of increased thermal damage margins ($< 40 \mu\text{m}$) and even some cavitation bubble formation at 3 kHz. Initial ablation trials on porcine intestinal tissue samples confirmed adequate intensities for plasma-mediated ablation with both optical setups. The beams showed similar ablation characteristics for single passes across the porcine intestinal tissue surfaces at 1 kHz with 70% spatially overlapped $85 \mu\text{J}$ pulses. However, with increased numbers of passes the Bessel-Gauss beam showed a trend of increased ablation depths with 70% spatially overlapped pulses at both 1 and 2 kHz, as well as 90% spatially overlapped pulses

at 1 kHz. Thermal damage margins were again promising across all of these cases ($< 25 \mu\text{m}$). 70% spatially overlapped 85 μJ pulses at 3 kHz in this porcine tissue led to some cavitation being observed with the Gaussian beam, causing thermal damage margins of almost 40 μm .

After vertically mounting the two optical setups side by side to allow for increased throughputs during the intrinsically time restricted tissue ablation tests, more ablation trials on porcine intestinal tissue samples at lower pulse repetition rates (1, 2 and 3 kHz) using higher spatial pulse overlaps were able to showcase very promising ablation depths, particularly for the Bessel-Gauss beam, through both surface profilometry and histological analysis. However, it was also observed that while increasing the spatial overlap of the pulses to 90% or 97% could achieve improved ablation depths for a given number of laser passes for both beams, this came at the expense of increased thermal build up/cavitation effects and longer procedure times, particularly for the latter case. Spatial pulse overlaps of 70% were able to provide distinct ablation depths along with high thermal confinement ($< 20 \mu\text{m}$) for the Bessel-Gauss beam, although for the Gaussian beam the prominence of cavitation bubble formation at both 2 and 3 kHz inhibited the respective ablation processes. While the 70% pulse overlap trials were encouraging for the Bessel-Gauss beam, faster and more efficient sets of parameters were still sought for both beam shapes.

After characterising some surface properties of non-ablated porcine intestine samples to try and quantify the inhomogeneity of the tissue surfaces, another set of ablation trials was performed at higher pulse repetition rates (5, 10 and 20 kHz, with these being limited by the maximum speeds of the LTS150/M translation stages used). These were again able to show promising thermal damage margins for both beams when the applied 85 μJ pulses were sufficiently spaced out by increasing the speeds at which the samples were translated relative to the incoming beams. It was observed that as the spatial overlap of the pulses was increased at these higher repetition rates, it became increasingly difficult to control the overall shape of the ablated volumes.

For the Bessel-Gauss beam, spatial pulse overlaps of up to around 50% at 5, 10 and 20 kHz offered excellent thermal confinement (with damage margins of $< 30 \mu\text{m}$, $< 50 \mu\text{m}$ and $< 25 \mu\text{m}$ respectively) and shape control, but at 70% pulse overlaps the shape of the ablated feature became hard to control despite good thermal confinement ($< 40 \mu\text{m}$). At 10 kHz, 85% spatial pulse overlaps even led to significant observable cavitation bubble formation via histology images, while for this same pulse overlap at 20 kHz some cavitation bubble formation was still observed but to a much lesser degree.

The Gaussian beam was found to be more prone to cavitation effects that inhibited the overall ablation process across all the tested pulse repetition rates in these upscaled ablation trials, with cavitation bubbles being observed in the histology images for spatial pulse overlaps as low as 15% for 5 kHz and 30% for both 10 and 20 kHz. From the histology images it is clear to see that these effects became more pronounced as the pulse repetition rate was increased (*i.e.* the temporal separation of the pulses was reduced), with peak damage margins as high as over 100 μm for 5 kHz, over 200 μm for 10 kHz and over 400 μm for 20 kHz. Conversely, the more consistent spot size of the Bessel-Gauss beam across its comparatively longer focal depth resulted in what appeared to be a higher tolerance to cavitation bubble formation for a given set of ablation parameters, albeit at pulse energies which provided sufficient intensities for both beams to achieve plasma formation. It is worthwhile noting however that the Gaussian beam did perform relatively well with spatial pulse overlaps of 0% (*i.e.* spot separations of 100% or more).

Across all of the ablation trials the reimaged Bessel-Gauss beam showed plasma formation on the tissue surfaces across axial ranges of just over 1 mm at the maximum input pulse energy of 85 μJ for the CB1-05 Carbide laser system. The Gaussian beam was only able to achieve plasma formation across an axial range of just over 400 μm for this same input pulse energy. The lower focal depth led to less consistency across the ablated features produced by the Gaussian beam, although it had the distinct advantage of achieving plasma formation at lower input pulse energies courtesy of the more confined axial intensity distribution.

The reimaged Bessel-Gauss beam on the other hand was able to demonstrate greater tolerances to both the inherent inhomogeneity of the tissue surfaces and to undesirable cavitation effects, while also showcasing a trend for improved ablation depths compared to the Gaussian beam for scans where the total applied laser energy was equated. This increased tolerance to precise focal positioning across the tissue sample surfaces offered by the reimaged Bessel-Gauss beam was also demonstrated via separate high-speed videos for each beam being scanned across porcine skin samples. However, the requirement of a demagnifying telescope and higher input powers to initially achieve consistent plasma formation across the various tested tissue surfaces for the Bessel-Gauss beam is important to note, as efficient transmission of the input laser energy through hollow core negative curvature fibres, while simultaneously avoiding any damage to the distal end optics, is a key consideration for translation towards an endoscopically deployable device.

Both beams were able to exhibit distinct ablation with high thermal confinement for certain parameters. This further highlights fibre delivered ultrashort laser pulses as a promising alternative to either endoscopic submucosal dissection, which carries a higher risk of perforation, or endoscopic full-thickness resection, which relies on triangle tip and insulated tip knives for dissecting the surrounding mucosal and submucosal tissue, as well as coagulation forceps to stop the resultant bleeding.

6.2 Future work

The ultimate goal of this research is to realise an endoscopically deployable device for performing minimally invasive surgical procedures within clinical environments, using ultrafast lasers to reduce collateral thermal damage when removing cancerous tissues. While promise has been showcased from the greater focal depths offered by Bessel-Gauss beams for equivalent spot sizes compared to conventional Gaussian beam shapes, the increased transmission efficiency of the latter (*i.e.* the capacity to achieve intensities that exceed the plasma-mediated ablation threshold of biological tissue at lower input pulse energies) potentially makes it more appealing for undertaking initial investigations into various other technical challenges prior to practical realisation of device designs. These include testing optimal beam scanning/manipulation techniques, microfabrication methods and potential compatibility with fluorescence-guidance for improved targeting of cancerous tissue regions.

With regards to validating an axicon-generated Bessel-Gauss beam for performing plasma-mediated ablation via fibre delivered ultrashort pulses, further experiments would need to be performed to test the effect that the range of angles emitted at the output facet of the fibre has upon the axial intensity distribution subsequently produced by the Bessel-Gauss beam (as opposed to the near normal incidence of the well collimated input beam relative to the planar surface of the axicon used in this work). In addition, further investigations would need to be carried out to address what the optimal conical angle would be for the micro-axicon to be fabricated at the end of this endoscopic probe design. This would need to factor in both the smaller input beam diameter, and thus comparatively more condensed Bessel zone regions than those

generated in this work using the unmodified CB1-05 Carbide laser input beam, as well as the pulse energies subsequently required to achieve consistent plasma formation, while avoiding damage to the hollow core negative curvature fibres. Recent work by Li *et al.* has shown a 20° axicon made from SU-8 photoresist of 100 µm diameter generating a Bessel zone length of over 160 µm (which is significantly greater than the typical 8.512 µm for a 10x conventional objective lens at 532 nm), albeit for low power light-sheet fluorescence microscopy applications [6.1]. Other recent work by Skora *et al.* has tested a 5° axicon of 500 µm diameter made from fused silica using laser-assisted wet etching, which achieved a 5.3 µm central core diameter over 3.5 mm [6.2].

Testing reimaging setups for both smaller and larger conical angles would also be very interesting by offering incredible flexibility in the range of possible spot sizes and focal depths, with smaller conical angles providing larger standoffs from the conical tip (thus being compatible with longer focal length reimaging setups), and larger conical angles providing higher intensities. While the higher standoff and longer axial intensity distributions provided by smaller angle axicons would of further interest to test with higher input pulse energies, the input pulse energy cannot be indefinitely increased due to the design limitations of the fibre input and output facet damage thresholds, as well as those of the fibre itself and the distal end optical components.

However, the conical angle should ideally be used in combination with the reduced input beam diameter to allow for a single axicon to be implemented without the need for a reimaging telescope. This would be optimal as a reimaging telescope would reduce both the overall transmission efficiency and the compatible range of input angles for the incident fibre delivered ultrashort pulses. Regardless, this would entail further theoretical modelling, potentially via the OpticStudio software used in this work, with comparisons being drawn to more conventional microlenses of various focal lengths. The range of potential acceptance angles could be tested by simulating the axicon and microlenses with relative tilt angles as high as those emitted at the extremities of the fibre output beam by factoring in the numerical aperture of these negative curvature fibres [6.3]. This range of acceptance angles is significant as beam scanning would need to be carried out at the distal end of the endoscopic device. Spiral scans would be ideal as this better matches the elliptical shape that cancerous polyps tend to have, as opposed to the rectangular shapes ablated with the raster scans within this work. It also allows for continuous emission as opposed to turning the laser on and off at the raster scan edges for optimal thermal confinement [6.4].

Futhermore, pre-shaping the beam could be potentially of interest, as if a doughnut-shaped input beam were to be used this could theoretically avoid the current manufacturing error of the oblate tip that is inherent to axicons, as may using a reflective axicon design. This would, however, require further optical beam shaping elements placed at the distal end of the fibre (*i.e.* within the endoscopic probe head), further increasing the total dimensions of the design. Alternatively, examining single diffractive optical elements for producing flat-top beams could also be of interest, although similar to a standalone axicon (which is itself a diffractive optical element), the axial range over which the flatness of the super-Gaussian flat-top beam remains constant (and therefore the depth of focus) increases with longer working distances for the single-DOE-based design [6.5]. This could inhibit implementation into an endoscopic device, where working ranges will be innately limited.

In this work the Bessel-Gauss and Gaussian beams were compared by roughly equating the spot sizes they offered. Another interesting avenue of comparison would be to equate the focal depths of the setups (*i.e.* using a larger focused spot size for the Gaussian beam), although this would involve using very different scanning speeds for the two beam shapes. An examination could then be carried out between the merits of the faster scanning speeds courtesy of the larger spot size (and therefore increased removal rates) with the resultant thermal damage margins obtained with both optical setups. Care would have to be taken to ensure appropriate working distances from both setups to make them suitable for potential incorporation into endoscopic probe designs. Additionally, as discussed in the previous chapter, the ablation features produced using higher pulse repetition rates will require further pre-clinical trials using both beam shapes to evaluate the extent of potential cell apoptosis induced by the shockwave generation from the plasma formation.

Recent work published by Subramanian *et al.* shows promise regarding the design of endoscopic probes capable of handling higher peak powers via the implementation of calcium fluoride as the miniaturised objective lens material [6.6]. The use of calcium fluoride prevented strong multiphoton absorption, but the maximum removal rate of bovine cortical bone ($> 0.1 \text{ mm}^3/\text{min}$) was limited by the transmission efficiency (53%) and the total available laser power (0.5 W for the 303 kHz fibre laser used). Beam steering was implemented in this instance using a piezo ceramic tube, with a 14 mm diameter stainless steel casing being incorporated to house all the optical and electrical components. While this probe was able to handle and deliver femtosecond pulses, this study highlights a number of practical limitations still to be overcome, including the total deliverable power and low focal position tolerances ($\pm 125 \text{ }\mu\text{m}$). While the work detailed in this thesis seeks to address the latter, the former issue relating to damage thresholds requires further work to be adequately addressed, which consequently could allow for the extended depths of focus offered by axicons to be further capitalised upon for surgical applications.

Advances in synergistic screening technologies include the relatively recent implementation of machine learning towards tumour diagnosis and predicting recurrence [6.7],[6.8]. This will not only help with detecting tumours earlier in their development cycle and improve targeting of these cancerous tissue regions, but could also result in increased demands in minimally invasive techniques for carrying out subsequent surgical resection. In a similar vein, intraoperative fluorescence imaging using Indocyanine green dye has shown promising early indications for reducing anastomotic leak cases post rectal cancer surgery [6.9],[6.10],[6.11]. This could potentially be paired with the plasma-mediated ultrafast laser ablation covered in this thesis to offer unparalleled precision in colorectal cancer resection procedures. Similar intraoperative feedback has also been verified using $^{99\text{m}}\text{Tc}$ -labelled prostate-specific membrane antigen (PSMA) ligands for radio-guided surgery in nodal metastatic prostate cancer cases [6.12].

The Piccolo research project is similarly focused on advancing early screening and diagnosis of colorectal cancer, proposing a new multimodal photonics endoscope, combining Optical Coherence Tomography (OCT) and Multi-Photon Tomography (MPT) with red-flag fluorescence technology and machine learning to perform *in vivo* diagnosis [6.13],[6.14],[6.15],[6.16]. The use of deep learning techniques have shown promise in improving polyp detection, localisation and classification. Upcoming research endeavours at Heriot-Watt University also seek to combine robotic-assisted surgery with mechanical measurements on the tissue surface to provide a quantitative means of determining optimal surgical margins [6.17].

For resection, recent work by York *et al.* has showcased an electromechanical device that can be integrated with existing endoscopes to focus and steer fibre delivered lasers at high speeds over a large range (± 10 degrees in two axes) with a static repeatability of 200 μm [6.18]. While the working distance of 25 mm is still potentially too long in some instances, scanning speeds of up to 5000 mm/s have been achieved via two piezo-actuated mirrors. Other tissue ablation work carried out by Truong *et al.* looked at using a fibre laser with a diffusing applicator in both *ex vivo* and *in vivo* porcine pancreatic tissue to develop an endoscopic ultrasound guided technique for treating pancreatic cancer [6.19]. While uniform ablation was achieved without carbonisation, the laser used was a continuous wave source which resulted in a significant amount of coagulated tissue. Additionally, the authors state that further miniaturisation of the diffusing applicator would be required to reduce mechanical trauma in clinic, and that porcine pancreatic tissue is not an accurate model for the human equivalent, particularly in the case of cancerous tissue.

Recent studies by Wang *et al.* looked at the use of photodynamic therapy to treat resected tumour margins, reducing the rate of recurrence of prostate tumours in mice models, thus highlighting it as a potential complementary treatment method [6.20]. Other potential complementary technologies include over-the-scope clips, which help to treat gastrointestinal bleeding, and even perforations, although as these clips reach the muscularis layer the risks associated with the removal procedure increase [6.21].

Future endeavours by the research group at Heriot-Watt overseen by Dr. Beck aim to test how laser parameters that worked optimally for ablating porcine intestine translate to other types of tissue, including throat and brain. In addition, characterisation and testing of endoscopic probe designs that incorporate either conventional microlenses or micro-axicons is to be carried out. These could be used in conjunction with the recently developed fibre-optic Raman probes [6.22]. Even with the brief coverage of recent research presented here, it is clear that there remains significant untapped potential for further improving surgical outcomes, reaping the benefits that this would offer both surgeons and patients in the future.

Looking even further forward, and uniting some of the research trends highlighted here, the concept of combining artificial intelligence with robotically controlled surgical tools could enable unparalleled accuracy and repeatability in both the detection and resection of various types of cancerous tissue. Combining this with further developments in ultrafast laser ablation techniques could enable economically viable resection procedures with damage margins down to the single cell scale. Additionally, the potential for automating these robot-controlled ablation processes via the incorporation of *in-vivo* diagnostics using various imaging techniques simultaneously to act as a comprehensive feedback mechanism could reduce both patient waiting lists and current demands on surgeons, with the constant strive for further miniaturisation of endoscopic devices enabling even less invasive procedures. Finally, implementing machine learning techniques to the *in-vivo* diagnostics could allow for these automated procedures to be tailored to each patient.

6.3 References

- [6.1] S. Li *et al.*, “Self-reconstructing Bessel beam created by two-photon-polymerized micro-axicon for light-sheet fluorescence microscopy,” *Results Phys.*, vol. 24, p. 104111, May 2021, doi: 10.1016/J.RINP.2021.104111.
- [6.2] J.-L. Skora *et al.*, “High-fidelity glass micro-axicons fabricated by laser-assisted wet etching,” Oct. 2021, Accessed: Nov. 24, 2021. [Online]. Available: <https://arxiv.org/abs/2110.12212v1>
- [6.3] B. Siwicki, R. M. Carter, J. D. Shephard, F. Yu, J. C. Knight, and D. P. Hand, “Negative-Curvature Anti-Resonant Fiber Coupling Tolerances,” *J. Light. Technol.*, vol. 37, no. 21, pp. 5548–5554, Nov. 2019, doi: 10.1109/JLT.2019.2937210.
- [6.4] R. J. Beck *et al.*, “Dynamics of picosecond laser ablation for surgical treatment of colorectal cancer,” *Sci. Rep.*, vol. 10, no. 1, Dec. 2020, doi: 10.1038/S41598-020-73349-W.
- [6.5] A. Brodsky *et al.*, “Generating flat-top beams with extended depth of focus,” *Appl. Opt. Vol. 57, Issue 16, pp. 4583-4589*, vol. 57, no. 16, pp. 4583–4589, Jun. 2018, doi: 10.1364/AO.57.004583.
- [6.6] A. Ben-Yakar *et al.*, “Ultrafast laser surgery probe with a calcium fluoride miniaturized objective for bone ablation,” *Biomed. Opt. Express, Vol. 12, Issue 8, pp. 4779-4794*, vol. 12, no. 8, pp. 4779–4794, Aug. 2021, doi: 10.1364/BOE.426149.
- [6.7] C. McGenity, A. Wright, and D. Treanor, “AIM in Surgical Pathology,” *Artif. Intell. Med.*, pp. 1–18, 2021, doi: 10.1007/978-3-030-58080-3_278-1.
- [6.8] A. Z. Paredes *et al.*, “A Novel Machine-Learning Approach to Predict Recurrence After Resection of Colorectal Liver Metastases,” *Ann. Surg. Oncol. 2020 2713*, vol. 27, no. 13, pp. 5139–5147, Aug. 2020, doi: 10.1245/S10434-020-08991-9.
- [6.9] A. Arezzo *et al.*, “Intraoperative use of fluorescence with indocyanine green reduces anastomotic leak rates in rectal cancer surgery: an individual participant data analysis,” *Surg. Endosc.*, vol. 34, no. 10, pp. 4281–4290, Oct. 2020, doi: 10.1007/S00464-020-07735-W.
- [6.10] S. Morales-Conde *et al.*, “Fluorescence angiography with indocyanine green (ICG) to evaluate anastomosis in colorectal surgery: where does it have more value?,” *Surg. Endosc. 2019 349*, vol. 34, no. 9, pp. 3897–3907, Oct. 2019, doi: 10.1007/S00464-019-07159-1.
- [6.11] S. Hayami *et al.*, “Visualization and quantification of anastomotic perfusion in colorectal surgery using near-infrared fluorescence,” *Tech. Coloproctol.*, vol. 23, no. 10, pp. 973–980, Oct. 2019, doi: 10.1007/S10151-019-02089-5.
- [6.12] M. Mix *et al.*, “^{99m}Tc-labelled PSMA ligand for radio-guided surgery in nodal metastatic prostate cancer: proof of principle,” *EJNMMI Res.*, vol. 11, no. 1, pp. 1–9, Mar. 2021, doi: 10.1186/S13550-021-00762-1/TABLES/3.
- [6.13] J. F. Ortega-Morán *et al.*, “Medical needs related to the endoscopic technology and colonoscopy for colorectal cancer diagnosis,” *BMC Cancer*, vol. 21, no. 1, pp. 1–12, Dec. 2021, doi: 10.1186/S12885-021-08190-Z/TABLES/2.
- [6.14] C. L. Saratxaga *et al.*, “Characterization of Optical Coherence Tomography Images for Colon Lesion Differentiation under Deep Learning,” *Appl. Sci. 2021, Vol. 11, Page 3119*, vol. 11, no. 7, p. 3119, Apr. 2021, doi: 10.3390/APP11073119.
- [6.15] E. Terradillos *et al.*, “Analysis on the Characterization of Multiphoton Microscopy Images for Malignant Neoplastic Colon Lesion Detection under Deep Learning Methods,” *J. Pathol. Inform.*, vol. 12, no. 1, p. 27, 2021, doi: 10.4103/JPI.JPI_113_20.
- [6.16] L. F. Sánchez-Peralta *et al.*, “PICCOLO White-Light and Narrow-Band Imaging Colonoscopic Dataset: A Performance Comparative of Models and Datasets,” *Appl. Sci. 2020, Vol. 10, Page 8501*, vol. 10, no. 23, p. 8501, Nov. 2020, doi: 10.3390/APP10238501.
- [6.17] ““Mechanically-intelligent” Intra-operative Tissue Assessment for Robot-Assisted Surgery (MIRAS).” <https://gow.epsrc.ukri.org/NGBOViewGrant.aspx?GrantRef=EP/V047612/1> (accessed Nov. 14, 2021).
- [6.18] P. A. York, R. Peña, D. Kent, and R. J. Wood, “Microbotic laser steering for minimally invasive surgery,” *Sci. Robot.*, vol. 6, no. 50, Jan. 2021, doi:

- [6.19] D. H. Lee *et al.*, “Endoscopic ultrasound (EUS)-guided cylindrical interstitial laser ablation (CILA) on in vivo porcine pancreas,” *Biomed. Opt. Express*, Vol. 12, Issue 7, pp. 4423-4437, vol. 12, no. 7, pp. 4423–4437, Jul. 2021, doi: 10.1364/BOE.427379.
- [6.20] X. Wang *et al.*, “Photodynamic Therapy Is an Effective Adjuvant Therapy for Image-Guided Surgery in Prostate Cancer,” *Cancer Res.*, vol. 80, no. 2, pp. 156–162, Jan. 2020, doi: 10.1158/0008-5472.CAN-19-0201.
- [6.21] Y. H. Ou *et al.*, “Methods for Endoscopic Removal of Over-the-Scope Clip: A Systematic Review,” *Canadian Journal of Gastroenterology and Hepatology*, vol. 2020. Hindawi Limited, 2020. doi: 10.1155/2020/5716981.
- [6.22] C. A. Ross *et al.*, “A Miniature Fibre-Optic Raman Probe Fabricated by Ultrafast Laser-Assisted Etching,” *Micromachines 2020, Vol. 11, Page 185*, vol. 11, no. 2, p. 185, Feb. 2020, doi: 10.3390/M11020185.

Appendix 1

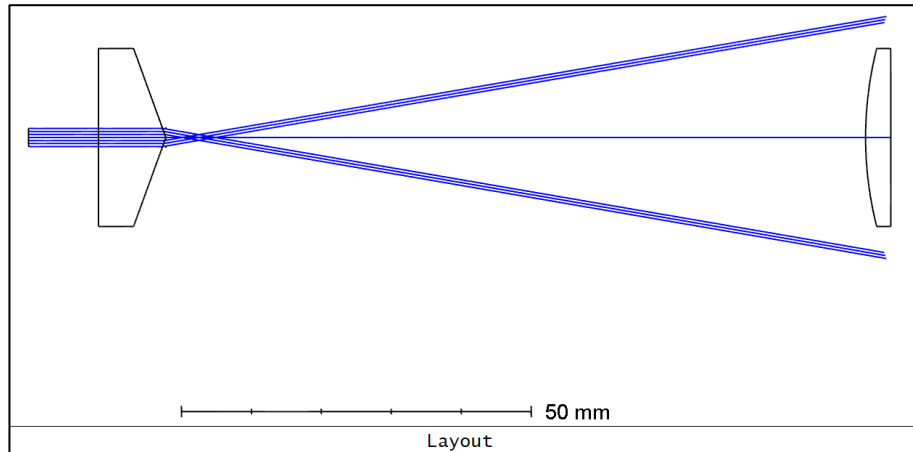


Figure 1a - Ray trace showcasing the clipping that occurs upon placing a 100 mm focal length plano-convex (LA1509-B, Thorlabs) lens a distance equal to its specified front focal length away from the conical tip of the 20° axicon. The axicon has its planar surface illuminated by a 2.6 mm $1/e^2$ diameter Gaussian input beam to simulate that produced by the CB1-05 Carbide laser.

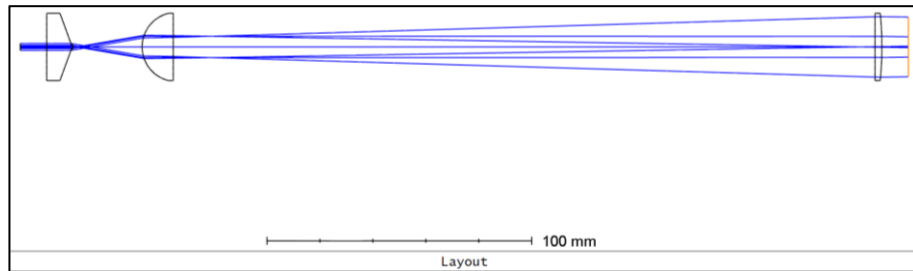


Figure 1b - Ray trace showcasing lack of beam clipping along the approximately 10x magnification telescope. This was achieved by placing a 25.4 mm focal length plano-convex (LA1951-B, Thorlabs) lens a distance slightly greater than its specified front focal length away from the conical tip of the 20° axicon, followed by a 250 mm focal length lens to obtain the desired extent of beam expansion. Again, the axicon has its planar surface illuminated by a 2.6 mm $1/e^2$ diameter Gaussian input beam to simulate that produced by the CB1-05 Carbide laser.

Appendix 2

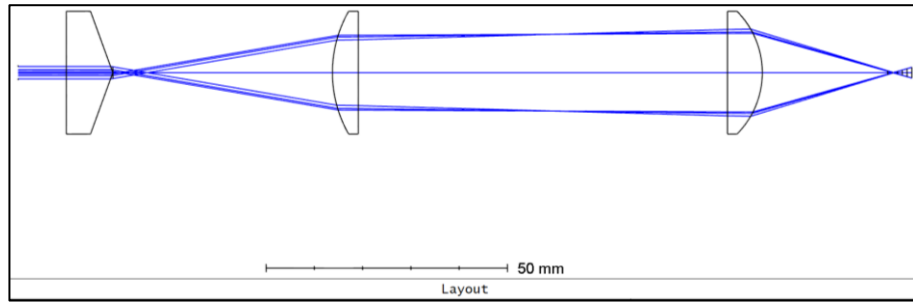


Figure 2a - Ray trace of 1.4x demagnified 20° axicon setup, using 50 mm and 35 mm focal length plano-convex lenses (LA1131-B and LA1027-B respectively, Thorlabs). The axicon again has its planar surface illuminated by a 2.6 mm $1/e^2$ diameter Gaussian input beam to simulate that produced by the CB1-05 Carbide laser.

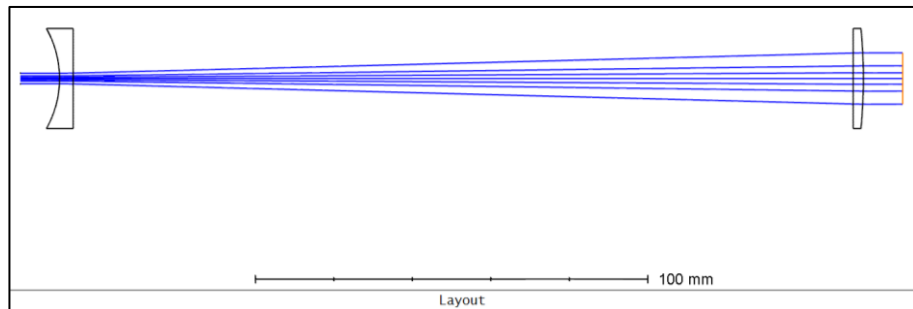


Figure 2b - Ray trace of 5x beam expander. The - 50 mm focal length concave lens has its curved surface illuminated by a 2.6 mm $1/e^2$ diameter Gaussian input beam to simulate that produced by the CB1-05 Carbide laser.

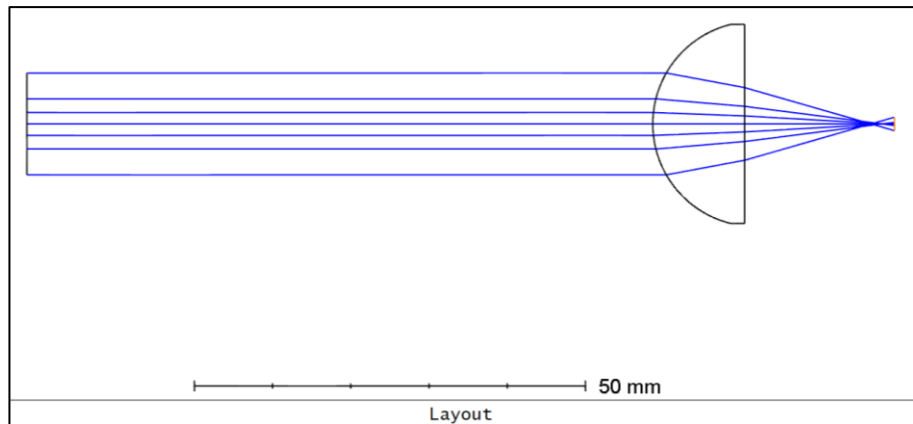


Figure 2c - Ray trace of the focussing 25.4 mm focal length convex lens. The input beam is modelled using the output beam properties of the 5x beam expanding telescope simulated previously to closely replicate those produced by the beam expander after being illuminated by the CB1-05 Carbide laser output. The curved surface of the lens is placed facing the incident collimated beam to reduce the spherical aberration.

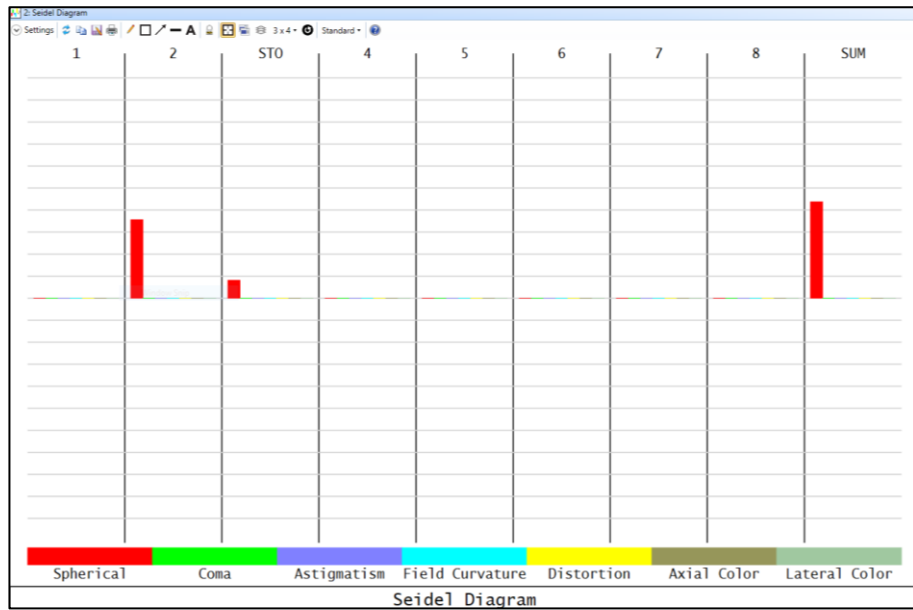


Figure 2d - Seidel plot of the simulated 25.4 mm focusing lens setup, showing the spherical aberration induced by the relatively high curvature of the lens. Aberration gridlines are spaced at 0.05 mm. Surface 2 corresponds to the curved surface of the lens. This plot shows that the spherical aberration is the only source of aberration in the system (in the simulated case of perfectly orthogonal alignment).